

Laser deposition-additive manufacturing of ceramics and ceramic reinforced  
composites

by

Yingbin Hu, B.S., M.S.

A Dissertation

In

Industrial, Manufacturing, and Systems Engineering

Submitted to the Graduate Faculty  
of Texas Tech University in  
Partial Fulfillment of  
the Requirements for  
the Degree of

DOCTOR OF PHILOSOPHY

Approved

Dr. Weilong Cong  
Chair of Committee

Dr. Hong-Chao Zhang

Dr. Changxue Xu

Dr. Nurxat Nuraje

Mark Sheridan  
Dean of the Graduate School

August, 2019

Copyright 2019, Yingbin Hu

**Dedication**

To my beloved family.

## ACKNOWLEDGMENTS

I am deeply indebted to my advisor, Dr. Weilong Cong, for his continually guidance and persistent help in regard to research and scholarship. I want to thank him for the freedom he has granted me to explore research directions and generate ideas on solving technical problems.

I would wish to express my appreciations to my committee members, Dr. Hong-Chao Zhang, Dr. Changxue Xu, and Dr. Nurxat Nuraje, who have made valuable and constructive suggestions on my dissertation. I would also render my warmest thanks to Dr. Wei Li to serve as the Dean's representative for my defense.

I am truly grateful for having such wonderful colleagues of Dr. Cong's research group, Dr. Fuda Ning, Mr. Hui Wang, Mr. Dongzhe Zhang, Mr. Yuanchen Li, and Mr. Xinlin Wang. I treasure every moment that we have in the journey toward completing my doctoral degree. Many great ideas of the dissertation are inspired by the technical discussions with them.

My sincere and special gratitude goes to my beloved wife Jinna Gu and my parents. Without their endless love and unconditional support, this dissertation would not have been completed and I would not be who I am now.

At last, I would like to give my gratitude to the Graduate School at Texas Tech University for awarding me the Doctoral Dissertation Completion Fellowship, which enables me to dedicate my time exclusively to dissertation research in the final year of my Ph.D. study.

## TABLE OF CONTENTS

<b>ACKNOWLEDGMENTS .....</b>	<b>iii</b>
<b>ABSTRACT .....</b>	<b>x</b>
<b>LIST OF TABLES .....</b>	<b>xii</b>
<b>LIST OF FIGURES .....</b>	<b>xiii</b>
<b>I. INTRODUCTION .....</b>	<b>1</b>
1.1 Introduction of high-performance materials .....	1
1.1.1 Zirconia toughened alumina (ZTA) .....	1
1.1.2 TiB reinforced titanium matrix composites (TiB-TMCs).....	1
1.2 Introduction of laser deposition-additive manufacturing process .....	2
1.3 Structures and objectives of this dissertation .....	3
References .....	6
<b>II. A REVIEW ON LD-AM OF CERAMICS AND CERAMIC REINFORCED COMPOSITES .....</b>	<b>9</b>
Abstract .....	10
2.1 Introduction .....	10
2.2 Laser deposition-additive manufacturing process.....	15
2.3 Bulk parts fabrication by laser deposition.....	18
2.3.1 Ceramics.....	18
2.3.1.1 Al <sub>2</sub> O <sub>3</sub> ceramics .....	18
2.3.1.2 ZTA and other ceramics .....	20
2.3.2 Ceramic reinforced MMCs .....	22
2.3.2.1 Ti-based composites.....	22
2.3.2.2 Other composites.....	24
2.4 Laser cladding .....	25
2.4.1 Ceramics.....	26
2.4.1.1 High wear performance applications .....	26
2.4.1.2 Biomedical applications .....	27
2.4.1.3 Other applications .....	27
2.4.2 Ceramic reinforced MMCs .....	27
2.4.2.1 High wear performance applications .....	27
2.4.2.2 Biomedical applications .....	29

2.4.2.3 Other applications .....	29
2.5 Existing main issues, corresponding solutions, and trend of development.....	30
2.5.1 Poor bonding problem in bulk parts fabrication and cladding.....	30
2.5.1.1 Optimizing process parameters .....	30
2.5.1.2 Adding a buffer layer / functionally gradient composite layers.....	30
2.5.1.3 Integrating with assisting technology of ultrasonic vibration .....	32
2.5.2 Cracking problem in bulk parts fabrication and cladding.....	33
2.5.2.1 Optimizing process parameters .....	33
2.5.2.2 Pre- /post- heating .....	35
2.5.2.3 Adding additive materials .....	36
2.5.2.4 Integrating with assisting technology of ultrasonic vibration .....	37
2.5.3 Lowered toughness problem in bulk parts fabrication.....	38
2.5.3.1 Tailoring novel microstructure.....	38
2.5.3.2 Integrating with assisting technology of ultrasonic vibration .....	40
2.6 Concluding Remarks .....	41
References .....	43
<b>III. LENS OF ZTA – EFFECTS OF ULTRASONIC VIBRATION .....</b>	<b>51</b>
Abstract .....	52
3.1 Introduction .....	52
3.2 Experimental procedures.....	55
3.2.1 Powder materials and powder treatment .....	55
3.2.2 Experimental set-up and parameters .....	57
3.2.3 Measurement procedures .....	58
3.3 Results and discussion .....	59
3.3.1 Effects of ultrasonic vibration on crack suppression under different laser power .....	59
3.3.2 Effects of ultrasonic vibration on microstructure.....	61
3.3.3 Effects of ultrasonic vibration on mechanical properties.....	65
3.3.3.1 Effects on microhardness .....	65
3.3.3.2 Effects on wear resistance .....	66
3.3.3.3 Effects on compressive properties .....	67

3.4 Conclusions .....	69
References .....	71
<b>IV. LENS OF ZTA – NOVEL MICROSTRUCTURE FORMATION AND MECHANICAL PERFORMANCE .....</b>	<b>75</b>
Abstract .....	76
4.1 Introduction .....	76
4.2 results and discussion.....	79
4.2.1 Effects of ZrO <sub>2</sub> content on microstructure characterizations.....	79
4.2.1.1 Three-dimensional quasi-continuous network microstructure.....	80
4.2.1.2 Eutectic microstructure .....	82
4.2.2 Effects of ZrO <sub>2</sub> content on mechanical properties .....	85
4.2.2.1 Effects on microhardness .....	85
4.2.2.2 Effects on fracture toughness .....	86
4.3 Conclusions .....	89
4.4 Materials and Methods.....	90
4.4.1 Powder materials and powder treatment .....	90
4.4.2 Experimental set-up and parameters .....	91
4.4.3 Measurement procedures .....	92
References .....	94
<b>V. SURFACE GRINDING OF ZTA PARTS FABRICATED BY LENS – EFFECTS OF ZRO2 CONTENT AND ULTRASONIC VIBRATION .....</b>	<b>97</b>
Abstract .....	98
5.1 Introduction .....	98
5.2 Experimental set-up and measurement procedures.....	101
5.2.1 Powder materials and powder treatment.....	101
5.2.2 Experimental set-up .....	102
5.2.3 Experimental conditions.....	103
5.2.4 Measurement procedures .....	104
5.3 Experiment result and discussion.....	105
5.3.1 Effects on microstructure .....	105
5.3.2 Effects on surface quality.....	107
5.3.2.1 Effects on flatness .....	108
5.3.2.2 Effects on surface roughness.....	109

5.3.2.3 Effects on cutting force in feeding direction.....	110
5.4 Conclusions .....	112
References .....	114
<b>VI. LENS OF TiB-TMCS – MICROSTRUCTURE AND WEAR PERFORMANCE .....</b>	<b>117</b>
Abstract .....	118
6.1 Introduction .....	118
6.2 Experiments and measurements procedures .....	120
6.2.1 Powder materials and powder treatment .....	120
6.2.2 Experimental set-up and experimental conditions .....	121
6.2.2.1 Experimental set-up .....	121
6.2.2.2 Experimental conditions.....	122
6.2.3 Phase analysis and microstructure characterization.....	123
6.2.4 Mechanical properties testing .....	123
6.3 Experiment result and discussion.....	124
6.3.1 Morphologies of the powders and the parts’ surfaces.....	124
6.3.2 Phase identification and microstructure analysis .....	126
6.3.3 Mechanical behavior .....	131
6.3.3.1 Effects on hardness .....	131
6.3.3.2 Effects on wear resistance .....	133
6.4 Conclusions .....	135
References .....	136
<b>VII. LENS OF TiB-TMCS – TiB GROWTH AND PART PERFORMANCE .....</b>	<b>141</b>
Abstract .....	142
7.1 Introduction .....	142
7.2 Experiments and measurements procedures .....	145
7.2.1 Powder materials and powder treatment .....	145
7.2.2 Experimental conditions.....	146
7.2.3 Measurement procedures .....	147
7.3 Experiment results and discussion .....	147
7.3.1 TiB growth .....	147
7.3.2 Part performance .....	150

7.3.2.1 Effects of laser power on density .....	150
7.3.2.2 Effects of Z-axis increment on density .....	151
7.3.2.3 Effects of laser power on microhardness .....	153
7.3.2.4 Effects of Z-axis increment on microhardness.....	154
7.3.2.5 Effects on compressive properties .....	155
7.4 Conclusions .....	157
References .....	159
<b>VIII. LENS OF TIB-TMCS – IN-SITU ULTRAFINE 3DQCN MICROSTRUCTURE.....</b>	<b>162</b>
Abstract .....	163
8.1 Introduction .....	163
8.2 Experiments and measurements procedures .....	164
8.3 Experiment Result and Discussion .....	165
8.3.1 Formation mechanisms .....	165
8.3.2 Microstructural characterizations.....	167
8.3.3 Mechanical properties .....	169
8.4 Conclusions .....	170
References .....	171
<b>IX. LENS OF TIB-TMCS – EFFECTS OF 3DQCN ON STRENGTHENING AND TOUGHENING.....</b>	<b>173</b>
Abstract .....	174
9.1 Introduction .....	174
9.2 Experiments and measurements procedures .....	176
9.2.1 Powder materials and powder treatment.....	176
9.2.2 Experimental set-up and experimental conditions .....	177
9.2.3 Measurement procedures .....	179
9.3 Results and discussion .....	182
9.3.1 Microstructure characterizations.....	182
9.3.2 Compressive properties.....	185
9.3.2.1 Strengthening mechanism .....	185
9.3.2.2 Toughening mechanism and fracture features .....	189

9.4 Conclusions .....	192
References .....	194
<b>X. CONCLUSIONS &amp; SCIENTIFIC CONTRIBUTIONS.....</b>	<b>199</b>
10.1 Conclusions .....	199
10.2 Scientific contributions .....	201
<b>A. PUBLICATIONS DURING PH.D. STUDY .....</b>	<b>203</b>

## **ABSTRACT**

High-performance materials, including ceramics and ceramic reinforced metal matrix composites (MMCs), are widely used in severe working conditions and have been applied in biomedical, aerospace, electronic, and other high-end engineering industries owing to their superior properties of high wear resistance, outstanding chemical inertness, and excellent properties at elevated temperatures. Among all types of high-performance materials, zirconia toughened alumina (ZTA) is favored due to the toughening effects induced by  $ZrO_2$ . In addition, the mechanical properties of zirconia toughened alumina (ZTA) can be controlled via changing  $ZrO_2$  content and powder preparation (such as changing particle shape or size) for specific applications. As another type of high-performance materials, TiB reinforced titanium matrix composites (TiB-TMCs) have attracted a great amount of attentions and been extensively investigated due to the specific benefits introduced by TiB reinforcement. Firstly, TiB is a stable phase since there is no intermediate phase between TiB and titanium (Ti). Secondly, TiB and Ti have similar densities and thermal expansion coefficients, therefore, thermal stresses at their interfaces can be minimized. Thirdly, the strength of TMCs can be effectively enhanced by adding a small amount of TiB.

The superior properties of high-performance materials, on the other hand, make it difficult to process these materials with conventional manufacturing methods, posing problems of high cost and energy consumptions. In addition, difficulties arise when fabricating complex-shaped components with these conventional manufacturing processes. Recently, a competitive manufacturing method, additive manufacturing (AM) with high design flexibility, high customization, lowered cost and energy usage, has gained popularity in fabrication of these high-performance materials. However, problems of low toughness, cracks, poor part quality, etc. still exist in AM manufactured high-performance materials. Facing to these problems, it is of great importance to develop new high-performance materials through establishing efficient and effective processes and tailoring novel microstructures.

In this dissertation, a comprehensive literature review on laser deposition-

additive manufacturing (LD-AM) of ceramics and ceramic reinforced metal matrix composites is provided. Main issues to be solved, corresponding solutions, and the trend of development are summarized and discussed. Afterwards, efforts have been made to provide engineering solutions to the existing problems in high-performance materials fabricated by LD-AM. An ultrasonic vibration-assisted LD-AM is established to reduce fabrication defects (such as porosities and cracks) in ZTA. The introduction of ultrasonic vibration is proven to be beneficial for refining grains, homogenizing material dispersion, smoothing out thermal gradient and thermal stress, reducing defects, and enhancing mechanical properties of fabricated parts. In addition to manufacturing process, the ultrasonic vibration is also effective in assisting machining process. For the purpose of reducing low precision problem (such as low dimensional accuracy and bad surface finish), a nontraditional rotary ultrasonic machining process is utilized to post-process LAM-fabricated ZTA parts. In order to reduce low toughness and ductility in TiB-TMCs, a novel network microstructure is tailored and the formation mechanism of such a microstructure is investigated. Experimental results evidence that the presence of this network microstructure is beneficial for toughening and strengthening LD-AM-fabricated TiB-TMCs.

## LIST OF TABLES

2.1.	AM processes for fabricating ceramics and ceramic reinforced MMCs .....	12
2.2.	Summary of ceramics fabricated by LD-AM process .....	19
2.3.	Chemical composition of Al <sub>2</sub> O <sub>3</sub> powder .....	20
2.4.	Summary of ceramic reinforced MMCs fabricated by LD-AM process.....	22
3.1.	Input fabrication variables .....	58
4.1.	Input fabrication variables .....	92
5.1.	Input fabrication variables .....	103
5.2.	Machining parameters and tool variables.....	104
6.1.	Wear performance of CP-Ti parts and TiB-TMCs.....	132
7.1.	Input fabrication variables in an experiment matrix.....	146
7.2.	Fixed input fabrication variables .....	146
8.1.	Comparisons of the microhardness and compressive properties.....	169
9.1.	Input fabrication variables .....	179
9.2.	Properties and parameters.....	187
9.3.	Compressive properties of CP-Ti parts and TiB-TMCs.....	188

## LIST OF FIGURES

1.1.	Schematic illustration of LD-AM process.....	3
2.1.	Schematic illustration of direct SLS and SLM processes. ....	14
2.2.	Part reparation using LENS [44]. (Photo courtesy of Optomec Inc.) .....	15
2.3.	Schematic illustration of LD-AM process.....	15
2.4.	Effects of relationship between Z-axis increment and layer thickness in LD-AM process. ....	17
2.5.	(a) Raster, (b) offset from inside to outside, (c) offset from outside to inside, and (d) fractal scanning patterns within one layer and (e) zigzag scanning pattern for multiple layers. ....	18
2.6.	LD-AM fabricated ZTA parts with different shapes: (a) Arc wall [59]; (b) Cylinder [59]; and (c) Cube [2]. (Reprinted from Ref. [59], copyright (2015), with permission from Emerald Publishing Limited; Reprinted from Ref. [2], copyright (2018), with permission from Elsevier). ....	21
2.7.	Eutectic microstructure of a LD-AM fabricated ZTA part [1]. (Reprinted from Ref. [1], copyright (2015), with permission from Elsevier). ....	21
2.8.	TiB growth: (a) Scanning electron microscope (SEM) image of cross-sectional TiB reinforcement; Schematic illustration of (b) trigonal prism building block and (c) crystal structure of TiB. (Reprinted from Ref. [64], copyright (2017), with permission from Springer).....	23
2.9.	Electron backscatter diffraction micrographs showing crystal structure characterizations of LD-AM fabricated Inconel 625 and TiC reinforced Inconel 625 matrix composite parts [80]. (Reprinted from Ref. [80], copyright (2015), with permission from Elsevier). ....	25
2.10.	A SEM image showing the dispersion of spherical CaF <sub>2</sub> in inter-plate regions of Al <sub>2</sub> O <sub>3</sub> matrix [55]. (Reprinted from Ref. [55], copyright (2002), with permission from Elsevier). ....	26
2.11.	Schematic illustration of two types of LD-AM fabricated structures with high wear resistance and low friction coefficient. ....	28
2.12.	A cross-section of coating layers observed by SEM imaging [48]. (Reprinted from Ref. [48], copyright (2007), with permission from Elsevier).....	31

2.13. A structure of step-wise FGC materials. ....	32
2.14. Actions and influences of ultrasonic vibration in ultrasonic vibration-assisted melting and solidification processes. (after [2, 96-100]) .....	33
2.15. Effects of ultrasonic vibration on crack suppression under different levels of laser power. (Reprinted from Ref. [2], copyright (2018), with permission from Elsevier). ....	34
2.16. (a) A fabricated Al <sub>2</sub> O <sub>3</sub> part with cracks and a (b) fabricated ZTA part without cracks [59]. (Reprinted from Ref. [59], copyright (2015), with permission from Emerald Publishing Limited). ....	37
2.17. 3DQCN microstructure within TiB reinforced TMCs fabricated by LD-AM process. (a) A stereo corner of a part; Detailed microstructures of (b) top side, (c) left side, and (d) right side. (Reprinted from Ref. [62], copyright (2017), with permission from Elsevier). ....	38
2.18. (a) A SEM image on cross-section of a ZTA part; (b) & (c) Element analysis on cross-section of the part by EDXS mapping. (Reprinted from Ref. [2], copyright (2018), with permission from Elsevier). ....	39
2.19. Toughening mechanisms and crack propagation in a ZTA part. (Reprinted from Ref. [2], copyright (2018), with permission from Elsevier). ....	39
2.20. Effects of ultrasonic vibration on compressive properties of the parts fabricated by LD-AM process. (Reprinted from Ref. [2], copyright (2018), with permission from Elsevier). ....	41
3.1. Schematic illustration of LENS process. ....	53
3.2. Actions and influences of ultrasonic vibration in ultrasonic vibration-assisted melting and solidification processes (after [24-26]). ....	55
3.3. Shapes and morphologies of the powders. ....	56
3.4. Schematic illustrations of ultrasonic vibration-assisted LENS experimental set-up. ....	57
3.5. Effects of ultrasonic vibration on crack suppression under different laser power. ....	60
3.6. Element analysis on cross-sections of parts fabricated without and with ultrasonic vibration by EDXS mapping. ....	62
3.7. Crack propagation and toughening mechanisms in ZTA. ....	63

3.8. Microstructure analysis on cross-sections of parts fabricated at laser power of 400 W. ....	64
3.9. Effects of ultrasonic vibration on microhardness of the parts fabricated by LENS process (UV: ultrasonic vibration). ....	65
3.10. Effects of ultrasonic vibration on wear resistance of the parts fabricated by LENS process (UV: ultrasonic vibration). ....	66
3.11. Effects of ultrasonic vibration on compressive properties of the parts fabricated by LENS process (UV: ultrasonic vibration). ....	67
3.12. Fracture features in compressive tests. ....	68
4.1. A schematic of the LD-AM process. ....	78
4.2. Microstructures on cross-sections of ZTA parts with different ZrO <sub>2</sub> contents. ....	79
4.3. SEM images and EBSD mapping analyses on a ZTA part with 10 wt.% ZrO <sub>2</sub> : (a) a SEM image with low magnification; (b) a SEM image with high magnification; (c) EBSD mapping analysis on (a); and (d) EBSD mapping analysis on (b). ....	80
4.4. Schematic illustration of the formation mechanism of 3DQCN microstructure. ....	81
4.5. Eutectic microstructure on the cross-section of a ZTA part with 41.5 wt.% ZrO <sub>2</sub> : (a) colonies; (b) boundaries of colonies; and (c) three-way intersectional structure. ....	82
4.6. EDXS mapping analyses on a ZTA part with 41.5 wt.% ZrO <sub>2</sub> : (a) eutectic microstructure; (b) detailed features on the eutectic microstructure; and EDXS element maps for (c) Al element, (d) Zr element, (e) and Y element. ....	83
4.7. TEM analysis on a ZTA part with 41.5 wt.% ZrO <sub>2</sub> : (a) BF image and (b) SAED patterns of tetragonal ZrO <sub>2</sub> with zone axis (ZA) = [113]. ....	84
4.8. (a) Part of the ZrO <sub>2</sub> -Al <sub>2</sub> O <sub>3</sub> phase diagram (redrawing from the [28]); (2) Alternative nucleation of ZrO <sub>2</sub> and Al <sub>2</sub> O <sub>3</sub> ; and (3) A schematic of the coupled growth of ZrO <sub>2</sub> and Al <sub>2</sub> O <sub>3</sub> during eutectic solidification. ....	85
4.9. Effects of ZrO <sub>2</sub> content on microhardness. ....	86

4.10. An indentation mark and toughening mechanisms in the ZTA part with 10 wt.% ZrO <sub>2</sub> .....	87
4.11. Effects of ZrO <sub>2</sub> content on fracture toughness. ....	88
4.12. Crack propagations in (a) the ZTA part with 10 wt.% ZrO <sub>2</sub> and (b) the ZTA part with 41.5 wt.% ZrO <sub>2</sub> .....	88
4.13. Shapes and morphologies of powders: As-received (a) Al <sub>2</sub> O <sub>3</sub> and (b) Y <sub>2</sub> O <sub>3</sub> -stabilized ZrO <sub>2</sub> powders; and (c) mixed powders with 10 wt.% ZrO <sub>2</sub> (for illustration purpose).....	91
5.1. Illustration of LENS process. ....	99
5.2. Illustration of rotary ultrasonic machining (RUM). ....	100
5.3. Shapes and morphologies of the powders. ....	101
5.4. RUM experimental set-up. ....	102
5.5. Microstructure analysis on cross-sections of LENS-fabricated parts.....	105
5.6. EDXS analysis on a ZTA part with 10 wt.% ZrO <sub>2</sub> content: (a) a SEM image and phase composition results at (b) boundary area and (c) matrix area. ....	106
5.7. LENS-fabricated ZTA parts (prior to RUM process).....	107
5.8. Surface topography analysis. ....	107
5.9. Effects of ZrO <sub>2</sub> content and ultrasonic vibration on flatness. ....	108
5.10. Effects of ZrO <sub>2</sub> content and ultrasonic vibration on surface roughness. ....	109
5.11. Effects of ZrO <sub>2</sub> content and ultrasonic vibration on cutting force in feeding direction.....	110
5.12. Effects of ZrO <sub>2</sub> content on microhardness of LENS-fabricated parts.....	111
6.1. LENS experimental set-up. ....	122
6.2. SEM imaging observed shapes and morphologies of the as-received (a) CP-Ti powder and (b) B powder as well as four-hour ball milling mixed CP-Ti and B powders (c) at lower and (d) at higher magnifications, respectively.....	125

6.3.	SEM imaging observed top surface morphologies of LENS-fabricated (a) CP-Ti part and (b) TiB-TMC. ....	125
6.4.	(a) SEM image of TiB-TMC after polishing and corresponding EDX maps on spatial distributions for (b) Ti element and (c) B element.....	126
6.5.	SEM imaging of microstructures of TiB-TMCs processed at 200 W: (a) Flower-like microstructure; (b) Crosslinking microstructure; (c) Quasi-continuous network microstructure (perpendicular to deposition direction); and (d) Quasi-continuous network microstructure (parallel to deposition direction). SEM imaging of microstructures of TiB-TMCs processed at 125 W: (e) Perpendicular to deposition direction; and (f) Parallel to deposition direction. ....	127
6.6.	The initial (a) and indexed (b) Kikuchi EBSD patterns derived from TiB. ....	128
6.7.	Illustrations of 3DQCN microstructure formation mechanism in LENS.....	129
6.8.	SEM imaging observed cross-section morphologies of (a) CP-Ti at 125 W; (b) CP-Ti at 200 W; (c) TiB-TMC at 125 W; and (d) TiB-TMC at 200 W (after polishing). ....	130
6.9.	Effects of TiB reinforcement and laser power on microhardness of the fabricated parts. ....	131
6.10.	(a) Depths after dry sliding wear tests under different conditions; (b) Effects of TiB reinforcement and laser power on wear rate of the fabricated parts. ....	133
6.11.	Worn surfaces of CP-Ti part at (a) lower magnification and (b) higher magnification as well as TiB-TMC at (c) lower magnification and (d) higher magnification.....	134
7.1.	Illustration of LD-AM process. ....	144
7.2.	SEM morphologies of (a) the as-received CP-Ti powder, (b) the as-received B powder, and (c) the four-hour premixed CP-Ti and B powders.....	145
7.3.	Phase composition analysis of a TiB-TMC sample: (a) SEM image; EDXS spectrums for compositions of (b) spectrum 1 and (c) spectrum 2. ....	148
7.4.	Formation mechanism of the flower-like microstructure: (a) Tomography image of TiB distribution among Ti matrix; Schematic illustration of TiB growth (b) before LD-AM process and (c) after LD-AM process. ....	149

7.5. TiB growth: (a) SEM image of cross-sectional TiB reinforcement; Schematic illustration of (b) trigonal prism building block and (c) crystal structure of TiB.....	149
7.6. Effects of laser power on density. ....	150
7.7. Optical Microscope (OM) imaging of cross sections of CP-Ti parts processed at (a) 125 W, (b) 150 W, (c) 175 W, and (d) 200 W laser power with the same magnification.....	151
7.8. Effects of Z-axis increment on density.....	152
7.9. Optical Microscope (OM) imaging of cross sections of CP-Ti parts processed at (a) 0.30 mm, (b) 0.36 mm, (c) 0.42 mm, and (d) 0.48 mm Z-axis increment with the same magnification. ....	152
7.10. Illustration of relationship between Z-axis increment and layer thickness. ....	153
7.11. Effects of laser power on microhardness.....	153
7.12. Effects of Z-axis increment on microhardness. ....	154
7.13. Compressive true stress-strain curves of TiB-TMCs and CP-Ti parts processed at different laser power. ....	155
7.14. Fracture features: (a) CP-Ti part at lower magnification; (b) CP-Ti part at higher magnification; (c) TiB-TMC at lower magnification; and (d) TiB-TMC at higher magnification. ....	157
8.1. Formation mechanisms of 3DQCN microstructure in (a) RHP (sintering), (b) casting, and (c) LENS processes.....	166
8.2. SEM observations of ultrafine 3DQCN microstructure: (a) The stereo corner taken from the fabricated parts; Detailed microstructure of (b) top side, (c) left side, and (d) right side. ....	167
8.3. SEM observations of TiB-TMCs microstructure characterizations: Processed at 125 W laser power at (a) low and (b) high magnifications; Processed at 200 W laser power at (c) low and (d) high magnifications. ....	168
9.1. Planetary ball milling process. (a) As-received CP-Ti powder; (b) As-received B powder; (c) Schematic illustration of ball milling process; (d) Four-hour ball milling mixed CP-Ti and B powders; and (e) High-magnification of a single CP-Ti particle with B particles embedded on the surface.....	177

9.2. Schematic illustration of LENS experimental set-up. ....	178
9.3. The cross-section of TiB-TMC with randomly distributed line segments. ....	180
9.4. SEM analysis on (a) a stereo corner image taken from the fabricated part and detailed 3DQCN microstructures on the (b) top side, (c) left side, and (d) right side. ....	181
9.5. EBSD analysis on TiB-rich region showing the (a) initial and (b) indexed Kikuchi patterns.....	182
9.6. Schematic illustration of the formation mechanism of 3DQCN microstructure.....	183
9.7. Effects of laser power on microstructures of the parts processed at (a) 125 W, (b) 150 W, (c) 175 W, and (d) 200 W, respectively. ....	184
9.8. Effects of laser power on yield strengths of CP-Ti parts and TiB-TMCs. ....	188
9.9. Illustration of different failures modes in compressive tests.....	190
9.10. Crack profiles in compressive tests. ....	191
9.11. Fracture features in compressive tests.....	191

## CHAPTER I

### INTRODUCTION

#### 1.1 Introduction of high-performance materials

##### 1.1.1 Zirconia toughened alumina (ZTA)

Alumina ceramics,  $\text{Al}_2\text{O}_3$ , are widely used in the high-end engineering, biomedical, and chemical industries [1, 2]. The widespread usage is attributed to their superior properties of high strength, good biocompatibility, and excellent corrosion and thermal resistance [1]. Despite these benefits,  $\text{Al}_2\text{O}_3$  show inferior reliability and shortened lifetime due to their low fracture toughness [3]. Facing to this problem, zirconia toughened alumina composites, ZTA, are fabricated to improve reliability and elongate lifetime of  $\text{Al}_2\text{O}_3$  by providing higher fracture toughness, as compared with pure  $\text{Al}_2\text{O}_3$  [3].

Laser additive manufacturing (LAM) is proved to be a successful process for fabrication of ZTA parts. The LAM mainly includes powder bed-based selective laser melting (SLM) process and laser deposition-additive manufacturing (LD-AM) process. Hagedorn et al. successfully fabricated almost 100% dense ZTA by SLM process [4]. To reduce cracks generated by thermal stress, the powder bed was preheated above  $1600^\circ\text{C}$  by a  $\text{CO}_2$  laser. Niu et al. fabricated cylindrical and arc-shaped structures from eutectic ZTA powders by LD-AM process [5]. Compared with the SLM process, the LD-AM process exhibits advantages of smaller part deformability, lower labor intensity, and higher fabrication efficiency [6]. However, the LD-AM fabricated ceramic parts still have problems of cracking, poor surface quality, low dimensional accuracy, etc. [5]. It is desirable to find solutions to the problems existed in LD-AM of ZTA.

##### 1.1.2 TiB reinforced titanium matrix composites (TiB-TMCs)

Titanium (Ti) and its alloys are widely applied to aeronautical, automobile, and biomedical industries due to their high strength-to-weight ratio and outstanding biocompatibility [7]. However, the poor wear resistance restricts Ti and its alloys'

applications in fabrication of parts (e.g. gears and bearings [8], jet engine compressors [3], etc.) those will work under severe wear conditions. Adding ceramic reinforcement is considered as an effective way of improving wear resistance of titanium matrix composites (TMCs) [7, 10]. In order to obtain TMCs with desired part quality and properties, it is important to choose proper ceramic reinforcements. Up till now,  $\text{Al}_2\text{O}_3$  [11], SiC [12], TiN [10], TiC [13], TiB [7], etc. are proved to be beneficial for enhancing TMCs' wear resistance. Among all these ceramic reinforcements, TiB is considered as an ideal reinforcement due to the following reasons. Firstly, owing to the compatible densities and thermal expansion coefficients between TiB and Ti, the residual stress within TMCs can be hugely reduced [14]. Secondly, a relatively small amount of TiB can hugely increase the TMCs' modulus and strength [15].

Laser additive manufacturing (LAM), which exhibits benefits of low manufacturing cost for small-scale production, no need of tooling or molding, free from complexity, short lead time, etc., has attracted a great amount of attentions [16]. As LAM processes, SLM and LD-AM processes are reported to be successfully applied in fabrication of ceramic reinforced TMCs. Based on a layer by layer powder spreading mechanism, SLM can produce near-full-dense parts with good mechanical properties. Compared with SLM, the LD-AM process demonstrates some specific advantages, including capabilities of parts remanufacturing and functionally gradient composite (FGC) materials fabrication, small heat-affected zone, etc. [16, 17]. Up till now, there are still many problems (such as lowered toughness), which need to be solved, in the LD-AM of ceramic reinforced TMCs.

## **1.2 Introduction of laser deposition-additive manufacturing process**

Cladding, performed by laser deposition of thin layers onto the substrate's surface, has been widely applied to improve surface properties (e.g. biocompatibility, wear resistance, oxidation and corrosion resistance, etc.) of the components (e.g. medical implants, cutting tools, heat exchanger tubes, etc.), those will be subjected to specific or severe working conditions [18-24]. Besides cladding, the laser deposition process also demonstrates its feasibility of producing near-net-shape parts by building

multiple layers [25]. LD-AM process is one of rapid prototyping processes that has been widely used for producing bulk metallic and ceramic parts [4,16,26]. Figure 1.1 shows the schematic illustration of LD-AM process. At the beginning, the substrate is selectively melted by heat from laser radiation, forming a molten pool which catches and melts powders supplied by the powder stream. When the laser beam moves away, the molten pool starts to solidify as a consequence of heat dissipation. The deposition head moves along the trajectory designed by a 3D file, forming the first layer. Afterwards, the deposition head ascends one layer thickness to the new set position for the next layer deposition. Served as the new “substrate”, the first layer is partially melted with the formation of the second layer. Similar process will be repeated until the designed near-net-shape component is built layer by layer [27]. In this dissertation, LD-AM process is performed on a laser engineered net shaping (LENS) machine.

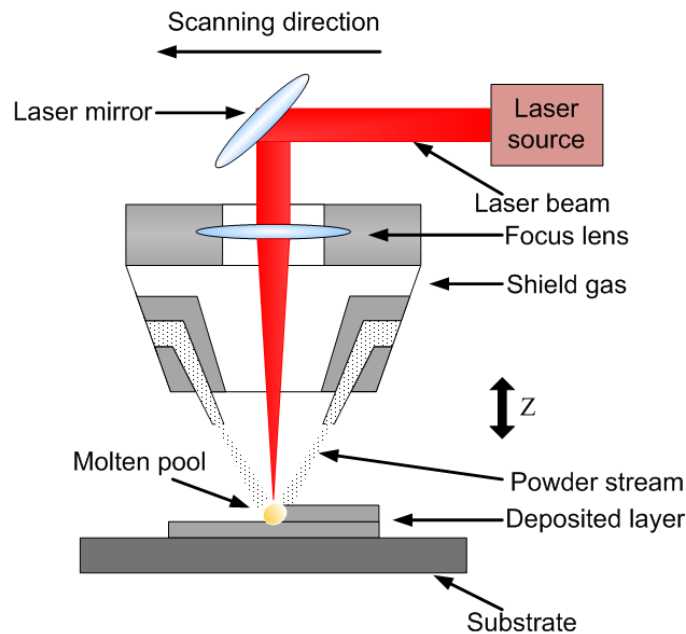


Figure 1.1 Schematic illustration of LD-AM process.

### 1.3 Structures and objectives of this dissertation

This dissertation consists ten chapters. Chapter I gives an introduction of the dissertation. Then, a literature review on laser deposition-additive manufacturing of

ceramics and ceramic reinforced composites is given in Chapter II. Chapters III ~ V present investigations on LENS of ZTA and surface grinding of ZTA parts fabricated by LENS. Research projects on LENS of TiB-TMCs are discussed in Chapter VI ~ IX. Afterwards, conclusions and contributions of this dissertation are given in Chapter X.

The objectives of the dissertation are in four folds, including (1) establishing an efficient and effective process for manufacturing of ceramic reinforced composites and ceramics, (2) generating knowledge and advancing fundamental understanding on laser deposition – additive manufacturing of ceramic reinforced composites and ceramics, (3) solving the problems existed and filling the gaps in the literature on laser deposition – additive manufacturing and fabrication of ceramic reinforced composites and ceramics, and (4) providing guidance on developing new materials with new technologies. The specific research tasks are as follows:

### **LENS of ZTA**

- Establishing a novel ultrasonic vibration-assisted LENS process for fabrication of bulk ZTA parts to reduce cracking problem and investigating the effects of ultrasonic vibration on crack suppression, microstructure, and mechanical properties of the fabricated parts;
- Identifying the significance of  $ZrO_2$  content on microstructure formation and mechanical performance of LENS fabricated ZTA parts;
- Developing a post-processing rotary ultrasonic machining method to surface-grind LENS fabricated ZTA parts to achieve better surface finish.

### **LENS of TiB-TMCs**

- Building the governing processing-microstructure-property relationships in LENS fabricated TiB-TMCs;
- Providing engineering solutions to toughen TiB-TMCs through tailoring 3DQCN microstructure;

- Exploring formation mechanisms of novel microstructures, such as 3DQCN microstructure and cross-linking microstructure;
- Developing models to build relationships between processing parameters and mechanical properties.

## References

- [1] De Portu, G., Fiori, C., & Sbaizero, O. (1986). Fabrication, microstructure, and properties of ZrO<sub>2</sub>-toughened Al<sub>2</sub>O<sub>3</sub> substrates. *Advances in Ceramics*, 24, 1063-1073.
- [2] Deville, S., Chevalier, J., Fantozzi, G., Bartolomé, J. F., Requena, J., Moya, J. S., Torrecillas, R., & Díaz, L. A. (2003). Low-temperature ageing of zirconia-toughened alumina ceramics and its implication in biomedical implants. *Journal of the European Ceramic Society*, 23(15), 2975-2982.
- [3] Lin, J. T., & Lu, H. Y. (1988). Grain growth inhibition and mechanical property enhancement by adding ZrO<sub>2</sub> to Al<sub>2</sub>O<sub>3</sub> matrix. *Ceramics International*, 14(4), 251-258.
- [4] Hagedorn, Y. C., Wilkes, J., Meiners, W., Wissenbach, K., & Poprawe, R. (2010). Net shaped high performance oxide ceramic parts by selective laser melting. *Physics Procedia*, 5, 587-594.
- [5] Niu, F. Y., Wu, D. J., Ma, G. Y., Wang, J. T., Guo, M. H., & Zhang, B. (2015). Nanosized microstructure of Al<sub>2</sub>O<sub>3</sub>- ZrO<sub>2</sub> (Y<sub>2</sub>O<sub>3</sub>) eutectics fabricated by laser engineered net shaping. *Scripta Materialia*, 95, 39-41.
- [6] Atwood, C. J., Smugeresky, J. E., & Gill, D. D. (2006). Laser engineered net shaping (LENS) for the repair and modification of NWC metal components. Sandia National Laboratories, No. SAND2006-6551.
- [7] Attar, H., Prashanth, K. G., Zhang, L. C., Calin, M., Okulov, I. V., Scudino, S., Yang, C., & Eckert, J. (2015). Effect of powder particle shape on the properties of in situ Ti-TiB composite materials produced by selective laser melting. *Journal of Materials Science & Technology*, 31(10), 1001-1005.
- [8] Guo, C., Zhou, J. S., Chen, J. M., Zhao, J. R., Yu, Y. J., & Zhou, H. D. (2010). Improvement of the oxidation and wear resistance of pure Ti by laser cladding at elevated temperature. *Surface and Coatings Technology*, 205(7), 2142-2151.
- [9] Grögler, T., Zeiler, E., Franz, A., Plewa, O., Rosiwal, S. M., & Singer, R. F. (1999). Erosion resistance of CVD diamond-coated titanium alloy for aerospace applications. *Surface and Coatings Technology*, 112(1), 129-132.
- [10] Balla, V. K., Bhat, A., Bose, S., & Bandyopadhyay, A. (2012). Laser processed TiN reinforced Ti6Al4V composite coatings. *Journal of the Mechanical Behavior of Biomedical Materials*, 6, 9-20.
- [11] Gülsoy, H. Ö., Özbey, S., Pazarlioglu, S., Çiftci, M., & Akyurt, H. (2016). Sintering and mechanical properties of titanium composites reinforced nano sized Al<sub>2</sub>O<sub>3</sub> particles. *International Journal of Materials, Mechanics and Manufacturing*, 4(2), 111-114.
- [12] Das, M., Balla, V. K., Kumar, T. S., Bandyopadhyay, A., & Manna, I. (2016). Tribological, electrochemical and in vitro biocompatibility properties of SiC reinforced composite coatings. *Materials & Design*, 95, 510-517.
- [13] Zhang, Y. Z., Wei, Z. M., Shi, L. K., & Xi, M. Z. (2008). Characterization of laser powder deposited Ti-TiC composites and functional gradient materials. *Journal of Materials Processing Technology*, 206(1), 438-444.

- [14] Gorsse, S., Le Petitcorps, Y., Matar, S., & Rebillat, F. (2003). Investigation of the Young's modulus of TiB needles in situ produced in titanium matrix composite. *Materials Science and Engineering: A*, 340(1), 80-87.
- [15] Tamirisakandala, S., Miracle, D. B., Srinivasan, R., & Gunasekera, J. S. (2006). Titanium alloyed with boron. *Advanced Materials and Processes*, 164(12), 41-43.
- [16] Gu, D. D., Meiners, W., Wissenbach, K., & Poprawe, R. (2012). Laser additive manufacturing of metallic components: materials, processes and mechanisms. *International Materials Reviews*, 57(3), 133-164.
- [17] Hu, Y. B, Ning, F. D, Wang, X. L, Wang, H., Zhao, B., Cong, W. L., & Li, Y. Z. (2017). Laser deposition-additive manufacturing of in situ TiB reinforced titanium matrix composites: TiB growth and part performance. *The International Journal of Advanced Manufacturing Technology*, doi:10.1007/s00170-017-0769-0.
- [18] Xu, X., Han, J., Wang, C., & Huang, A. (2016). Laser cladding of composite bioceramic coatings on titanium alloy. *Journal of Materials Engineering and Performance*, 25(2), 656-667.
- [19] Gao, Y. L., Wang, C. S., Yao, M., & Liu, H. B. (2007). The resistance to wear and corrosion of laser-cladding Al<sub>2</sub>O<sub>3</sub> ceramic coating on Mg alloy. *Applied Surface Science*, 253(12), 5306-5311.
- [20] Yu, Z., Wang, H., & Li, M. (2012). Microstructure and mechanical properties of an in situ synthesized TiB and TiC reinforced titanium matrix composite coating. *Journal of Wuhan University of Technology-Mater. Sci. Ed.*, 27(1), 1-8.
- [21] Mateos, J. J. M. E., Cuetos, J. M., Fernandez, E., & Vijande, R. (2000). Tribological behaviour of plasma-sprayed WC coatings with and without laser remelting. *Wear*, 239(2), 274-281.
- [22] Guo, C., Zhou, J. S., Chen, J. M., Zhao, J. R., Yu, Y. J., & Zhou, H. D. (2011). High temperature wear resistance of laser cladding NiCrBSi and NiCrBSi/WC-Ni composite coatings. *Wear*, 270(7), 492-498.
- [23] Wang, H. M., Yu, Y. L., & Li, S. Q. (2002). Microstructure and tribological properties of laser clad CaF<sub>2</sub>/Al<sub>2</sub>O<sub>3</sub> self-lubrication wear-resistant ceramic matrix composite coatings. *Scripta Materialia*, 47(1), 57-61.
- [24] Khanna, A. S., Kumari, S., Kanungo, S., & Gasser, A. (2009). Hard coatings based on thermal spray and laser cladding. *International Journal of Refractory Metals and Hard Materials*, 27(2), 485-491.
- [25] Toyserkani, E., Khajepour, A., & Corbin, S. F. (2004). *Laser cladding*. CRC press.
- [26] Griffith, M. L., Keicher, D. M., Atwood, C. L., Romero, J. A., Smugeresky, J. E., Harwell, L. D., & Greene, D. L. (1996). Free form fabrication of metallic components using laser engineered net shaping (LENS). In *Proceedings of the Solid Freeform Fabrication Symposium* (pp. 125-131). Austin, TX: University of Texas at Austin.
- [27] Atwood, C., Ensz, M., Greene, D., Griffith, M., Harwell, L., Reckaway, D., Romero, T., Schlienger, E., & Smugeresky, J. (1998). *Laser engineered net*

shaping (LENS (TM)): a tool for direct fabrication of metal parts (No. SAND98-2473C). Sandia National Laboratories, Albuquerque, NM, and Livermore, CA.

## CHAPTER II

### A REVIEW ON LD-AM OF CERAMICS AND CERAMIC REINFORCED COMPOSITES

Paper title:

A review on laser deposition-additive manufacturing of ceramics and ceramic reinforced metal matrix composites

Published in:

Ceramics International, 2018, Vol. 44, No. 17, pp. 20599-20612

Authors' names:

Yingbin Hu<sup>a</sup>, and Weilong Cong<sup>a,\*</sup>

Authors' affiliations:

<sup>a</sup>Department of Industrial, Manufacturing, & Systems Engineering, Texas Tech University, Lubbock, Texas, 79409, USA

\*Corresponding author:

Department of Industrial, Manufacturing, & Systems Engineering, Texas Tech University, Lubbock, TX 79409-3061, USA. Email address: weilong.cong@ttu.edu

## **Abstract**

Ceramics and ceramic reinforced metal matrix composites (MMCs) are widely used in severe working conditions and have been applied in biomedical, aerospace, electronic, and other high-end engineering industries owing to their superior properties of high wear resistance, outstanding chemical inertness, and excellent properties at elevated temperatures. These superior properties, on the other hand, make it difficult to process these materials with conventional manufacturing methods, posing problems of high cost and energy consumptions. In response to this problem, direct additive manufacturing (AM), which is equipped with a high-power-density laser beam as heat source, has been developed and extensively employed for processing ceramics and ceramic reinforced MMCs. Compared with other direct AM processes, laser deposition-additive manufacturing (LD-AM) process excels in several aspects, such as lower labor intensity, higher fabrication efficiency, and capabilities of parts remanufacturing and functionally gradient composite materials fabrication. Besides these benefits, problems of poor bonding, cracking, lowered toughness, etc. still exist in LD-AM fabricated parts. This paper reviews developments on LD-AM of ceramics and ceramic reinforced MMCs in both bulk parts fabrication and cladding. Main issues to be solved, corresponding solutions, and the trend of development are summarized and discussed.

## **Keywords**

B. Composites; B. Defects; C. Mechanical properties; D. Traditional ceramics; Laser deposition-additive manufacturing.

## **2.1 Introduction**

Ceramics and ceramic reinforced metal matrix composites (MMCs) demonstrate superior properties of high modulus and strength, good wear resistance, outstanding chemical inertness, and excellent properties at elevated temperatures [1-4]. Owing to the benefits exhibited, ceramics and ceramic reinforced MMCs have been widely used in severe working conditions (e.g. high-load condition, high-wear/friction condition, high-temperature condition, etc. [3, 5, 6]) and gain their

popularity in many commercial applications, including biomedical (e.g. acetabular cups, dental restoration frameworks, etc. [7, 8]), aerospace (e.g. engine components, heat-resistant tiles, etc. [9]), electronic (e.g. insulators, transducers, etc. [10]) and other high-end engineering (e.g. machining tools, bearing components, etc. [11, 12]) industries.

Because of their high hardness and high melting point, ceramics and ceramic reinforced MMCs are difficult to process by conventional manufacturing methods [13-16]. Zhang et al. published a work on diamond grinding of hot-pressed  $\text{Si}_3\text{N}_4$ , hot-pressed  $\text{Al}_2\text{O}_3$ , slip-casted  $\text{ZrO}_2$ , and sintered  $\text{SiC}$  ceramics [16]. Hot-pressing, slip-casting, and sintering caused high cost and energy consumptions. In addition, damages of pulverization and microcracking were induced by grinding. With increased competitiveness, additive manufacturing (AM) has attracted a great deal of attentions and is under intensive investigations for fabricating ceramics and ceramic reinforced MMCs [1, 2, 4, 17-32]. AM is described by the American Society for Testing and Materials (ASTM) as “a process of joining materials to make objects from 3D model data, usually layer upon layer, as opposed to subtractive manufacturing technologies” [33]. Compared with conventional manufacturing methods, AM has extended capability of fabricating complex-shaped parts and benefits of high design flexibility, high customization, shortened lead time, no need of assembly or molds, lowered energy use, etc. [34, 35].

Table 2.1 AM processes for fabricating ceramics and ceramic reinforced MMCs

Process	Type of starting material	Layer creation technique	Ceramic / Ceramic reinforced MMC	refs
<b>Indirect</b>	FDM	Filament	Ceramic Ceramic reinforced MMC	[17] [18]
	SLA	Photocurable resin and powders	Ceramic	[19-21]
	DIP	Powder suspension	Ceramic	[22]
	LSD	Slurry	Ceramic Ceramic reinforced MMC	[23] [24]
<b>Direct</b>	LOM	Sheet	Ceramic Ceramic reinforced MMC	[25] [26]
	Direct SLS	Powder in bed	Ceramic Ceramic reinforced MMC	[27] [28]
	SLM	Powder in bed	Ceramic Ceramic reinforced MMC	[29] [30]
	LD-AM	Powder injected through nozzle	Ceramic Ceramic reinforced MMC	[1, 2, 31] [4, 32]

Table 1 provides a summary of AM processes for fabricating ceramics and ceramic reinforced MMCs. It can be seen that AM mainly includes indirect AM method and direct AM method. In indirect AM method (e.g. fused deposition modeling (FDM), stereolithography (SLA), direct inkjet printing (DIP), layer-wise slurry deposition (LSD), laminated object manufacturing (LOM), etc.), preliminary 3D structures (green bodies) are built with binder materials. Afterwards, the green bodies are sintered to eliminate the binder materials and densified by conventional manufacturing processes. Different from indirect AM method, direct AM method combines the forming and densification procedures and generates final components without post-sintering process. Therefore, direct AM method can produce components with relatively higher density, higher purity, better mechanical properties, less energy- and time-consuming, as compared with indirect AM method [36, 37]. In addition, direct AM method uses a laser as heat source and the laser has high directionality and high energy intensity and can deliver a great amount of energy to a micro-scale focal region, being capable of processing a wide range of materials [38].

Direct selective laser sintering (direct SLS) used to be a dominant direct AM process in fabrication of ceramics and ceramic reinforced MMCs [27, 28]. However, due to the fact that direct SLS can only partially melt starting powders and fabricated parts have low density and poor mechanical properties, the applications of direct SLS are restricted. To meet the requirement of producing near-full-dense parts with better mechanical properties, selective laser melting (SLM), which can fully melt starting powders, has been developed [39]. A schematic illustration of direct SLS and SLM is shown in Figure 2.1. At first, the substrate is driven downward by a mounted build piston, leaving one-layer-thickness space. Then, a powder distributor doses a certain amount of powder and evenly spreads the supplied powder on the substrate to fill the space. The generated laser beam, which is controlled and directed by X-Y scanning mirrors and an f- $\theta$  lens, selectively melts the powder and forms the first layer. Afterwards, the substrate descends another layer thickness for the next layer creation. Layer upon layer, the designed near-net-shape component will be fabricated by

repeating these steps [40].

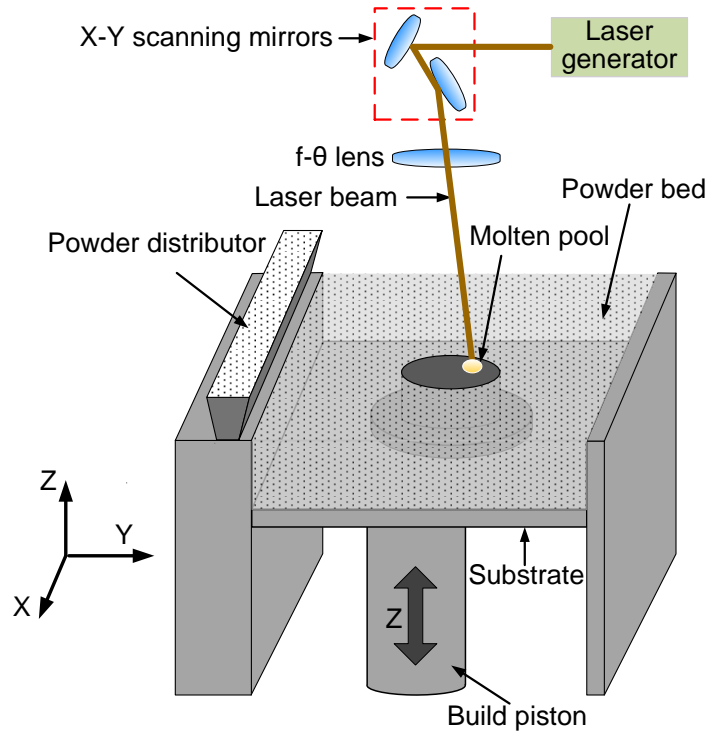


Figure 2.1 Schematic illustration of direct SLS and SLM processes.

In comparison with powder-bed based direct SLS and SLM processes, laser deposition-additive manufacturing (LD-AM, mainly including laser engineered net shaping (LENS) and direct metal deposition (DMD)) process possesses advantages of lower labor intensity and higher fabrication efficiency and shows capabilities of parts remanufacturing and functionally gradient composite (FGC) materials fabrication [41-43]. Figure 2.2 shows a part being repaired by LENS process [44]. Besides these benefits, problems of poor bonding, cracking, lowered toughness, etc. exist in LD-AM of ceramics and ceramic reinforced MMCs [2, 4, 45]. For the purpose of reducing or solving the problems mentioned above, researchers have been dedicated to understanding formation mechanisms of these problems and seeking solutions to them. The solutions include (but are not limited to) optimizing process parameters, adding a buffer layer / FGC layers, integrating with assisting technology of ultrasonic vibration,

pre- / post- heating, adding additive materials, tailoring novel microstructure, etc. [1, 2, 4, 31, 42, 46-62]. This paper reviews developments on LD-AM of ceramics and ceramic reinforced MMCs. In addition, main issues to be solved, corresponding solutions, and the trend of development are also discussed.



Figure 2.2 Part repairation using LENS [44]. (Photo courtesy of Optomec Inc.)

## 2.2 Laser deposition-additive manufacturing process

Figure 2.3 shows the schematic illustration of LD-AM process. At the beginning, the substrate is selectively melted by heat from laser radiation, forming a molten pool which catches and melts powders supplied by a powder stream. When the

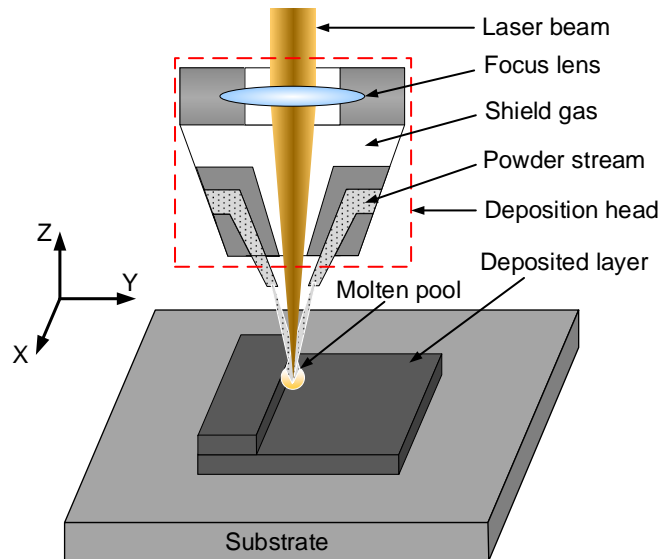


Figure 2.3 Schematic illustration of LD-AM process.

laser beam moves away, the molten pool starts to solidify as a consequence of heat dissipation. The deposition head moves along the designed trajectory based on a 3D file, forming the first layer on the substrate. Afterwards, the deposition head ascends one layer thickness to a new set position for the next layer deposition. Served as the new “substrate”, the first layer is partially melted with the formation of the second layer. Similar steps will be repeated many times until the designed near-net-shape component is built layer by layer [36].

In LD-AM process, part quality depends on energy input which can be controlled via changing process parameters of laser power, scanning speed, hatch distance, and powder feeding rate [63]. Besides energy input, layer thickness will also be determined by these process parameters. It is of great importance to set layer thickness as Z-axis increment since the mismatch between layer thickness and Z-axis increment will impair energy utilization and negatively affect dimensional accuracy along Z direction, thus resulting in poor part quality (such as low density [64]) or even failure of part fabrication. As shown in Figure 2.4, if the Z-axis increment value equals the layer thickness (Case 1), the focal point will be on the top surface of each layer and the layer thickness will be uniform. After fabrication of the first layer, if the focal point is above the top surface (Case 2), the laser energy input will be weakened, generating a thinner second layer. The distance between the focal point and the top surface of the second layer will be even further, generating even thinner third layer. The layers fabricated will be thinner and thinner until nothing will be further fabricated. After fabrication of the first layer, if the focal point is below the top surface (Case 3), the laser energy input will be reduced, generating a thinner second layer, comparing with the first layer. Then, the distance between the top surface of the second layer and the focal point will be smaller and then a thicker third layer is generated, in comparison with the second layer. Based on analysis, it can be concluded that Case 1 is the ideal case which exhibits following advantages: (1) The layer thickness is uniform and the build height can be expected; (2) The laser energy input

for each layer is stable, rendering uniform properties of fabricated layers; (3) The laser energy can be efficiently and effectively utilized.

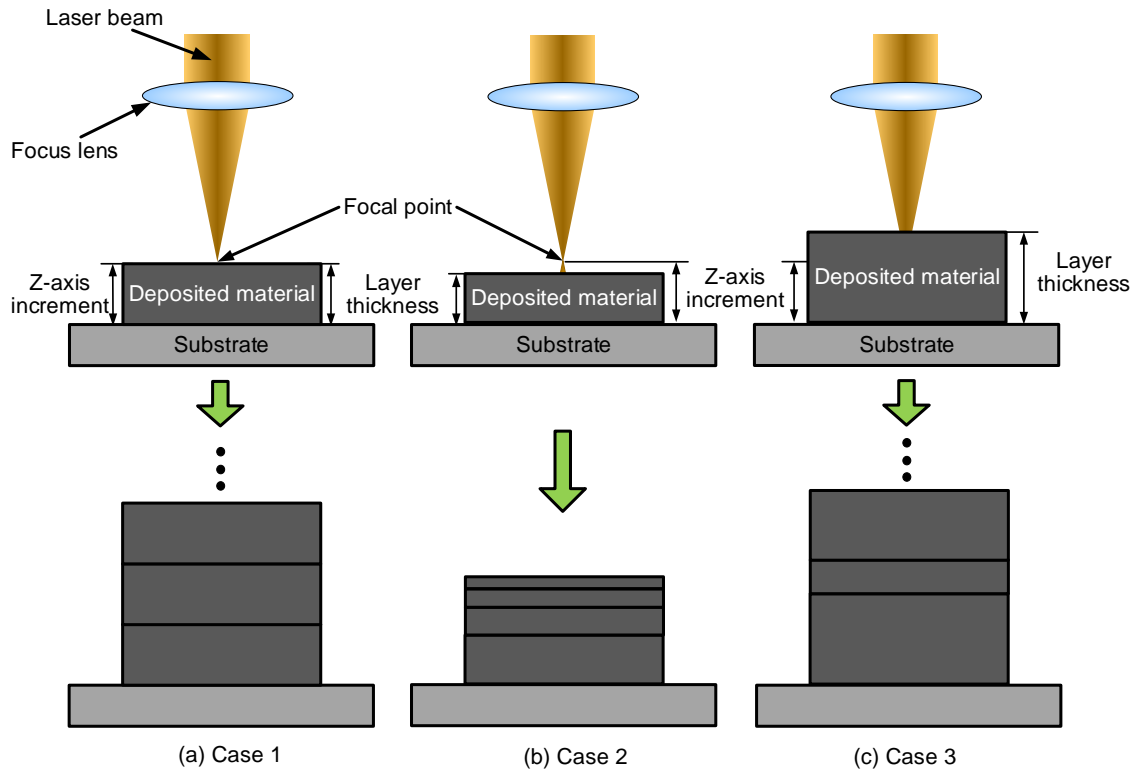


Figure 2.4 Effects of relationship between Z-axis increment and layer thickness in LD-AM process.

Within each layer, there are four common scanning patterns, including raster, offset from inside to outside, offset from outside to inside, and fractal patterns, as shown in Figures 2.5(a)-5(d) [65]. Yu et al. conducted research on effects of scanning patterns on part distortion and part quality in LD-AM process. Results showed that the offset from outside to inside and fractal patterns generated smaller thermal gradient, smaller substrate deformation, and better part quality, as compared with raster and offset from inside to outside patterns. For multiple layers, Hu et al. reported a zigzag scanning pattern with  $90^\circ$  orientation changing for each layer, as shown in Figure 2.5(e) [36]. Such scanning pattern could attenuate side effects of high thermal stress and part distortion induced by scanning orientation.

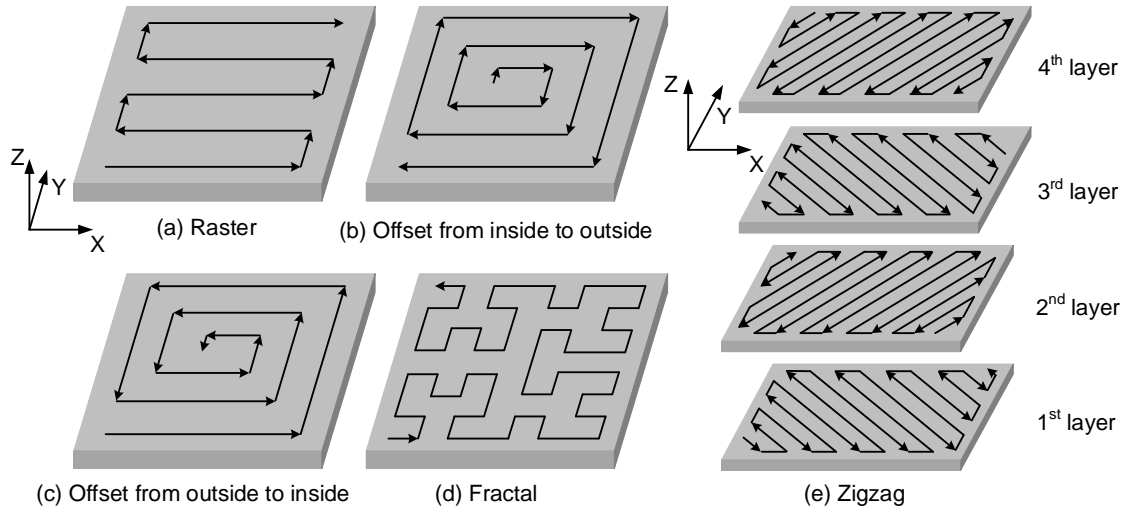


Figure 2.5 (a) Raster, (b) offset from inside to outside, (c) offset from outside to inside, and (d) fractal scanning patterns within one layer and (e) zigzag scanning pattern for multiple layers.

## 2.3 Bulk parts fabrication by laser deposition

On account of the capability of depositing multiple layers, LD-AM demonstrates its feasibility of producing near-net-shape parts.

### 2.3.1 Ceramics

Equipped with high-power-density laser beams, LD-AM process finds applications in processing high hardness and high-melting-point (up to 3000°C) ceramics, such as  $\text{Al}_2\text{O}_3$  and  $\text{ZrO}_2$  toughened  $\text{Al}_2\text{O}_3$  (ZTA) [1, 31, 52, 59, 66]. A summary on ceramics fabricated by LD-AM process is provided in Table 2.

#### 2.3.1.1 $\text{Al}_2\text{O}_3$ ceramics

Balla et al. successfully fabricated dense and net-shaped structures (e.g. cylinder, cube, gear, etc.) of  $\text{Al}_2\text{O}_3$  by LD-AM process [31]. Experimental results showed that columnar grains formed along the build direction and fabricated parts exhibited anisotropy in mechanical properties. In Li et al.'s work, process parameters of laser power, scanning speed, and powder feeding rate were varied to shed light on their effects on deposition qualities (including dimensions, surface roughness, flatness, powder efficiency, and microhardness) in LD-AM of  $\text{Al}_2\text{O}_3$  [37]. Besides deposition

Table 2.2 Summary of ceramics fabricated by LD-AM process

	Particle size ( $\mu\text{m}$ )	Process parameters	Refs
$\text{Al}_2\text{O}_3$	$\text{Al}_2\text{O}_3$ : 44-74	Laser power (W): 175 Scanning speed (mm/s): 10.00 Powder feeding rate (g/s): 0.230	[31]
	$\text{Al}_2\text{O}_3$ : 40-80	Laser power (W): 175-250 Scanning speed (mm/s): 8.33-25.00	[37]
	$\text{Al}_2\text{O}_3$ : 42-90	Laser power (W): 175-298; 398-520 Scanning speed (mm/s): 5.00-8.33; 6.67-8.67; 18.33-21.67 Powder feeding rate (g/s): 0.020-0.023; 0.033-0.047 Z-axis increment (mm): 0.05; 0.15	[67]
	$\text{Al}_2\text{O}_3$ : 42-90	Laser power (W): 230; 255; 326; 410; 510 Scanning speed (mm/s): 5.00 Powder feeding rate (g/s): 0.023	[52]
ZTA	$\text{ZrO}_2$ & $\text{Al}_2\text{O}_3$ : 42-90	Laser power (W): 410 Scanning speed (mm/s): 6.67 Powder feeding rate (g/s): 0.020 ( $\text{Al}_2\text{O}_3$ ); 0.015 ( $\text{ZrO}_2$ ) Z-axis increment (mm): 0.25	[1]
	$\text{ZrO}_2$ & $\text{Al}_2\text{O}_3$ : 40-90	Laser power (W): 360 Scanning speed (mm/s): 6.33 Powder feeding rate (g/s): 0.027 Z-axis increment (mm): 0.22	[61]
	$\text{ZrO}_2$ : 1-5; $\text{Al}_2\text{O}_3$ : 45-75	Laser power (W): 325; 350; 375; 400 Scanning speed (mm/s): 10.00 Powder feeding rate (g/s): 0.033 Z-axis increment (mm): 0.51	[2]
PZT	PTZ: 50-150	Laser power (W): 150; 200; 250; 300 Scanning speed (mm/s): 5.00-10.00; 15.00 Powder feeding rate (g/s): 0.022; 0.033; 0.050	[72]

qualities, Wu et al. reported that different process parameters of LD-AM resulted in different colors (white / black) of fabricated  $\text{Al}_2\text{O}_3$  thin-wall structures [67]. Table 3 shows the chemical composition of  $\text{Al}_2\text{O}_3$  powder used in that investigation. According to analysis, the essential reason for the black appearance was the generation

of second  $\text{Ca-}\beta\text{-Al}_2\text{O}_3$ ,  $\text{NaAl}_6\text{O}_{9.5}$ , and  $\text{CaAl}_2\text{Si}_2\text{O}_8$  phases and unmelted  $\text{Al}_2\text{O}_3$  particles under low energy input. The emergence of these second phases would give rise to the formation and propagation of inner defects and increase volatility degree of oxide impurities, amount of encapsulated gas, and shrinkage differences, thus resulting in the black color. The authors also found that dense and evenly-distributed cracks were presented on the surfaces of black structure and grew along the build direction. Compared with the black structure, the white structure contained much fewer cracks, which were mainly on the top portion of surfaces. Aiming at acquiring desired part qualities and properties, process parameters of LD-AM should be optimized. To avoid tremendous experiments for finding optimal process parameters, a mathematical model, which could reveal the relationship between process parameters and physical properties of fabricated  $\text{Al}_2\text{O}_3$  parts, was developed by Niu et al. [52].

Table 2.3 Chemical composition of  $\text{Al}_2\text{O}_3$  powder

Chemical composition	$\text{Al}_2\text{O}_3$	$\text{Na}_2\text{O}$	$\text{Fe}_2\text{O}_3$	$\text{SiO}_2$	$\text{CaO}$
wt.%	99.732	0.110	0.068	0.056	0.034

### 2.3.1.2 ZTA and other ceramics

ZTA excels pure  $\text{Al}_2\text{O}_3$  in several aspects, including enhanced toughness, superior properties of excellent corrosion and thermal resistances, good biocompatibility, and controllable mechanical properties via changing  $\text{ZrO}_2$  content and powder preparation parameters [2, 68-70]. Because of these strengths, ZTA gains its popularity among researchers and has been widely used in many commercial applications, including biomedical (e.g. orthopaedic parts [68], dental components [71], etc.), chemical (e.g. valve seats, tubes [69], etc.), and high-end engineering (e.g. machining tools [11], bearing components [12], etc.) industries. Figure 2.6 shows LD-AM fabricated  $\text{ZrO}_2\text{-Al}_2\text{O}_3$  parts with arc-wall, cylindrical, and cubic shapes [2, 59]. Niu et al. successfully fabricated cylindrical and arc-shaped ZTA eutectic microstructure by LD-AM process using pure  $\text{ZrO}_2$  and  $\text{Al}_2\text{O}_3$  powders with an eutectic ratio of 41.5 wt.% : 58.5 wt.% [1]. Due to the rapid melting / solidification

process of LD-AM, a fine-grained microstructure with eutectic spacing of 100 nm was formed, as shown in Figure 2.7. Such microstructure was reported to be refined and uniformized by introducing ultrasonic vibration to LD-AM process [61]. Compared with parts fabricated by LD-AM without ultrasonic vibration, parts fabricated by LD-AM with ultrasonic vibration showed improved mechanical properties. Using ultrasonic vibration-assisted LD-AM process, Hu et al. fabricated ZTA bulk parts with

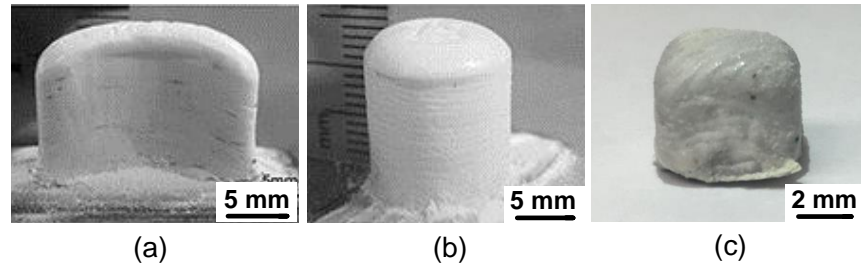


Figure 2.6 LD-AM fabricated ZTA parts with different shapes: (a) Arc wall [59]; (b) Cylinder [59]; and (c) Cube [2]. (Reprinted from Ref. [59], copyright (2015), with permission from Emerald Publishing Limited; Reprinted from Ref. [2], copyright (2018), with permission from Elsevier).

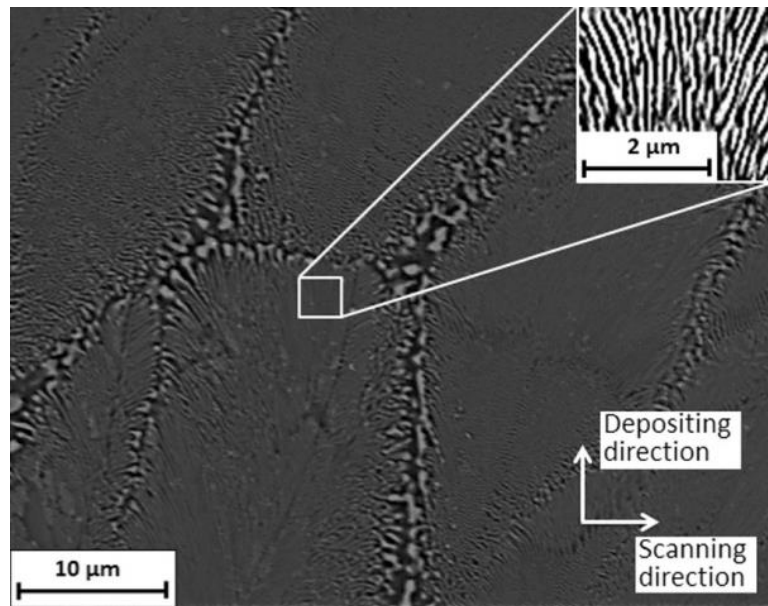


Figure 2.7 Eutectic microstructure of a LD-AM fabricated ZTA part [1]. (Reprinted from Ref. [1], copyright (2015), with permission from Elsevier).

a weight ratio of 10 wt.% : 90 wt.% between ZrO<sub>2</sub> and Al<sub>2</sub>O<sub>3</sub> [2]. The effects of ultrasonic vibration on microstructure and mechanical properties were analyzed, showing that the introduction of ultrasonic vibration helped to reduce grain size and improve microhardness, wear resistance, and compressive properties.

Besides Al<sub>2</sub>O<sub>3</sub> and ZTA, LD-AM process was reported for fabrication of bulk lead zirconate titanate (PZT) ceramic parts. Results showed that desired dielectric properties were obtained, therefore, LD-AM process demonstrated its potential application in fabricating structural components of PZT based sensors and transducers [72].

### 2.3.2 Ceramic reinforced MMCs

Ceramic reinforced MMCs are made from no less than two types of materials (e.g. ceramics, non-metals, metals, alloys, etc.). In LD-AM process, these materials are either premixed using ball milling machine (option 1) or mixed from powder feeders (option 2). For option 2, the weight ratio between different materials can be controlled via regulating feeding rate of each powder feeder. Table 4 provides a summary on ceramic reinforced MMCs fabricated by LD-AM process.

Table 2.4 Summary of ceramic reinforced MMCs fabricated by LD-AM process

	Materials used	Ceramic reinforcement	Metal matrix	Refs
Ti-based	TA15, TiC	TiC	Ti matrix	[73]
	Ti6Al4V, TiC	TiC	Ti matrix	[74]
	Ti-Mo, N <sub>2</sub>	TiN	Ti-Mo matrix	[32]
	Ti, B	TiB	Ti matrix	[64]
Others	Ni, Ti, Ni coated graphite	TiC	Ni matrix	[79]
	TiC, IN625	TiC	IN625 matrix	[80]
	Invar, TiC	TiC	Invar	[81]

#### 2.3.2.1 Ti-based composites

By reason of their high strength-to-weight ratio and excellent biocompatibility, ceramic reinforced titanium matrix composites (TMCs) have been widely applied in

aeronautical and biomedical industries. In TMCs, ceramic reinforcement materials mainly include TiC [73, 74], TiN [32], TiB [64], etc. Liu et al. successfully fabricated TiC reinforced TMCs using LD-AM process and studied effects of TiC content on microstructure and tensile properties [73]. Compared with Ti alloy, TMC with 5 vol.% TiC exhibited better ultimate tensile strength (UTS) but worse ductility. With TiC content increasing from 5 vol.% to 15 vol.%, both UTS and ductility of TMCs were dramatically deteriorated. Borkar et al. introduced nitrogen to LD-AM process and formed TiN reinforcement. The in situ reacted TiN reinforcement homogeneously distributed throughout the Ti-Mo (90 wt.% : 10 wt.%) matrix [32]. Via changing the ratio between nitrogen and argon gases, the nitrogen content was tuned. Among all types of ceramic materials, in situ reacted TiB is considered as one of the most suitable ceramic reinforcements for TMCs allowing for following reasons: (1) Adding a small amount of TiB will hugely improve mechanical properties of TMCs; (2) Thermal stresses at interfaces of TiB and Ti can be minimized because of their similar densities and thermal expansion coefficients; (3) TiB is a stable phase and there is no intermediate phase between TiB and Ti; (4) The in situ process enables metallurgical

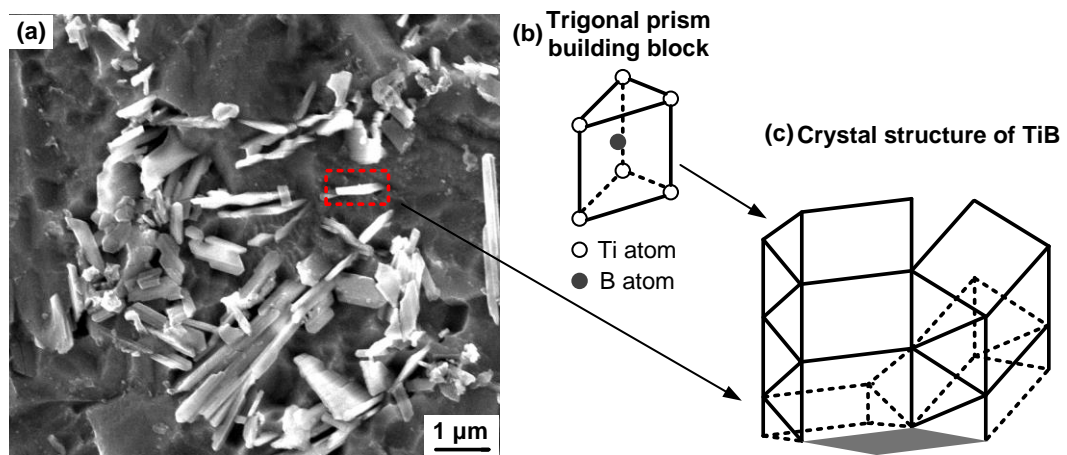


Figure 2.8 TiB growth: (a) Scanning electron microscope (SEM) image of cross-sectional TiB reinforcement; Schematic illustration of (b) trigonal prism building block and (c) crystal structure of TiB. (Reprinted from Ref. [64], copyright (2017), with permission from Springer).

bonding between TiB and Ti; (5) TiB is biocompatible and favors biomedical applications of TMCs [4, 36, 64, 75]. Figure 2.8(a) shows a typical microstructure of in situ synthesized TiB in LD-AM fabricated TMC [64]. The TiB exhibited B27 structure and formed a long prismatic shape with a high aspect ratio [76]. The formation mechanism of such a shape was studied by Lu et al. [77]. As shown in Figure 2.8(b), a B atom located at the center of a trigonal prism building block with six Ti atoms at vertexes. The trigonal prism building blocks stacked in columnar arrays, sharing two of their rectangular faces with neighboring prisms along the B27[010] direction (in Figure 2.8(c)) [76, 77]. Based on the “Periodic Bond Chain” theory, TiB grains grew faster along [010] direction than along any other direction, forming the long prismatic shape [77, 78].

### **2.3.2.2 Other composites**

Ceramic reinforced Ni matrix composites (NMCs, in possession of high corrosion resistance and high fatigue resistance of Ni matrix as well as high hardness and high wear resistance of ceramic reinforcement) are considered as promising materials in a wide range of applications, such as aerospace, chemical, and petrochemical industries [79]. Hong et al. fabricated TiC reinforced NMCs using LD-AM process and proved that the presence of TiC reinforcement was to the benefit of refining grain size, as shown in Figure 2.9 [80]. Compared with parts without reinforcement, the average grain size of TiC reinforced NMCs was hugely reduced from 34.1  $\mu\text{m}$  to 27.2  $\mu\text{m}$ . In the investigation, effects of energy input per unit length on microstructure and mechanical properties (including wear and tensile properties) were studied. Results showed that high energy input led to efficient Marangoni convection within the molten pool and then refined and homogenized dispersion of TiC reinforcement, thus achieving enhanced wear and tensile properties. However, too high the energy input per unit length would coarsen columnar dendrites of the Ni matrix and weaken wear and tensile properties of NMCs.

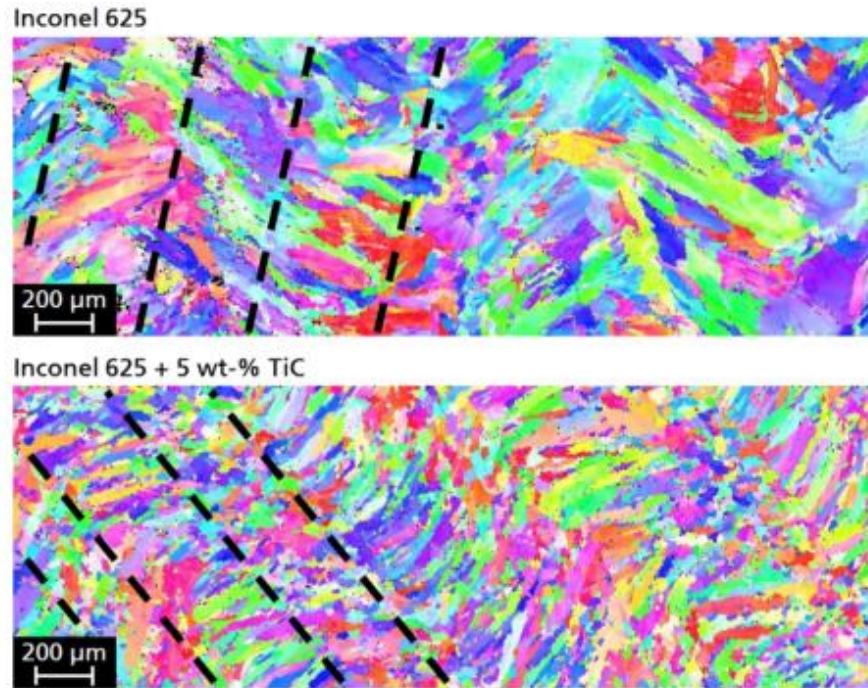


Figure 2.9 Electron backscatter diffraction micrographs showing crystal structure characterizations of LD-AM fabricated Inconel 625 and TiC reinforced Inconel 625 matrix composite parts [80]. (Reprinted from Ref. [80], copyright (2015), with permission from Elsevier).

As a rapid solidification process, LD-AM generates high temperature gradient and high thermal stress within fabricated parts and bring about defects of cracks, warpage, and even delamination. The use of Invar, which had low coefficient of thermal expansion (CTE), was reported to be an effective solution to such an issue [81]. Li et al. fabricated TiC reinforced Invar (64 wt.% Fe + 36 wt.% Ni) matrix composites (IMCs) using LD-AM process [81]. Experimental results showed that TiC reinforced IMCs had low CTE, high hardness, and high yield strength.

## 2.4 Laser cladding

Surface modification is the act of modifying the surface of a bulk material with purposes of enhancing surface properties or bringing biological or chemical characteristics to the material. These materials can be used for fabrication of specific

products, such as load bearing implants, heat exchanger tubes, and coal slurry pipelines [3, 5, 6]. In the meantime, surface modification will not change bulk properties of the material. By virtue of the directionality and high energy density of its laser source, LD-AM of thin layers (known as laser cladding) is considered as an effective and efficient surface modification method [82]. In addition, a minimized heat input size leads to a small heat affected zone and low distortion of the bulk material [83].

## 2.4.1 Ceramics

### 2.4.1.1 High wear performance applications

Cladding ceramics is proved to be resultful for enhancing wear resistance of materials those will be subject to rigorous friction conditions. Wang et al. laser cladded self-lubrication  $\text{CaF}_2/\text{Al}_2\text{O}_3$  ceramic on  $\text{Al}_2\text{O}_3$  substrate using mixed  $\text{CaF}_2$  and  $\text{Al}_2\text{O}_3$  powders by LD-AM process [55]. A scanning electron microscope (SEM) image of deposited layers (in Figure 2.10) showed that spherical  $\text{CaF}_2$  particles were uniformly dispersed in inter-plate regions of  $\text{Al}_2\text{O}_3$  matrix. The solid lubricating phase

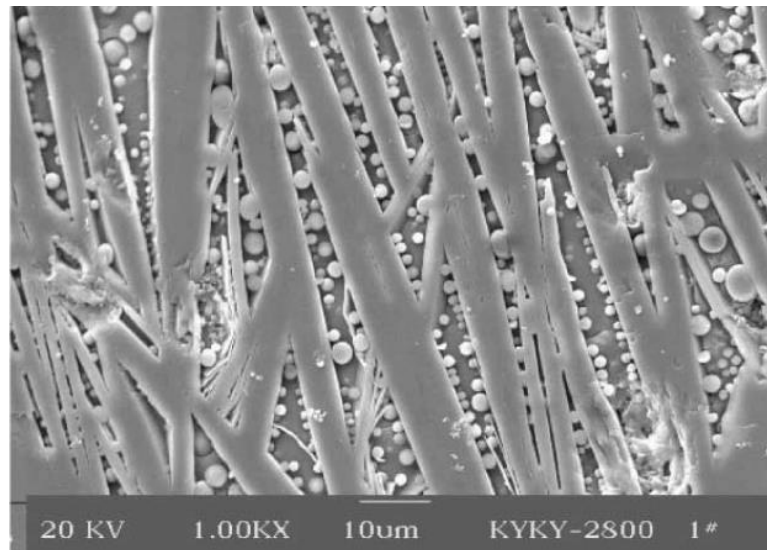


Figure 2.10 A SEM image showing the dispersion of spherical  $\text{CaF}_2$  in inter-plate regions of  $\text{Al}_2\text{O}_3$  matrix [55]. (Reprinted from Ref. [55], copyright (2002), with permission from Elsevier).

of  $\text{CaF}_2$  had noticeably low friction coefficient and brought about significant enhancements in self-lubricating and wear resistance of deposited layers, as compared with  $\text{Al}_2\text{O}_3$  substrate.

#### ***2.4.1.2 Biomedical applications***

In biomedical industries, not only enhanced wear resistance but also biocompatibility is required. To meet these requirements, Xu et al. laser cladded  $\text{Si}_3\text{N}_4$  and calcium phosphate tribasic (TCP) bio-ceramic on a Ti6Al4V substrate [84]. Within cladded layers,  $\text{Si}_3\text{N}_4$  was non-cytotoxic and could protect the Ti6Al4V substrate from wearing away. The bioresorbability of TCP facilitated fast bone growth and contributed to its integration with bone tissue [85].

#### ***2.4.1.3 Other applications***

Besides excellent mechanical and biomedical properties (such as high wear resistance and bioresorbability), ceramics are also characterized by chemical stability. In order to protect heat exchanger tubes from fireside erosion and corrosion, Khanna et al. laser cladded hard WC/Co layers on a substrate by LD-AM process [86].

### **2.4.2 Ceramic reinforced MMCs**

#### ***2.4.2.1 High wear performance applications***

Ceramic materials used for laser cladding are very limited since defects of delamination (i.e. poor bonding) are easily formed especially between the first deposited layer and the substrate. Facing to this problem, researchers have been focused on employing ceramic reinforced MMCs as cladding materials. In ceramic reinforced MMCs, hard ceramic reinforcements in the matrix function as load bearing portion, which can restrain plastic deformation and prevent matrix material from wearing away. The detailed enhancement mechanisms can be summarized as: (1) Ceramic reinforcements possess high strength and high stiffness [36]; (2) The wear resistance of fine-grained microstructure (induced by high heating and high solidification rate in LD-AM process) within cladded layers is higher than that of coarse-grained microstructure within substrates. [45]. Man et al. in-situ cladded a TiN

reinforced MMC layer on a NiTi substrate by LD-AM in a nitrogen atmosphere [5]. Results showed that the wear resistance of NiTi substrate was increased by a factor of two. In order to take the advantages possessed by TiB and TiN, Das et al. in situ synthesized TiB+TiN reinforced TMC on a Ti substrate by LD-AM using premixed BN powder and Ti6Al4V powder [87]. The fine TiB and TiN reinforcements were homogeneously distributed among Ti matrix, remarkably improving wear resistance of the Ti substrate. Van Acker et al. laser cladded WC/W<sub>2</sub>C reinforced NMC composites on steel substrates using LD-AM and investigated effects of WC/W<sub>2</sub>C content as well as carbide size on wear performance [88]. It was evidenced that an increase in WC/W<sub>2</sub>C content and a decrease in carbide size favored the enhancement of wear resistance. In addition, a small amount of carbides was sufficient enough to significantly improve wear resistance. In Wang et al.'s work, in-situ formed TiC reinforced Fe matrix composite (FMC) layers were cladded on a steel substrate, tremendously increasing the wear resistance of steel substrate [89]. Under more demanding conditions (e.g. dry friction with high contact loads) in heavy industry and aerospace areas, both high wear resistance and low friction coefficient are desired. In other words, high wear resistance alone will not satisfy requirements. In response to this problem, Smurov et al. developed two types of cladding structures using LD-AM process, as shown in Figure 2.11 [90]. For the first structure (in Figure 2.11(a)), ceramic reinforcement of WC/Co and solid lubricant of CuSn comprised deposited layer. Similar to the first structure, the second structure (in Figure 2.11(b)) also

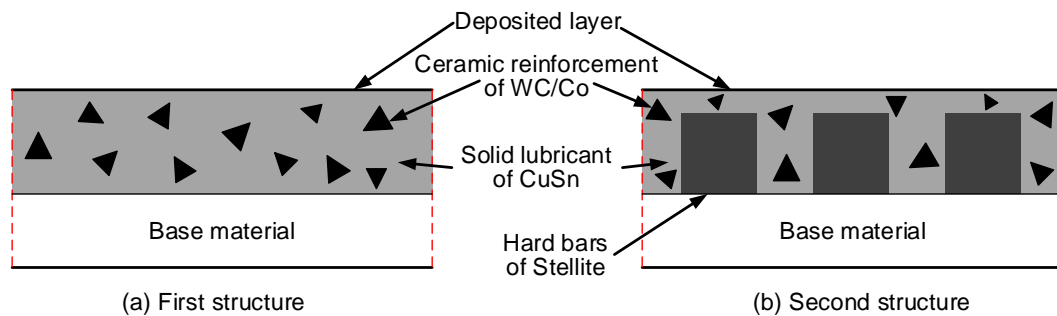


Figure 2.11 Schematic illustration of two types of LD-AM fabricated structures with high wear resistance and low friction coefficient.

contained WC/Co reinforced CuSn matrix composite. Besides, the deposited layer of the second structure had hard bars with certain spaces between the bars. The hard bars were made of Stellite and acted as barriers against fast moving of deposited layer and crack propagation when external force was applied. Based on experimental results, both structures demonstrated high wear resistance as well as low friction coefficient.

#### **2.4.2.2 Biomedical applications**

The capability of high load bearing and excellent wear resistance of ceramic reinforced MMCs enable them to find applications in implants with minimized wear induced osteolysis and aseptic loosening [91]. Compared with other types of ceramic reinforced MMCs, ceramic reinforced TMCs (such as TiN reinforced TMC [92] and SiC reinforced TMC [93]) possess high biocompatibility, therefore, they are widely used as cladding layers on metallic substrates to enable or improve the applicability of metallic substrates to biomedical areas. In *vitro* biocompatibility study, these cladding layers exhibited excellent cell-material interactions and no toxicity and showed their high potential as articular surfaces for load bearing implants, such as hip, knee, and shoulder.

#### **2.4.2.3 Other applications**

Wang et al. successfully fabricated Ni<sub>2</sub>Si/NiSi nickel silicide composite onto a steel substrate by LD-AM process [3]. The cladded layer demonstrated outstanding chemical and electrochemical corrosion resistance under immersion and anodic polarization corrosion test. To improve the slurry erosion wear rate, Tucker et al. laser cladded a variety of novel composite layers (including TiC reinforced Stellite 6 matrix composites, WC reinforced cobalt matrix composites, MoSi<sub>2</sub> reinforced Stellite 6 matrix composites, and MoSi<sub>2</sub> reinforced steel matrix composites) onto a metal substrate [6]. The effects of composite species and volume fraction of ceramic on the composites were investigated.

## **2.5 Existing main issues, corresponding solutions, and trend of development**

### **2.5.1 Poor bonding problem in bulk parts fabrication and cladding**

In general, ceramic materials are hard to be bonded to metallic substrates. One major reason is ascribed to poor compatibility, resulting from distinctions in melting point, coefficient of thermal expansion, Young's modulus, etc., between deposited layers and substrates [45]. In addition, low wettability (the ability of a liquid to maintain contact with a solid surface) between deposited layers and substrates also accounts for such phenomenon and may cause failure of metallurgical bonding formation [94]. In bulk parts fabrication, if the deposited first several layers are poorly bonded with the substrate, successive layers deposition will lead to an upwarp of these layers, resulting in fabrication failure. In cladding, the deposited layers will be easily worn off from the substrate during usage as a result of poor bonding. Facing to these problems, methods on improving bonding properties and bonding strength have been extensively explored.

#### ***2.5.1.1 Optimizing process parameters***

For the purpose of obtaining desired bonding, it is indispensable to control and optimize process parameters to melt deposited layers onto a substrate. Wu et al. investigated effects of laser power on bonding conditions in LD-AM of VC-Cr<sub>7</sub>C<sub>3</sub> ceramic on a steel substrate [46]. Bonding was successfully formed when laser power was high enough. When laser power was too low, the deposited VC-Cr<sub>7</sub>C<sub>3</sub> ceramic failed to be bonded with the steel substrate. Emamian et al. systematically studied the effects of process parameters (including laser power, scanning speed, and powder feeding rate) on bonding qualities between deposited TiC layers and a steel substrate [47]. Results showed that a certain range of these process parameters for forming a strong bonding existed. Should improper process parameters be selected, partial bonding or even no bonding would be formed.

#### ***2.5.1.2 Adding a buffer layer / functionally gradient composite layers***

Adding a buffer layer is proved to be good for improving compatibility

between deposited ceramic layers and metallic substrates and renders a firm bonding between them. As shown in Figure 2.12, Gao et al. added an Al-Si buffer layer between an Al<sub>2</sub>O<sub>3</sub> layer and an Mg substrate to release interfacial stresses induced by poor compatibility between them [48]. It was evidenced that bonding interfaces between Al<sub>2</sub>O<sub>3</sub> and Al-Si, Al-Si and Mg were strong and free from obvious defects.

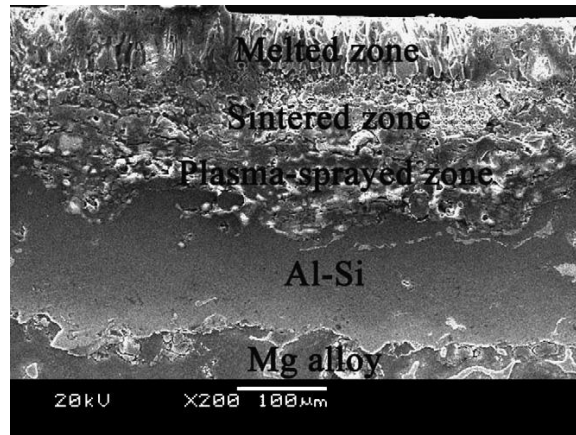


Figure 2.12 A cross-section of coating layers observed by SEM imaging [48]. (Reprinted from Ref. [48], copyright (2007), with permission from Elsevier).

The purpose of using FGC materials is also to provide “buffer layer” between deposited layers and the substrate. The major difference is that in FGC, the “buffer layer” is multi-layers with gradually compositional variation [95]. Figure 2.13 shows a typical structure of step-wise FGC layers. By using FGC, the discontinuity of properties between deposited layers and the substrate can be reduced, therefore improving compatibilities between adjacent layers. Balla et al. successfully laser cladmed functionally gradient yttria-stabilized ZrO<sub>2</sub> layers on a stainless steel substrate using LD-AM [42]. In LD-AM process, it was proved that the coatings with FGC layers exhibited better bonding strength with the steel substrate than those without FGC layers. In medical field, the utilization of FGC was also proved to be effective of creating sound bonding between ceramic coatings and metallic substrates. Zhu et al. laser cladmed bioceramic material, which contained  $\beta$ -tricalcium phosphate and hydroxyapatite, onto a Ti6Al4V substrate [49]. The weight ratio of Ti6Al4V gradually

decreased (substrate:100%; gradient layer 1: 70%; gradient layer 2: 40%; gradient layer 3: 10%; coating layer: 0%) until the bioceramic material dominated the cladded layers. Results showed that the cladded bioceramic layers were chemically and metallurgically bonded with the substrate.

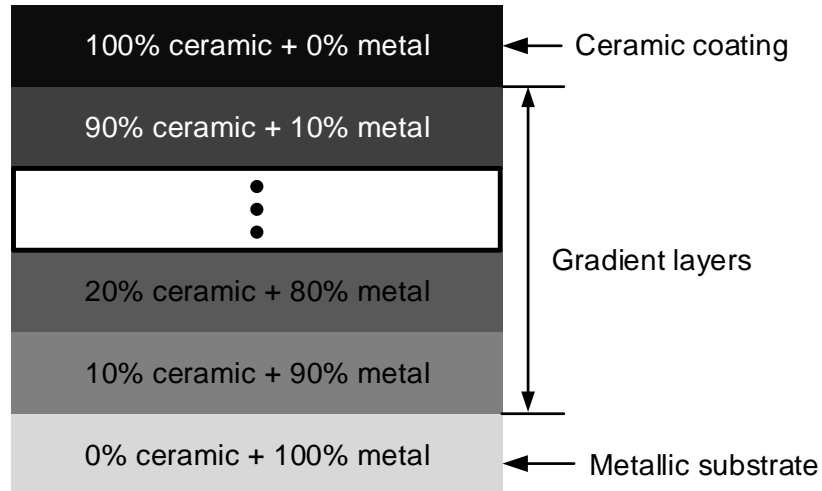


Figure 2.13 A structure of step-wise FGC materials.

### 2.5.1.3 Integrating with assisting technology of ultrasonic vibration

With periodical positive-negative pressures, ultrasonic vibration can give rise to two non-linear actions of acoustic streaming and transient cavitation, as shown in Figure 2.14 [2, 96-100]. The absorption of acoustic oscillations in liquid materials will generate a steady flow, which is known as acoustic streaming. Transient cavitation involves the formation, growth, pulsation, and collapse of micro-sized bubbles in liquid materials. These two non-linear actions facilitate material movements in liquid and render direct and ultimate influences, which are beneficial for homogenizing material dispersion, smoothing out thermal gradient and thermal stress, reducing cracks, refining grains, etc. [2, 98-101]. Therefore, ultrasonic vibration is considered as a potential technology for enhancing bonding strength. Wu et al. deposited a  $Y_2O_3$  stabilized  $ZrO_2$  layer onto a Ti6Al4V substrate using LD-AM without and with ultrasonic vibration, respectively [50]. By applying ultrasonic vibration, the dilution

rate (reflecting the mixture degree between the deposited layers and the substrate [102]) was increased and the bonding was dramatically strengthened.

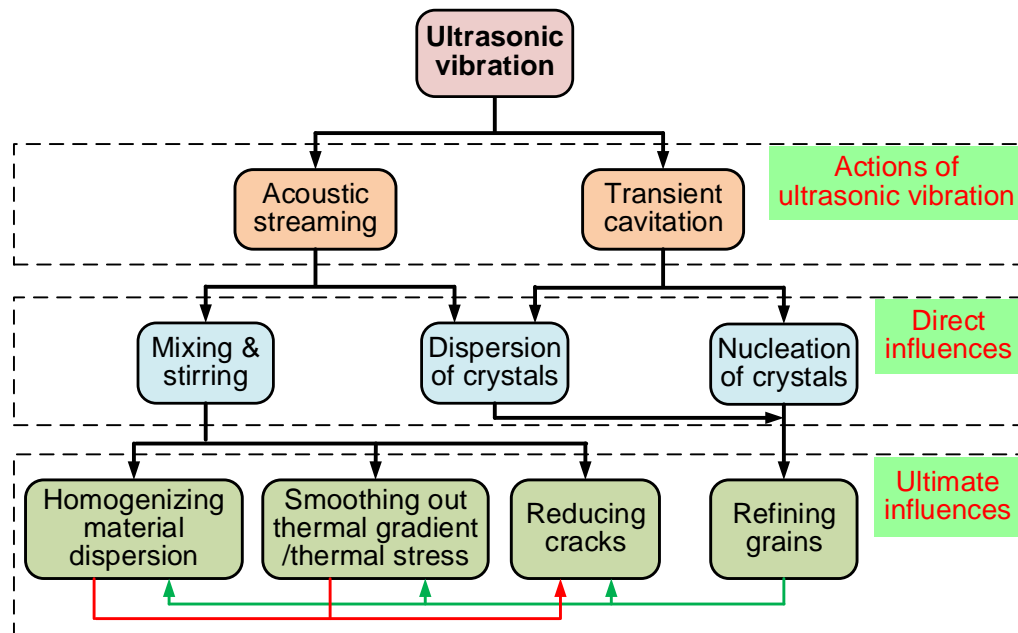


Figure 2.14 Actions and influences of ultrasonic vibration in ultrasonic vibration-assisted melting and solidification processes. (after [2, 96-100])

## 2.5.2 Cracking problem in bulk parts fabrication and cladding

As a rapid solidification process, cracks induced by large thermal gradient are prone to form during LD-AM of brittle ceramic materials [2]. The exhibition of cracks leads to weakened mechanical properties and shortened lifetime of deposited ceramic materials. In addition, the presence of cracks will easily cause the failure of ceramic components or claddings under constant or cyclic loading during operation [103]. In order to improve mechanical properties of the deposited layers as well as to meet the basic demand desired by industries, it is of great importance to suppress cracks and to produce full-dense ceramic parts and claddings.

### 2.5.2.1 Optimizing process parameters

Process optimization is a basic and easy-to-control method for researchers to obtain high quality parts and it is applied to suppress cracks in LD-AM process. Hu et

al. investigated the effects of laser power on cracking in LD-AM of ZTA [2]. As shown in Figure 2.15(a), all fabricated parts demonstrated cracks, which initiated at the bottom and propagated along the build direction. As reported, the tensile stress induced by laser deposition in horizontal direction was larger than that in vertical direction (build direction), leading to cracks propagating along the vertical direction [104]. The tensile stress in the horizontal direction ( $\sigma_H$ ) can be expressed as [104]:

$$\sigma_H = \frac{\pi k E \beta (T_M - T_o) R^2 u}{12 (1 - \nu) P} \propto \frac{1}{P} \quad (2.1)$$

where,  $k$  is the thermal conductivity;  $E$  is the Young's modulus;  $\beta$  is the thermal expansion coefficient;  $T_M$  is the melting temperature;  $T_o$  is the environmental temperature;  $R$  is the radius of laser spot;  $\nu$  is the Poisson's ratio;  $u$  is the scanning speed;  $P$  is the laser power. It can be concluded from Equation 2.1 that when all the

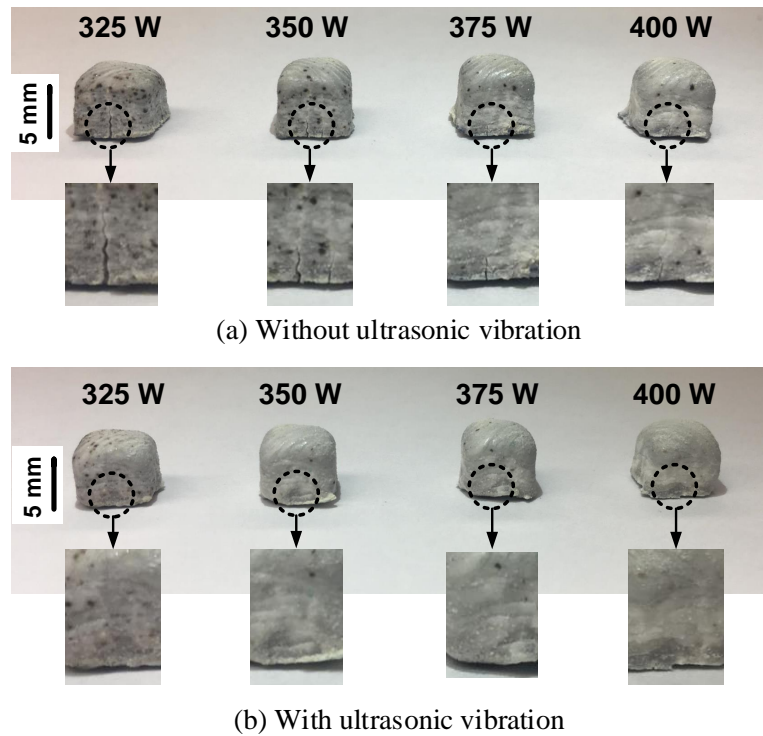


Figure 2.15 Effects of ultrasonic vibration on crack suppression under different levels of laser power. (Reprinted from Ref. [2], copyright (2018), with permission from Elsevier).

other parameters were fixed, the tensile stress in the horizontal direction ( $\sigma_H$ ) had a positive correlation with the inverse of laser power ( $1/P$ ). In other words, high laser power resulted in reduced tensile stress in the horizontal direction, thus decreasing crack propagation degree along build direction. Such tendency was evidenced by experimental results. As shown in Figure 2.15(a), the lengths and widths of cracks were hugely reduced by increasing laser power. Niu et al. studied the effects of scanning speed on crack characterizations and concluded that with the scanning speed increasing, both the crack size and crack number were decreased [51]. This was mainly ascribed to the fact that cooling rate would be increased with high scanning speed. High cooling rate rendered fine microstructure, which accounted for decreased crack size and crack number. By optimizing laser power, scanning speed, and powder feeding rate in LD-AM process, Balla et al. fabricated near-full-density  $\text{Al}_2\text{O}_3$  parts, which were almost free from cracks [31].

Although process optimization is an easy-to-control and effective method of reducing cracks, the process parameter window for producing crack-free parts is difficult to find (sometimes even inexistent) and may involve a large number of experiments [52].

#### **2.5.2.2 Pre- /post- heating**

Pre-heating, the purpose of which is to decrease thermal gradient between deposited materials and a substrate, is proved to be successful of suppressing cracks in LD-AM process [53, 54]. Zhou et al. deposited WC reinforced Ni-based matrix composite on a mild steel substrate using LD-AM [53]. By pre-heating the substrate to  $900^\circ\text{C}$ , the deposited composite layers were free from cracks and were metallurgically bonded with the substrate. Meanwhile, the deposition efficiency with pre-heating was increased four times higher than that without pre-heating. Liu et al. employed the LD-AM process for fabrication of carbide reinforced TiAl matrix composites on a Ti6Al4V substrate, which was preheated to  $450^\circ\text{C} \sim 500^\circ\text{C}$ . Results showed that the bulk parts fabricated had no cracks [54]. In addition to pre-heating an  $\text{Al}_2\text{O}_3$  substrate before depositing  $\text{CaF}_2/\text{Al}_2\text{O}_3$  ceramic onto it, Wang et al. also cooled down the

substrate slowly on a hot plate after depositing to avoid cracks [55]. For the purpose of healing cracks those already existed, Balla et al. post-heated LD-AM fabricated  $\text{Al}_2\text{O}_3$  parts at  $1000^\circ\text{C}$  and  $1600^\circ\text{C}$ . After post-heating, not only the cracks were reduced, but also the density was increased from 94% to 98% and the compressive strength was remarkably improved [31].

In general, pre- / post- heating treatments are time- and cost-consuming since additional procedures and equipment are required. In addition, pre- / post- heating treatments may change desired properties of or even damage LD-AM fabricated parts [105].

### ***2.5.2.3 Adding additive materials***

Rare earth oxides (REOs), which can change the dynamics of molten pool, are reported to be capable of preventing crack initiation and crack propagation via inhibiting dislocation movements [45, 58, 106]. Li et al. investigated effects of  $\text{Y}_2\text{O}_3$  on cracking in LD-AM of TiB-TiC reinforced TMC on a Ti6Al4V substrate and concluded that the cracking susceptibility of deposited layers was reduced due to the addition of  $\text{Y}_2\text{O}_3$  [56]. One major reason was that the Y element would accelerate the spheroidization of primary phase and then refine the microstructure. In addition, Y element also reduced the activity of carbon and prevented it from moving into and traversing the interface of primary phase. Li et al. deposited NbC reinforced FMC layers on a substrate by LD-AM process and proved that the addition of  $\text{CeO}_2$  was resultful in reducing inner defects and cracks [57]. Wu et al. deposited carbide reinforced FMC layers on a metal substrate and evidenced that besides  $\text{Y}_2\text{O}_3$  and  $\text{CeO}_2$ , the addition of other types of REOs (including  $\text{La}_2\text{O}_3$ ,  $\text{Pr}_6\text{O}_{11}$ , and  $\text{Nd}_2\text{O}_3$ ) was also favorable for reducing cracks inside deposited layers [58]. As regarded to near-net-shape bulk parts, Niu et al. successfully suppressed crack formation in LD-AM process by adding  $\text{Y}_2\text{O}_3$  into  $\text{Al}_2\text{O}_3$  [52].

In addition to REOs,  $\text{ZrO}_2$  also has positive influence on crack suppression [59]. Figures 2.16(a) and (b) show the photographs of a LD-AM fabricated  $\text{Al}_2\text{O}_3$  part

and a ZTA part, respectively. The  $\text{Al}_2\text{O}_3$  part had a great number of cracks along the build direction. By adding  $\text{ZrO}_2$ , the amount of cracks was remarkably reduced. Besides, the shape of ZTA part was much better than that of  $\text{Al}_2\text{O}_3$  part according to the design. The mixture usage of REOs and  $\text{ZrO}_2$ , such as  $\text{Y}_2\text{O}_3$  stabilized  $\text{ZrO}_2$ , was proved to be even more efficient in suppressing cracks in LD-AM process [1, 2].

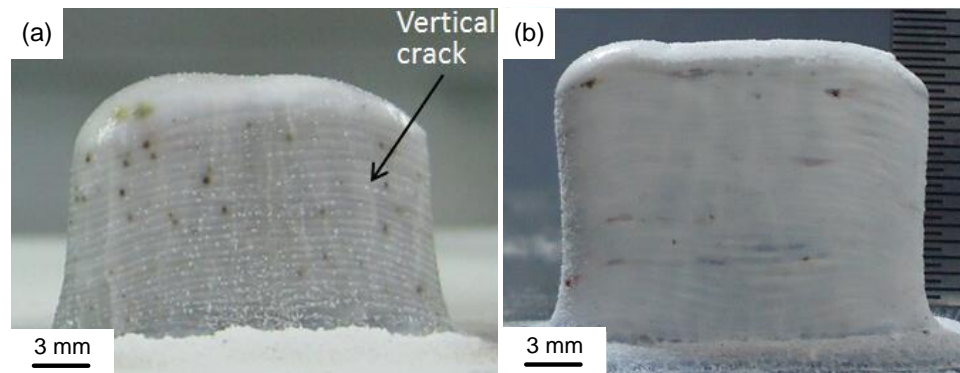


Figure 2.16 (a) A fabricated  $\text{Al}_2\text{O}_3$  part with cracks and a (b) fabricated ZTA part without cracks [59]. (Reprinted from Ref. [59], copyright (2015), with permission from Emerald Publishing Limited).

#### 2.5.2.4 Integrating with assisting technology of ultrasonic vibration

Due to the advantages exhibited (in Figure 2.14), ultrasonic vibration has been introduced and integrated with LD-AM process, aiming at reducing cracks [2, 60, 61]. Ma et al. deposited  $\text{Y}_2\text{O}_3$  stabilized  $\text{ZrO}_2$  layers on a Ti alloy substrate [60]. Experimental results showed that the layers deposited with ultrasonic vibration demonstrated refined microstructure, which increased crack propagation energy and inhibited crack propagation. The addition of ultrasonic vibration was also proved to be effective in LD-AM of bulk parts. A novel ultrasonic vibration-assisted LD-AM process for fabrication of ZTA parts was proposed by Hu et al. [2]. As shown in Figure 2.15(b), the parts fabricated with ultrasonic vibration had no cracks. Besides grain refinement, Hu et al. pointed out that the introduction of ultrasonic vibration would contribute to homogenizing material dispersion and smoothing out thermal gradient, thus being beneficial for reducing thermal stress and reducing crack

propagation tendency. Such crack suppression phenomenon was also reported by Yan et al. in ultrasonic vibration-assisted LD-AM of eutectic ZTA parts [61].

### 2.5.3 Lowered toughness problem in bulk parts fabrication

Despite strengthening effects, ceramic reinforced MMCs suffer severe problems resulted from lowered toughness and ductility due to the presence of rigid ceramic phases [4, 30, 62]. Therefore, how to strengthen matrix materials without sacrificing too much toughness and ductility becomes an urgent issue which needs to be solved.

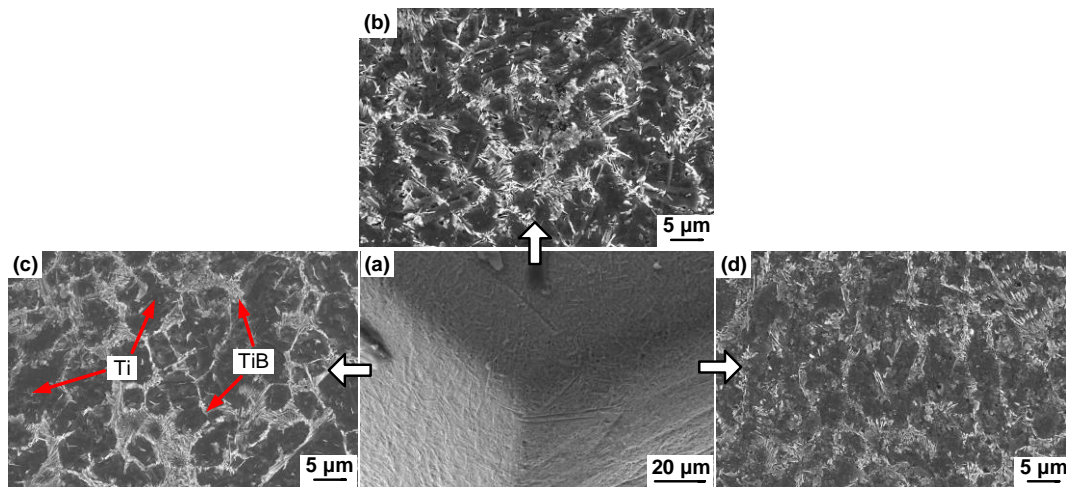


Figure 2.17 3DQCN microstructure within TiB reinforced TMCs fabricated by LD-AM process. (a) A stereo corner of a part; Detailed microstructures of (b) top side, (c) left side, and (d) right side. (Reprinted from Ref. [62], copyright (2017), with permission from Elsevier).

#### 2.5.3.1 Tailoring novel microstructure

It was reported by Attar et al. that the ductility of TiB reinforced TMCs was only one third of that of Ti parts [30]. To reduce this problem, Hu et al. tailored a three-dimensional quasi-continuous network (3DQCN) microstructure within TiB reinforced TMCs using LD-AM [62]. Figure 2.17 shows a stereo corner image taken from a fabricated part and corresponding microstructures on each side of the corner. The bright regions and dark regions were identified as TiB reinforcement and Ti

matrix, respectively. As reported, the TiB regions were beneficial for strengthening the composites and the Ti regions were able to improve the toughness and ductility of composites [4, 62, 107]. In addition, the 3D structure could enable uniform load transferring and distributing.

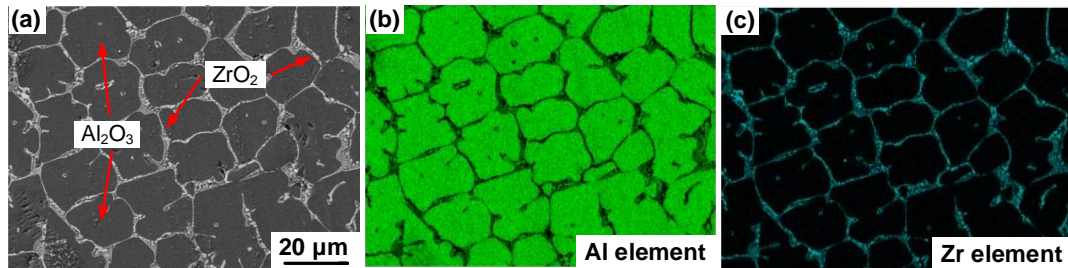


Figure 2.18 (a) A SEM image on cross-section of a ZTA part; (b) & (c) Element analysis on cross-section of the part by EDXS mapping. (Reprinted from Ref. [2], copyright (2018), with permission from Elsevier).

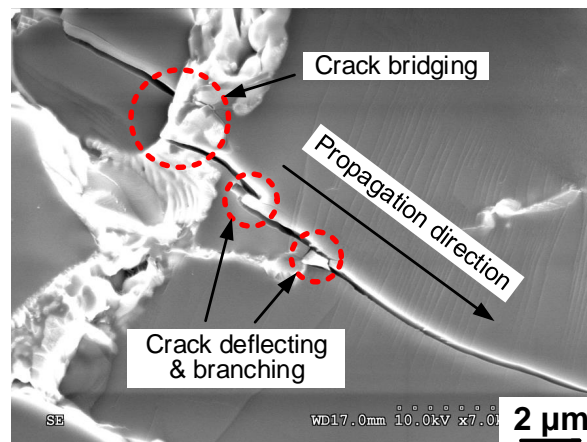


Figure 2.19 Toughening mechanisms and crack propagation in a ZTA part. (Reprinted from Ref. [2], copyright (2018), with permission from Elsevier).

Similar network microstructure was reported in LD-AM of ZTA [2]. Due to the structural incompatibility between  $\text{ZrO}_2$  and  $\text{Al}_2\text{O}_3$ ,  $\text{ZrO}_2$  was expelled and pushed to the boundaries of  $\text{Al}_2\text{O}_3$  matrix. At these boundaries,  $\text{ZrO}_2$  grew and connected with the formation of a network microstructure, as shown in Figure 2.18(a). Element analysis on the network microstructure was conducted with energy-dispersive X-ray

spectroscopy (EDXS) mapping, proving that the Al element (representing  $\text{Al}_2\text{O}_3$ ) was rich at the matrix (in Figure 2.18(b)) whereas the Zr element (representing  $\text{ZrO}_2$ ) was rich at the boundaries (in Figure 2.18(c)). This network microstructure was beneficial for toughening  $\text{Al}_2\text{O}_3$  matrix through crack bridging, crack deflecting, and crack branching. Toughening mechanisms and crack propagation in the ZTA part are shown in Figure 2.19. The propagation of initial main crack was blocked by the  $\text{ZrO}_2$  phase and a new crack was generated on the other side of the  $\text{ZrO}_2$ . This phenomenon, known as crack bridging, could reduce the driving force of cracking and increase the energy required for crack propagation. As the newly generated crack continued propagating, its tip was blunted and deflected by  $\text{ZrO}_2$  (crack deflecting) and the crack was branched into two cracks (crack branching). Due to the fact that additional energy was required for deflecting and branching the crack, the  $\text{Al}_2\text{O}_3$  matrix was toughened [108].

#### ***2.5.3.2 Integrating with assisting technology of ultrasonic vibration***

As discussed in Section 5.2.3, the  $\text{ZrO}_2$  at boundaries could impede crack propagation and then toughened  $\text{Al}_2\text{O}_3$  matrix. It was confirmed by Hu et al. that the introduction of ultrasonic vibration could further toughen  $\text{Al}_2\text{O}_3$  matrix in LD-AM fabricated ZTA [2]. In comparison with the part fabricated without ultrasonic vibration, an increment of 60% in ultimate compressive strength and an increment of 15% in ductility were achieved by introducing ultrasonic vibration to LD-AM process, as shown in Figure 2.20. In addition, the area under the true stress-strain curve (i.e. toughness) of the part fabricated with ultrasonic vibration was larger than that fabricated without ultrasonic vibration. The major reasons for such phenomena were summarized as: (1) The introduction of ultrasonic vibration could reduce thermal stress and inhibit crack propagation, therefore, the energy required for breaking the part was increased and the part was toughened; (2) The total length of cracks upon fracture was elongated due to the homogenization of material dispersion caused by ultrasonic vibration; (3) The introduction of ultrasonic vibration would render grain refinement and raise the chance of crack bridging, crack deflecting, and crack

branching, thus further toughening  $\text{Al}_2\text{O}_3$  matrix [2].

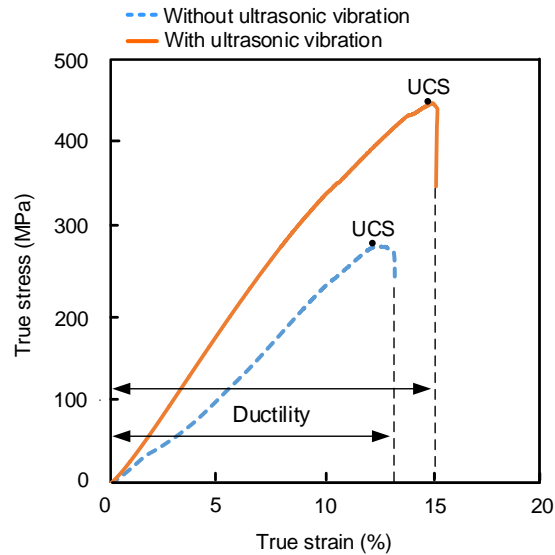


Figure 2.20 Effects of ultrasonic vibration on compressive properties of the parts fabricated by LD-AM process. (Reprinted from Ref. [2], copyright (2018), with permission from Elsevier).

## 2.6 Concluding Remarks

In this paper, the research status on LD-AM of ceramics and ceramic reinforced MMCs has been reviewed. The main conclusions are drawn as follows:

(1) The effects of process parameters (e.g. laser power, scanning speed, Z-axis increment, scanning pattern, etc.) in LD-AM have been reviewed, indicating that a proper selection of process parameters contributes to increasing melting degree and uniformizing properties of fabricated parts. In addition, side effects of high thermal stress and part distortion can be reduced or even eliminated by process optimization.

(2) Equipped with high-power-density laser beams, LD-AM process demonstrates its feasibilities of processing high hardness and high-melting-point ceramics and ceramic reinforced MMCs, such as  $\text{Al}_2\text{O}_3$ , ZTA, TMCs, NMCs, etc. Another important application field of LD-AM process is to clad layers on surfaces of bulk materials with purposes of enhancing surface properties or bringing biological or

chemical characteristics to the materials, which will be used in aerospace, biomedical, chemical, electrochemical industries.

(3) In LD-AM process, strong bonding between deposited ceramics / ceramic reinforced MMC layers and the substrate is of great importance not only for bulk parts fabrication but also for cladding. To obtain desired bonding strength, researchers usually start with optimizing process parameters. In situations where process optimization fails to work, adding a buffer layer/ FGC layers and integrating with assisting technology of ultrasonic vibration will be good alternatives for forming a firm bonding between deposited layers and the substrate.

(4) As regard to LD-AM-deposited ceramic materials, cracks caused by large thermal gradient are prone to form. Such problem is detrimental since the exhibition of cracks will give rise to weakened mechanical properties and shortened lifetime of fabricated bulk parts and claddings. By optimizing process parameters, the cracking problem can be reduced but cannot be completely eliminated. Besides process optimization, methods of pre-heating the substrate prior to LD-AM process, post-heating the deposited materials to heal existed cracks, adding additive materials (e.g. REOs, ZrO<sub>2</sub>, etc.), and integrating LD-AM with assisting technology of ultrasonic vibration are also proposed and proved to be successful in suppressing cracks.

(5) Due to the presence of rigid ceramic phases, LD-AM-fabricated ceramics and ceramic reinforced MMCs suffer severe problems resulted from lowered toughness and ductility. Such issue was alleviated by tailoring innovative 3DQCN microstructures within the fabricated parts and by integrating LD-AM process with ultrasonic vibration.

## References

- [1] Niu, F. Y., Wu, D. J., Ma, G. Y., Wang, J. T., Guo, M. H., & Zhang, B. (2015). Nanosized microstructure of  $\text{Al}_2\text{O}_3\text{-ZrO}_2$  ( $\text{Y}_2\text{O}_3$ ) eutectics fabricated by laser engineered net shaping. *Scripta Materialia*, 95, 39-41.
- [2] Hu, Y. B., Ning, F. D., Cong, W. L., Li, Y. C., Wang, X. L., & Wang, H. (2018). Ultrasonic vibration-assisted laser engineered net shaping of  $\text{ZrO}_2\text{-Al}_2\text{O}_3$  bulk parts: effects on crack suppression, microstructure, and mechanical properties. *Ceramics International*, 44(3), 2752-2760.
- [3] Wang, H. M., Wang, C. M., & Cai, L. X. (2003). Wear and corrosion resistance of laser clad  $\text{Ni}_2\text{Si/NiSi}$  composite coatings. *Surface and Coatings Technology*, 168(2), 202-208.
- [4] Hu, Y. B., Cong, W. L., Wang, X. L., Li, Y. C., Ning, F. D., & Wang, H. (2018). Laser deposition-additive manufacturing of TiB-Ti composites with novel three-dimensional quasi-continuous network microstructure: effects on strengthening and toughening. *Composites Part B: Engineering*, 133, 91-100.
- [5] Man, H. C., Zhang, S., Cheng, F. T., & Guo, X. (2006). In situ formation of a TiN/Ti metal matrix composite gradient coating on NiTi by laser cladding and nitriding. *Surface and Coatings Technology*, 200(16), 4961-4966.
- [6] Tucker, T. R., Clauer, A. H., Wright, I. G., & Stropki, J. T. (1984). Laser-processed composite metal cladding for slurry erosion resistance. *Thin Solid Films*, 118(1), 73-84.
- [7] Nevelos, J. E., Ingham, E., Doyle, C., Nevelos, A. B., & Fisher, J. (2001). The influence of acetabular cup angle on the wear of “BIOLOX Forte” alumina ceramic bearing couples in a hip joint simulator. *Journal of Materials Science: Materials in Medicine*, 12(2), 141-144.
- [8] Höland, W., Schweiger, M., Watzke, R., Peschke, A., & Kappert, H. (2008). Ceramics as biomaterials for dental restoration. *Expert Review of Medical Devices*, 5(6), 729-745.
- [9] Miracle, D. B. (2005). Metal matrix composites—from science to technological significance. *Composites Science and Technology*, 65(15-16), 2526-2540.
- [10] Kurtz, A. D., Mallon Jr, J. R., & Nunn, T. A. (1984). U.S. Patent No. 4,481,497. Washington, DC: U.S. Patent and Trademark Office.
- [11] Mandal, N., Doloi, B., & Mondal, B. (2013). Predictive modeling of surface roughness in high speed machining of AISI 4340 steel using yttria stabilized zirconia toughened alumina turning insert. *International Journal of Refractory Metals and Hard Materials*, 38, 40-46.
- [12] He, X., Zhang, Y. Z., Mansell, J. P., & Su, B. (2008). Zirconia toughened alumina ceramic foams for potential bone graft applications: fabrication, bioactivation, and cellular responses. *Journal of Materials Science: Materials in Medicine*, 19(7), 2743-2749.
- [13] Bansal, N. P., & Boccaccini, A. R. (Eds.). (2012). *Ceramics and composites processing methods*. John Wiley & Sons.
- [14] Zeng, W. M., Li, Z. C., Pei, Z. J., & Treadwell, C. (2005). Experimental observation of tool wear in rotary ultrasonic machining of advanced ceramics.

- International Journal of Machine Tools and Manufacture, 45(12-13), 1468-1473.
- [15] Rosso, M. (2006). Ceramic and metal matrix composites: Routes and properties. *Journal of Materials Processing Technology*, 175(1-3), 364-375.
- [16] Zhang, B., Zheng, X. L., Tokura, H., & Yoshikawa, M. (2003). Grinding induced damage in ceramics. *Journal of Materials Processing Technology*, 132(1-3), 353-364.
- [17] Bandyopadhyay, A., Panda, R. K., McNulty, T. F., Mohammadi, F., Danforth, S. C., & Safari, A. (1998). Piezoelectric ceramics and composites via rapid prototyping techniques. *Rapid Prototyping Journal*, 4(1), 37-49.
- [18] Bandyopadhyay, A., Atisivan, R., Kuhn, G., & Yeruva, S. (2000). Mechanical properties of interconnected phase alumina-Al composites. *Pro SFF*, 24-31.
- [19] Chartier, T., Chaput, C., Doreau, F., & Loiseau, M. (2002). Stereolithography of structural complex ceramic parts. *Journal of Materials Science*, 37(15), 3141-3147.
- [20] Corcione, C. E., Greco, A., Montagna, F., Licciulli, A., & Maffezzoli, A. (2005). Silica moulds built by stereolithography. *Journal of Materials Science*, 40(18), 4899-4904.
- [21] Corbel, S., Dufaud, O., & Roques-Carmes, T. (2011). Materials for stereolithography. In *Stereolithography* (pp. 141-159). Springer, Boston, MA.
- [22] Ebert, J., Özkol, E., Zeichner, A., Uibel, K., Weiss, Ö., Koops, U., Telle, R., & Fischer, H. (2009). Direct inkjet printing of dental prostheses made of zirconia. *Journal of Dental Research*, 88(7), 673-676.
- [23] Waetjen, A. M., Polsakiewicz, D. A., Kuhl, I., Telle, R., & Fischer, H. (2009). Slurry deposition by airbrush for selective laser sintering of ceramic components. *Journal of the European Ceramic Society*, 29(1), 1-6.
- [24] Scheithauer, U., Bergner, A., Schwarzer, E., Richter, H. J., & Moritz, T. (2014). Studies on thermoplastic 3D printing of steel-zirconia composites. *Journal of Materials Research*, 29(17), 1931-1940.
- [25] Klosterman, D. A., Chartoff, R. P., Osborne, N. R., Graves, G. A., Lightman, A., Han, G., Bezeredi, A., & Rodrigues, S. (1999). Development of a curved layer LOM process for monolithic ceramics and ceramic matrix composites. *Rapid Prototyping Journal*, 5(2), 61-71.
- [26] Zhang, Y. M., Han, J. C., Zhang, X. H., He, X. D., Li, Z. Q., & Du, S. Y. (2001). Rapid prototyping and combustion synthesis of TiC/Ni functionally gradient materials. *Materials Science and Engineering: A*, 299(1-2), 218-224.
- [27] Bertrand, P., Bayle, F., Combe, C., Gœuriot, P., & Smurov, I. (2007). Ceramic components manufacturing by selective laser sintering. *Applied Surface Science*, 254(4), 989-992.
- [28] Ghosh, S. K., & Saha, P. (2011). Crack and wear behavior of SiC particulate reinforced aluminium based metal matrix composite fabricated by direct metal laser sintering process. *Materials & Design*, 32(1), 139-145.
- [29] Wilkes, J., Hagedorn, Y. C., Meiners, W., & Wissenbach, K. (2013). Additive manufacturing of ZrO<sub>2</sub>-Al<sub>2</sub>O<sub>3</sub> ceramic components by selective laser melting. *Rapid Prototyping Journal*, 19(1), 51-57.

- [30] Attar, H., Bönisch, M., Calin, M., Zhang, L. C., Scudino, S., & Eckert, J. (2014). Selective laser melting of in situ titanium-titanium boride composites: processing, microstructure and mechanical properties. *Acta Materialia*, 76, 13-22.
- [31] Balla, V. K., Bose, S., & Bandyopadhyay, A. (2008). Processing of bulk alumina ceramics using laser engineered net shaping. *International Journal of Applied Ceramic Technology*, 5(3), 234-242.
- [32] Borkar, T., Gopagoni, S., Nag, S., Hwang, J. Y., Collins, P. C., & Banerjee, R. (2012). In situ nitridation of titanium-molybdenum alloys during laser deposition. *Journal of Materials Science*, 47(20), 7157-7166.
- [33] ASTM. (2015). Standard terminology for additive manufacturing Technologies (F-2792- 12a).
- [34] Huang, S. H., Liu, P., Mokasdar, A., & Hou, L. (2013). Additive manufacturing and its societal impact: a literature review. *The International Journal of Advanced Manufacturing Technology*, 67, 1191-1203.
- [35] Ning, F. D., Cong, W. L., Hu, Y. B., & Wang, H. (2017). Additive manufacturing of carbon fiber-reinforced plastic composites using fused deposition modeling: effects of process parameters on tensile properties. *Journal of Composite Materials*, 51(4), 451-462.
- [36] Hu, Y. B., Ning, F. D., Wang, H., Cong, W. L., & Zhao, B. (2018). Laser engineered net shaping of quasi-continuous network microstructural TiB reinforced titanium matrix bulk composites: microstructure and wear performance. *Optics & Laser Technology*, 99, 174-183.
- [37] Li, Y. Z., Hu, Y. B., Cong, W. L., Zhi, L., & Guo, Z. N. (2017). Additive manufacturing of alumina using laser engineered net shaping: effects of deposition variables. *Ceramics International*, 43(10), 7768-7775.
- [38] Lee, H., Lim, C. H. J., Low, M. J., Tham, N., Murukeshan, V. M., & Kim, Y. J. (2017). Lasers in additive manufacturing: A review. *International Journal of Precision Engineering and Manufacturing-Green Technology*, 4(3), 307-322.
- [39] Kruth, J. P., Levy, G., Klocke, F., & Childs, T. H. C. (2007). Consolidation phenomena in laser and powder-bed based layered manufacturing. *CIRP annals*, 56(2), 730-759.
- [40] Hu, Y. B., & Li, J. Z. (2017). Selective laser alloying of elemental titanium and boron powder: thermal models and experiment verification. *Journal of Materials Processing Technology*, 249, 426-432.
- [41] Gu, D. D., Meiners, W., Wissenbach, K., & Poprawe, R. (2012). Laser additive manufacturing of metallic components: materials, processes and mechanisms. *International Materials Reviews*, 57(3), 133-164.
- [42] Balla, V. K., Bandyopadhyay, P. P., Bose, S., & Bandyopadhyay, A. (2007). Compositionally graded yttria-stabilized zirconia coating on stainless steel using laser engineered net shaping (LENS™). *Scripta Materialia*, 57(9), 861-864.
- [43] Hu, Y. B., Wang, H., Ning, F. D., & Cong, W. L. (2016). Laser engineered net shaping of commercially pure titanium: effects of fabricating variables. *Proceedings of the ASME 2016 International Manufacturing Science and*

- Engineering Conference (MSEC2016-8812), June 27 – July 01, 2016, Blacksburg, Virginia, USA. DOI:10.1115/MSEC2016-8812.
- [44] Optomec. (2018). LENS<sup>®</sup> for 3D printed metals. Retrieved from <https://www.optomec.com/>
  - [45] Weng, F., Chen, C. Z., & Yu, H. J. (2014). Research status of laser cladding on titanium and its alloys: a review. *Materials & Design*, 58, 412-425.
  - [46] Wu, Q. L., Li, W. G., Zhong, N., Gang, W., & Haishan, W. (2013). Microstructure and wear behavior of laser cladding VC-Cr<sub>7</sub>C<sub>3</sub> ceramic coating on steel substrate. *Materials & Design*, 49, 10-18.
  - [47] Emamian, A., Corbin, S. F., & Khajepour, A. (2010). Effect of laser cladding process parameters on clad quality and in-situ formed microstructure of Fe-TiC composite coatings. *Surface and Coatings Technology*, 205(7), 2007-2015.
  - [48] Gao, Y. L., Wang, C. S., Yao, M., & Liu, H. B. (2007). The resistance to wear and corrosion of laser-cladding Al<sub>2</sub>O<sub>3</sub> ceramic coating on Mg alloy. *Applied Surface Science*, 253(12), 5306-5311.
  - [49] Zhu, W. D., Liu, Q. B., Zheng, M., & Wang, X. D. (2008). Biocompatibility of a functionally graded bioceramic coating made by wide-band laser cladding. *Journal of Biomedical Materials Research Part A*, 87(2), 429-433.
  - [50] Wu, D. J., Guo, M. H., Ma, G. Y., & Niu, F. Y. (2015). Dilution characteristics of ultrasonic assisted laser clad yttria-stabilized zirconia coating. *Materials Letters*, 141, 207-209.
  - [51] Niu, F. Y., Wu, D. J., Yan, S., Ma, G. Y., & Zhang, B. (2016). Process optimization for suppressing cracks in laser engineered net shaping of Al<sub>2</sub>O<sub>3</sub> ceramics. *JOM*, 69(3), 557-562.
  - [52] Niu, F. Y., Wu, D. J., Zhou, S. Y., & Ma, G. Y. (2014). Power prediction for laser engineered net shaping of Al<sub>2</sub>O<sub>3</sub> ceramic parts. *Journal of the European Ceramic Society*, 34(15), 3811-3817.
  - [53] Zhou, S., Huang, Y., Zeng, X., & Hu, Q. (2008). Microstructure characteristics of Ni-based WC composite coatings by laser induction hybrid rapid cladding. *Materials Science and Engineering: A*, 480(1), 564-572.
  - [54] Liu, W. P., & DuPont, J. N. (2004). Fabrication of carbide-particle-reinforced titanium aluminide-matrix composites by laser-engineered net shaping. *Metallurgical and Materials Transactions A*, 35(3), 1133-1140.
  - [55] Wang, H. M., Yu, Y. L., & Li, S. Q. (2002). Microstructure and tribological properties of laser clad CaF<sub>2</sub>/Al<sub>2</sub>O<sub>3</sub> self-lubrication wear-resistant ceramic matrix composite coatings. *Scripta Materialia*, 47(1), 57-61.
  - [56] Li, J., Luo, X., & Li, G. J. (2014). Effect of Y<sub>2</sub>O<sub>3</sub> on the sliding wear resistance of TiB/TiC-reinforced composite coatings fabricated by laser cladding. *Wear*, 310(1-2), 72-82.
  - [57] Li, Q. T., Lei, Y. P., & Fu, H. G. (2014). Laser cladding in-situ NbC particle reinforced Fe-based composite coatings with rare earth oxide addition. *Surface and Coatings Technology*, 239, 102-107.
  - [58] Wu, C. F., Ma, M. X., Liu, W. J., Zhong, M. L., Zhang, H. J., & Zhang, W. M. (2009). Laser cladding in-situ carbide particle reinforced Fe-based composite

- coatings with rare earth oxide addition. *Journal of Rare Earths*, 27(6), 997-1002.
- [59] Niu, F. Y., Wu, D. J., Ma, G. Y., Zhou, S. Y., & Zhang, B. (2015). Effect of second-phase doping on laser deposited  $\text{Al}_2\text{O}_3$  ceramics. *Rapid Prototyping Journal*, 21(2), 201-206.
- [60] Ma, G. Y., Yan, S., Wu, D. J., Miao, Q. Y., Liu, M. R., & Niu, F. Y. (2017). Microstructure evolution and mechanical properties of ultrasonic assisted laser clad yttria stabilized zirconia coating. *Ceramics International*, 43(13), 9622-9629.
- [61] Yan, S., Wu, D. J., Niu, F. Y., Ma, G. Y., & Kang, R. K. (2017).  $\text{Al}_2\text{O}_3$ - $\text{ZrO}_2$  eutectic ceramic via ultrasonic-assisted laser engineered net shaping. *Ceramics International*, 43(17), 15905-15910.
- [62] Hu, Y. B., Zhao, B., Ning, F. D., Wang, H., & Cong, W. L. (2017). In-situ ultrafine three-dimensional quasi-continuous network microstructural TiB reinforced titanium matrix composites fabrication using laser engineered net shaping. *Materials Letters*, 195, 116-119.
- [63] España, F. A., Balla, V. K., Bose, S., & Bandyopadhyay, A. (2010). Design and fabrication of CoCrMo alloy based novel structures for load bearing implants using laser engineered net shaping. *Materials Science and Engineering: C*, 30(1), 50-57.
- [64] Hu, Y. B., Ning, F. D., Wang, X. L., Wang, H., Zhao, B., Cong, W. L., & Li, Y. Z. (2017). Laser deposition-additive manufacturing of in situ TiB reinforced titanium matrix composites: TiB growth and part performance. *The International Journal of Advanced Manufacturing Technology*, 93(9-12), 3409-3418.
- [65] Shamsaei, N., Yadollahi, A., Bian, L., & Thompson, S. M. (2015). An overview of direct laser deposition for additive manufacturing; part II: mechanical behavior, process parameter optimization and control. *Additive Manufacturing*, 8, 12-35.
- [66] Niu, F. Y., Wu, D. J., Ma, G. Y., & Zhang, B. (2015). Additive manufacturing of ceramic structures by laser engineered net shaping. *Chinese Journal of Mechanical Engineering*, 28(6), 1117-1122.
- [67] Wu, D. J., Sun, B., Niu, F. Y., Ma, G. Y., Zhang, Y. L., & Jin, Z. J. (2013). Microstructure and crack in color  $\text{Al}_2\text{O}_3$  samples by laser engineered net shaping. *Journal of the Chinese Ceramic Society*, 41(12), 1621-1626.
- [68] Gutknecht, D., Chevalier, J., Garnier, V., & Fantozzi, G. (2007). Key role of processing to avoid low temperature ageing in alumina zirconia composites for orthopaedic application. *Journal of the European Ceramic Society*, 27(2), 1547-1552.
- [69] Ganesh, I., Olhero, S. M., Torres, P. M., Alves, F. J., & Ferreira, J. M. (2009). Hydrolysis-induced aqueous gelcasting for near-net shape forming of ZTA ceramic composites. *Journal of the European Ceramic Society*, 29(8), 1393-1401.
- [70] Wang, J., & Stevens, R. (1989). Zirconia-toughened alumina (ZTA) ceramics. *Journal of Materials science*, 24(10), 3421-3440.
- [71] Denry, I., & Kelly, J. R. (2008). State of the art of zirconia for dental

- applications. *Dental Materials*, 24(3), 299-307.
- [72] Bernard, S. A., Balla, V. K., Bose, S., & Bandyopadhyay, A. (2010). Direct laser processing of bulk lead zirconate titanate ceramics. *Materials Science and Engineering: B*, 172(1), 85-88.
- [73] Liu, D., Zhang, S. Q., Li, A., & Wang, H. M. (2009). Microstructure and tensile properties of laser melting deposited TiC/TA15 titanium matrix composites. *Journal of Alloys and Compounds*, 485(1-2), 156-162.
- [74] Mahamood, R. M., Akinlabi, E. T., Shukla, M., & Pityana, S. (2013). Scanning velocity influence on microstructure, microhardness and wear resistance performance of laser deposited Ti6Al4V/TiC composite. *Materials & Design*, 50, 656-666.
- [75] Tamirisakandala, S., Miracle, D. B., Srinivasan, R., & Gunasekera, J. S. (2006). Titanium alloyed with boron. *Advanced Materials and Processes*, 164(12), 41.
- [76] Decker, B. F., & Kasper, J. S. (1954). The crystal structure of TiB. *Acta Crystallographica*, 7(1), 77-80.
- [77] Lu, W. J., Xiao, L., Geng, K., Qin, J. N., & Zhang, D. (2008). Growth mechanism of in situ synthesized TiBw in titanium matrix composites prepared by common casting technique. *Materials Characterization*, 59(7), 912-919.
- [78] Chandrasekar, P., Balusamy, V., Chandran, K. R., & Kumar, H. (2007). Laser surface hardening of titanium-titanium boride (Ti-TiB) metal matrix composite. *Scripta Materialia*, 56(7), 641-644.
- [79] Gopagani, S., Hwang, J. Y., Singh, A. R. P., Mensah, B. A., Bunce, N., Tiley, J., Scharf, T. W., & Banerjee, R. (2011). Microstructural evolution in laser deposited nickel-titanium-carbon in situ metal matrix composites. *Journal of Alloys and Compounds*, 509(4), 1255-1260.
- [80] Hong, C., Gu, D. D., Dai, D. H., Alkhayat, M., Urban, W., Yuan, P. P., Cao, S. N., Gasser, A., Weisheit, A., Kelbassa, I., Zhong, M. L., & Poprawe, R. (2015). Laser additive manufacturing of ultrafine TiC particle reinforced Inconel 625 based composite parts: tailored microstructures and enhanced performance. *Materials Science and Engineering: A*, 635, 118-128.
- [81] Li, X. C., Stampfl, J., & Prinz, F. B. (2000). Mechanical and thermal expansion behavior of laser deposited metal matrix composites of Invar and TiC. *Materials Science and Engineering: A*, 282(1), 86-90.
- [82] Watanabe, I., McBride, M., Newton, P., & Kurtz, K. S. (2009). Laser surface treatment to improve mechanical properties of cast titanium. *Dental Materials*, 25(5), 629-633.
- [83] Majumdar, J. D., & Manna, I. (Eds.). (2012). *Laser-assisted fabrication of materials* (Vol. 161). Springer Science & Business Media.
- [84] Xu, X., Han, J. G., Wang, C. M., & Huang, A. G. (2016). Laser cladding of composite bioceramic coatings on titanium alloy. *Journal of Materials Engineering and Performance*, 25(2), 656-667.
- [85] Roy, M., Krishna, B. V., Bandyopadhyay, A., & Bose, S. (2008). Laser processing of bioactive tricalcium phosphate coating on titanium for load-bearing implants. *Acta Biomaterialia*, 4(2), 324-333.

- [86] Khanna, A. S., Kumari, S., Kanungo, S., & Gasser, A. (2009). Hard coatings based on thermal spray and laser cladding. *International Journal of Refractory Metals and Hard Materials*, 27(2), 485-491.
- [87] Das, M., Balla, V. K., Basu, D., Manna, I., Kumar, T. S., & Bandyopadhyay, A. (2012). Laser processing of in situ synthesized TiB–TiN-reinforced Ti6Al4V alloy coatings. *Scripta Materialia*, 66(8), 578-581.
- [88] Van Acker, K., Vanhoyweghen, D., Persoons, R., & Vangrunderbeek, J. (2005). Influence of tungsten carbide particle size and distribution on the wear resistance of laser clad WC/Ni coatings. *Wear*, 258(1-4), 194-202.
- [89] Wang, X. H., Zhang, M., Liu, X. M., Qu, S. Y., & Zou, Z. D. (2008). Microstructure and wear properties of TiC/FeCrBSi surface composite coating prepared by laser cladding. *Surface and Coatings Technology*, 202(15), 3600-3606.
- [90] Smurov, I. (2008). Laser cladding and laser assisted direct manufacturing. *Surface and Coatings Technology*, 202(18), 4496-4502.
- [91] Das, M., Balla, V. K., Kumar, T. S., & Manna, I. (2013). Fabrication of biomedical implants using laser engineered net shaping (LENS™). *Transactions of the Indian Ceramic Society*, 72(3), 169-174.
- [92] Balla, V. K., Bhat, A., Bose, S., & Bandyopadhyay, A. (2012). Laser processed TiN reinforced Ti6Al4V composite coatings. *Journal of the Mechanical Behavior of Biomedical Materials*, 6, 9-20.
- [93] Das, M., Balla, V. K., Kumar, T. S., Bandyopadhyay, A., & Manna, I. (2016). Tribological, electrochemical and in vitro biocompatibility properties of SiC reinforced composite coatings. *Materials & Design*, 95, 510-517.
- [94] Amin, J. S., Nikooee, E., Ayatollahi, S., & Alamdari, A. (2010). Investigating wettability alteration due to asphaltene precipitation: Imprints in surface multifractal characteristics. *Applied Surface Science*, 256(21), 6466-6472.
- [95] Bandyopadhyay, P. P., Balla, V. K., Bose, S., & Bandyopadhyay, A. (2007). Compositionally graded aluminum oxide coatings on stainless steel using laser processing. *Journal of the American Ceramic Society*, 90(7), 1989-1991.
- [96] Yang, Y., Lan, J., & Li, X. C. (2004). Study on bulk aluminum matrix nano-composite fabricated by ultrasonic dispersion of nano-sized SiC particles in molten aluminum alloy. *Materials Science and Engineering: A*, 380(1-2), 378-383.
- [97] Ning, F. D., Hu, Y. B., Liu, Z. C., Wang, X. L., Li, Y. Z., & Cong, W. L. (2018). Ultrasonic vibration-assisted laser engineered net shaping of Inconel 718 parts: microstructural and mechanical characterization. *Journal of Manufacturing Science and Engineering-Transactions of the ASME*, 140(6), 061012.
- [98] Abramov, O. V. (1987). Action of high intensity ultrasound on solidifying metal. *Ultrasonics*, 25(2), 73-82.
- [99] Cong, W. L., & Ning, F. D. (2017). A fundamental investigation on ultrasonic vibration-assisted laser engineered net shaping of stainless steel. *International Journal of Machine Tools and Manufacture*, 121, 61-69.
- [100] Moraru, L. (2006). Ultrasound action on strength properties of polycrystalline

metals.

- [101] Ning, F. D., Hu, Y. B., Liu, Z. C., Cong, W. L., Li, Y. Z., & Wang, X. L. (2017). Ultrasonic vibration-assisted laser engineered net shaping of Inconel 718 parts: a feasibility study. *Procedia Manufacturing*, 10, 771-778.
- [102] Toyserkani, E., Khajepour, A., & Corbin, S. F. (2004). *Laser cladding*. CRC press.
- [103] Munz, D., & Fett, T. (2013). *Ceramics: mechanical properties, failure behavior, materials selection* (Vol. 36). Springer Science & Business Media.
- [104] Triantafyllidis, D., Li, L., & Stott, F. H. (2006). Crack-free densification of ceramics by laser surface treatment. *Surface and Coatings Technology*, 201(6), 3163-3173.
- [105] Zhou, S. F., Zeng, X. Y., Hu, Q. W., & Huang, Y. J. (2008). Analysis of crack behavior for Ni-based WC composite coatings by laser cladding and crack-free realization. *Applied Surface Science*, 255(5), 1646-1653.
- [106] Quazi, M. M., Fazal, M. A., Haseeb, A. S. M. A., Yusof, F., Masjuki, H. H., & Arslan, A. (2016). Effect of rare earth elements and their oxides on tribo-mechanical performance of laser claddings: a review. *Journal of Rare Earths*, 34(6), 549-564.
- [107] Huang, L. J., Geng, L., & Peng, H. X. (2015). Microstructurally inhomogeneous composites: is a homogeneous reinforcement distribution optimal?. *Progress in Materials Science*, 71, 93-168.
- [108] Zhang, S., Sun, D., Fu, Y. Q., & Du, H. J. (2005). Toughening of hard nanostructural thin films: a critical review. *Surface and Coatings Technology*, 198(1-3), 2-8.

## CHAPTER III

### LENS OF ZTA – EFFECTS OF ULTRASONIC VIBRATION

Paper title:

Ultrasonic vibration-assisted laser engineered net shaping of ZrO<sub>2</sub>-Al<sub>2</sub>O<sub>3</sub> bulk parts: effects on crack suppression, microstructure, and mechanical properties

Published in:

Ceramics International, 2018, Vol. 44, No. 3, pp. 2752-2760

Authors' names:

Yingbin Hu<sup>a</sup>, Fuda Ning<sup>a</sup>, Weilong Cong<sup>a,\*</sup>, Yuanchen Li<sup>a,b</sup>, Xinlin Wang<sup>a,c</sup>,  
and Hui Wang<sup>a</sup>

Authors' affiliations:

<sup>a</sup>Department of Industrial, Manufacturing, & Systems Engineering, Texas Tech University, Lubbock, Texas, 79409, USA

<sup>b</sup>Key Laboratory of Mechanism Theory and Equipment Design of Ministry of Education, Tianjin University, Tianjin, 300072, China

<sup>c</sup>School of Mechanical Engineering, Dalian University of Technology, Dalian, Liaoning, 116024, China

\*Corresponding author:

Department of Industrial, Manufacturing, & Systems Engineering, Texas Tech University, Lubbock, TX 79409-3061, USA. Email address: weilong.cong@ttu.edu

## **Abstract**

Laser additive manufactured zirconia toughened alumina (ZTA) ceramic parts demonstrate severe problems resulting from cracking and inhomogeneous material dispersion. To reduce these problems, we propose a novel ultrasonic vibration-assisted laser engineered net shaping (LENS) process for fabrication of bulk ZTA parts. Results showed that the initiation of cracks and the crack propagation were suppressed in the parts fabricated by LENS process with ultrasonic vibration. For the parts fabricated without ultrasonic vibration, the sizes of cracks decreased with the increase of laser power. Scanning electron microscope analyses proved that the introduction of ultrasonic vibration was beneficial for grain refinement and uniform material dispersion. Due to the suppressed cracking, refined grains, and homogenized material dispersion, the parts fabricated with ultrasonic vibration demonstrated better mechanical properties (including higher microhardness, higher wear resistance, and better compressive properties), compared with the parts fabricated without ultrasonic vibration.

## **Keywords**

Grain size; Mechanical properties; Toughness and toughening; zirconia toughened alumina (ZTA); Ultrasonic vibration; Laser engineered net shaping.

## **3.1 Introduction**

Due to their superior properties of good biocompatibility, excellent corrosion and thermal resistance, and high strength, the zirconia toughened alumina (ZTA) ceramics are widely used in biomedical, chemical, and other high-end engineering industries [1-3]. Compared with pure  $ZrO_2$  or  $Al_2O_3$ , the ZTA exhibit higher toughness [4,5]. Conventional manufacturing processes for fabrication of ceramic materials include slip casting [6] and injection moulding with subsequent debinding and sintering [7]. When fabricating a single or a small amount of products, slip casting and injection molding are considered as cost-intensive processes due to the fact that both processes require molds [8]. In addition, difficulties arise when fabricating complex-shaped components with these conventional manufacturing processes [9-11].

Facing to these problems, additive manufacturing (AM) processes have been developed and widely used to produce ceramic components [8,12,13]. Opposing to subtractive manufacturing processes, the AM processes make objects from three-dimensional (3D) model data layer upon layer [14]. Among all types of AM processes, laser additive manufacturing (LAM) is regarded as the most attractive AM process for fabrication of ceramic materials [15]. LAM process, mainly including powder-bed based selective laser melting (SLM) and beam-deposition based laser engineered net shaping (LENS) methods, needs no moulds and enables fabrication of complex-shaped components [16]. Compared with the SLM method, the LENS method exhibits advantages of lower labor intensity, higher fabrication efficiency, and parts remanufacturing capability [17].

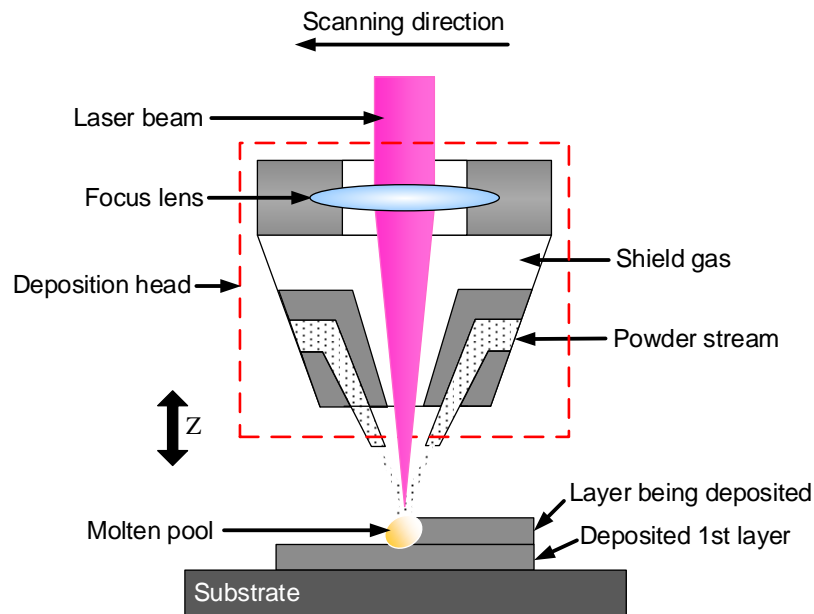


Figure 3.1 Schematic illustration of LENS process.

Figure 3.1 shows the schematic illustration of LENS process. At the beginning, the substrate is selectively melted by heat from laser radiation, forming a molten pool which catches and melts powders supplied by the powder stream. When the laser beam moves away, the molten pool starts to solidify as a consequence of heat dissipation. The deposition head moves along the designed trajectory based on the 3D

file, forming the first layer on the substrate. Afterwards, the deposition head ascends one layer thickness to the new set position for the next layer deposition. Served as the new “substrate”, the first layer is partially melted with the formation of the second layer. Similar process will be repeated many times until the designed near-net-shape component is built layer by layer [18].

Several investigations have been reported on the  $\text{Al}_2\text{O}_3$ -based ceramic materials fabricated by LENS process [12,13]. By optimizing processing parameters, Balla et al. successfully fabricated dense and net-shaped structures of  $\text{Al}_2\text{O}_3$  by LENS [19]. Ma et al. studied the effects of powder distribution on the surface morphology of LENS fabricated thin-wall structures of  $\text{Al}_2\text{O}_3$  [20]. Niu et al. fabricated cylindrical and arc-shaped ZTA structures by LENS. Results showed that the microhardness and toughness of LENS fabricated parts were comparable to those fabricated by conventional manufacturing processes [13]. Wu et al. analyzed the effects of laser power and deposit head scanning speed on qualities of the LENS fabricated ZTA thin-wall structures [12]. In the rapid-solidification LENS process, cracks induced by large thermal gradient were prone to be formed in these brittle ceramic materials [13]. The exhibition of cracks led to weakened mechanical properties and shortened lifetime of the ceramic parts [21]. In addition, the local homogeneity of  $\text{ZrO}_2$  and  $\text{Al}_2\text{O}_3$  could not be guaranteed.

In order to suppress cracks and homogenize material dispersion, this investigation, for the first time, proposes a novel ultrasonic vibration-assisted LENS process for fabrication of bulk ZTA parts. Figure 3.2 shows the actions and influences of ultrasonic vibration in ultrasonic vibration-assisted melting and solidification processes. With periodical positive-negative pressures, two important nonlinear actions of the ultrasonic vibration will be generated, including acoustic streaming and transient cavitation [22,23]. Acoustic streaming is a steady flow driven by the absorption of acoustic oscillations in the liquid materials. Transient cavitation involves the formation, growth, pulsation, and collapse of micro-sized bubbles in liquid materials [24]. These two non-linear actions facilitate material movements in liquid,

leading to direct and ultimate influences. The influences are beneficial for homogenizing material dispersion, smoothing out thermal gradient and thermal stress, reducing cracks, refining grains, etc. [24-27].

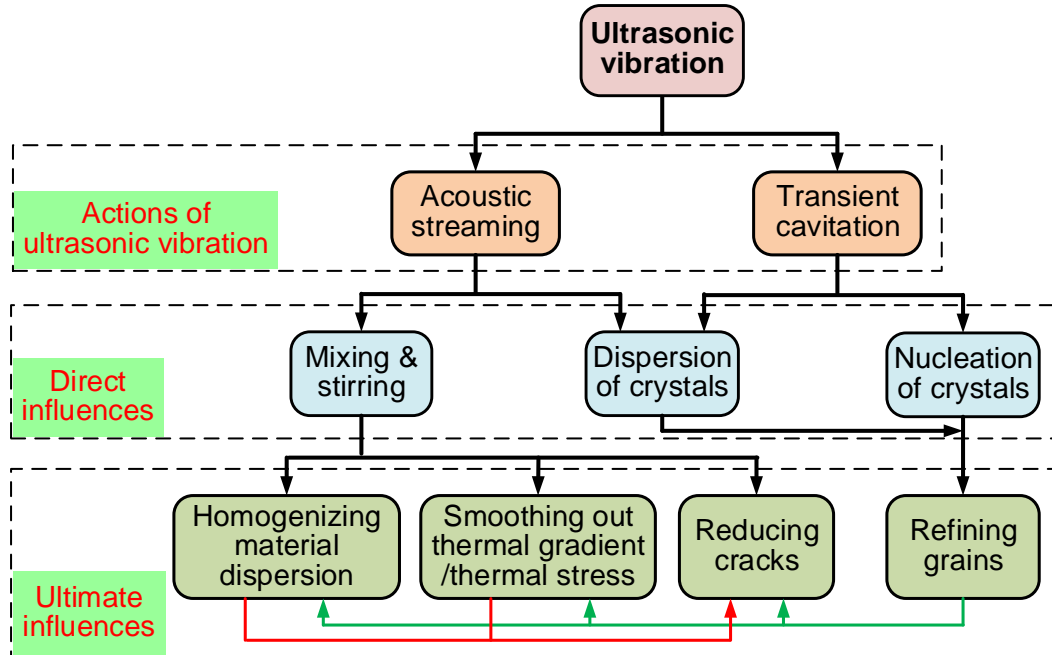


Figure 3.2 Actions and influences of ultrasonic vibration in ultrasonic vibration-assisted melting and solidification processes (after [24-26]).

## 3.2 Experimental procedures

### 3.2.1 Powder materials and powder treatment

The  $\text{Al}_2\text{O}_3$  powder used in this investigation had a particle size range of 45 – 75  $\mu\text{m}$ . The chemical compositions of the as-received  $\text{Al}_2\text{O}_3$  powder were 99.9% of  $\text{Al}_2\text{O}_3$ , 0.04% of  $\text{SiO}_2$ , 0.04% of  $\text{Fe}_2\text{O}_3$ , and 0.02% of  $\text{CaO}$ . The fused yttria-stabilized  $\text{ZrO}_2$  had a particle size range of 1 – 5  $\mu\text{m}$  and a purity of 99.9%. The different particle size ranges could ensure an interactive mixture between  $\text{Al}_2\text{O}_3$  and  $\text{ZrO}_2$  powders. The interactive mixture was beneficial to powder mixture and could avoid powder separation as, for example, lighter particles traveled to the top whereas heavier particles were kept at the bottom of the mixture [28,29]. It was reported by Lin et al. that when the  $\text{ZrO}_2$  content was 10 wt.%, the  $\text{ZrO}_2$  would exert effective grain refinement effects on  $\text{Al}_2\text{O}_3$ , thus rendering enhanced mechanical properties [4]. The

weight ratio of 10% : 90% between  $ZrO_2$  and  $Al_2O_3$  powders was adopted in this investigation. Prior to LENS process, the  $Al_2O_3$  and  $ZrO_2$  powders were mixed using a planetary ball milling machine (ND2L, Torrey Hills Technologies LLC., San Diego, CA, USA). The parameters were fixed based on preliminary experiments, including ball-to-powder weight ratio of 1:1, fixed rotation speed of 130 rpm, and milling time of 6 hours. The shapes and morphologies of the as-received  $Al_2O_3$  and  $ZrO_2$  powders are shown in Figures 3.3(a) and 3.3(b), respectively. After ball milling process, the  $Al_2O_3$  powder exhibited no obvious shape change and size reduction and the  $Al_2O_3$  and  $ZrO_2$  powders were well mixed (in Figures 3.3(c) and 3.3(d)).

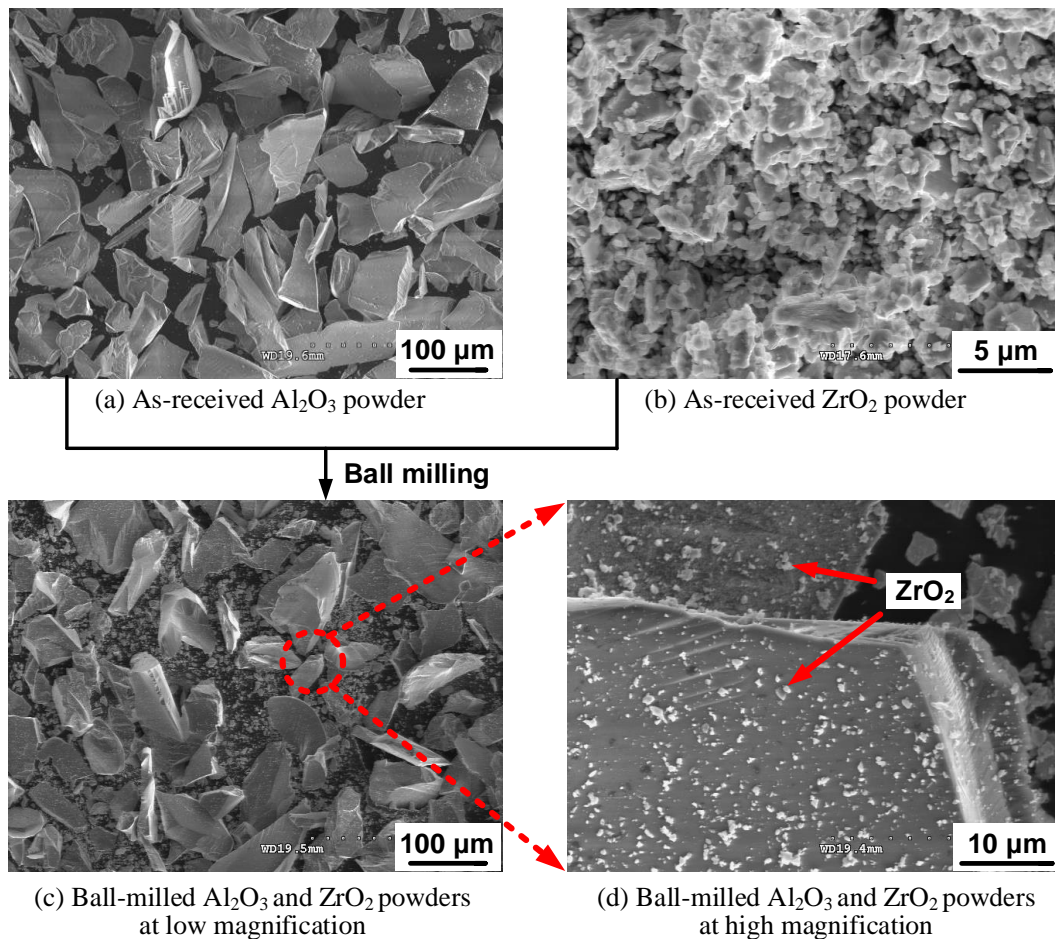


Figure 3.3 Shapes and morphologies of the powders.

### 3.2.2 Experimental set-up and parameters

In this investigation, the LENS process was carried out on a LAM system (450XL, Optomec Inc., Albuquerque, NM, USA). Figure 3.4 shows the schematic illustration of ultrasonic vibration-assisted LENS experimental set-up. The experimental set-up comprised four systems: a laser system, a chamber system, a powder and inert gas delivery system, and a control system with integrated computer. For the chamber system, an ultrasonic vibration unit was integrated. The ultrasonic vibration unit would provide vertical ultrasonic vibration to the workpiece during LENS fabrication process. In the ultrasonic vibration unit, the high-frequency electrical energy was generated from the ultrasonic power supply. Then, the electrical energy was provided to the piezoelectric converter which would convert electrical

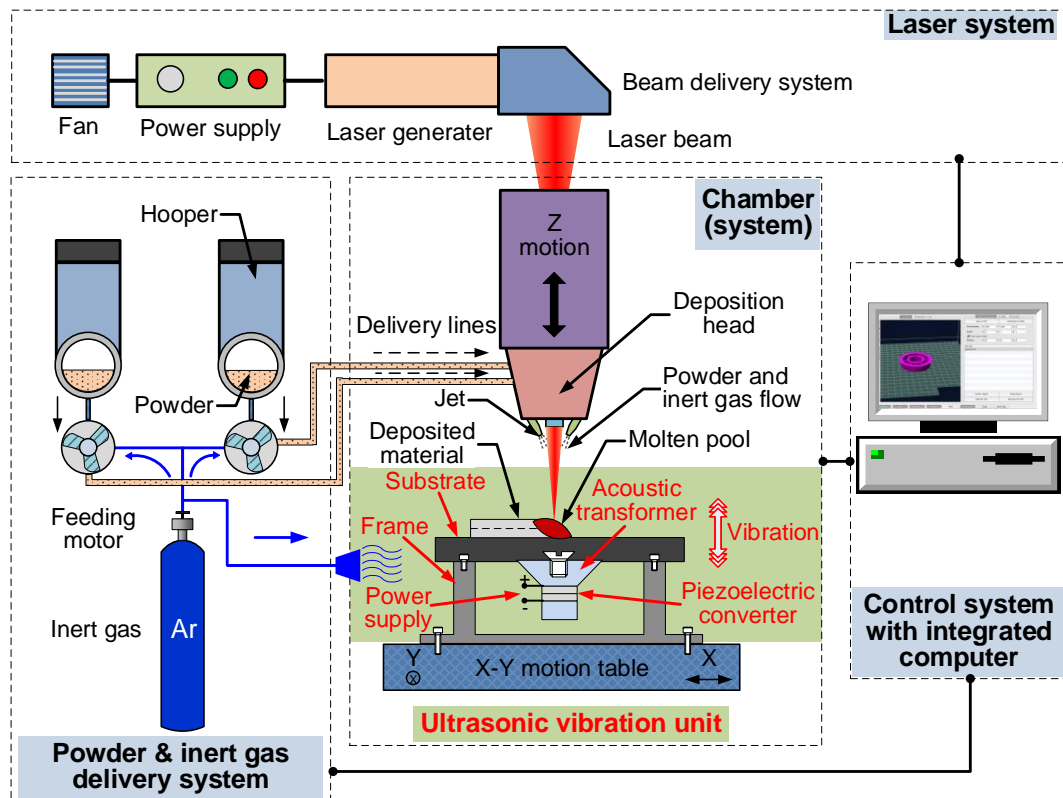


Figure 3.4 Schematic illustrations of ultrasonic vibration-assisted LENS experimental set-up.

energy into ultrasonic vibration in vertical direction. The ultrasonic vibration was transmitted to the surface of the substrate via an acoustic transformer.

Table 3.1 lists the values or ranges of input fabrication variables. The laser source provided had a continuous wave and the wavelength was kept constant at 1.07  $\mu\text{m}$ . The ultrasonic frequency and ultrasonic amplitude were fixed at 41 kHz and 5  $\mu\text{m}$  for all the experiments, respectively. To avoid experimental error, three replicated parts were fabricated on the titanium substrate under each processing condition. Based on preliminary experiments, the reasons of selecting titanium as the substrate material included: (1) ZTA could be successfully fabricated onto titanium substrate; (2) Compared with ceramic substrate, titanium substrate would not be broken into pieces during LENS process. The dimensions of the parts were 7 mm  $\times$  7 mm  $\times$  10 layers.

Table 3.1 Input fabrication variables

<b>Input fabrication variables</b>	<b>Values or ranges</b>
Laser power (W)	325, 350, 375, and 400
Laser mode	Continuous
Beam diameter of laser ( $\mu\text{m}$ )	400
Wavelength of laser ( $\mu\text{m}$ )	1.07
Deposit head scanning speed (mm/s)	10
Hatch distance ( $\mu\text{m}$ )	380
Layer thickness ( $\mu\text{m}$ )	510
Powder feeding rate (g/min)	2
Number of layers	10
Scanning orientation ( $^\circ$ )	45, alternate 90 per layer
Ultrasonic frequency (kHz)	41
Ultrasonic Amplitude ( $\mu\text{m}$ )	5

### 3.2.3 Measurement procedures

The scanning electron microscope (SEM) (Crossbeam 540, Carl Zeiss AG, Oberkochen, Germany), equipped with an energy-dispersive x-ray spectroscopy (EDXS) system, was used to observe the microstructure characterizations of the fabricated parts, as well as the shapes and morphologies of the powders. Before observation, the parts were ground and polished using a MetaServ 250 single grinder-polisher machine (49-10055, Buehler, Lake Bluff, IL, USA). Phase composition

analysis was carried out with the EDXS system. The average grain size were measured based on the ASTM E112-13 linear intercept method [30].

The microhardness was tested on the polished surfaces (perpendicular to the deposition direction) of fabricated parts using a Vickers hardness tester (900-390, Phase II, Upper Saddle River, NJ, USA). The microhardness tests were performed with 9.8 N load and ten-second dwell time. On each fabricated part, five indents were taken at different locations where the distance between adjacent locations was 0.5 mm.

The wear resistance could be obtained by conducting dry sliding wear tests. The tests were performed at room temperature, using a silicon carbide ball (with a diameter ( $D$ ) of 3 mm) as the counter-face material, under the constant sliding speed ( $v$ ) of 0.003 m/s, the normal load ( $F$ ) of 2 N, the sliding distance ( $L$ ) of 5 mm, and the duration time ( $T$ ) of one hour. The width ( $W$ ) of the sliding track was measured by SEM. The wear rate ( $w_r$ ) was then derived as:

$$w_r = \frac{L}{4F(vT)} \left( D^2 \arcsin \frac{W}{D} - W \sqrt{D^2 - W^2} \right) \quad (3.1)$$

Cylindrical parts with dimensions of  $\Phi 8 \text{ mm} \times 4 \text{ mm}$  were fabricated for conducting compressive tests. The compressive properties were tested using a universal tester (AGS-50kNXD, Shimadzu, Kyoto, Kyoto Prefecture, Japan) at a constant cross-head speed of 0.005 mm/s. The tests were repeated three times under each condition. Prior to tests, both end faces of each part were ground on the single grinder-polisher machine.

### 3.3 Results and discussion

#### 3.3.1 Effects of ultrasonic vibration on crack suppression under different laser power

Figure 3.5 shows the effects of ultrasonic vibration on crack suppression under different laser power. Compared with the parts fabricated without ultrasonic vibration, the parts fabricated with ultrasonic vibration exhibited no cracks. There were two major reasons. Firstly, the introduction of ultrasonic vibration would contribute to

homogenizing material dispersion and smoothing out thermal gradient, resulting in the reduced thermal stress [26]. Both the initiation of cracks and the crack propagation tendency were inhibited with the reduction of thermal stress. Secondly, the grain refinement (the evidence can be found in Figures 3.6 and 3.8) induced by ultrasonic vibration would generate more barriers, which could help to suppress the propagation of cracks [31].

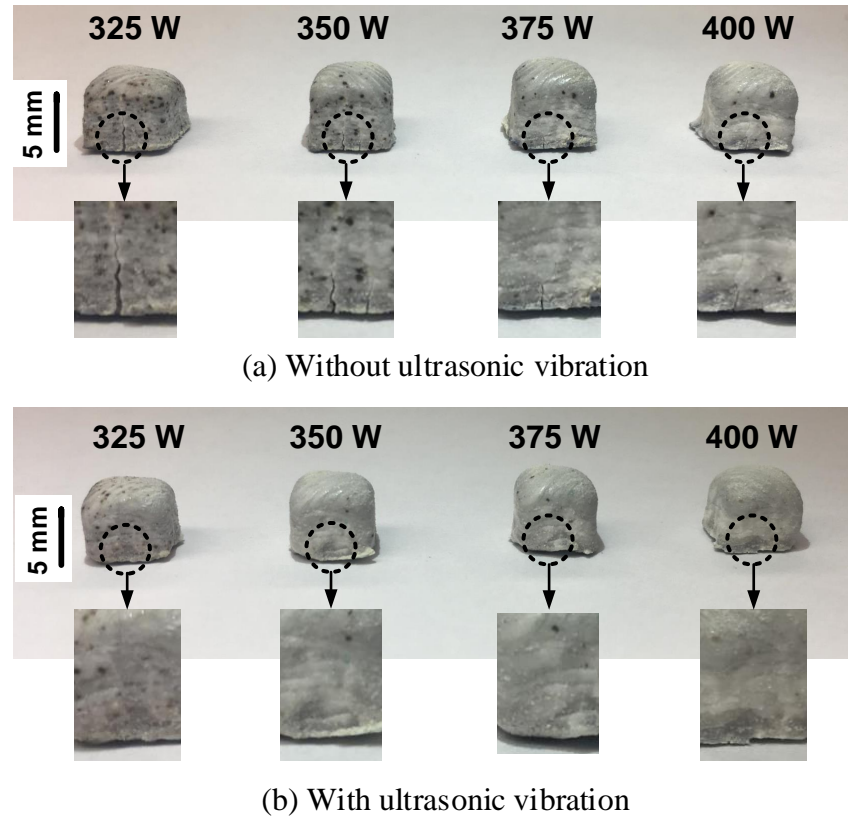


Figure 3.5 Effects of ultrasonic vibration on crack suppression under different laser power.

It can be seen from Figure 3.5(a) that all the parts (fabricated without ultrasonic vibration) demonstrated cracks, which initiated at the bottom and propagated along the deposition direction. The crack initiation, at the interface between the deposited part and the substrate, was ascribed to the mismatch of thermal conductivities between the ZTA and the titanium substrate. Since the brittle ZTA had

low thermal conductivity, which would result in high thermal gradient and large thermal stress, cracks would be easily generated at the brittle ZTA side [32,33]. It was reported that during the laser deposition of ceramics, the tensile stress in horizontal direction was large, leading to the crack propagating along the deposition direction (vertical direction) [33]. The tensile stress in the horizontal direction ( $\sigma_H$ ) of ZTA could be expressed as [33]:

$$\sigma_H = \frac{\pi k E \beta (T_M - T_o) R^2 u}{12 (1 - \nu) P} \propto \frac{1}{P} \quad (3.2)$$

where,  $k$  is the thermal conductivity;  $E$  is the Young's modulus;  $\beta$  is the thermal expansion coefficient;  $T_M$  is the melting temperature;  $T_o$  is the environmental temperature;  $R$  is the radius of laser spot;  $\nu$  is the Poisson's ratio;  $u$  is the deposit head scanning speed;  $P$  is the laser power. Based on Equation 3.2, the tensile stress in the horizontal direction had a positive correlation with the inverse of laser power when all the other parameters were fixed. In another word, with the laser power increasing, the tensile stress in the horizontal direction and the crack propagation degree were decreased. The experimental results obtained conformed such tendency. As shown in Figure 3.5(a), the lengths and widths of cracks were reduced by increasing laser power. Owing to the fact that better part quality with smaller cracking size could be obtained at higher laser power, 400 W laser power was fixed for the following experiments.

### 3.3.2 Effects of ultrasonic vibration on microstructure

Figures 3.6(a) and 3.6(d) show the SEM images on cross-sections of parts fabricated without and with ultrasonic vibration, respectively. The phase compositions of Figures 3.6(a) and 3.6(d) were tested with EDXS mapping analysis (in Figures 3.6(b), 3.6(c), 3.6(e), and 3.6(f)). Results show that the Zr element (representing  $ZrO_2$ ) was rich at the boundaries whereas the Al element (representing  $Al_2O_3$ ) was rich at the matrix. It can be concluded that the  $ZrO_2$  was prone to aggregate at the grain boundaries of  $Al_2O_3$  in LENS process both without and with ultrasonic vibration.

Since  $ZrO_2$  and  $Al_2O_3$  were structurally incompatible with each other [34], during melting and solidification process, the  $ZrO_2$  would be expelled to grain boundaries of  $Al_2O_3$  matrix, where  $ZrO_2$  grew and connected with the formation of a network microstructure. Such network microstructure could contribute to toughening effects on

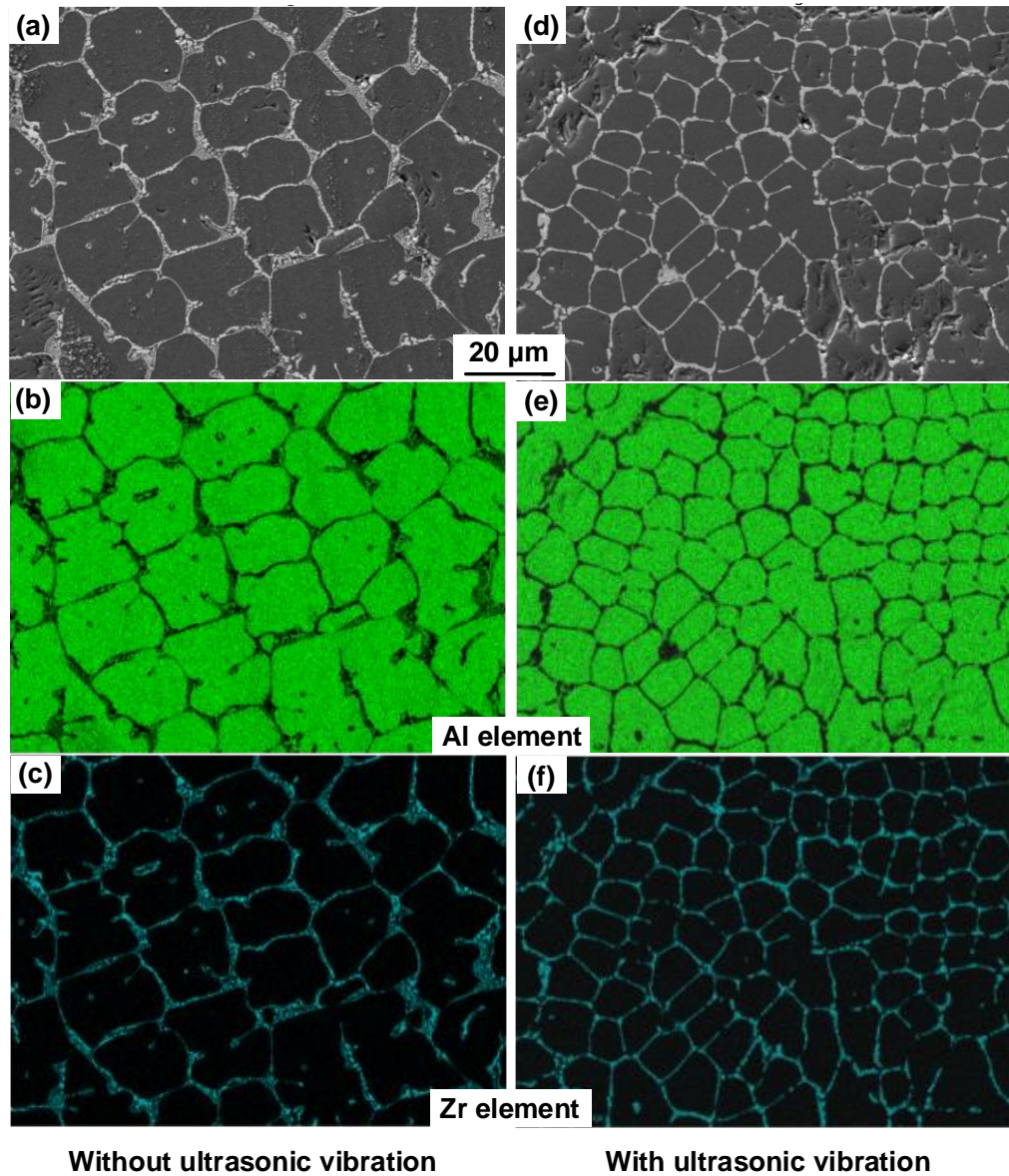


Figure 3.6 Element analysis on cross-sections of parts fabricated without and with ultrasonic vibration by EDXS mapping.

ZTA through crack bridging, crack deflecting, and crack branching [35].

Figure 3.7 shows crack propagation and toughening mechanisms in ZTA. It can be seen that the propagation of the initial main crack was blocked by the  $ZrO_2$  phase with the generation of a new crack on the other side of the  $ZrO_2$  phase. This toughening mechanism was known as crack bridging, which could reduce driving forces of cracks and increase the energy required for crack propagation. As the new crack continued propagating, its crack tip was blunted and deflected by the  $ZrO_2$  phase (crack deflecting). The crack deflecting could retard crack propagation and reduce crack tip stress. At the crack deflecting areas, the main crack was branched into two cracks. Such toughening mechanism was known as crack branching. The deflection of main crack and the generation of new cracks required additional energy, therefore, the ZTA was toughened [36]. In general, the  $ZrO_2$  phase at grain boundaries could act as barriers to crack propagation, thus toughening ZTA.

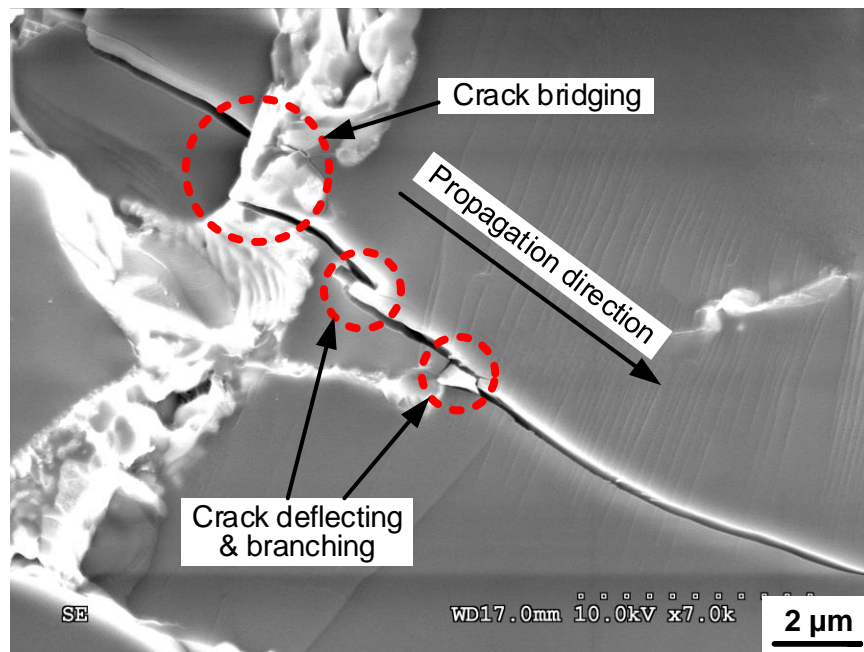


Figure 3.7 Crack propagation and toughening mechanisms in ZTA.

Figure 3.8 shows comparisons of microstructure characterizations between the parts fabricated without and with ultrasonic vibration. The average grain size ( $8\ \mu\text{m}$ )

of the part fabricated with ultrasonic vibration was much smaller, compared with that (16  $\mu\text{m}$ ) of the part fabricated without ultrasonic vibration. It was reported that the introduction of ultrasonic vibration in the molten material would cause the generation of more active nuclei within a certain volume [37]. Since each nucleus grew into one grain, more grains and dramatic grain refinement could be expected with ultrasonic vibration. For the part fabricated without ultrasonic vibration (in Figure 3.8(a)), eutectic solidification between  $\text{ZrO}_2$  and  $\text{Al}_2\text{O}_3$  occurred at the intersections of grain boundaries of  $\text{Al}_2\text{O}_3$  matrix, leading to the generation of eutectic microstructure with alternate  $\text{Al}_2\text{O}_3$  and  $\text{ZrO}_2$  phases. One intersection was magnified and shown on the top-right corner of Figure 3.8(a). It was measured that the interphase spacing of the eutectic microstructure was 150 nm. The fine interphase spacing could be ascribed to the rapid solidification of LENS process and high thermal gradient in the molten pool [38,39]. As reported, eutectic solidification occurred with the generation of eutectic microstructure, when the weight ratio between  $\text{ZrO}_2$  and  $\text{Al}_2\text{O}_3$  was 41.5% : 58.5% [13]. Even though the global weight ratio of 10% : 90% between  $\text{ZrO}_2$  and  $\text{Al}_2\text{O}_3$  was adopted in this investigation, some local weight ratios in the molten pool could be much higher in LENS process without ultrasonic vibration. In contrast, in ultrasonic vibration-assisted LENS process, no fabricated parts had observable eutectic microstructure. In addition, the width of grain boundaries ( $\text{ZrO}_2$ -rich areas) was

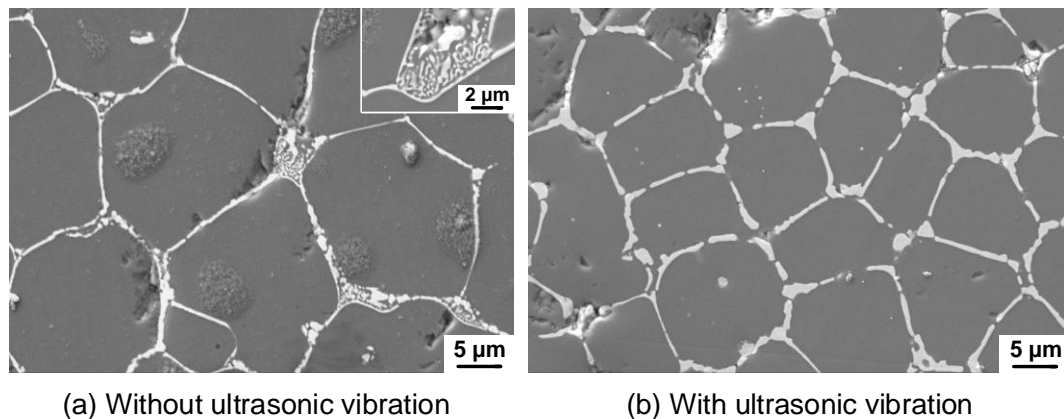


Figure 3.8 Microstructure analysis on cross-sections of parts fabricated at laser power of 400 W.

uniform throughout the cross-section. This was due to the fact that the introduction of ultrasonic vibration was beneficial to homogenize material dispersion [24].

### 3.3.3 Effects of ultrasonic vibration on mechanical properties

#### 3.3.3.1 Effects on microhardness

Figure 3.9 shows the effects of ultrasonic vibration on microhardness of the parts fabricated by LENS process. Boxplots were used to represent the data distribution of microhardness and had identical representations of mean, median, confidence intervals of 25% and 75%, and outliers. The mean values were primarily used for comparisons of microhardness between the parts fabricated by LENS without and with ultrasonic vibration assistance.

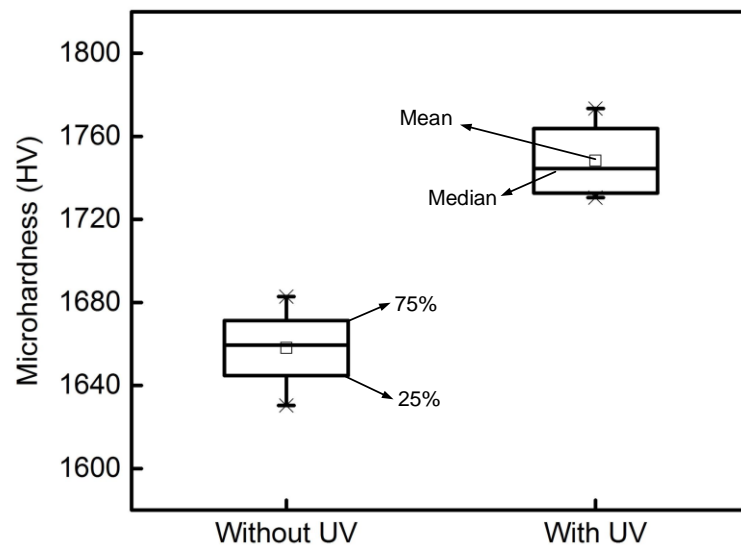


Figure 3.9 Effects of ultrasonic vibration on microhardness of the parts fabricated by LENS process (UV: ultrasonic vibration).

It can be seen that compared with the parts fabricated without ultrasonic vibration, the parts fabricated with ultrasonic vibration demonstrated larger microhardness. Based on the classic Hall-Petch relationship, the microhardness value ( $H$ ) of the ZTA could be expressed as [40-42]:

$$H = H_0 + \frac{k_{HP}}{\sqrt{d}} \quad (3.3)$$

where,  $H_0$  is the intrinsic hardness;  $k_{HP}$  is the Hall-Petch coefficient;  $d$  is the average grain size. According to Equation 3.3, the smaller grain size led to the larger microhardness. With the evidence shown in Figures 3.6 and 3.8, the ultrasonic vibration-assisted LENS resulted in the grain refinement, thus enhancing the microhardness of fabricated parts.

### 3.3.3.2 Effects on wear resistance

Figure 3.10 shows the effects of ultrasonic vibration on wear resistance of the parts fabricated by LENS process. Experimental data clearly indicated that the parts fabricated with ultrasonic vibration had superior wear resistance (smaller wear rate) in comparison to the parts fabricated without ultrasonic vibration. Grain refinement and homogenized material dispersion favored the improvement of wear resistance [43].

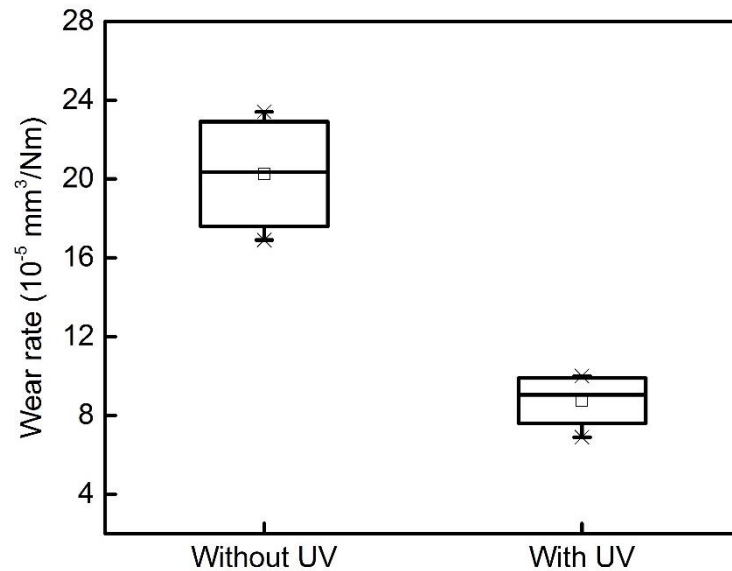


Figure 3.10 Effects of ultrasonic vibration on wear resistance of the parts fabricated by LENS process (UV: ultrasonic vibration).

### 3.3.3.3 Effects on compressive properties

In this investigation, compressive tests were conducted and compressive properties were analyzed. Compared with tensile test, the compressive test was less susceptible to minor internal defects, such as micro-pores. These internal defects could cause premature failure and would negatively affect property analysis, especially for brittle ceramic materials [29,44]. Figure 3.11 shows the effects of ultrasonic vibration on compressive properties of the parts fabricated by LENS processes without and with ultrasonic vibration. The part fabricated with ultrasonic vibration exhibited remarkably enhanced ultimate compressive strength (UCS), being 60% larger than that of the part fabricated without ultrasonic vibration. The enhancement was resulted from the refined grain size induced by ultrasonic vibration [40,41,45]. Compared with the part fabricated without ultrasonic vibration, a 15% increment of ductility was obtained by introducing ultrasonic vibration to LENS process. This was mainly ascribed to the reduced thermal stress caused by ultrasonic vibration.

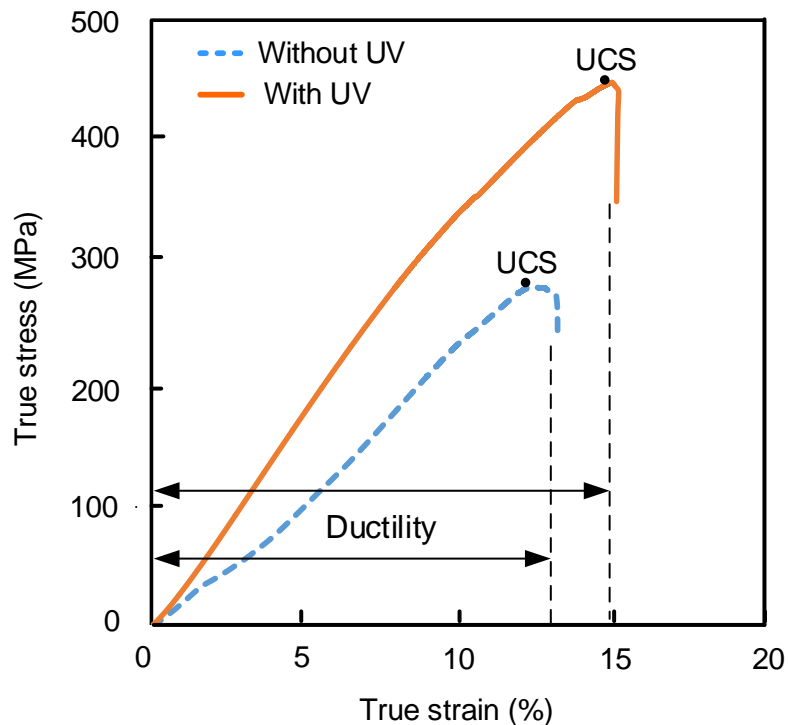


Figure 3.11 Effects of ultrasonic vibration on compressive properties of the parts fabricated by LENS process (UV: ultrasonic vibration).

Toughness, the ability of a material to absorb energy upon fracture failure, was related to the true stress-true strain curve and could be expressed as [46]:

$$U_T = \int_0^{\epsilon_T} \sigma(\epsilon) d\epsilon \quad (3.4)$$

where,  $\epsilon_T$  is the true strain; and  $\sigma(\epsilon)$  is the stress function. As shown in Figure 3.11, the area (toughness) under the true stress-true strain curve of the part fabricated with ultrasonic vibration was larger than that fabricated without ultrasonic vibration. The major reasons for the toughness improvement with ultrasonic vibration were summarized as: (1) As discussed in Section 3.3.1, the thermal-stress reduction induced by ultrasonic vibration was beneficial to inhibit crack propagation, thus increasing the energy required for breaking up the part and enhancing the toughness; (2) The homogenization of material dispersion caused by ultrasonic vibration enabled cracks to propagate both along the grain boundaries (intercrystalline cracking) and across grains of  $\text{Al}_2\text{O}_3$  (transcrystalline cracking), elongating the total length of cracks upon fracture [47]; (3) On account of the grain refinement induced by ultrasonic vibration, the intersection number between the main crack and the  $\text{ZrO}_2$  phase over a certain crack length was remarkably raised, increasing the chances of crack bridging, crack deflecting, crack branching, and toughening the part to be tested.

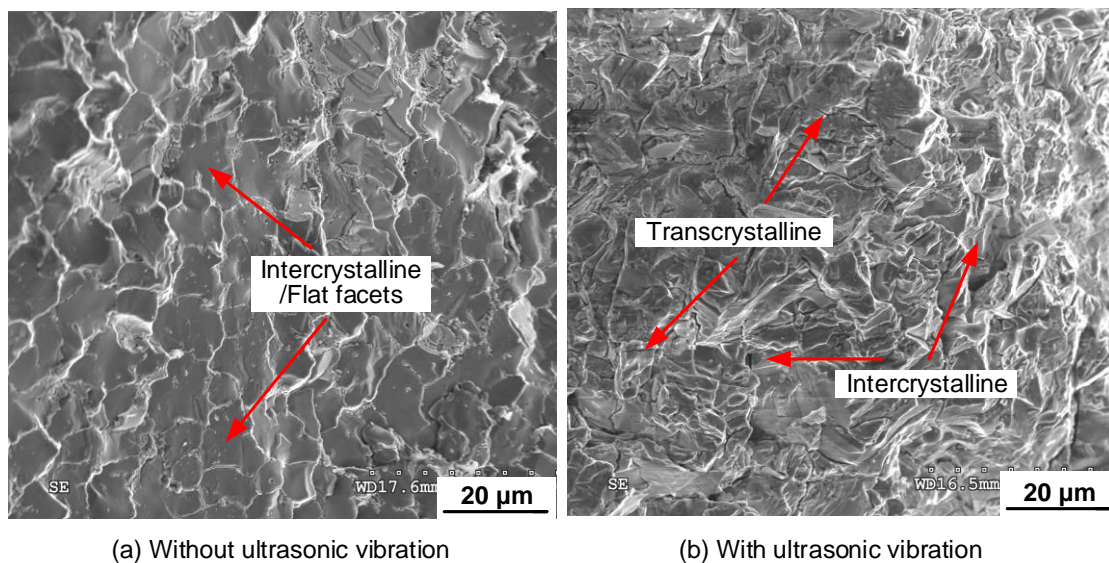


Figure 3.12 Fracture features in compressive tests.

In compressive tests, the tested parts were fractured into two or more fragments. Figure 3.12 shows the features on fracture interfaces of parts fabricated without and with ultrasonic vibration, respectively. The part fabricated without ultrasonic vibration (in Figure 3.12(a)), exhibited flat facets of grains on its fracture interface. The cracks mainly propagated along the grain boundaries of  $\text{Al}_2\text{O}_3$ . For the part fabricated with ultrasonic vibration (in Figure 3.12(b)), the split  $\text{Al}_2\text{O}_3$  grains confirmed the transcrystalline propagation of the crack.

### **3.4 Conclusions**

In this investigation, a novel ultrasonic vibration-assisted LENS process for fabrication of bulk ZTA is proposed. The objective is to investigate the effects of ultrasonic vibration on crack suppression, microstructure, and mechanical properties of the fabricated parts in the LENS process. The major conclusions are drawn as follows:

(1) The introduction of ultrasonic vibration to LENS process generated nonlinear acoustic streaming and transient cavitation actions and contributed to homogenizing material dispersion, smoothing out thermal gradient, reducing cracks, refining grains, and enhancing mechanical properties.

(2) The initiation of cracks and the crack propagation in the deposition direction were suppressed in the parts fabricated by LENS process with ultrasonic vibration. Such phenomena were mainly resulted from the reduced thermal stress and grain refinement induced by ultrasonic vibration. For the parts fabricated without ultrasonic vibration, the crack propagation degree could be reduced by increasing laser power.

(3) In the parts fabricated by both processes, the  $\text{ZrO}_2$  aggregated and connected at the grain boundaries of  $\text{Al}_2\text{O}_3$ , forming a network microstructure. This network microstructure was beneficial to toughen the workpiece through crack bridging, crack deflecting, and crack branching. In the LENS process without ultrasonic vibration, the local weight ratio between  $\text{ZrO}_2$  and  $\text{Al}_2\text{O}_3$  could be higher

than global weight ratio and eutectic solidification would occur with the generation of eutectic microstructure. Compared with the part fabricated without ultrasonic vibration, the part fabricated with ultrasonic vibration exhibited smaller grain size and better material dispersion.

(4) The effects of ultrasonic vibration on mechanical properties (including microhardness, wear resistance, and compressive properties) were analyzed. The results showed that ultrasonic vibration-assisted LENS generated higher microhardness, higher wear resistance, and better compressive properties. In compressive tests, the fracture interface of parts fabricated without ultrasonic vibration mainly demonstrated intercrystalline cracking, however, both intercrystalline cracking and transcrystalline cracking occurred in the parts fabricated with ultrasonic vibration.

### **Acknowledgement**

The work was partially supported by the Department of Defense of the United States-Army Research Office (DOD-ARO) in Defense University Research Instrumentation Program (DURIP) (grant number W911NF-17-1-0270, 2017).

## References

- [1] Yves-Christian, H., Jan, W., Wilhelm, M., Konrad, W., & Reinhart, P. (2010). Net shaped high performance oxide ceramic parts by selective laser melting. *Physics Procedia*, 5, 587-594.
- [2] De Portu, G., Fiori, C., & Sbaizero, O. (1986). Fabrication, microstructure, and properties of ZrO<sub>2</sub>-toughened Al<sub>2</sub>O<sub>3</sub> substrates. *Advances in Ceramics*, 24, 1063-1073.
- [3] Deville, S., Chevalier, J., Fantozzi, G., Bartolomé, J. F., Requena, J., Moya, J. S., Torrecillas, R., & Díaz, L. A. (2003). Low-temperature ageing of zirconia-toughened alumina ceramics and its implication in biomedical implants. *Journal of the European Ceramic Society*, 23(15), 2975-2982.
- [4] Lin, J. T., & Lu, H. Y. (1988). Grain growth inhibition and mechanical property enhancement by adding ZrO<sub>2</sub> to Al<sub>2</sub>O<sub>3</sub> matrix. *Ceramics International*, 14(4), 251-258.
- [5] De Aza, A. H., Chevalier, J., Fantozzi, G., Schehl, M., & Torrecillas, R. (2002). Crack growth resistance of alumina, zirconia and zirconia toughened alumina ceramics for joint prostheses. *Biomaterials*, 23(3), 937-945.
- [6] Fries, R., & Rand, B. (2005). Slip-Casting and Filter-Pressing. *Materials science and technology*.
- [7] Evans, J. R. (2005). Injection moulding. *Materials Science and Technology*, Wiley VCH Verlag, Weinheim, 268-311.
- [8] Wilkes, J., Hagedorn, Y. C., Meiners, W., & Wissenbach, K. (2013). Additive manufacturing of ZrO<sub>2</sub>-Al<sub>2</sub>O<sub>3</sub> ceramic components by selective laser melting. *Rapid Prototyping Journal*, 19(1), 51-57.
- [9] Wu, D. J., Lu, W. F., Chen, Y. X., Ma, G. Y., Guo, Y. Q., & Guo, D. M. (2012). Experimental study on ceramic of ZrO<sub>2</sub>-13% Al<sub>2</sub>O<sub>3</sub> by laser engineered net shaping. *Chinese Journal of Lasers*, 7, 013.
- [10] Niu, F. Y., Wu, D. J., Ma, G. Y., Wang, J. T., Guo, M. H., & Zhang, B. (2015). Nanosized microstructure of Al<sub>2</sub>O<sub>3</sub>-ZrO<sub>2</sub> (Y<sub>2</sub>O<sub>3</sub>) eutectics fabricated by laser engineered net shaping. *Scripta Materialia*, 95, 39-41.
- [11] ASTM F2792-12a, 2012, Standard terminology for additive manufacturing technologies, ASTM International, West Conshohocken, PA, USA.
- [12] Li, Y. Z., Hu, Y. B., Cong, W. L., Zhi, L., & Guo, Z. N. (2017). Additive manufacturing of alumina using laser engineered net shaping: Effects of deposition variables. *Ceramics International*, 43(10), 7768-7775.
- [13] Hu, Y. B., Cong, W. L., Wang, X. L., Li, Y. C., Ning, F. D., & Wang, H. (2018). Laser deposition-additive manufacturing of TiB-Ti composites with novel three-dimensional quasi-continuous network microstructure: effects on strengthening and toughening. *Composites Part B: Engineering*, 133, 91-100.
- [14] Atwood, C. J., Smugeresky, J. E., & Gill, D. D. (2006). Laser engineered net shaping (LENS) for the repair and modification of NWC metal components. Sandia National Laboratories, No. SAND2006-6551.
- [15] Hu, Y. B., Ning, F. D., Wang, H., Cong, W. L., & Zhao, B. (2018). Laser engineered net shaping of quasi-continuous network microstructural TiB

- reinforced titanium matrix bulk composites: microstructure and wear performance. *Optics & Laser Technology*, 99, 174-183.
- [16] Atwood, C., Ensz, M., Greene, D., Griffith, M., Harwell, L., Reckaway, D., Romero, T., Schlienger, E., & Smugeresky, J. (1998). Laser engineered net shaping (LENS (TM)): a tool for direct fabrication of metal parts (No. SAND98-2473C). Sandia National Laboratories, Albuquerque, NM, and Livermore, CA.
- [17] Balla, V. K., Bose, S., & Bandyopadhyay, A. (2008). Processing of bulk alumina ceramics using laser engineered net shaping. *International Journal of Applied Ceramic Technology*, 5(3), 234-242.
- [18] Ma, G. Y., Wang, J. T., Niu, F. Y., Sun, B., & Wu, D. J. (2015). Influence of powder distribution on the Al<sub>2</sub>O<sub>3</sub> thin-wall ceramic formed by laser engineered net shaping. *Chinese Journal of Lasers*, 42(1), 0103006.
- [19] Munz, D., & Fett, T. (2013). *Ceramics: mechanical properties, failure behavior, materials selection* (Vol. 36). Springer Science & Business Media.
- [20] Ning, F. D., & Cong, W. L. (2016). Microstructures and mechanical properties of Fe-Cr stainless steel parts fabricated by ultrasonic vibration-assisted laser engineered net shaping process. *Materials Letters*, 179, 61-64.
- [21] Yang, Y., Lan, J., & Li, X. C. (2004). Study on bulk aluminum matrix nano-composite fabricated by ultrasonic dispersion of nano-sized SiC particles in molten aluminum alloy. *Materials Science and Engineering: A*, 380(1), 378-383.
- [22] Cong, W. L., & Ning, F. D. (2017). A fundamental investigation on ultrasonic vibration-assisted laser engineered net shaping of stainless steel. *International Journal of Machine Tools and Manufacture*, 121, 61-69.
- [23] Abramov, O. V. (1987). Action of high intensity ultrasound on solidifying metal. *Ultrasonics*, 25(2), 73-82.
- [24] Moraru, L. (2007). Ultrasound action on strength properties of polycrystalline metals. *The Annals of University Dunarea de Jos Galati, Fascicle VIII Tribology*, 74-77.
- [25] Ning, F. D., Hu, Y. B., Liu, Z. C., Cong, W. L., Li, Y. Z., & Wang, X. L. (2017). Ultrasonic vibration-assisted laser engineered net shaping of Inconel 718 parts: A feasibility study. *Procedia Manufacturing*, 10, 771-778. 45th SME North American Manufacturing Research Conference, June 4-8, 2017, Los Angeles, CA, USA.
- [26] Bridgwater, J. (1976). Fundamental powder mixing mechanisms. *Powder Technology*, 15(2), 215-236.
- [27] Hu, Y. B., Ning, F. D., Wang, X. L., Wang, H., Zhao, B., Cong, W. L., & Li, Y. Z. (2017). Laser deposition-additive manufacturing of in-situ TiB reinforced titanium matrix composites: TiB growth and part performance. *The International Journal of Advanced Manufacturing Technology*, doi: 10.1007/s00170-017-0769-0.
- [28] ASTM E112-13. (2013). *Standard test methods for determining average grain size*, ASTM international, West Conshohocken, PA.

- [29] Wang, Y., Liang, J., Han, W., & Zhang, X. (2009). Mechanical properties and thermal shock behavior of hot-pressed ZrB<sub>2</sub>-SiC-AlN composites. *Journal of Alloys and Compounds*, 475(1), 762-765.
- [30] Lu, T. C., Yang, J., Suo, Z., Evans, A. G., Hecht, R., & Mehrabian, R. (1991). Matrix cracking in intermetallic composites caused by thermal expansion mismatch. *Acta Metallurgica et Materialia*, 39(8), 1883-1890.
- [31] Triantafyllidis, D., Li, L., & Stott, F. H. (2006). Crack-free densification of ceramics by laser surface treatment. *Surface and Coatings Technology*, 201(6), 3163-3173.
- [32] Feighery, A. J., & Irvine, J. T. S. (1999). Effect of alumina additions upon electrical properties of 8 mol.% yttria-stabilised zirconia. *Solid State Ionics*, 121(1), 209-216.
- [33] Song, K., Zhang, J., Lin, X., Liu, L., & Huang, W. D. (2014). Microstructure and mechanical properties of Al<sub>2</sub>O<sub>3</sub>/Y<sub>3</sub>Al<sub>5</sub>O<sub>12</sub>/ZrO<sub>2</sub> hypereutectic directionally solidified ceramic prepared by laser floating zone. *Journal of the European Ceramic Society*, 34(12), 3051-3059.
- [34] Zhang, S., Sun, D., Fu, Y., & Du, H. (2005). Toughening of hard nanostructural thin films: a critical review. *Surface and Coatings Technology*, 198(1), 2-8.
- [35] Srivastava, N., Chaudhari, G. P., & Qian, M. (2017). Grain refinement of binary Al-Si, Al-Cu and Al-Ni alloys by ultrasonication. *Journal of Materials Processing Technology*, 249, 367-378.
- [36] Wang, L., Felicelli, S. D., & Craig, J. E. (2009). Experimental and numerical study of the LENS rapid fabrication process. *Journal of Manufacturing Science and Engineering*, 131(4), 041019.
- [37] Calderon-Moreno, J. M., & Yoshimura, M. (2005). Stabilization of zirconia lamellae in rapidly solidified alumina-zirconia eutectic composites. *Journal of the European Ceramic Society*, 25(8), 1369-1372.
- [38] Hall, E. O. (1951). The deformation and ageing of mild steel: III discussion of results. *Proceedings of the Physical Society. Section B*, 64(9), 747.
- [39] Petch, N. J. (1953). The cleavage strength of polycrystals. *Journal of Iron and Steel Research, International*, 174, 25-28.
- [40] Liu, W. H., Wu, Y., He, J. Y., Nieh, T. G., & Lu, Z. P. (2013). Grain growth and the Hall-Petch relationship in a high-entropy FeCrNiCoMn alloy. *Scripta Materialia*, 68(7), 526-529.
- [41] Zum Gahr, K. H., Bundschuh, W., & Zimmerlin, B. (1993). Effect of grain size on friction and sliding wear of oxide ceramics. *Wear*, 162, 269-279.
- [42] Attar, H., Bönisch, M., Calin, M., Zhang, L. C., Scudino, S., & Eckert, J. (2014). Selective laser melting of in situ titanium-titanium boride composites: processing, microstructure and mechanical properties. *Acta Materialia*, 76, 13-22.
- [43] Hu, Y. B., Zhao, B., Ning, F. D., Wang, H., & Cong, W. L. (2017). In-situ ultrafine three-dimensional quasi-continuous network microstructural TiB reinforced titanium matrix composites fabrication using laser engineered net shaping. *Materials Letters*, 195, 116-119.

- [44] Roylance, D. (2001). Stress-strain curves. Massachusetts Institute of Technology study, Cambridge.
- [45] Huang, L. J., Geng, L., & Peng, H. X. (2015). Microstructurally inhomogeneous composites: is a homogeneous reinforcement distribution optimal?. *Progress in Materials Science*, 71, 93-168.

## CHAPTER IV

### LENS OF ZTA – NOVEL MICROSTRUCTURE FORMATION AND MECHANICAL PERFORMANCE

Paper title:

Laser deposition-additive manufacturing of zirconia toughened alumina: novel microstructure formation and mechanical performance

Submitted to:

Scientific Reports

Authors' names:

Yingbin Hu<sup>a</sup>, Hui Wang<sup>a</sup>, Weilong Cong<sup>a,\*</sup>, and Bo Zhao<sup>b</sup>

Authors' affiliations:

<sup>a</sup>Department of Industrial, Manufacturing, & Systems Engineering, Texas Tech University, Lubbock, Texas, 79409, USA

<sup>b</sup>College of Arts and Sciences Microscopy, Texas Tech University, Lubbock, Texas, 79409, USA.

\*Corresponding author:

Department of Industrial, Manufacturing, & Systems Engineering, Texas Tech University, Lubbock, TX 79409-3061, USA. Email address: weilong.cong@ttu.edu

**Abstract**

In fabricating low-volume or complex-shaped zirconia toughened alumina (ZTA) parts, conventional manufacturing processes, including slip casting and powder metallurgy, are regarded as time-consuming and cost-intensive. In response to these problems, laser deposition-additive manufacturing (LD-AM) has been proposed and utilized to fabricate ZTA parts with low volume or highly flexible features in a shorter cycle time at a lower cost. Investigations have been reported on studying effects of input variables (such as laser power) in LD-AM of ZTA parts, however, there are very limited investigations on effects of  $ZrO_2$  content. In this investigation, the effects of  $ZrO_2$  content on microstructures and mechanical properties of LD-AM fabricated ZTA parts are studied. Experimental results show that at lower levels of  $ZrO_2$  contents (5 wt.%, 10 wt.%, and 20 wt.%), a novel three-dimensional quasi-continuous network (3DQCN) microstructure is tailored, whereas at higher levels of  $ZrO_2$  contents (30 wt.%, 35 wt.%, and 41.5 wt.%), eutectic microstructure dominates the whole part. Both the 3DQCN microstructure and the eutectic microstructure are beneficial for toughening ZTA parts. In addition, the 3DQCN microstructure contributes to hardening ZTA parts.

**4.1 Introduction**

Alumina ( $Al_2O_3$ ) ceramics demonstrate superior properties of high hardness, excellent corrosion, thermal, and wear resistances, and good biocompatibility [1-3]. However, the inherently brittle nature of  $Al_2O_3$  limits its applications [4]. In order to reduce brittleness, significant progress has been made in toughening  $Al_2O_3$  composites. Due to its phase-transformation (tetragonal zirconia ( $t-ZrO_2$ ) phase to monoclinic zirconia ( $m-ZrO_2$ ) phase) toughening effects [5],  $ZrO_2$  is considered as such an attractive material to enhance toughness of  $Al_2O_3$ . In addition, the mechanical properties of zirconia toughened alumina (ZTA) can be controlled via changing  $ZrO_2$  content and powder preparation (such as changing particle shape or size) for specific applications [6, 7]. Due to the exhibited benefits, ZTA has been widely used in many commercial industries, including high-end engineering (e.g. machining tools [8],

bearing components [9], etc.), chemical (e.g. valve seats, tubes [10], etc.), and biomedical (e.g. orthopaedic [11], dental components [12], etc.) industries.

Conventional manufacturing processes for ZTA fabrication, including slip casting and powder metallurgy, require molds preparing, debinding, and sintering [13, 14]. Therefore, these two processes are considered as time-consuming when fabricating low-volume parts [15]. In addition, cost increases by creating or assembling complex structures with conventional manufacturing processes [16]. Facing to these problems, it is crucial to manufacture ZTA parts with low volume or highly flexible features in a shorter cycle time at a lower cost.

Laser additive manufacturing (LAM) is one of the possible solutions to the problems encountered by conventional manufacturing processes and has been successfully applied for fabricating ZTA materials [15-19]. LAM excels conventional manufacturing processes in the following aspects: (1) LAM requires no molds and is with no following debinding and sintering; (2) LAM can manufacture low-volume or highly flexible-featured parts in a shorter cycle time at a lower cost; and (3) LAM can produce hard-to-machine or high-value components in a cost-effective manner [20]. Among all types of LAM process, laser deposition-additive manufacturing (LD-AM) is favored due to its remanufacturing capability, hard coating application, easy-to-control cooling rate, and changeable dilution [17, 21]. Figure 4.1 shows the schematic of the LD-AM process. During LD-AM processing, the laser generator ejects a laser beam onto the substrate, forming a molten pool. In the meantime, powders (carried by the argon gas flow) are delivered through four symmetric nozzles to the molten pool area. The powders are then melted and deposited onto the molten pool. After the laser beam moving to another position, heat dissipates and the molten material starts to solidify into a bump. The movement of deposition head follows the trajectory designed by a 3D model, forming the first layer. Afterwards, the deposition head is ascended one layer thickness to maintain a constant focal distance for the subsequent layer deposition. The first layer serves as a new “substrate” for the subsequent layer fabrication. Similar process will be repeated layer upon layer until the designed 3D

structure is completed.

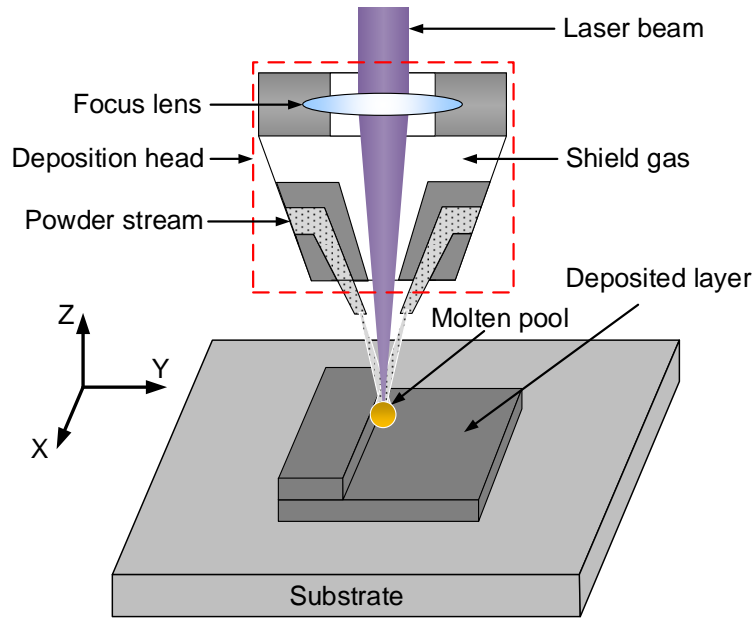


Figure 4.1 A schematic of the LD-AM process.

In recent years, LD-AM manufacturing of ZTA has attracted attentions in both academia and industry [17-19]. Niu et al. successfully fabricated ZTA parts with cylindrical and arc shapes using LD-AM process [17]. Hu et al. proposed an ultrasonic vibration-assisted LD-AM process to reduce cracks in fabricated ZTA parts [18]. Experimental results proved that the introduction of ultrasonic vibration was beneficial for inhibiting crack propagation. Yan et al. tailored a periodic-banded microstructure in LD-AM fabricated ZTA parts [19]. The formation mechanisms and effects of input fabrication variables on this microstructure were studied. Among all these reported literature, the  $ZrO_2$  content was kept fixed. However, there are no reported comprehensive investigations on studying the effects of  $ZrO_2$  content. In this investigation, the effects of  $ZrO_2$  content (from 0 wt.% up to an eutectic ratio of 41.5 wt.%) on microstructure characterizations and mechanical properties are studied. In addition, the formation mechanisms of novel microstructures at different levels of  $ZrO_2$  content and their effects on mechanical performance have been investigated.

## 4.2 results and discussion

### 4.2.1 Effects of $ZrO_2$ content on microstructure characterizations

Figures 4.2(a)-4.2(g) show effects of  $ZrO_2$  content (0 wt.%, 5 wt.%, 10 wt.%, 20 wt.%, 30 wt.%, 35 wt.%, and 41.5 wt.%) on microstructures of ZTA parts. Phase compositions were tested and identified with EDS and EBSD analyses. Results show that the bright areas were  $ZrO_2$  and the dark areas were  $Al_2O_3$ . The cross-section of the pure  $Al_2O_3$  part without  $ZrO_2$  exhibited defects of cavities resulting from lack of fusion. A network microstructure was initiated at  $ZrO_2$  content of 5 wt.% and was fully formed at  $ZrO_2$  content of 10 wt.%. With the  $ZrO_2$  content increasing to 20 wt.%, eutectic solidification between  $ZrO_2$  and  $Al_2O_3$  occurred at the intersections of grain boundaries. The reason for the formation of eutectic microstructure was that some local weight ratios between  $ZrO_2$  and  $Al_2O_3$  might be higher than the designated ratio of 20 wt.% : 80 wt.%, reaching to the eutectic ratio of 41.5 wt.% : 58.5 wt.%. With the increase of  $ZrO_2$  content from 20 wt.% to 41.5 wt.%, the network microstructure boundaries were gradually filled by eutectic microstructure until all the structure turning to the eutectic structure.

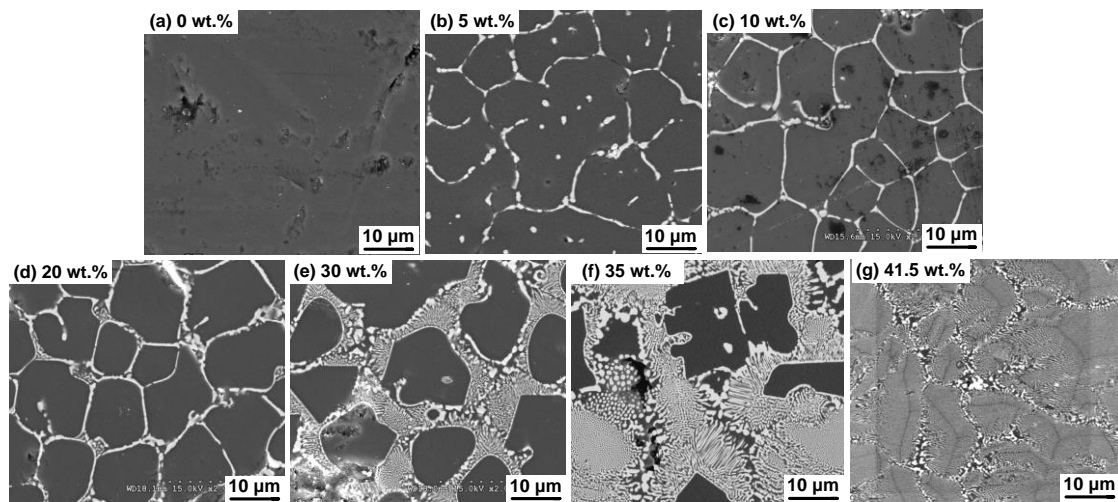


Figure 4.2 Microstructures on cross-sections of ZTA parts with different  $ZrO_2$  contents.

#### 4.2.1.1 Three-dimensional quasi-continuous network microstructure

Figure 4.3 shows SEM images and corresponding EBSD maps on a horizontal cross-section of ZTA part with 10 wt.% ZrO<sub>2</sub>. Figure 4.3(a) shows that ZrO<sub>2</sub> aggregated at grain boundaries of Al<sub>2</sub>O<sub>3</sub> grains, forming a network microstructure. High magnified SEM image of the network boundary area, as shown in Figure 4.3(b), shows that gaps existed in the ZrO<sub>2</sub> boundaries and the network microstructure was quasi-continuous. Such quasi-continuous network microstructure could be found on all different orientations of a fabricated part and was spatially distributed as a three-dimensional quasi-continuous network (3DQCN) microstructure. In a crystal-orientation EBSD map, as shown in Figure 4.3(c), crystals within the tolerance angle of 10° were in the same color and different colors represented different crystal orientations (>10°) for Al<sub>2</sub>O<sub>3</sub>. With the tolerance angle of 10°, one crystal orientation

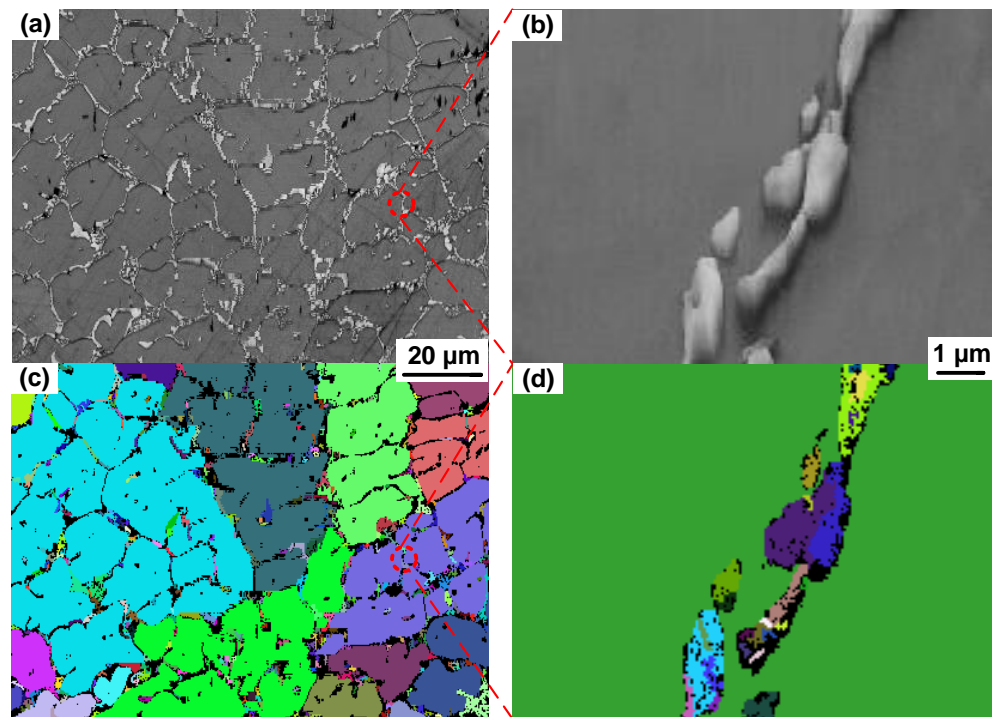


Figure 4.3 SEM images and EBSD mapping analyses on a ZTA part with 10 wt.% ZrO<sub>2</sub>: (a) a SEM image with low magnification; (b) a SEM image with high magnification; (c) EBSD mapping analysis on (a); and (d) EBSD mapping analysis on (b).

contained multiple grains. It was reported that more grains would be identified by using a smaller tolerance angle [22]. Crystal-orientation EBSD mapping analysis was also conducted on the boundary areas, as shown in Figure 4.3(d), indicating that  $\text{ZrO}_2$  at boundary areas demonstrated different orientations. Based on EBSD phase detection results,  $\text{ZrO}_2$  and  $\text{Al}_2\text{O}_3$  exhibited tetragonal phase and  $\alpha$  phase, respectively. The retention of metastable  $t\text{-ZrO}_2$  was ascribed to the reason that the yttrium (Y) element in  $\text{Y}_2\text{O}_3$  suppressed the transformation from the  $t\text{-ZrO}_2$  to  $m\text{-ZrO}_2$  during solidification process [23].

Figure 4.4 shows the formation of 3DQCN microstructure, which followed three stages. In stage 1,  $\text{ZrO}_2$  and  $\text{Al}_2\text{O}_3$  powders were radiated and fully melted by laser with the generation of molten material. After the laser beam left in stage 2, solidification would occur once the temperature of molten material dropped below its liquidus line.  $\text{Al}_2\text{O}_3$  started to nucleate as nuclei, in the meantime,  $\text{ZrO}_2$  nucleated and grew into  $\text{ZrO}_2$  particles. Since there was little wetting tendency between  $\text{Al}_2\text{O}_3$  and  $\text{ZrO}_2$ , most of  $\text{ZrO}_2$  particles would be expelled into the liquid, residing at the liquid/solid interface of  $\text{Al}_2\text{O}_3$  nuclei [24]. In stage 3, with the  $\text{Al}_2\text{O}_3$  nuclei grew into grains,  $\text{ZrO}_2$  particles would aggregate at grain boundaries of  $\text{Al}_2\text{O}_3$ , forming a 3DQCN microstructure.

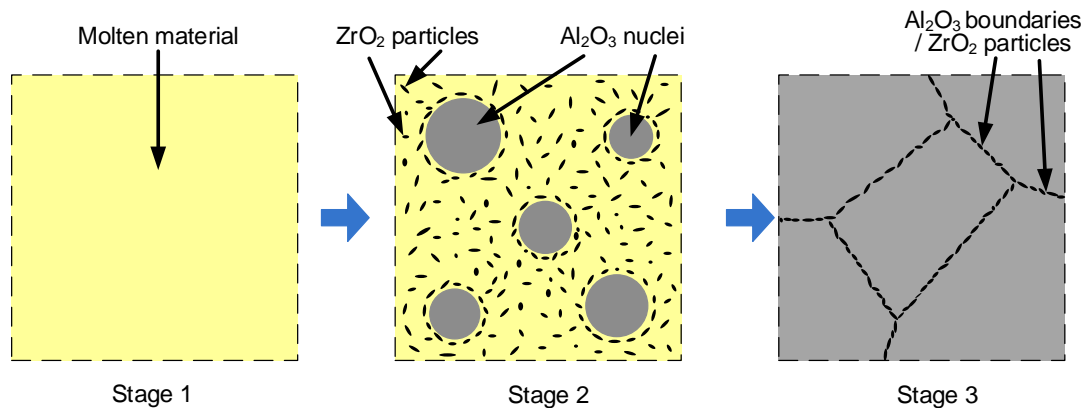


Figure 4.4 Schematic illustration of the formation mechanism of 3DQCN microstructure.

#### 4.2.1.2 Eutectic microstructure

Figure 4.5(a) shows the eutectic microstructure in a ZTA part with 41.5 wt.%  $\text{ZrO}_2$ . Randomly oriented colonies can be observed from the cross-sectional surface. The formation of colonies mainly resulted from the constitutional undercooling and the growth restriction of different-oriented eutectic microstructures [25]. Micro-sized granular  $\text{ZrO}_2$  grains formed at the boundaries of these colonies, as shown in Figure 4.5(b). It was reported that in rapid solidification process,  $\text{ZrO}_2$  and  $\text{Al}_2\text{O}_3$  phases exhibited strong-faceted growth with the generation of faceted structures, which consisted a three-way intersectional dispersion of eutectic microstructure [23, 26]. This was evidenced by experimental results from this investigation, as shown in Figure 4.5(c).

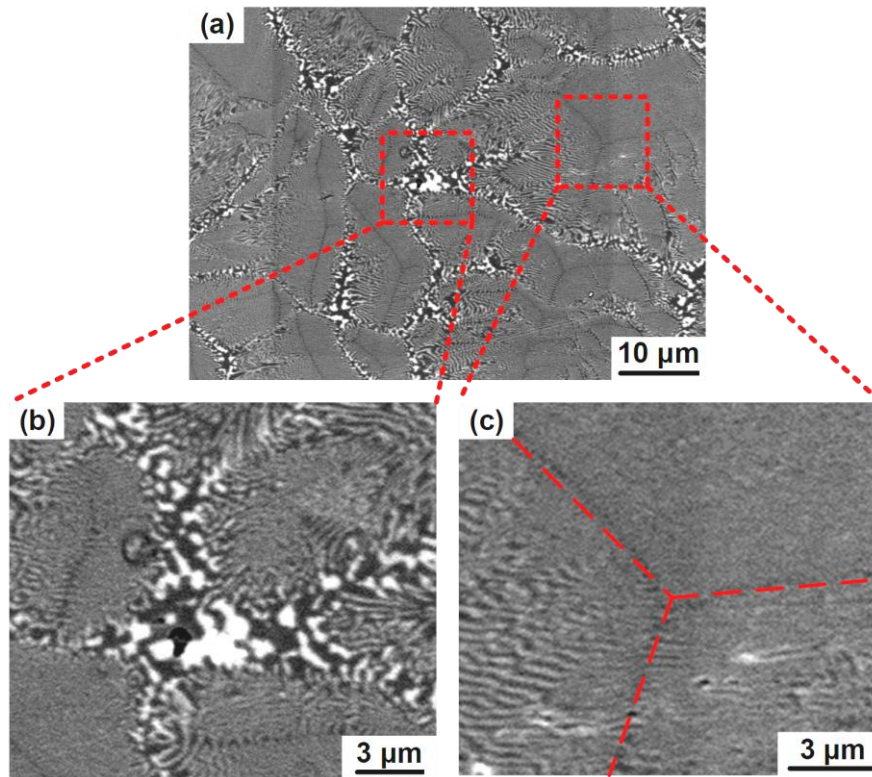


Figure 4.5 Eutectic microstructure on the cross-section of a ZTA part with 41.5 wt.%  $\text{ZrO}_2$ : (a) colonies; (b) boundaries of colonies; and (c) three-way intersectional structure.

Figure 4.6(a) shows the detailed eutectic microstructure of one colony. The phase composition analyses were conducted on the eutectic microstructure (as shown in Figure 6(b)) with EDXS element mapping function (as shown in Figures 4.6(c)-4.6(e)). Results show that the dark areas in Figure 4.6(b) were  $\text{Al}_2\text{O}_3$  (represented by Al element), whereas the bright areas in Figure 4.6(b) were both  $\text{ZrO}_2$  (represented by Zr element) and  $\text{Y}_2\text{O}_3$  (represented by Y element). The  $\text{Y}_2\text{O}_3$  was completely dissolved into the  $\text{ZrO}_2$  without segregation from  $\text{ZrO}_2$  to  $\text{Al}_2\text{O}_3$ . It also can be seen from Figure 4.6(a) that the eutectic microstructure contained interpenetrating and alternate  $\text{ZrO}_2$  and  $\text{Al}_2\text{O}_3$  phases with fine interphase spacing free of grain boundaries. The interphase spacing of the eutectic microstructure was measured as 300 nm. At the central region of colony,  $\text{ZrO}_2$  rods were well-defined and orderly distributed among  $\text{Al}_2\text{O}_3$  matrix. At the edge of colony,  $\text{ZrO}_2$  gradually changed from the rod shape to the lamella shape.

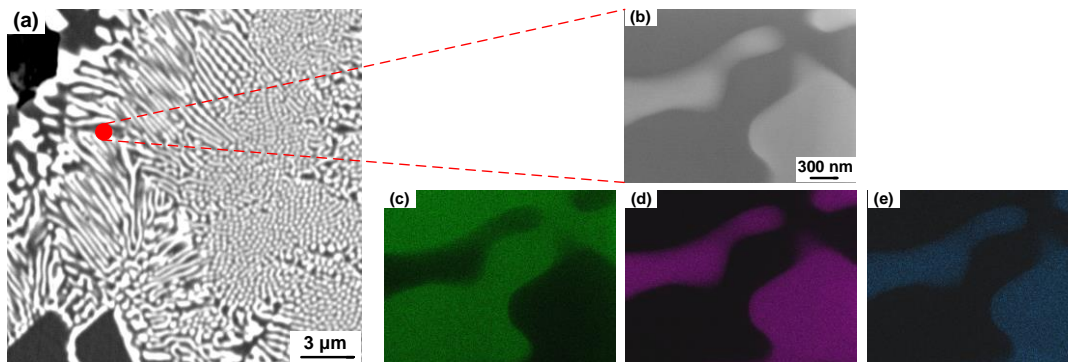


Figure 4.6 EDXS mapping analyses on a ZTA part with 41.5 wt.%  $\text{ZrO}_2$ : (a) eutectic microstructure; (b) detailed features on the eutectic microstructure; and EDXS element maps for (c) Al element, (d) Zr element, (e) and Y element.

Figure 4.7(a) shows a bright-field (BF) TEM image on a single lamella structure, in which dark areas and bright areas were  $\text{ZrO}_2$  and  $\text{Al}_2\text{O}_3$ , respectively. The average width of lamella-shaped  $\text{ZrO}_2$  was around 500 nm, which was larger than the average size of rod-shaped  $\text{ZrO}_2$ . Selected area electron diffraction (SAED) analysis, as shown in Figure 4.7(b), was conducted on the lamella structure (the area enclosed

by red dashed square in Figure 4.7(a)). SAED results show that the  $\text{ZrO}_2$  demonstrates tetragonal phase, which matches the EBSD phase detection result.

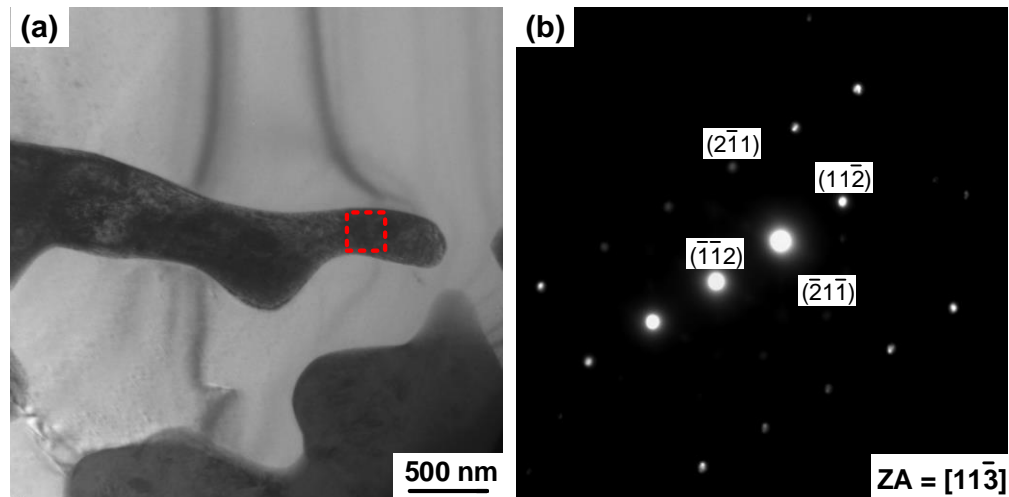


Figure 4.7 TEM analysis on a ZTA part with 41.5 wt.%  $\text{ZrO}_2$ : (a) BF image and (b) SAED patterns of tetragonal  $\text{ZrO}_2$  with zone axis (ZA) =  $[\bar{1}1\bar{3}]$ .

Figure 4.8(a) shows part of the  $\text{ZrO}_2 - \text{Al}_2\text{O}_3$  phase diagram (redrawing from the [27]). In eutectic solidification, the liquid phase is directly transformed into solid  $\text{ZrO}_2$  and  $\text{Al}_2\text{O}_3$  phases. Assume that the initial liquid composition  $C_0$  is close to but smaller than the eutectic composition  $C_E$ , as shown in Figure 4.8(b). At a certain undercooling temperature  $T_U$ , which is below the eutectic temperature  $T_E$ ,  $\text{Al}_2\text{O}_3$  phase starts to nucleate firstly. In the meantime, the surrounding liquid is enriched in  $\text{ZrO}_2$ . With the nucleation of  $\text{Al}_2\text{O}_3$  phase, the liquid composition reaches  $C_{\text{Al}_2\text{O}_3-l}$ , which is still close to but larger than  $C_E$ . Since  $C_{\text{Al}_2\text{O}_3-l}$  is a point on the  $\text{Al}_2\text{O}_3$ -liquid interface line,  $\text{Al}_2\text{O}_3$  is at equilibrium while  $\text{ZrO}_2$  starts to nucleate on the  $\text{Al}_2\text{O}_3$ -liquid interface due to the undercooling  $\Delta T$ . The surrounding liquid is gradually in short of  $\text{ZrO}_2$  but in rich of  $\text{Al}_2\text{O}_3$  until the liquid composition reaches  $C_{\text{ZrO}_2-l}$ , which is on the  $\text{ZrO}_2$ -liquid interface line. At this point,  $\text{ZrO}_2$  is at equilibrium while  $\text{Al}_2\text{O}_3$  begins to nucleate. Such process will repeat with the nucleation and growth in alternating sequence between  $\text{Al}_2\text{O}_3$  phase and  $\text{ZrO}_2$  phase, as shown in Figure 4.8(c), forming the eutectic microstructure [28, 29]. The interphase spacing ( $\lambda$ ), which was discussed in Figure

4.6, was defined in Figure 4.8(c).

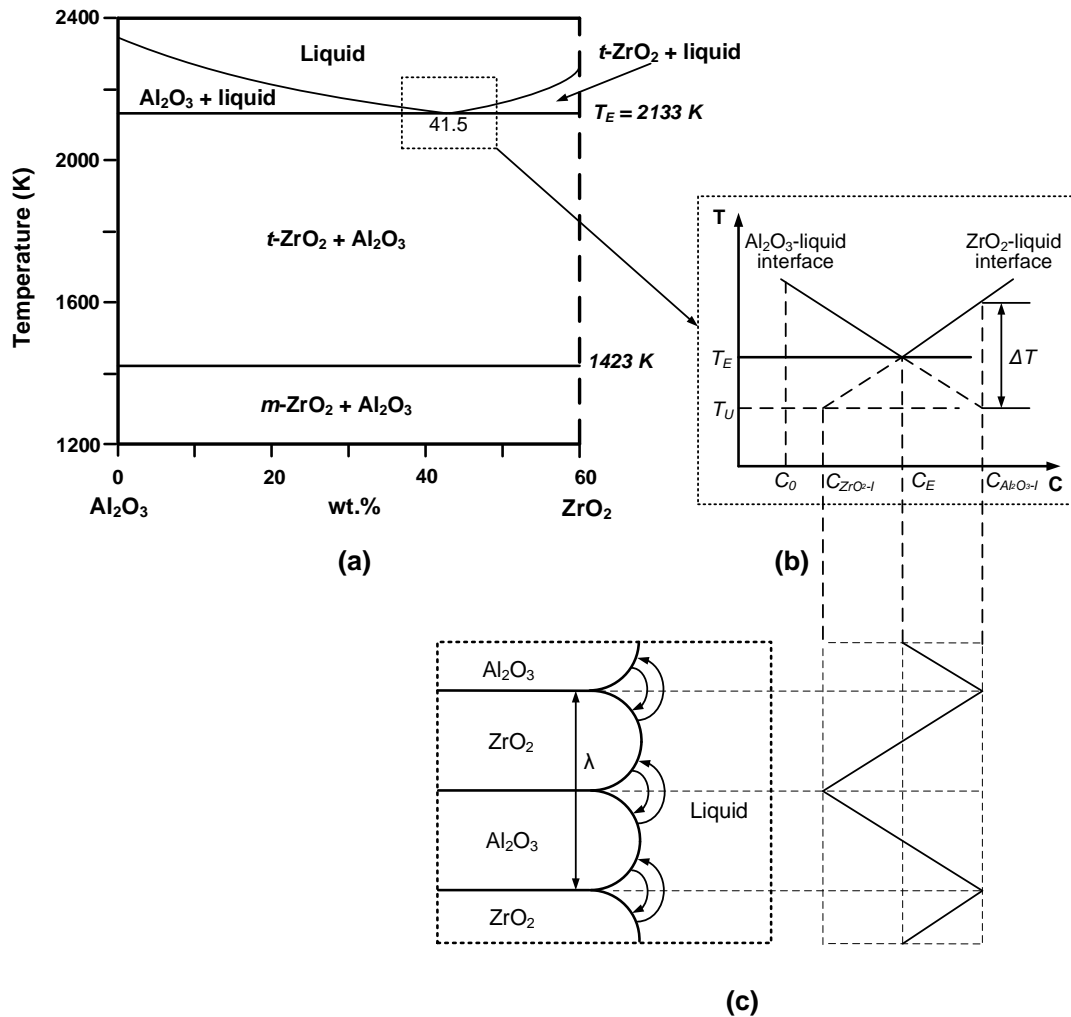


Figure 4.8 (a) Part of the  $ZrO_2$ - $Al_2O_3$  phase diagram (redrawing from the [28]); (2) Alternative nucleation of  $ZrO_2$  and  $Al_2O_3$ ; and (3) A schematic of the coupled growth of  $ZrO_2$  and  $Al_2O_3$  during eutectic solidification.

## 4.2.2 Effects of $ZrO_2$ content on mechanical properties

### 4.2.2.1 Effects on microhardness

Figure 4.9 shows the effects of  $ZrO_2$  content on microhardness of ZTA parts. The average value from five measurements was used to represent experimental results. The standard error of four measurements was used to represent both positive and

negative values of each error bar. It can be seen that the microhardness firstly increased with the  $ZrO_2$  content increasing from 0 wt.% to 20 wt.%, then decreased with  $ZrO_2$  content further increasing from 20 wt.% to 41.5 wt.%. The hardness of ZTA parts were affected by three factors, including grain refinement, precipitation hardening, and  $ZrO_2$  content. At lower levels of  $ZrO_2$  content, a 3DQCN microstructure was formed. The grain growth of  $Al_2O_3$  would be hindered by the 3DQCN microstructure, therefore, the grain size of  $Al_2O_3$  was reduced [30, 31]. Based on the classic Hall-Petch relationship, the reduced grain size would result in the hardness increasing [32, 33]. The precipitation hardening induced by second-phase  $ZrO_2$  also contributed to improving microhardness [34]. Due to these reasons, the microhardness was increased with the  $ZrO_2$  content increasing from 0 wt.% to 20 wt.%. At higher levels of  $ZrO_2$  contents ( $> 20$  wt.%), the increase of  $ZrO_2$  content led to the decrease of microhardness since the  $ZrO_2$  was much softer than  $Al_2O_3$  [35].

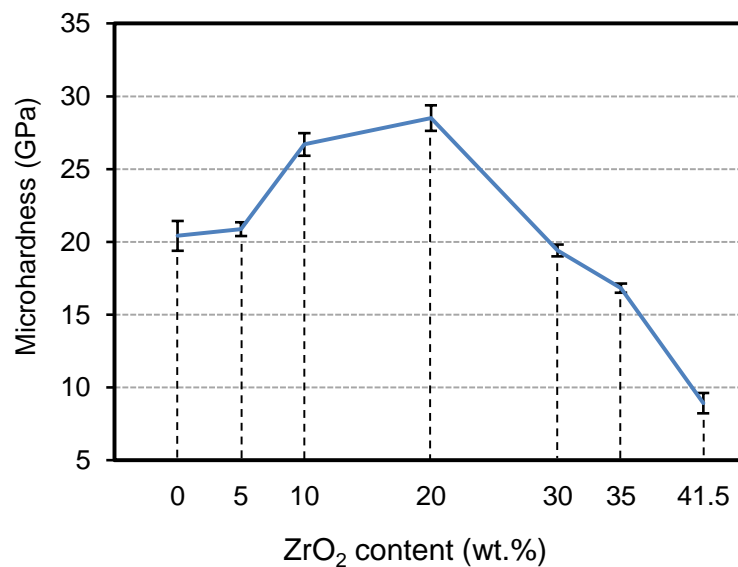


Figure 4.9 Effects of  $ZrO_2$  content on microhardness.

#### 4.2.2.2 Effects on fracture toughness

In this investigation, the fracture toughness was tested by applying Vickers indentation technique. During testing, the polished part was indented with a high load of 9.8 N to create a rhombic region beneath. At this time, cracks emanated from end

points of the indent to surrounding areas, as shown in Figure 4.10. The average length of cracks ( $c$ ), along with the tested Young's Modulus ( $E$ ), hardness ( $H$ ), and applied load ( $P$ ) were used to calculate the fracture toughness ( $K_{IC}$ ) of the material using the following equation [36]:

$$K_{IC} = \alpha \left( \frac{E}{H} \right)^{1/2} \left( \frac{P}{c^{3/2}} \right) \quad (4.1)$$

where,  $\alpha$  is a dimensionless constant and equals 0.016 for a Vickers indenter.

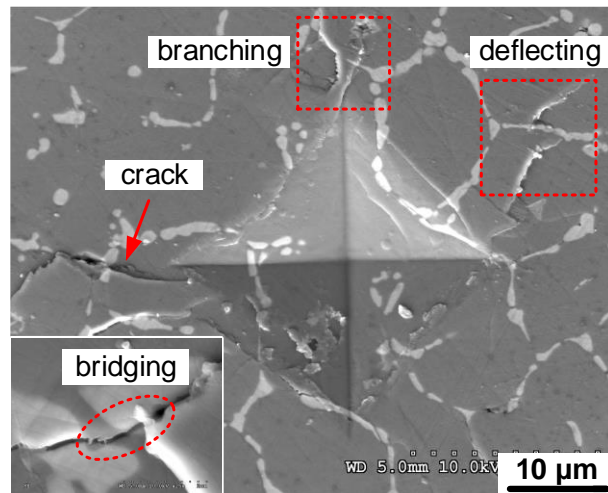


Figure 4.10 An indentation mark and toughening mechanisms in the ZTA part with 10 wt.%  $ZrO_2$ .

The effects of  $ZrO_2$  content on fracture toughness are shown in Figure 4.11. An overall increment of fracture toughness was found with the increase of  $ZrO_2$  content from 0 wt.% to 41.5 wt.%. Transformation toughening effects induced by  $ZrO_2$  was the major reason of this relationship [5]. In this investigation,  $Y_2O_3$ -stabilized  $ZrO_2$  was formed and maintained as metastable tetragonal phase after LD-AM process. When external force was applied, the metastable  $t$ - $ZrO_2$  would be transformed into a stable  $m$ - $ZrO_2$ , causing stress-induced volume increase [37]. The process of volume increasing could absorb energy which would otherwise be utilized by crack propagation. In another word, the phase transformation would partially take away the

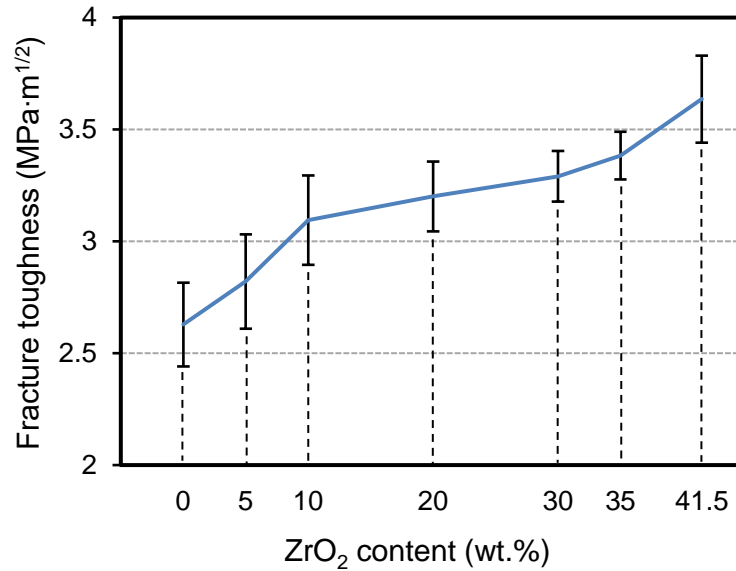


Figure 4.11 Effects of ZrO<sub>2</sub> content on fracture toughness.

energy for crack propagation, thus suppressing the propagation of indentation-generated cracks. In addition, the formation of *m*-ZrO<sub>2</sub> required additional energy, and the formed *m*-ZrO<sub>2</sub> could mitigate elastic strain at crack tips, thus toughening ZTA [38]. Other toughening mechanisms included crack bridging, crack branching, and crack deflecting, as shown in Figure 4.10. It was reported that crack bridging, crack branching, and crack deflecting could reduce driving forces, retard crack propagation,

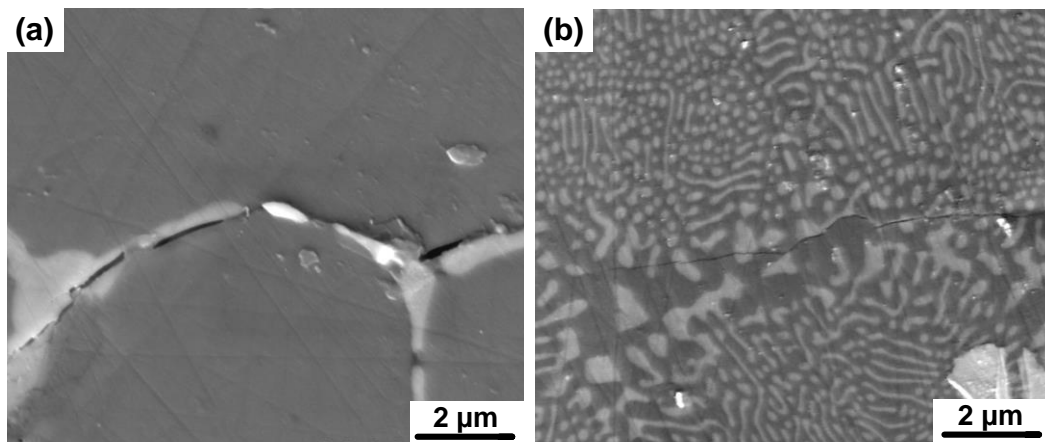


Figure 4.12 Crack propagations in (a) the ZTA part with 10 wt.% ZrO<sub>2</sub> and (b) the ZTA part with 41.5 wt.% ZrO<sub>2</sub>.

and reduce crack tip stress, thus increasing the energy required for crack propagation [2]. Therefore, it can be concluded that the  $ZrO_2$  at grain boundaries of  $Al_2O_3$  acted as barriers to crack propagation and toughened ZTA parts. In addition to the propagations across the  $Al_2O_3$  grains (transcrystalline propagation, in Figure 4.10), cracks were also evidenced to propagate along the grain boundaries of  $Al_2O_3$  (intercrystalline propagation, in Figure 4.12(a)). Compared to ZTA part with 10 wt.%  $ZrO_2$ , the crack width was thinner and crack path was more straight in ZTA part with 41.5 wt.%  $ZrO_2$ , as shown in Figure 4.12(b). In addition, the crack propagated with no preference toward  $ZrO_2$  nor  $Al_2O_3$  and cut through both  $ZrO_2$  and  $Al_2O_3$  regions.

### 4.3 Conclusions

In this investigation, the effects of  $ZrO_2$  content on microstructures (mainly including 3DQCN and eutectic microstructures) and mechanical properties (including microhardness and fracture toughness) of LD-AM fabricated ZTA parts were studied. The formations mechanisms of microstructures and their effects on mechanical properties were also investigated. The major conclusions are drawn as follows:

(1) At lower levels of  $ZrO_2$  content,  $ZrO_2$  particles tended to aggregate at grain boundaries of  $Al_2O_3$  matrix, forming a network microstructure. The network microstructure was quasi-continuous and spatially distributed as a 3DQCN microstructure, which benefited ZTA parts on enhancing their mechanical performance.

(2) At higher levels of  $ZrO_2$  content, eutectic microstructure dominated the whole part. The eutectic microstructure contained randomly oriented colonies with granular  $ZrO_2$  grains presenting at boundaries of these colonies. Within one colony, orderly-distributed  $ZrO_2$  rods located at the central region, and lamella-shaped  $ZrO_2$  located at the edge region.

(3) By increasing  $ZrO_2$  content from 0 wt.% to 41.5 wt.%, the microhardness of ZTA parts was firstly increased then decreased. The microhardness of ZTA parts were affected by three factors, including grain refinement, precipitation hardening and

the ZrO<sub>2</sub> content.

(4) An overall increment of fracture toughness was found by increasing ZrO<sub>2</sub> content from 0 wt.% to 41.5 wt.%. The primary reason is the phase transformation (*t*-ZrO<sub>2</sub> to *m*-ZrO<sub>2</sub>) toughening effects. In addition, crack bridging, crack branching, and crack deflecting were also beneficial for toughening ZTA parts. Indentation-generated marks propagated both across the grains (transcrystalline propagation) and along grain boundaries (intercrystalline propagation).

## 4.4 Materials and Methods

### 4.4.1 Powder materials and powder treatment

In this investigation, the LD-AM process was carried out on a laser engineered net shaping (LENS) machine (450XL, Optomec Inc., Albuquerque, NM, USA). The suggested particle size range of this LENS machine was 30 – 150 μm. To meet this requirement and keep good powder flowability, a particle size range of 45 – 75 μm was selected for the majorly used Al<sub>2</sub>O<sub>3</sub> powder (AL-604, Atlantic Equipment Engineers, Upper Saddle, NJ, USA). The purity of the Al<sub>2</sub>O<sub>3</sub> powder was 99.9%. To retain metastable *t*-ZrO<sub>2</sub> to room temperature after rapid-solidification LD-AM process, 10% – 15% stabilizing yttria (Y<sub>2</sub>O<sub>3</sub>) was added to the ZrO<sub>2</sub> powder. The fused Y<sub>2</sub>O<sub>3</sub>-stabilized ZrO<sub>2</sub> (ZR-604, Atlantic Equipment Engineers, Upper Saddle, NJ, USA) had a lower particle size range of 1 – 5 μm with a purity of 99.9%. Figures 4.13(a) and 4.13(b) show the as-received Al<sub>2</sub>O<sub>3</sub> and Y<sub>2</sub>O<sub>3</sub>-stabilized ZrO<sub>2</sub> powders, respectively. Differing the particle size range of ZrO<sub>2</sub> powder from Al<sub>2</sub>O<sub>3</sub> powder was to prevent powder separation during powder mixing process. Powder separation referred to the phenomenon that heavier ZrO<sub>2</sub> particles were kept at the bottom whereas lighter Al<sub>2</sub>O<sub>3</sub> particles traveled to the top during mixing [39]. In this investigation, the Al<sub>2</sub>O<sub>3</sub> and ZrO<sub>2</sub> powders were mixed using a planetary ball milling machine (ND2L, Torrey Hills Technologies LLC., San Diego, CA, USA) with different ZrO<sub>2</sub> contents, including 5 wt.%, 10 wt.%, 20 wt.%, 30 wt.%, 35 wt.%, and 41.5 wt.%. Based on preliminary results, ball-milling parameters were set at fixed

rotation speed of 130 rpm, ball-to-powder weight ratio of 1:1, and milling time of 6 hours. It can be seen from Figure 4.13(c) that after ball-milling processing, the  $\text{Al}_2\text{O}_3$  powder exhibited no obvious size reduction and shape change, and the  $\text{Al}_2\text{O}_3$  and  $\text{ZrO}_2$  powders were well mixed.

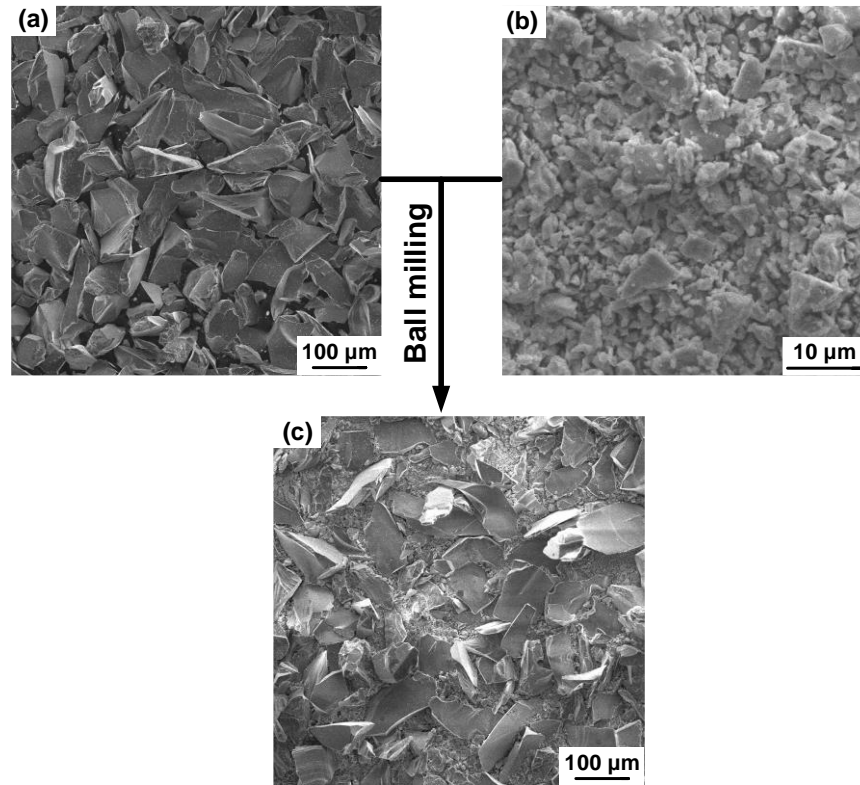


Figure 4.13 Shapes and morphologies of powders: As-received (a)  $\text{Al}_2\text{O}_3$  and (b)  $\text{Y}_2\text{O}_3$ -stabilized  $\text{ZrO}_2$  powders; and (c) mixed powders with 10 wt.%  $\text{ZrO}_2$  (for illustration purpose).

#### 4.4.2 Experimental set-up and parameters

The values or ranges of input fabrication variables are listed in Table 4.1. The laser source of the machine had a continuous wave with a constant wavelength of 1064 nm. The dimensions of the parts were 8 mm  $\times$  8 mm  $\times$  10 layers. Four parts under each  $\text{ZrO}_2$  content were fabricated on the titanium substrate to avoid experimental errors. The selection of titanium as the substrate material was based on the following reasons: (1) ZTA parts could be successfully fabricated onto titanium

substrate; and (2) Compared with ceramic substrate, the titanium substrate would not be shocked into pieces by laser.

Table 4.1 Input fabrication variables

<b>Input fabrication variables</b>	<b>Values or ranges</b>
Laser power (W)	350
Laser mode	Continuous
Beam diameter of laser (mm)	0.40
Wavelength of laser (nm)	1064
Scanning speed (mm/s)	10
Hatch distance (mm)	0.38
Layer thickness (mm)	0.51
Powder feeding rate (g/min)	2
Number of layers	10
Scanning orientation (°)	45, alternate 90 per layer

#### **4.4.3 Measurement procedures**

The two scanning electron microscopy (SEM) machines (Phenom Pharos, ThermoFisher Scientific, Waltham, MA, USA & S4300, Hitachi, Ltd., Tokyo, Japan) were used to observe the shapes and morphologies of the powders and study the microstructure characterizations of fabricated parts. Prior to SEM observation, the parts were cut and ground using a grinder-polisher machine (MetaServ 250/AutoMet 250, Buehler, Lake Bluff, IL, USA). Phase composition and element distribution were analyzed with an energy-dispersive X-ray spectroscopy (EDXS) system (Crossbeam 540, Carl Zeiss AG, Oberkochen, Germany). Crystal orientation and grain orientation mapping analyses were conducted on an electron backscatter diffraction (EBSD) system (Crossbeam 540, Carl Zeiss AG, Oberkochen, Germany). The detailed lamella structure and crystal structure of  $ZrO_2$  were examined by a transmission electron microscopy (TEM) machine (H8100, Hitachi, Ltd., Tokyo, Japan).

The microhardness and fracture toughness were tested on the polished surfaces (perpendicular to the deposition direction) of fabricated parts using a nano-mechanical

testing system (PB1000, Nanovea, Irvine, CA, USA). The microhardness tests and fracture toughness tests were conducted with load of 9.8 N and loading/unloading rate of 3 N/min. Tests were conducted at five different locations with more than 0.5 mm distance.

### **Data Availability**

The datasets generated/or analyzed during the current study are available from the corresponding author on reasonable request.

## References

- [1] De Aza, A. H., Chevalier, J., Fantozzi, G., Schehl, M., & Torrecillas, R. (2002). Crack growth resistance of alumina, zirconia and zirconia toughened alumina ceramics for joint prostheses. *Biomaterials*, 23(3), 937-945.
- [2] Zhang, S., Sun, D., Fu, Y. Q., & Du, H. J. (2005). Toughening of hard nanostructural thin films: a critical review. *Surface and Coatings Technology*, 198(1), 2-8.
- [3] Li, Y. Z., Hu, Y. B., Cong, W. L., Zhi, L., & Guo, Z. N. (2017). Additive manufacturing of alumina using laser engineered net shaping: effects of deposition variables. *Ceramics International*, 43(10), 7768-7775.
- [4] Tang, D., Lim, H. B., Lee, K. J., Lee, C. H., & Cho, W. S. (2012). Evaluation of mechanical reliability of zirconia-toughened alumina composites for dental implants. *Ceramics International*, 38(3), 2429-2436.
- [5] Bocanegra-Bernal, M. H., & Torre, D. D. L. (2002). Phase transitions in zirconium dioxide and related materials for high performance engineering ceramics. *Journal of Materials Science*, 37(23), 4947-4971.
- [6] Wang, J., & Stevens, R. (1989). Zirconia-toughened alumina (ZTA) ceramics. *Journal of Materials Science*, 24(10), 3421-3440.
- [7] Hu, Y. B., & Cong, W. L. (2018) A review on laser deposition-additive manufacturing of ceramics and ceramic reinforced metal matrix composites. *Ceramics International*, 44(17), 20599-20612.
- [8] Mandal, N., Doloi, B., & Mondal, B. (2013). Predictive modeling of surface roughness in high speed machining of AISI 4340 steel using yttria stabilized zirconia toughened alumina turning insert. *International Journal of Reactory Metals and Hard Materials*, 38, 40-46.
- [9] He, X., Zhang, Y. Z., Mansell, J. P., & Su, B. (2008). Zirconia toughened alumina ceramic foams for potential bone graft applications: fabrication, bioactivation, and cellular responses. *Journal of Materials Science: Materials in Medicine*, 19(7), 2743-2749.
- [10] Ganesh, I., Olhero, S. M., Torres, P. M., Alves, F. J., & Ferreira, J. M. (2009). Hydrolysis-induced aqueous gelcasting for near-net shape forming of ZTA ceramic composites. *Journal of European Ceramic Society*, 29(8), 1393-1401.
- [11] Gutknecht, D., Chevalier, J., Garnier, V., & Fantozzi, G. (2007). Key role of processing to avoid low temperature ageing in alumina zirconia composites for orthopaedic application. *Journal of European Ceramic Society*, 27(2), 1547-1552.
- [12] Denry, I., & Kelly, J. R. (2008). State of the art of zirconia for dental applications. *Dental Materials*, 24(3), 299-307.
- [13] Fries, R., & Rand, B. (2006). Slip-casting and filter-pressing. *Materials Science and Technology*.
- [14] Evans, J. R. (2005). Injection moulding. *Journal of Materials Science & Technology*. Wiley VCH Verlag, Weinheim, 268-311.
- [15] Wilkes, J., Hagedorn, Y. C., Meiners, W., & Wissenbach, K. (2013). Additive manufacturing of ZrO<sub>2</sub>-Al<sub>2</sub>O<sub>3</sub> ceramic components by selective laser melting.

- Rapid Prototyping Journal, 19(1), 51-57.
- [16] Yves-Christian, H., Jan, W., Wilhelm, M., Konrad, W., & Reinhart, P. (2010). Net shaped high performance oxide ceramic parts by selective laser melting. *Physics Procedia*, 5, 587-594.
- [17] Niu, F. Y., Wu, D. J., Ma, G. Y., Wang, J. T., Guo, M. H., & Zhang, B. (2015). Nanosized microstructure of  $\text{Al}_2\text{O}_3\text{-ZrO}_2$  ( $\text{Y}_2\text{O}_3$ ) eutectics fabricated by laser engineered net shaping. *Scripta Materialia*, 95, 39-41.
- [18] Hu, Y. B., Ning, F. D., Cong, W. L., Li, Y. C., Wang, X. L., & Wang, H. (2018). Ultrasonic vibration-assisted laser engineered net shaping of  $\text{ZrO}_2\text{-Al}_2\text{O}_3$  bulk parts: effects on crack suppression, microstructure, and mechanical properties. *Ceramics International*, 44(3), 2752-2760.
- [19] Yan, S., Wu, D. J., Ma, G. Y., Niu, F. Y., Kang, R. K., & Guo, D. M. (2017). Formation mechanism and process optimization of nano  $\text{Al}_2\text{O}_3\text{-ZrO}_2$  eutectic ceramic via laser engineered net shaping (LENS). *Ceramics International*, 43(17), 14742-14747.
- [20] Gasser, A., Backes, G., Kelbassa, I., Weisheit, A., & Wissenbach, K. (2010). Laser additive manufacturing. *Laser Technik Journal*, 7(2), 58-63.
- [21] Huang, Y. J., Zeng, X. Y., Hu, Q. W., & Zhou, S. F. (2008). Analysis model and experimental research of dilution in laser induction hybrid cladding. *Journal of Applied Optics*, 29(2), 248-252. (in Chinese)
- [22] Zhilyaev, A. P., Kim, B. K., Szpunar, J. A., Baró, M. D., & Langdon, T. G. (2005). The microstructural characteristics of ultrafine-grained nickel. *Materials Science and Engineering: A*, 391(1-2), 377-389.
- [23] Zhao, Z. M., Zhang, L., Song, Y. G., & Wang, W. G. (2008).  $\text{Al}_2\text{O}_3/\text{ZrO}_2$  ( $\text{Y}_2\text{O}_3$ ) self-growing composites prepared by combustion synthesis under high gravity. *Scripta Materialia*, 58(3), 207-210.
- [24] Lebeau, T. (1994). Wetting of alumina-based ceramics by aluminum alloys. McGill University.
- [25] Liu, Z., Song, K., Gao, B., Tian, T., Yang, H. O., Lin, X., & Huang, W. D. (2016). Microstructure and mechanical properties of  $\text{Al}_2\text{O}_3/\text{ZrO}_2$  directionally solidified eutectic ceramic prepared by laser 3D printing. *Journal of Materials Science & Technology*, 32(4), 320-325.
- [26] Su, H. J., Zhang, J., Tian, J. J., Liu, L., & Fu, H. Z. (2008). Preparation and characterization of  $\text{Al}_2\text{O}_3/\text{Y}_3\text{Al}_5\text{O}_{12}/\text{ZrO}_2$  ternary hypoeutectic in situ composites by laser rapid solidification. *Journal of Applied Physics*, 104(2), 023511.
- [27] Chraska, T., Neufuss, K., Dubský, J., Ctibor, P., & Rohan, P. (2008). Fabrication of bulk nanocrystalline alumina-zirconia materials. *Ceramics International*, 34(5), 1229-1236.
- [28] LLorca, J., & Orera, V. M. (2006). Directionally solidified eutectic ceramic oxides. *Progress in Materials Science*, 51(6), 711-809.
- [29] Dantzig, J. A., & Rappaz, M. (2009). Solidification. EPFL press.
- [30] Casellas, D., Nagl, M. M., Llanes, L., & Anglada, M. (2003). Fracture toughness of alumina and ZTA ceramics: microstructural coarsening effects.

- Journal of Materials Processing Technology, 143, 148-152.
- [31] Meunier, C., Zuo, F., Peillon, N., Saunier, S., Marinel, S., & Goeuriot, D. (2017). In situ study on microwave sintering of ZTA ceramic: effect of ZrO<sub>2</sub> content on densification, hardness, and toughness. *Journal of the American Ceramic Society*, 100(3), 929-936.
  - [32] Hall, E. O. (1951). The deformation and ageing of mild steel: III discussion of results. *Proceedings of the Physical Society of London, Section B*, 64(9), 747.
  - [33] Petch, N. J. (1953). The cleavage strength of polycrystals. *Journal of Iron and Steel Research International*, 174, 25-28.
  - [34] Pelleg, J. (2014). *Mechanical properties of ceramics*. Springer Science+Business, 213.
  - [35] Heros, R. J. (1998). Ceramic in total hip arthroplasty: history, mechanical properties, clinical results, and current manufacturing state of the art. In *Seminars in Arthroplasty*. 9, 114-122.
  - [36] Bhushan, B., & Li, X. (2003). Nanomechanical characterisation of solid surfaces and thin films. *International Materials Reviews*, 48(3), 125-164.
  - [37] Gupta, T. K., Lange, F. F., & Bechtold, J. H. (1978). Effect of stress-induced phase transformation on the properties of polycrystalline zirconia containing metastable tetragonal phase. *Journal of Materials Science*, 13(7), 1464-1470.
  - [38] Kirchner, H. P., Gruver, R. M., Swain, M. V., & Garvie, R. C. (1981). Crack branching in transformation-toughened zirconia. *Journal of the American Ceramic Society*, 64(9), 529-533.
  - [39] Bridgwater, J. (1976). Fundamental powder mixing mechanisms. *Powder Technology*, 15(2), 215-236.

### **Acknowledgements**

The microhardness and fracture toughness were tested on a nano-mechanical testing system (PB1000, Nanovea, Irvine, CA, USA), which was supported by the Defense University Research Instrumentation Program through award W911NF-17-1-0270 ARO 2017.

### **Author Contributions Statement**

Y.H. and W.C. undertook the research design and original draft writing. Samples were fabricated and processed by Y.H. and H.W. Microstructure characterizations were analyzed by Y.H. and B.Z. Y.H. conducted experiments on testing mechanical properties.

### **Additional Information**

Competing interests: The authors declare no competing interests.

## CHAPTER V

### **SURFACE GRINDING OF ZTA PARTS FABRICATED BY LENS – EFFECTS OF ZRO<sub>2</sub> CONTENT AND ULTRASONIC VIBRATION**

Paper title:

Surface grinding of ZTA parts fabricated by laser engineered net shaping process: effects of ZrO<sub>2</sub> content and ultrasonic vibration

Published in:

Proceedings of the 2018 Manufacturing Science and Engineering Conference

Authors' names:

Yingbin Hu<sup>a</sup>, Hui Wang<sup>a</sup>, Yanchen Li<sup>a,b</sup>, Fuda Ning<sup>a</sup>, Weilong Cong<sup>a,\*</sup>

Authors' affiliations:

<sup>a</sup>Department of Industrial, Manufacturing, & Systems Engineering, Texas Tech University, Lubbock, Texas, 79409, USA

<sup>b</sup>Key Laboratory of Mechanism Theory and Equipment Design of Ministry of Education, Tianjin University, Tianjin, 300072, China

\*Corresponding author:

Department of Industrial, Manufacturing, & Systems Engineering, Texas Tech University, Lubbock, TX 79409-3061, USA. Email address: weilong.cong@ttu.edu

## **Abstract**

The zirconia toughened alumina (ZTA) parts fabricated by laser engineered net shaping (LENS) process demonstrate problems resulted from poor surface quality. To improve surface quality and to reduce related problems, rotary ultrasonic machining (RUM) process, which combines both grinding process and ultrasonic machining process, has been introduced. In this investigation, the effects of  $ZrO_2$  content and ultrasonic vibration on flatness, surface roughness, microhardness, and cutting force in feeding direction of LENS-fabricated ZTA parts have been studied. Results showed that with the  $ZrO_2$  content increasing, the flatness value increased, the surface roughness value decreased, and the microhardness value firstly increased then decreased. Compared with LENS-fabricated parts, the parts processed by RUM machine exhibited better surface quality with significantly reduced flatness value and surface roughness value. In RUM process, the introduction of ultrasonic vibration was beneficial for reducing cutting force.

## **Keywords**

Zirconia toughened alumina; Rotary ultrasonic machining; Flatness; Surface roughness; Microhardness; Cutting force.

## **5.1 Introduction**

As a kind of brittle material, alumina ( $Al_2O_3$ ) demonstrates severe problems resulted from low toughness [1, 2]. Compared with  $Al_2O_3$ , zirconia toughened alumina (ZTA) ceramics exhibit higher toughness and have been widely applied in biomedical, chemical, and other high-end engineering industries [3, 4]. In recent years, extensive investigations have been done on fabricating ZTA parts using laser additive manufacturing (LAM) processes to take their advantages of high design flexibility, high customization, shortened lead time, no need of assembly or molds, etc. [5]. Among all types of LAM processes, laser engineered net shaping (LENS) process has benefits of low labor intensity, high fabrication efficiency, parts remanufacturing capability, etc., and is considered as an attractive process for processing ceramics [6].

Figure 5.1 schematically illustrates the LENS process. At beginning, the laser beam generated by the laser generator and the powder supplied by powder stream are simultaneously ejected to the substrate, forming a molten pool which can continuously

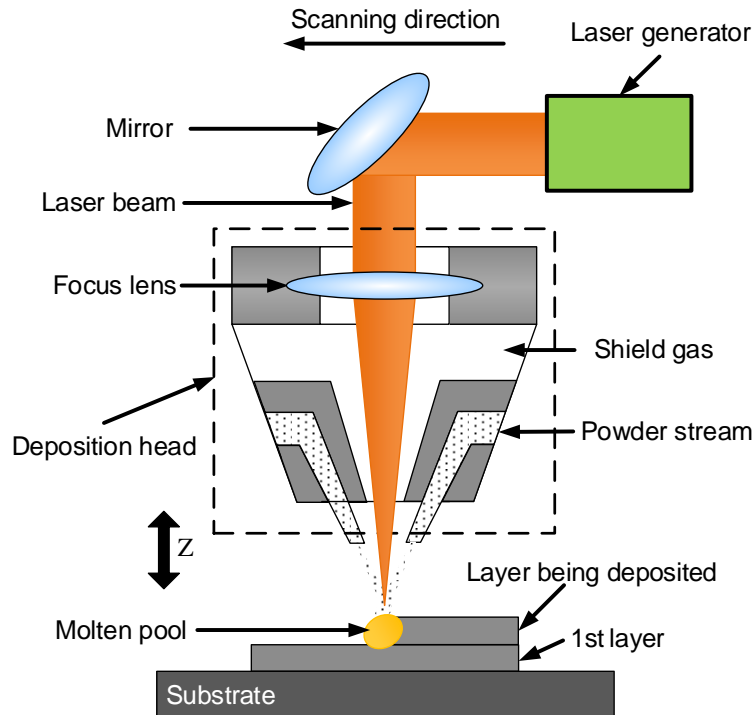


Figure 5.1 Illustration of LENS process.

catch and melt powders. When the laser beam moves away, the molten pool starts to solidify. The deposition head moves along the trajectory designed by the three-dimensional file, creating the first layer on the substrate. Afterwards, the deposition head will ascend one layer thickness to the new set position for the second layer deposition. Similar process will be repeated many times until the designed near-net-shape part is built layer by layer [7, 8].

Despite the benefits demonstrated by LENS process, the LENS fabricated parts still have many problems (such as low dimensional accuracy and high surface roughness), which negatively affect their applications [9, 10]. Therefore, it is crucial to integrate the LENS process with an effective and efficient post-processing process. In this investigation, a nontraditional rotary ultrasonic machining (RUM) process, which

combines both grinding process and ultrasonic machining process, has been introduced to fulfill the requirements. Compared with both grinding process and ultrasonic machining process, the RUM process can hugely reduce the cutting force in feeding direction [11, 12].

Figure 5.2 shows the illustration of RUM process. The typical structure of a cutting tool is shown in Figure 5.2(b). In RUM process, the feeding direction of cutting tool is perpendicular to the spindle axis and along the top surface of the workpiece. Being horizontally fed, the cutting tool is also ultrasonically vibrated in the axial direction. To wash away generated chips and to prevent the interface between the cutting tool and workpiece from overheating, the coolant is pumped through the core of the cutting tool [13, 14].

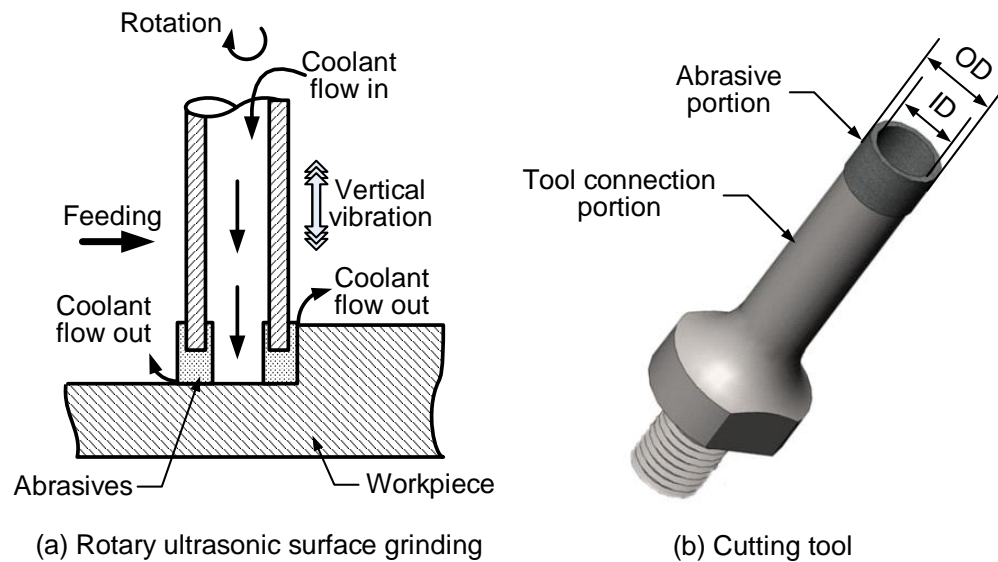


Figure 5.2 Illustration of rotary ultrasonic machining (RUM).

In this investigation, effects of  $ZrO_2$  content and ultrasonic vibration on flatness, surface roughness, microhardness, and cutting force in feeding direction of LENS fabricated ZTA parts have been investigated. The obtained results will provide guidance on improving the surface quality of parts fabricated by LAM processes.

## 5.2 Experimental set-up and measurement procedures

### 5.2.1 Powder materials and powder treatment

In this investigation, Al<sub>2</sub>O<sub>3</sub> powder (AL-604, Atlantic Equipment Engineers, Upper Saddle, NJ, USA) with a particle size range of 45 – 75 μm was used. Fused yttria-stabilized ZrO<sub>2</sub> (ZR-604, Atlantic Equipment Engineers, Upper Saddle, NJ, USA) had a particle size range of 1 – 5 μm and a purity of 99.9%. Prior to LENS process, the Al<sub>2</sub>O<sub>3</sub> and ZrO<sub>2</sub> powders were mixed using a planetary ball milling machine (ND2L, Torrey Hills Technologies LLC., San Diego, CA, USA). The parameters were fixed based on preliminary experiments, including ball-to-powder weight ratio of 1:1, fixed rotation speed of 130 rpm, and milling time of 6 hours. The shapes and morphologies of the as-received Al<sub>2</sub>O<sub>3</sub> and ZrO<sub>2</sub> powders are shown in Figures 5.3(a) and 5.3(b), respectively. After ball milling process, the Al<sub>2</sub>O<sub>3</sub> powder

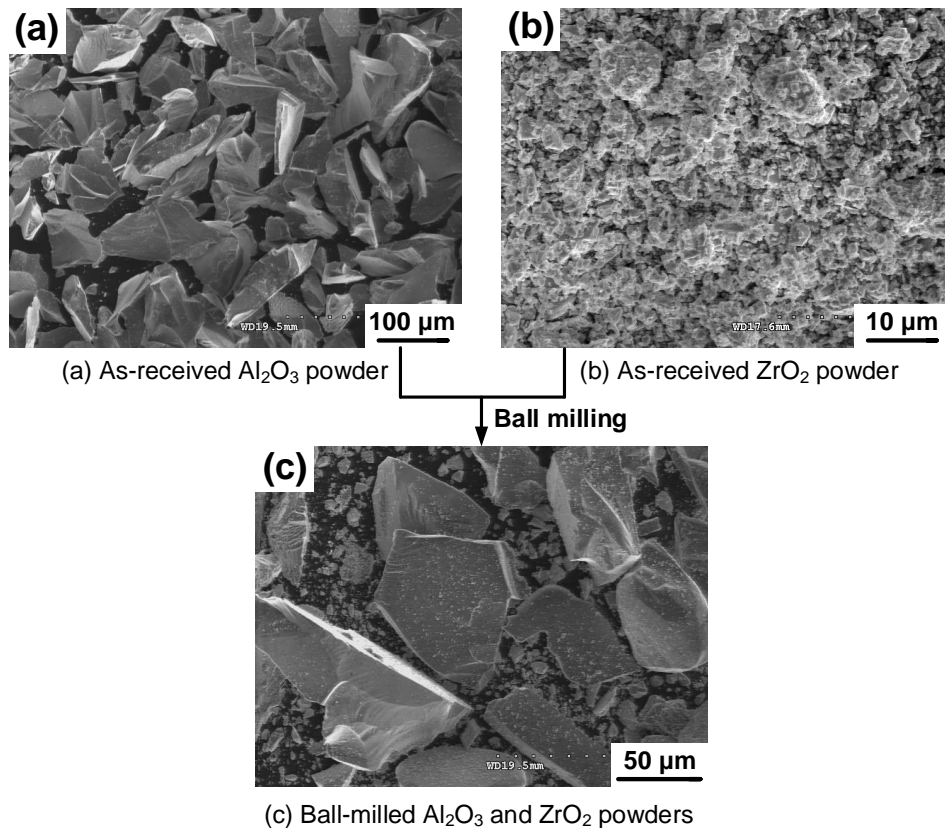


Figure 5.3 Shapes and morphologies of the powders.

exhibited no obvious shape change and size reduction and the  $\text{Al}_2\text{O}_3$  and  $\text{ZrO}_2$  powders were well mixed (in Figure 5.3(c)).

### 5.2.2 Experimental set-up

In this investigation, the ZTA parts were fabricated using a LENS machine (LENS450, Optomec Inc., Albuquerque, NM, USA). Then, the LENS fabricated parts were surface-grinded on a rotary ultrasonic machine (Series 10, Sonic-Mill, Albuquerque, New Mexico, USA). As shown in Figure 5.4, the rotary ultrasonic machine comprised four major systems: an ultrasonic spindle system, a horizontal feeding system, a data acquisition (DAQ) system, and a coolant system. The ultrasonic spindle system consisted an ultrasonic spindle, a motor with rotation-speed controller, and an ultrasonic power supply. The ultrasonic power supply could convert low frequency (60 Hz) line electricity to high frequency (20 kHz) electrical energy. Then, the high frequency electrical energy was converted into high frequency amplified ultrasonic vibration via the piezoelectric converter, which was mounted inside the ultrasonic spindle. Afterwards, the generated ultrasonic vibration was transmitted to

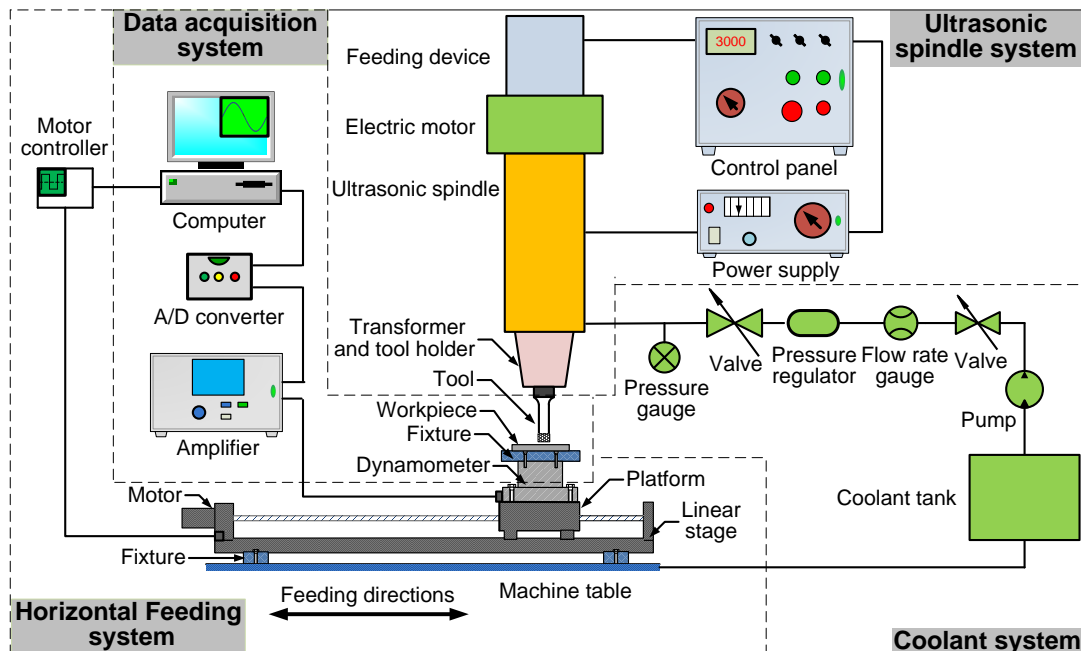


Figure 5.4 RUM experimental set-up.

the RUM cutting tool for surface grinding. The motor inside the ultrasonic spindle enabled the rotation motion of the spindle. The controllable horizontal feeding motion was provided by a linear stage (NSC-A1, Newmark, Rancho Santa Margarita, California, USA) and the associated software. The function of the DAQ system was to acquire and analyze real-time data collected from the dynamometer (Type 9272, Kistler Inc., Switzerland).

### 5.2.3 Experimental conditions

Table 5.1 lists the values of input fabrication variables in LENS process. These values were optimized and fixed based on preliminary results. Three replicated parts were fabricated on the titanium substrate under each level (0 wt.%, 10 wt.%, 20 wt.%, and 30 wt.%) of ZrO<sub>2</sub> content. The dimensions of the parts were 8 mm × 8 mm × 10 layers.

Table 5.1 Input fabrication variables

Machining parameters	Unit	Values
Laser power	W	350
Wavelength of laser	μm	1.07
Scanning speed	mm/s	10
Layer thickness	μm	508
Powder feeding rate	g/min	2
Scanning orientation	°	45, alternate 90 per layer

In this investigation, effects of ZrO<sub>2</sub> content and ultrasonic vibration (0% and 40%) in RUM process were investigated. 40% ultrasonic power means that 40% power from the ultrasonic power supply was utilized. To have reliable results, three tests were conducted under each combination of experimental conditions. For all RUM tests, the machining parameters (including depth of cut, tool rotation speed, and feedrate) were fixed at optimal values based on parametric selection results, as shown in Table 5.2. Besides, Table 5.2 also shows the basic tool variables.

Table 5.2 Machining parameters and tool variables

Machining parameters	Unit	Values
Ultrasonic power level	%	0 and 40
Depth of cut, <i>DOC</i>	mm	0.5
Tool rotation speed, <i>S</i>	rpm	2000
Feedrate, <i>Fr</i>	mm/s	0.5
Tool abrasive size	mm	0.16
Tool geometry		Flat
Abrasive material		Diamond

### 5.2.4 Measurement procedures

In this investigation, the scanning electron microscope (SEM) (S-4300, Hitachi America, Ltd., NY, USA) was used to analyze the microstructure characterizations of the parts. Phase composition analysis was conducted on an energy-dispersive X-ray spectroscopy (EDXS) system (Phenom, nanoScience Instruments, Phoenix, AZ, USA). Prior to SEM observations and EDXS analysis, the parts were ground on a MetaServ 250 single grinder-polisher machine (49-10, 055, Buehler, Laker Bluff, IL, USA). The average grain size was measured based on the ASTM E112-13 linear intercept method [15]. The three-dimensional surface topography analysis, flatness, and surface roughness were conducted on a microscope (DSX510, Olympus Corporation, Shinjuku, Tokyo, Japan), on which the flatness values were obtained using global backside ideal focal plane range (GBIR) measurement. To avoid experimental error, tests were conducted at five randomly selected positions of each part. The microhardness was tested using a Vickers hardness tester (900-390, Phase II, Upper Saddle River, NJ, USA) under 1.96 N load and 10-second dwell time. 10 indents were taken at different locations of each part where the distance between adjacent locations was at least 0.5 mm. The cutting force in feeding direction was measured and collected by the DAQ system, as shown in Figure 5.4. At beginning, the dynamometer measured the cutting force in feeding direction and generated electrical signals. The electrical signals were amplified by the charge amplifier (Type 5070, Kistler Inc., Winterthur, Switzerland) and then were converted into digital signals using an A/D converter (Type 5697A, Kistler Inc., Winterthur, Switzerland).

Afterwards, these digital signals were read and processed by the DynoWare software (Type 2825D-02, Kistler Inc., Winterthur, Switzerland), presenting the results via a computer screen.

### 5.3 Experiment result and discussion

#### 5.3.1 Effects on microstructure

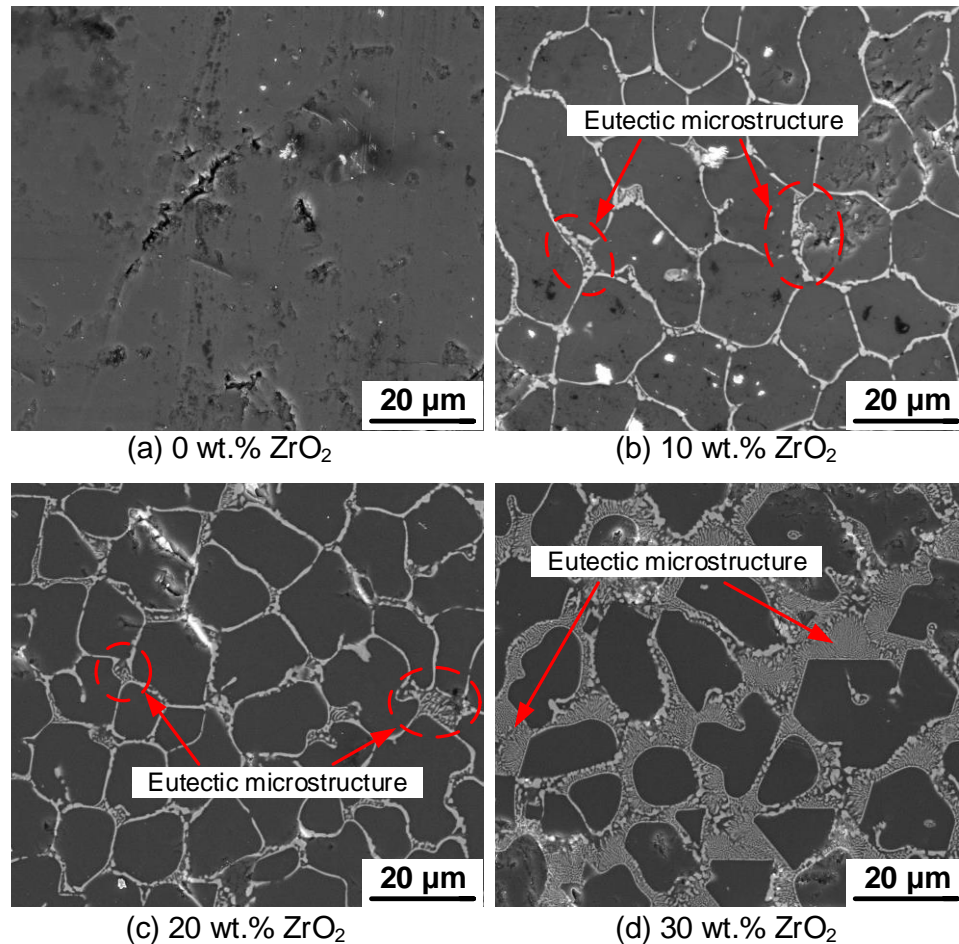


Figure 5.5 Microstructure analysis on cross-sections of LENS-fabricated parts

Figures 5.5(a), 5.5(b), 5.5(c), and 5.5(d) show the SEM images on cross-sections of LENS-fabricated parts with 0 wt.%, 10 wt.%, 20 wt.%, and 30 wt.% ZrO<sub>2</sub> content, respectively. It can be seen from Figure 5.5(b) – 5.5(d) that the ZrO<sub>2</sub> was rich at the boundaries whereas the Al<sub>2</sub>O<sub>3</sub> was rich at the matrix. This was evidenced by EDXS analysis on a ZTA part with 10 wt.% ZrO<sub>2</sub> content, as shown in Figure 5.6. The

phenomenon that  $ZrO_2$  aggregating at boundaries of  $Al_2O_3$  matrix was mainly due to the fact that  $ZrO_2$  and  $Al_2O_3$  were structurally incompatible with each other [16]. During melting and solidification process, the  $ZrO_2$  was expelled to grain boundaries of  $Al_2O_3$  matrix, where  $ZrO_2$  grew and connected with the formation of a network microstructure. When the  $ZrO_2$  content was 0 wt.%, the cross-section exhibited defects of pores and cracks but no network microstructure.

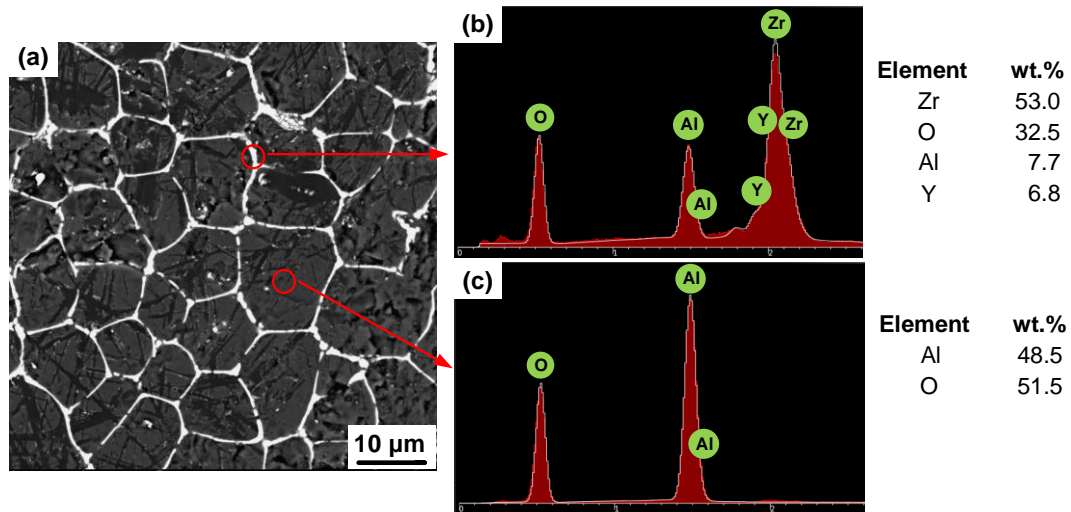


Figure 5.6 EDXS analysis on a ZTA part with 10 wt.%  $ZrO_2$  content: (a) a SEM image and phase composition results at (b) boundary area and (c) matrix area.

When the  $ZrO_2$  content was 10 wt.%, the network microstructure was shown on the cross-section and the average size of network unit (grain size of  $Al_2O_3$ ) was 13.5  $\mu m$ . At several intersections of  $Al_2O_3$  grain boundaries, eutectic solidification between  $ZrO_2$  and  $Al_2O_3$  occurred with generation of eutectic microstructure. As reported, such eutectic microstructure was formed when the weight ratio between  $ZrO_2$  and  $Al_2O_3$  was 41.5% : 58.5% [17]. Even though the global weight ratio of 10% : 90% was adopted when mixing  $ZrO_2$  and  $Al_2O_3$  powders, some local weight ratios in the molten pool could be as high as 41.5% : 58.5%, resulting in the formation of eutectic microstructure. When the  $ZrO_2$  content increased from 10 wt.% to 20 wt.%, the number of eutectic microstructure areas increased and the total eutectic microstructure area size was enlarged. When the  $ZrO_2$  content was 20 wt.%, the

average size of network unit was 11.5  $\mu\text{m}$ , which was smaller than that with 10 wt.%  $\text{ZrO}_2$ . When the  $\text{ZrO}_2$  content was increased up to 30 wt.%, almost half of the cross-section area was dominated with the eutectic microstructure and the average size of network unit was decreased to 10.8  $\mu\text{m}$ .

### 5.3.2 Effects on surface quality

Figure 5.7 shows the parts fabricated by LENS process with different levels of  $\text{ZrO}_2$  content. It can be seen that all the parts demonstrated poor surface quality, including large flatness and large surface roughness. With the  $\text{ZrO}_2$  content increasing, the heights of parts decreased. This was mainly due to the fact that high  $\text{ZrO}_2$  content would generate high fluidity, making the liquid materials in the molten pool being expanded in the horizontal directions and being shortened in the vertical direction (height). Surface topography analysis was conducted on LENS-fabricated part, RUM-processed part without ultrasonic vibration, and RUM-processed part with ultrasonic vibration, as shown in Figure 5.8. Different colors represent different heights. It can be



Figure 5.7 LENS-fabricated ZTA parts (prior to RUM process).

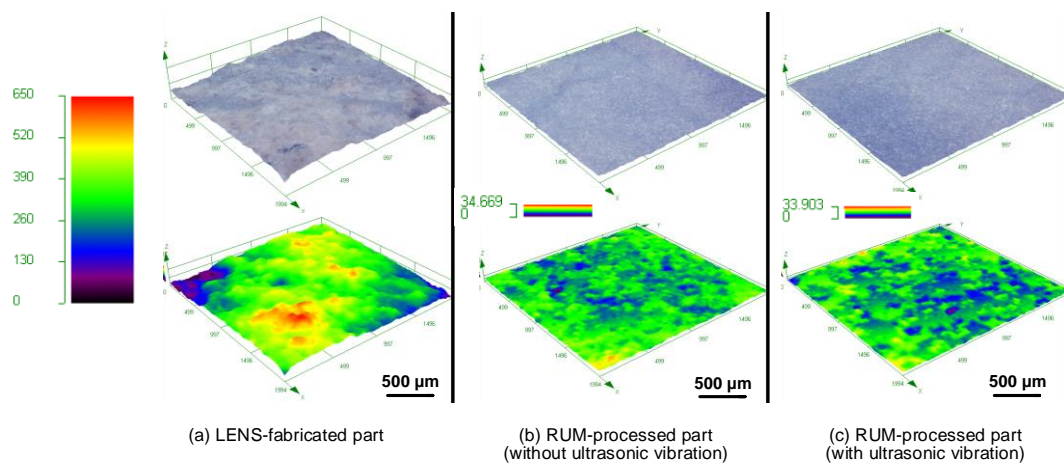


Figure 5.8 Surface topography analysis.

seen that before RUM process, the LENS-fabricated part exhibited rough surface with high peaks and deep valleys. For the RUM-processed parts both without and with ultrasonic vibration, the surfaces were much smooth, indicating that the surface-grinded parts demonstrated better surface quality than LENS-fabricated parts.

### 5.3.2.1 Effects on flatness

Figure 5.9 shows the effects of  $ZrO_2$  content on flatness. The average value from five measurements, under each specific condition, was used to represent the experimental values and was used for comparisons. The standard deviation of five measurements was used to represent both positive and negative values of error bars.

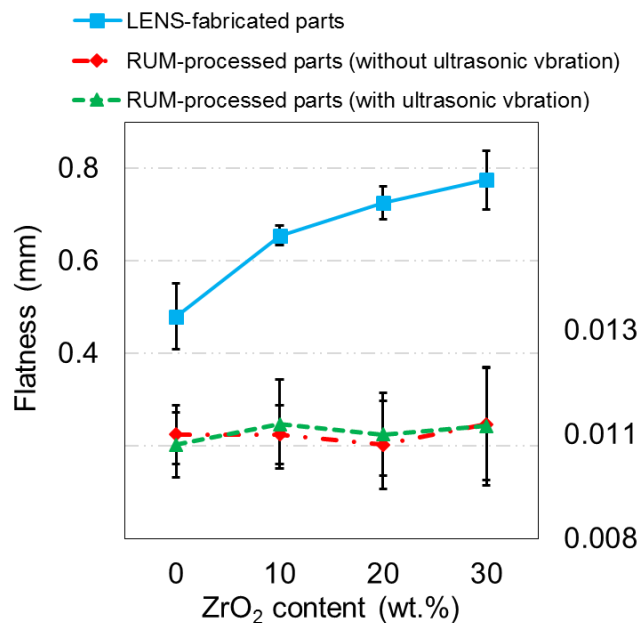


Figure 5.9 Effects of  $ZrO_2$  content and ultrasonic vibration on flatness.

It can be seen that an overall increment of the average flatness was observed when the  $ZrO_2$  content increased from 0 wt.% to 30 wt.% for the LENS-fabricated parts. The reason for this phenomenon was that high fluidity induced by  $ZrO_2$  content would impair the formability of the fabricated parts, resulting in uneven surfaces. Measurements were also conducted on the RUM-processed parts both without and with ultrasonic vibration, showing that the flatness was significantly reduced to the

range of 0.008 ~ 0.013 mm. There was no big difference of flatness between the parts grinded without and with ultrasonic vibration.

### 5.3.2.2 Effects on surface roughness

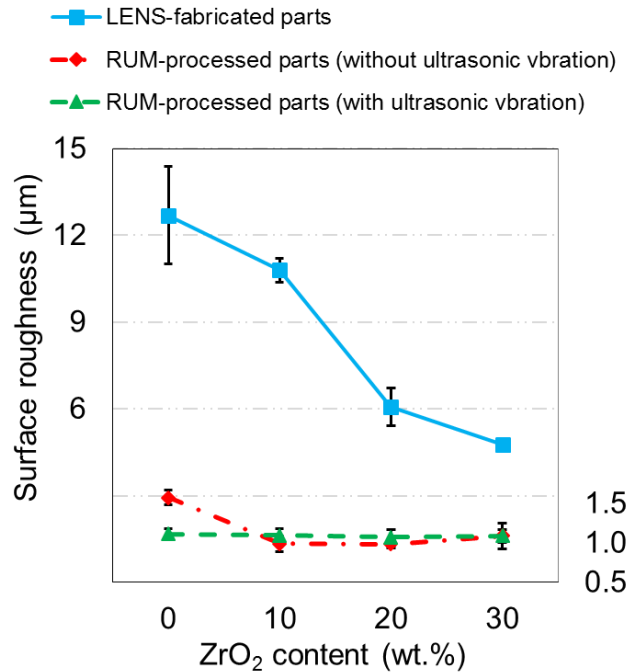


Figure 5.10 Effects of ZrO<sub>2</sub> content and ultrasonic vibration on surface roughness.

Figure 5.10 shows the effects of ZrO<sub>2</sub> content and ultrasonic vibration on surface roughness. For the LENS-fabricated parts, an overall decrease in surface roughness was found when the ZrO<sub>2</sub> content increased from 0 wt.% to 30 wt.%, indicating that the addition of ZrO<sub>2</sub> to the Al<sub>2</sub>O<sub>3</sub> was beneficial for reducing surface roughness value. The surface roughness variance of the ZTA parts was much smaller than that of pure Al<sub>2</sub>O<sub>3</sub> part, proving that the introduction of ZrO<sub>2</sub> could make the LENS fabricated parts maintain consistency. For the RUM-processed parts (both without and with ultrasonic vibration), the surface roughness of parts slightly changed with the increase of ZrO<sub>2</sub> content. Compared with the LENS-fabricated parts, the RUM-processed parts (both without and with ultrasonic vibration) exhibited much smaller surface roughness. Therefore, it can be concluded that the surface grinding

process implemented by RUM machine could hugely improve surface roughness property of LENS fabricated parts.

### 5.3.2.3 Effects on cutting force in feeding direction

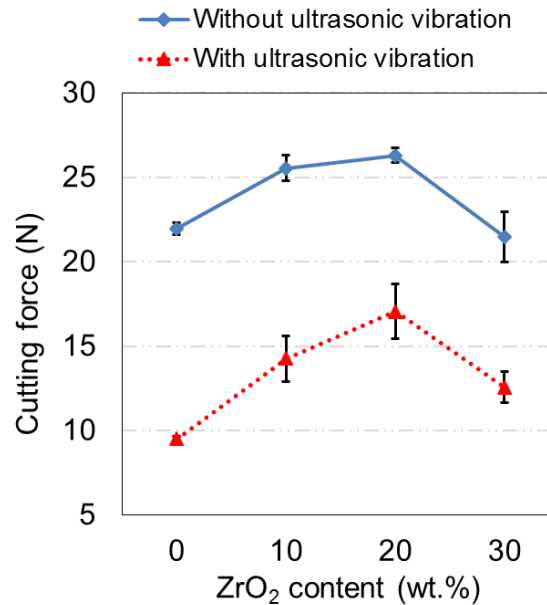


Figure 5.11 Effects of ZrO<sub>2</sub> content and ultrasonic vibration on cutting force in feeding direction.

Figure 5.11 shows the effects of ZrO<sub>2</sub> content and ultrasonic vibration on cutting force in feeding direction. The cutting force in feeding direction firstly increased then decreased with the ZrO<sub>2</sub> content increasing from 0 wt.% to 30 wt.% both without and with ultrasonic vibration. As reported, the cutting force was positively related to the hardness [18]. In another word, the higher the hardness of the ZTA parts was, the larger the cutting force for machining ZTA parts would be. In this investigation, the hardness of the ZTA parts was affected by two competing factors, including grain refinement and ZrO<sub>2</sub> content. At low level of ZrO<sub>2</sub> content, the addition of ZrO<sub>2</sub> would hinder the grain growth of Al<sub>2</sub>O<sub>3</sub>, resulting in the grain refinement of ZTA parts [3, 19]. Experimental results proved that the grain size of Al<sub>2</sub>O<sub>3</sub> decreased with the ZrO<sub>2</sub> content increasing from 0 wt.% to 20 wt.%. Based on

the classic Hall-Petch relationship, the microhardness value ( $H$ ) could be expressed as [20, 21]:

$$H = H_0 + \frac{k_{HP}}{\sqrt{d}} \quad (5.1)$$

where,  $H_0$  is the intrinsic hardness;  $k_{HP}$  is the Hall-Petch coefficient;  $d$  is the average grain size. According to Equation (5.1), the grain refinement led to the increase of microhardness. Therefore, the increase of  $ZrO_2$  content from 0 wt.% to 20 wt.% resulted in the increase of microhardness (in Figure 5.12) and increase of cutting force (in Figure 5.11). At high level (30 wt.%) of  $ZrO_2$  content, the microhardness was decreased due to the fact that the  $ZrO_2$  was softer than  $Al_2O_3$ , leading to the decrease of cutting force [22].

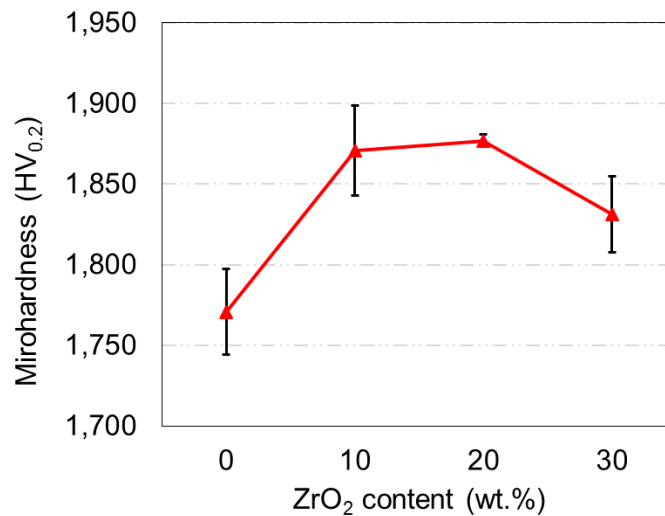


Figure 5.12 Effects of  $ZrO_2$  content on microhardness of LENS-fabricated parts.

Compared with cutting force obtained without ultrasonic vibration, the cutting force obtained with ultrasonic vibration was significantly smaller at the same level of  $ZrO_2$  content. To have a better understanding of effects of ultrasonic vibration on cutting force, several key equations were provided [23-25]:

$$F = N \cdot F^1 \quad (5.2)$$

where,  $F$  is the cutting force in feeding direction;  $N$  is the number of active abrasive grains on the side face of the cutting tool;  $F^1$  is the average cutting force of a single grain in feeding direction.

$$F^1 = \frac{2\sqrt{2}}{3} \cdot \frac{E\sqrt{D}}{(1-\nu^2)} \cdot \delta^{3/2} \quad (5.3)$$

where,  $E$  is the elastic modulus of the workpiece;  $D$  is the size of the abrasive grain;  $\nu$  is the Poisson's ratio of the workpiece;  $\delta$  is the indentation depth of abrasive grains in feeding direction.

As reported, the ultrasonic vibration amplitude ( $A$ ) induced by introducing ultrasonic vibration could lead to the decrease of indentation depth of the abrasive grain in feeding direction ( $\delta$ ) [11, 12]. Based on Equation (5.3), the decrease of  $\delta$  would result in the decrease of  $F^1$ . In the meantime, the  $N$  would not change by introducing ultrasonic vibration [24]. Therefore, according to Equation (5.2), the cutting force in feeding direction would decrease by introducing ultrasonic vibration to RUM process. In addition, it was reported that the introduction of ultrasonic vibration could also contribute to effective cooling process and good machining and lubricating interface between the cutting tool and the workpiece, thus rendering smaller cutting force in feeding direction [26, 27].

#### 5.4 Conclusions

In this investigation, an efficient and effective RUM process was utilized for surface grinding of brittle ZTA and  $\text{Al}_2\text{O}_3$  parts. The effects of  $\text{ZrO}_2$  content and ultrasonic vibration on flatness, surface roughness, microhardness, and cutting force in feeding direction were analyzed. The main conclusions of this investigation were drawn as follows:

(1) The  $\text{ZrO}_2$  aggregated at the boundaries of  $\text{Al}_2\text{O}_3$  matrix, forming a network microstructure. With the  $\text{ZrO}_2$  content increasing from 0 wt.% to 30 wt.%, the grain size was decreased. When the  $\text{ZrO}_2$  content was 30 wt.%, the eutectic microstructure occupied almost half of the cross-section area.

(2) The LENS-fabricated parts with different levels of  $ZrO_2$  content exhibited poor surface quality, including large flatness value and large surface roughness value. After surface grinding, which is implemented by the RUM machine, the flatness and surface roughness values of these parts were significantly reduced.

(3) In RUM process, the cutting force in feeding direction was firstly increased then decreased. This phenomenon was mainly ascribed to the combined action of grain refinement and  $ZrO_2$  content. The cutting force in feeding direction obtained with ultrasonic vibration, at the same level of  $ZrO_2$  content, was much smaller than that without ultrasonic vibration, proving that the introduction of ultrasonic vibration was beneficial for reducing cutting force.

### **Acknowledgement**

The work was supported by the National Science Foundation through award CMMI-1538381.

## References

- [1] Li, Y. Z., Hu, Y. B., Cong, W. L., Zhi, L., & Guo, Z. N. (2017). Additive manufacturing of alumina using laser engineered net shaping: effects of deposition variables. *Ceramics International*, 43(10), 7768-7775.
- [2] Wang, J., & Stevens, R. (1989). Zirconia-toughened alumina (ZTA) ceramics. *Journal of Materials Science*, 24(10), 3421-3440.
- [3] Hu, Y. B., Ning, F. D., Cong, W. L., Li, Y. Z., Wang, X. L., & Wang, H. (2018). Ultrasonic vibration-assisted laser engineering net shaping of  $ZrO_2-Al_2O_3$  bulk parts: effects on crack suppression, microstructure, and mechanical properties. *Ceramics International*, 44(3), 2752-2760.
- [4] Deville, S., Chevalier, J., Fantozzi, G., Bartolomé, J. F., Requena, J., Moya, J. S., Torrecillas, R., & Díaz, L. A. (2003). Low-temperature ageing of zirconia-toughened alumina ceramics and its implication in biomedical implants. *Journal of the European Ceramic Society*, 23(15), 2975-2982.
- [5] Huang, S. H., Liu, P., Mokasdar, A., & Hou, L. (2013). Additive manufacturing and its societal impact: a literature review. *The International Journal of Advanced Manufacturing Technology*, 67(5-8), 1191-1203.
- [6] Hu, Y. B., Cong, W. L., Wang, X. L., Li, Y. C., Ning, F. D., & Wang, H. (2018). Laser deposition-additive manufacturing of TiB-Ti composites with novel three-dimensional quasi-continuous network microstructure: effects on strengthening and toughening. *Composites Part B: Engineering*, 133, 91-100.
- [7] Atwood, C., Ensz, M., Greene, D., Griffith, M., Harwell, L., Reckaway, D., Romero, T., Schlienger, E., & Smugeresky, J. (1998). Laser engineered net shaping (LENS (TM)): a tool for direct fabrication of metal parts (No. SAND98-2473C). Sandia National Laboratories, Albuquerque, NM, and Livermore, CA.
- [8] Hu, Y. B., Ning, F. D., Wang, X. L., Wang, H., Zhao, B., Cong, W. L., & Li, Y. Z. (2017). Laser deposition-additive manufacturing of in situ TiB reinforced titanium matrix composites: TiB growth and part performance. *The International Journal of Advanced Manufacturing Technology*, 93(9-12), 3409-3418.
- [9] Mingareev, I., Bonhoff, T., El-Sherif, A. F., Meiners, W., Kelbassa, I., Biermann, T., & Richardson, M. (2013). Femtosecond laser post-processing of metal parts produced by laser additive manufacturing. *Journal of Laser Applications*, 25(5), 052009.
- [10] Hu, Y. B., Wang, H., Ning, F. D., & Cong, W. L. (2016). Laser engineered net shaping of commercially pure titanium: effects of fabricating variables. *Proceedings of the ASME 2016 International Manufacturing Science and Engineering Conference (MSEC2016-8812)*, June 27-July 01, 2016, Blacksburg, VA, USA. DOI: 10.1115/MSEC2016-8812.
- [11] Ning, F. D., Cong, W., Wang, H., Hu, Y., Hu, Z., & Pei, Z. (2017). Surface grinding of CFRP composites with rotary ultrasonic machining: a mechanistic model on cutting force in the feed direction. *The International Journal of Advanced Manufacturing Technology*, 92(1-4), 1217-1229.

- [12] Wang, H., Ning, F. D., Hu, Y. B., Fernando, P. K. S. C., Pei, Z. J., & Cong, W. L. (2016). Surface grinding of carbon fiber-reinforced plastic composites using rotary ultrasonic machining: Effects of tool variables. *Advances in Mechanical Engineering*, 8(9), 1687814016670284.
- [13] Hu, Y. B., Wang, H., Ning, F. D., Cong, W. L., & Ericson, H. (2017). Surface grinding of optical BK7/K9 glass using rotary ultrasonic machining: an experimental study. *Proceedings of the ASME 2017 International Manufacturing Science and Engineering Conference (MSEC2017-3110)*, June 4-8, 2017, Los Angeles, CA, USA. DOI: 10.1115/MSEC2017-2780.
- [14] Wang, H., Ning, F. D., Hu, Y. B., & Cong, W. L. (2017). Surface grinding of CFRP composites using rotary ultrasonic machining: a comparison of workpiece machining orientations. *The International Journal of Advanced Manufacturing Technology*, DOI: 10.1007/s00170-017-1401-z.
- [15] ASTM E112-13. (2013). *Standard test methods for determining average grain size*, ASTM international, West Conshohocken, PA.
- [16] Feighery, A. J., & Irvine, J. T. S. (1999). Effect of alumina additions upon electrical properties of 8 mol.% yttria-stabilised zirconia. *Solid State Ionics*, 121(1), 209-216.
- [17] Niu, F. Y., Wu, D. J., Ma, G. Y., Wang, J. T., Guo, M. H., & Zhang, B. (2015). Nanosized microstructure of  $\text{Al}_2\text{O}_3\text{-ZrO}_2$  ( $\text{Y}_2\text{O}_3$ ) eutectics fabricated by laser engineered net shaping. *Scripta Materialia*, 95, 39-41.
- [18] Kumar, A. S., Durai, A. R., & Sornakumar, T. (2003). Machinability of hardened steel using alumina based ceramic cutting tools. *International Journal of Refractory Metals and Hard Materials*, 21(3), 109-117.
- [19] Casellas, D., Nagl, M. M., Llanes, L., & Anglada, M. (2003). Fracture toughness of alumina and ZTA ceramics: microstructural coarsening effects. *Journal of Materials Processing Technology*, 143, 148-152.
- [20] Hall, E. O. (1951). The deformation and ageing of mild steel: III discussion of results. *Proceedings of the Physical Society. Section B*, 64(9), 747.
- [21] Petch, N. J. (1953). The cleavage strength of polycrystals. *Journal of Iron and Steel Research, International*, 174, 25-28.
- [22] Heros, R. J. (1998). Ceramic in total hip arthroplasty: history, mechanical properties, clinical results, and current manufacturing state of the art. In *Seminars in Arthroplasty*, 9, 114-122.
- [23] Pei, Z. J., Prabhakar, D., Ferreira, P. M., & Haselkorn, M. (1995). A mechanistic approach to the prediction of material removal rates in rotary ultrasonic machining. *Journal of Engineering for Industry*, 117(2), 142-151.
- [24] Cong, W. L., Pei, Z. J., Sun, X., & Zhang, C. L. (2014). Rotary ultrasonic machining of CFRP: a mechanistic predictive model for cutting force. *Ultrasonics*, 54(2), 663-675.
- [25] Wang, H., Ning, F. D., Hu, Y. B., Du, D. P., & Cong, W. L. (2017). Surface grinding of CFRP composites using rotary ultrasonic machining: design of experiment on cutting force, torque, and surface roughness. *International Journal of Manufacturing Research*, 12(4), 461-479.

- [26] Ning, F. D, Wang, H., Hu, Y. B., Cong, W. L., Zhang, M., & Li, Y. Z. (2017). Rotary ultrasonic surface machining of CFRP composites: a comparison with conventional surface grinding. *Procedia Manufacturing*, 10, 557-567.
- [27] Nik, M. G., Movahhedy, M. R., & Akbari, J. (2012). Ultrasonic-assisted grinding of Ti6Al4V alloy. *Procedia CIRP*, 1, 353-358.

## CHAPTER VI

### LENS OF TiB-TMCS – MICROSTRUCTURE AND WEAR PERFORMANCE

Paper title:

Laser engineered net shaping of quasi-continuous network microstructural TiB reinforced titanium matrix bulk composites: microstructure and wear performance

Published in:

Optics and Laser Technology, 2018, Vol. 99, pp. 174-183

Author's names:

Yingbin Hu<sup>a</sup>, Fuda Ning<sup>a</sup>, Hui Wang<sup>a</sup>, Weilong Cong<sup>a,\*</sup>, and Bo Zhao<sup>b</sup>

Authors' affiliations:

<sup>a</sup>Department of Industrial, Manufacturing, & Systems Engineering, Texas Tech University, Lubbock, Texas, 79409, USA

<sup>b</sup>College of Arts & Science Microscopy, Texas Tech University, Lubbock, Texas, 79409, USA

\*Corresponding author:

Department of Industrial, Manufacturing, & Systems Engineering, Texas Tech University, Lubbock, TX 79409-3061, USA. Email address: weilong.cong@ttu.edu

## **Abstract**

Titanium (Ti) and its alloys have been successfully applied to the aeronautical and biomedical industries. However, their poor tribological properties restrict their fields of applications under severe wear conditions. Facing to these challenges, this study investigated TiB reinforced Ti matrix composites (TiB-TMCs), fabricated by in-situ laser engineered net shaping (LENS) process, through analyzing parts quality, microstructure formation mechanisms, microstructure characterizations, and workpiece wear performance. At high B content areas (original B particle locations), reaction between Ti and B particles took place, generating flower-like microstructure. At low B content areas, eutectic TiB nanofibers contacted with each other with the formation of crosslinking microstructure. The crosslinking microstructural TiB aggregated and connected at the boundaries of Ti grains, forming a three-dimensional quasi-continuous network microstructure. The results show that compared with commercially pure Ti bulk parts, the TiB-TMCs exhibited superior wear performance (i.e. indentation wear resistance and friction wear resistance) due to the present of TiB reinforcement and the innovative microstructures formed inside TiB-TMCs. In addition, the qualities of the fabricated parts were improved with fewer interior defects by optimizing laser power, thus rendering better wear performance.

## **Keywords**

Laser processing; Titanium matrix composites; Microstructural characterization; Grain refinement; Wear property.

## **6.1 Introduction**

Owing to their high strength-to-weight ratio and outstanding biocompatibility, titanium (Ti) and its alloys have attracted a great deal of attentions in aeronautical and biomedical industries [1,2]. However, Ti and its alloys exhibit poor wear performance which limits their applications in fabrication of parts (e.g. gears and bearings [3,4], jet engine compressors [5], etc.) those will work under severe wear conditions. In addition, Ti alloys, such as Ti-6Al-4V, releases aluminum and vanadium ions for long time usage, causing health-related problems [6,7].

To improve Ti and its alloys' wear performance (including indentation and friction wear resistances), adding ceramic reinforcements (e.g. Al<sub>2</sub>O<sub>3</sub> [8], SiC [9], TiN [10], TiC [11], TiB [12], etc.) to form titanium matrix composites (TMCs) gains its popularity [8-12]. Compared with other ceramic reinforced TMCs, TiB reinforced TMCs (TiB-TMCs) exhibit more specific benefits and have been extensively investigated in recent years [2,3,9,13-17]. The major reasons include: (1) The residual stresses at interfaces of TiB and Ti can be reduced or even eliminated owing to their similar densities and thermal expansion coefficients [14,18]; (2) A relatively small amount of TiB reinforcement can largely increase the composites' modulus and wear performance on account of the long-whisker shape of TiB [18]; and (3) Surface modified pure Ti with TiB shows good cell growth by performing *in-vitro* biocompatibility test under static condition [13].

TiB-TMCs can be fabricated by both ex-situ and in-situ processes. Compared with ex-situ ceramic reinforced TMCs, the in-situ ceramic reinforced TMCs demonstrate following advantages: (1) The in-situ process provides a way of uniformly embedding the rigid ceramic reinforcement in the metal or alloy matrix; (2) The ceramic reinforcement and the Ti matrix are thermodynamically stable with the in-situ process, thus rendering less degradation of TMCs at elevated temperature [12,19]; (3) The size of the in-situ formed ceramic reinforcement is much finer; and (4) The heat generated during the in-situ reaction can be utilized. Based on the aforementioned advantages, excellent physical and mechanical properties can be expected with the in-situ process [10,20].

Traditional ceramics reinforced TMCs manufacturing processes include casting [15] and powder metallurgy [16]. These traditional manufacturing processes have problems of high energy consumption and high cost for additional machining [17,21,22]. In addition, difficulties arise when producing complex-shaped parts by traditional manufacturing processes [23,24]. To overcome the shortcomings associated with traditional manufacturing processes, additive manufacturing (AM) technology has been developed and widely used to produce metallic components, including TMCs

[25]. Laser additive manufacturing (LAM) technology, mainly including selective laser sintering/melting (SLS/M) and laser engineered net shaping (LENS), is regarded as one of the most attractive AM technologies for fabrication of metal based materials [26-28]. Based on a layer by layer powder spreading mechanism, SLS can partially melt the powder via sintering [26]. To meet the demand of producing near-full-dense parts with better mechanical properties, SLM has been developed to fully melt the powder [3,29]. Compared with powder-bed based SLS/SLM processes, the beam-deposition based LENS process exhibits more advantages, such as lower labor intensity, higher fabrication efficiency [30,31], and parts remanufacturing capability [32-36]. To improve materials' surface properties, laser coating (aka, laser cladding) is widely used by LENS process [1,9,10,13,17,27,37]. Laser coating's drawbacks of poor coating-substrate adherence [38] and lacking in uniformity [39] restrict its fields of applications.

Facing to these problems, this paper has fabricated bulk TiB-TMCs, on which limited investigations have been conducted, with uniform distribution of TiB reinforcement inside TMCs by in-situ LENS process. The effects of reinforcement (TiB) and energy input (laser power) on the qualities, microstructure characterizations, and wear performance of the fabricated bulk parts are also analyzed.

This paper is organized as follows: Following with this introduction, Section 6.2 describes the experiments set-up and measurements procedures. Then, in Section 6.3, phase identification and microstructure analysis are discussed to provide insight into effects of TiB reinforcement and laser power on wear performance of the fabricated bulk parts. Conclusions are drawn in Section 6.4.

## **6.2 Experiments and measurements procedures**

### **6.2.1 Powder materials and powder treatment**

In this paper, commercially pure Ti (CP-Ti) powders (Atlantic Equipment Engineers Inc., Upper Saddle River, NJ, USA) with the purity of 99.7% and the average particle size of 150  $\mu\text{m}$  were used. The purity of B powders (Chemsavers,

Inc., Bluefield, WV, USA) was higher than 96% and the average particle size was 2  $\mu\text{m}$ .

According to the binary Ti-B phase diagram, when the B content was 1.6 wt.%, eutectic solidification process would occur with the generation of ultrafine eutectic TiB, which was beneficial to fracture toughness and bending strength [3,40,41]. Therefore, the weight ratio of 98.4 : 1.6 between Ti and B powders was adopted in this paper. The powders were premixed by planetary ball mill machine (ND2L, Torrey Hills Technologies LLC., San Diego, CA, USA) prior to LENS process. To well distribute B powders into Ti powders without significant size reduction and reaction between Ti and B, ball milling parameters were optimized, including the ball-to-powder weight ratio of 5:1, the fixed rotation speed of 200 rpm, and the milling time of four hours.

## **6.2.2 Experimental set-up and experimental conditions**

### ***6.2.2.1 Experimental set-up***

The fabrication experiments were performed on a LENS machine (450, Optomec Inc., Albuquerque, NM, USA) which consisted of a laser system (with 400 W IPG fiber laser), a chamber system, a powder and inert gas delivery system (with coaxial four-nozzle), and a control system (with integrated computer), as illustrated in Figure 6.1.

To prevent Ti from being oxidized at high temperature, the sealed chamber was purged with the inert argon gas to keep a low oxygen level ( $< 200$  ppm) before the fabrication process. Then, the powder and inert gas stream (generated by the powder and inert gas delivery system) as well as the laser beam (generated by the laser system) were simultaneously ejected to the targeted substrate workpiece through deposition head. The laser beam melted the certain area of substrate, forming a molten pool. Powders were caught and melted by the molten pool, resulting in an increased molten pool volume. Then, the deposited powders solidified due to heat dissipation once the laser beam left. Based on the designed structures, the laser beam and the

powder stream would follow the trajectory generated by the control system to deposit the first layer. Afterwards, the deposition head ascended one layer thickness to a new set position for the next layer deposition. Treated as the new “substrate”, the first layer would be selectively melted to catch powders for forming the second layer. Similar process was repeated many times until the designed 3D structure was finally built layer by layer.

### 6.2.2.2 Experimental conditions

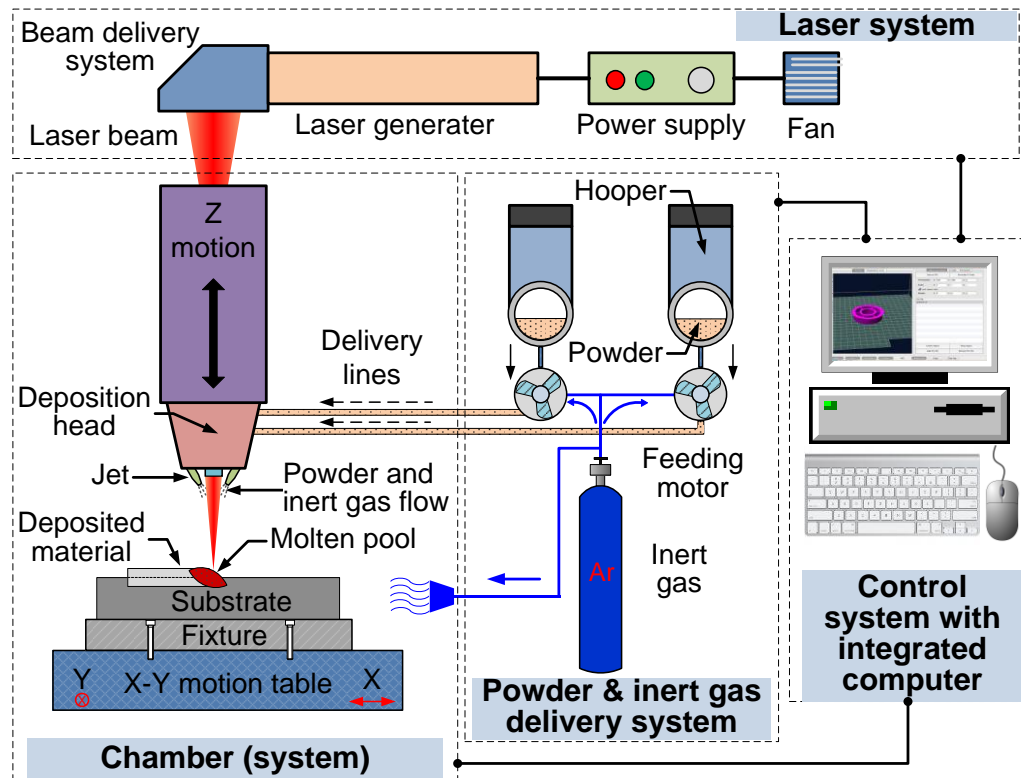


Figure 6.1 LENS experimental set-up.

In this investigation, four parts were fabricated on the Ti substrate under each combination of input variables. The dimensions of the parts were  $8\text{ mm} \times 8\text{ mm} \times 20$  layers. Based on preliminary results, the LENS parameters were fixed at optimal values, including the deposition head scanning speed of  $11\text{ mm/s}$ , the hatch distance of  $381\text{ }\mu\text{m}$ , the layer thickness of  $420\text{ }\mu\text{m}$ , and the powder feeding rate of  $1.65\text{ g/min}$ . A zigzag scanning pattern with  $90^\circ$  orientation changing for each layer was adopted to

reduce the effect of scanning orientation.

### **6.2.3 Phase analysis and microstructure characterization**

To observe and analyze the microstructure of the fabricated parts, the cutted parts were ground and polished using a MetaServ 250 single grinder-polisher machine (49-10055, Buehler, Lake Bluff, IL, USA), and then etched by Kroll's Reagent (HF: 3%; HNO<sub>3</sub>: 6%; water: balance) (Etchant Store, Suite N Glendora, CA, USA) for ten seconds. To have a better observation of the TiB structure, 20% HCl was used to etch some of the polished surfaces for ten hours. The Scanning Electron Microscope (SEM) (Crossbeam 540, Carl Zeiss AG, Oberkochen, Germany), equipped with Energy-Dispersive X-ray spectroscopy (EDX) system and Electron BackScatter Diffraction (EBSD) system, was used to observe the microstructures of the polished and etched cross-sections of the parts, as well as the morphologies and shapes of the powders. Phase composition analysis (EDX spectrums for phases and phase fractions) was conducted with Oxford EDX system. As required by EBSD pattern acquisition, the stage was tilted to the 70° orientation with 20 kV acceleration voltage to study the structures and phases of the materials in the SEM. The basic processes for indexing an EBSD pattern included detecting the diffraction bands, measuring the angles between these bands, and matching these bands to the database for the given material [42]. Such EBSD indexing processes were implemented using an integrated AZtec software.

### **6.2.4 Mechanical properties testing**

Wear performance (including indentation wear resistance and friction wear resistance) was tested on the polished surfaces (perpendicular to the deposition direction) of fabricated parts. The microhardness value, which was measured using a Vickers hardness tester (900-390, Phase II, Upper Saddle River, NJ, USA), could represent the material's indentation wear resistance. The microhardness tests were performed with 9.8 N load and ten-second dwell time. On each fabricated part, ten indents were taken at different locations where the distance between adjacent locations was 0.5 mm.

The friction wear resistance could be obtained by conducting dry sliding wear tests. The dry sliding wear tests were performed at room temperature, using a 1 mm radius ( $R$ ) bearing steel (HRC60) ball as the counter-face material, under the constant sliding speed ( $v$ ) of 3 mm/s, the normal load ( $F$ ) of 0.2 N, the sliding distance ( $L$ ) of 5 mm, and the duration time ( $T$ ) of one hour. The depth ( $d$ ) of the sliding track was measured by a surface profilometer (SJ-210, Mitutoyo Corporation, Kanagawa, Japan). The wear volume losses ( $V_l$ ) were derived as:

$$V_l = \left( R^2 \arcsin \frac{\sqrt{2Rd - d^2}}{R} - (R - d) \sqrt{2Rd - d^2} \right) \quad (6.1)$$

The wear rate ( $w_r$ ) was expressed as:

$$w_r = \frac{V_l}{F(vT)} \quad (6.2)$$

### 6.3 Experiment result and discussion

#### 6.3.1 Morphologies of the powders and the parts' surfaces

Figures 6.2(a) and 6.2(b) show the shapes and morphologies of the as-received CP-Ti and B powders before ball milling treatment. It can be seen that both CP-Ti and B powders exhibited irregular shapes. As shown in Figure 6.2(c), the mixed CP-Ti and B powders after four-hour ball milling were more spherical in shape and more uniform in size, thus making the powders have high compactability, flowability, and apparent density [43]. Niu et al. reported that the spherical powder shape could not only strengthen the bonding between adjacent laser scanning tracks, but also reduce porosities, resulting in better qualities of the manufactured parts [44]. Figure 6.2(d) shows the detailed surface morphology of the four-hour ball milling mixed powders at higher magnification. It can be seen that the B particles were well distributed and embedded onto the surfaces of the CP-Ti particles after ball milling treatment. The homogenous dispersion of B particles among CP-Ti particles could be proved by EDX patterns analysis, which would be discussed in Section 6.3.2. These four-hour ball milling mixed CP-Ti and B powders would act as the starting powder for the

following LENS process.

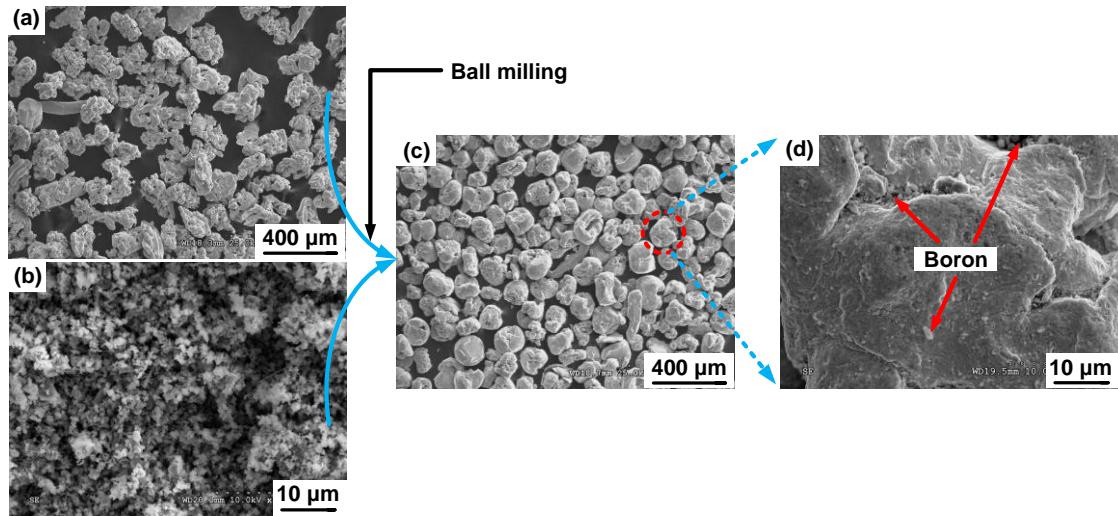


Figure 6.2 SEM imaging observed shapes and morphologies of the as-received (a) CP-Ti powder and (b) B powder as well as four-hour ball milling mixed CP-Ti and B powders (c) at lower and (d) at higher magnifications, respectively.

The top surface morphologies of the CP-Ti part and the TiB-TMC fabricated by LENS at laser power of 200 W are shown in Figures 6.3(a) and 6.3(b), respectively. No apparent cracks or pores were observed on top surfaces of both parts. With the same LENS processing parameters, the marked distances between adjacent laser

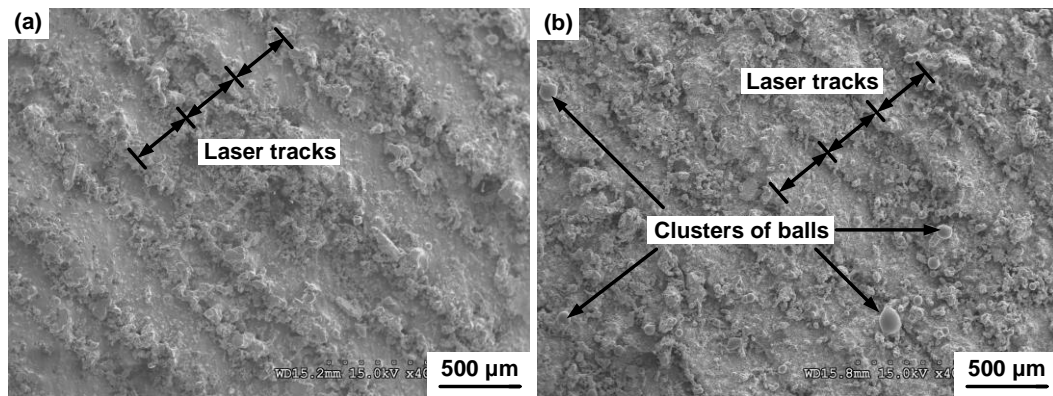


Figure 6.3 SEM imaging observed top surface morphologies of LENS-fabricated (a) CP-Ti part and (b) TiB-TMC.

scanning tracks of LENS-fabricated CP-Ti part were in good accordance with those of LENS-fabricated TiB-TMC. The average distance was  $380\ \mu\text{m}$  and agreed well with the designed hatch distance of  $381\ \mu\text{m}$ . Besides irregular-shaped particles, clusters of spherical balls (tens of microns in diameter) were shown on top surface of LENS fabricated-TiB-TMC, but were hardly seen on top surface of LENS-fabricated CP-Ti part. The major reason of this “balling” effect was that the present of brittle ceramic TiB led to poor wettability, resulting in the formation of balls [45,46].

### 6.3.2 Phase identification and microstructure analysis

Figure 6.4 shows the results of EDX mapping on the etched surface of TiB-TMC processed at 200 W laser power. As shown in Figure 6.4(a), the black dots circled by dashed lines were interior defects (e.g. micro-pores). Figures 6.4(b) and 6.4(c) show the spatial distributions of Ti element and B element, respectively. From a macroscopic point of view, the B element was homogeneously distributed within TiB-

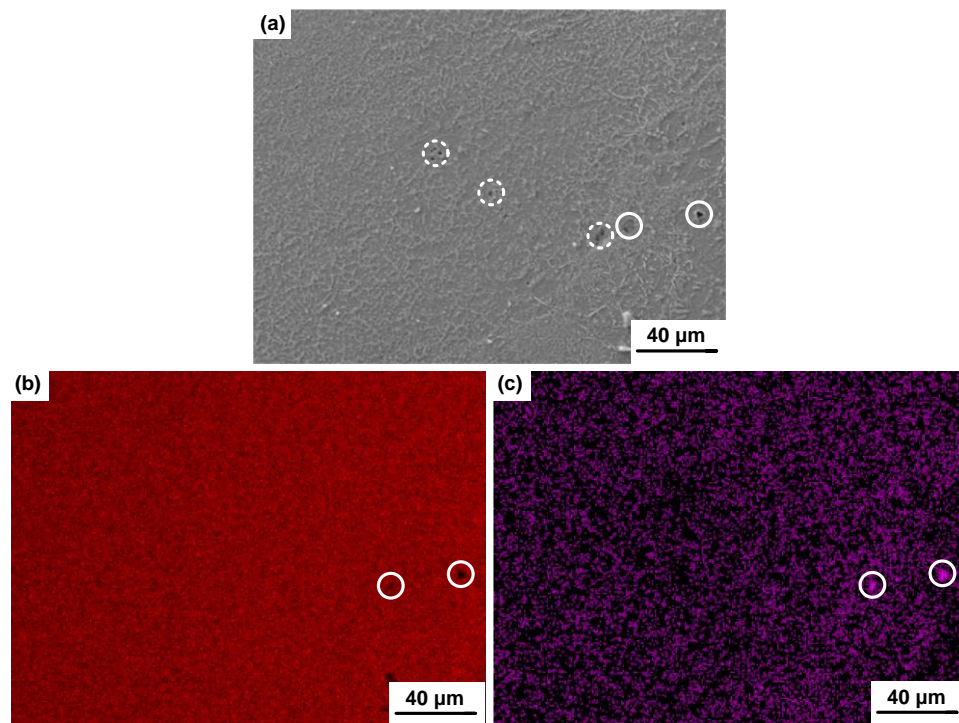


Figure 6.4 (a) SEM image of TiB-TMC after polishing and corresponding EDX maps on spatial distributions for (b) Ti element and (c) B element.

TMCs, indicating that the ball milling treatment could provide adequate mixture of CP-Ti and B powders. However, from a microscopic point of view, B element was rich in some regions but lean in the other regions, which was related to the three-dimensional quasi-continuous network (3DQCN) microstructure formed inside TiB-TMCs. The B element concentrated areas circled by solid lines in Figure 6.4(c) exhibited black color in Figures 6.4(a) and 6.4(b). It can be concluded that two incompletely reacted elemental B particles were located at these areas. Tamirisakandala et al. and Tang et al. reported that the solid solubility of B in Ti was very low ( $< 0.02\%$ ), therefore, the unreacted B particles would be embedded in the TMCs [47,48].

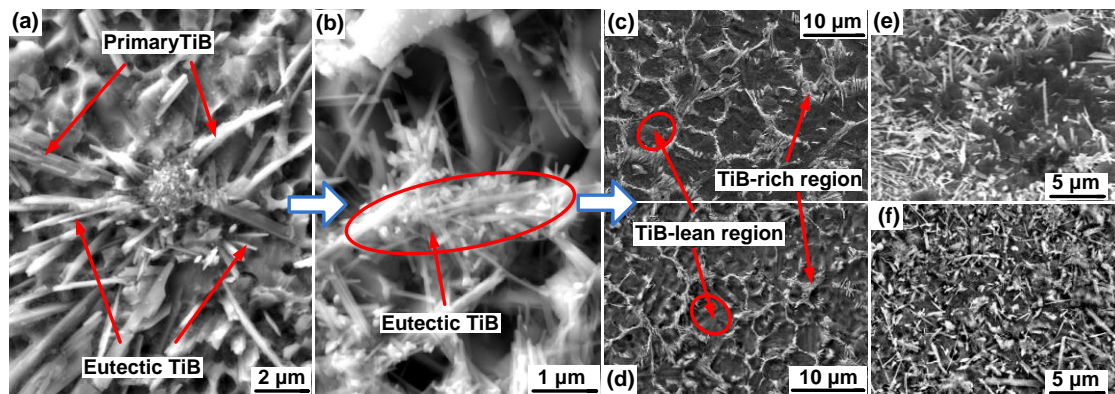


Figure 6.5 SEM imaging of microstructures of TiB-TMCs processed at 200 W: (a) Flower-like microstructure; (b) Crosslinking microstructure; (c) Quasi-continuous network microstructure (perpendicular to deposition direction); and (d) Quasi-continuous network microstructure (parallel to deposition direction). SEM imaging of microstructures of TiB-TMCs processed at 125 W: (e) Perpendicular to deposition direction; and (f) Parallel to deposition direction.

Figure 6.5(a) shows a flower-like microstructure with newly formed prismatic primary TiB and needle-like eutectic TiB particles emanating from the central “stamen” (which used to be a B particle) to the surrounding area. Such phenomenon was not reported in previous work. Before LENS process, B particles were embedded into the Ti particles by ball milling treatment. During LENS process, the in-situ exothermic reaction took place between Ti and B particles as a result of laser

radiation, forming TiB. The B content in premixed powder was set to 1.6 wt.%, however, it was higher than 1.6 wt.% (hypereutectic composition) at some local areas close to B particles. Therefore, after laser radiation, the liquid molten pool solidified following: Liquid  $\rightarrow$  Liquid + Primary TiB  $\rightarrow$  Primary TiB + Eutectic TiB +  $\beta$ Ti  $\rightarrow$  Primary TiB + Eutectic TiB +  $\alpha$ Ti [41,49]. Based on microstructure analysis, eutectic TiB took up a bigger portion in comparison with primary TiB. At high magnification, it can be seen from Figure 6.5(b) that the generated needle-like eutectic TiB nanofibers contacted and formed interlock or crosslinking microstructures, which were beneficial to strengthening effect [50]. The crosslinking microstructural TiB aggregated and connected with each other at the boundaries of newly crystallized Ti grains during solidification, forming a 3DQCN microstructure, as shown in Figures 6.5(c) and 6.5(d). The light boundaries were TiB-rich regions, while the dark interior regions were TiB-lean regions [12]. It was reported that the TiB-rich regions contributed to strengthening the TiB-TMCs, and TiB-lean regions positively affected the ductility of the TiB-TMCs [12,50,51]. In addition, the specific three-dimensional microstructure enabled isotropic reinforcement in all directions, which was beneficial to load uniformly transferring and even distribution. The 3DQCN microstructure was sensitive to laser power and was not formed at low laser power of 125 W, as shown in

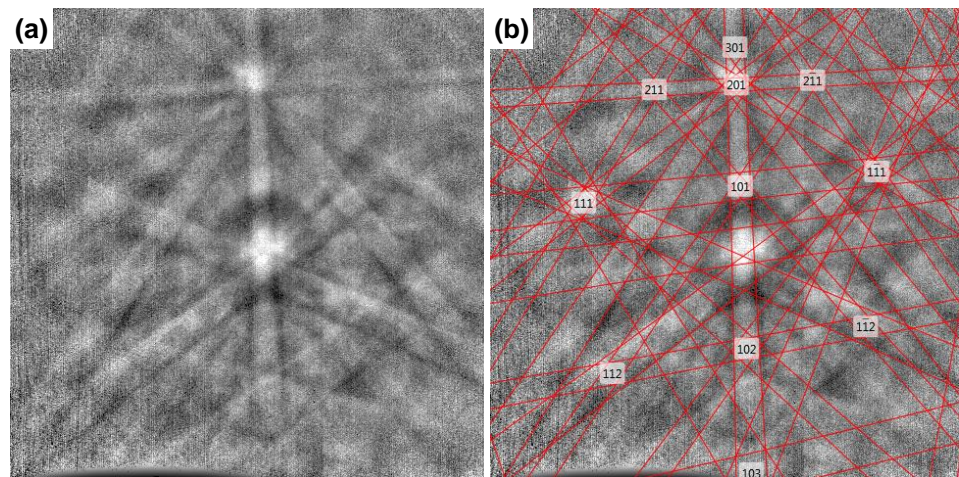


Figure 6.6. The initial (a) and indexed (b) Kikuchi EBSD patterns derived from TiB.

Figures 6.5(e) and 6.5(f). The major reason was that the low levels of laser power resulted in weak Marangoni convection, restricting the rearrangement of TiB reinforcement and leading to no 3DQCN microstructure generating [12, 52]. As a result, the TiB reinforcement randomly distributed within the Ti matrix. The TiB-rich regions (in Figures 6.5(c) and 6.5(d)) and the randomly distributed whiskers (in Figures 6.5(e) and 6.5(f)) were identified by EBSD as orthorhombic TiB with crystal structure of Pearson symbol  $oP8$ , spacegroup  $Pnma$ , No. 62. Figures 6.6(a) and 6.6(b) show the initial and indexed Kikuchi EBSD patterns derived from TiB, respectively.

Figure 6.7 illustrates the formation mechanism of 3DQCN microstructure in LENS. At beginning, due to laser radiation, the premixed Ti and B powders were fully melted and reacted in the molten pool with the generation of TiB. During solidification,  $\beta$ Ti nuclei were firstly formed/separated from the liquid and then grown into crystal grains. In the meantime, TiB was expelled from  $\beta$ Ti nuclei to the surrounding liquid owing to the extremely low solid solubility of B in Ti matrix [47,48]. The TiB aggregated at the boundaries of Ti grains, forming the 3DQCN microstructure inside TiB-TMC.

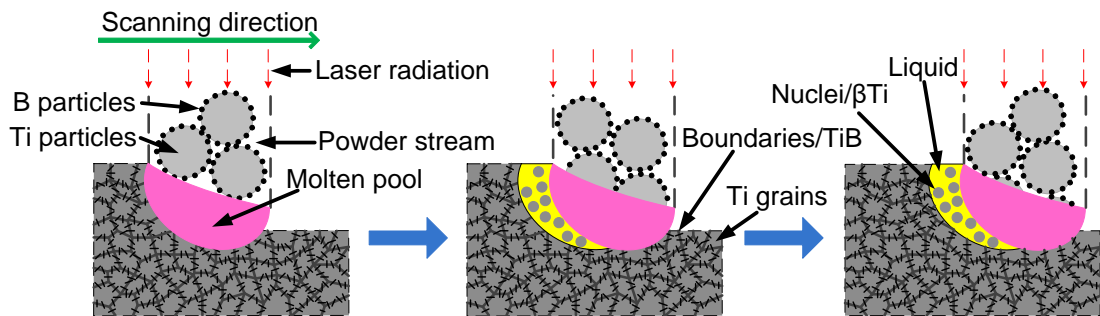


Figure 6.7 Illustrations of 3DQCN microstructure formation mechanism in LENS.

Figure 6.8 shows the effects of TiB reinforcement and laser power on the interior defects, including lack of fusion and micro-pores. At low laser power of 125 W, lack of fusion occurred at the interfaces of adjacent layers due to the insufficiently input energy, resulting in poor bonding and residual thermal stresses at these locations [25,53]. When laser power increased to 200 W, the energy generated was high enough

to remelt the top part of the former layer, resulting in a better metallurgical bonding between adjacent layers without lack of fusion. As is reported, the cracks induced by lack of fusion were stress concentrators, detrimentally affecting the mechanical properties of the built parts [54]. Due to the unbalanced viscosity of the molten pool and incomplete melting of the powders, micro-pores were formed inside both CP-Ti parts and TiB-TMCs with different levels of laser power, as shown through Figure 6.8(a) to Figure 6.8(d) [25,26]. The present of micro-pores could be attributed to the “balling” effect [25]. As discussed in Section 6.3.1, “balling” phenomenon easily occurred associated with the formation of TiB, resulting in more micro-pores inside TiB-TMC (in Figure 6.8(d)), as compared with those inside CP-Ti part (in Figure 6.8(b)). Due to the fact that the low laser power of 125 W was not sufficient enough to

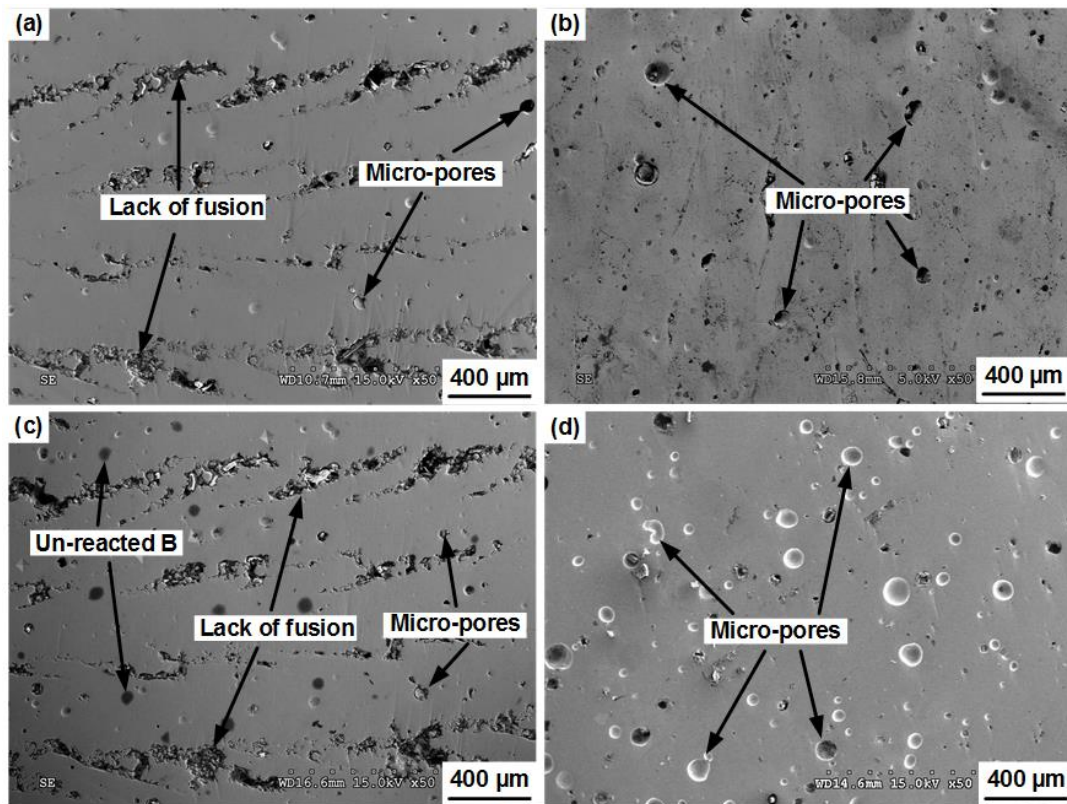


Figure 6.8 SEM imaging observed cross-section morphologies of (a) CP-Ti at 125 W; (b) CP-Ti at 200 W; (c) TiB-TMC at 125 W; and (d) TiB-TMC at 200 W (after polishing).

guarantee the complete reaction between Ti and B, the unreacted B (black dots) still existed, as shown in Figure 6.8(c).

### 6.3.3 Mechanical behavior

#### 6.3.3.1 Effects on hardness

Figure 6.9 shows the effects of TiB reinforcement and laser power on the microhardness (indentation wear resistance) of the fabricated parts. The average value of ten measured data under each specific condition was used to represent central tendency, and the standard deviation was used to represent both maximum and minimum values of error bars. In microhardness calculation, small indentation area means high microhardness. For CP-Ti parts, the microhardness of the parts increased from 125 W to 175 W, and then slightly decreased from 175 W to 200 W. Higher densification degree with fewer interior defects, greater grain refinement, and larger residual stress contributed to the enhancement of the microhardness with the laser power increasing [3]. However, when the laser power reached to its optimal level, further increasing laser power could not further enhance microhardness. One of

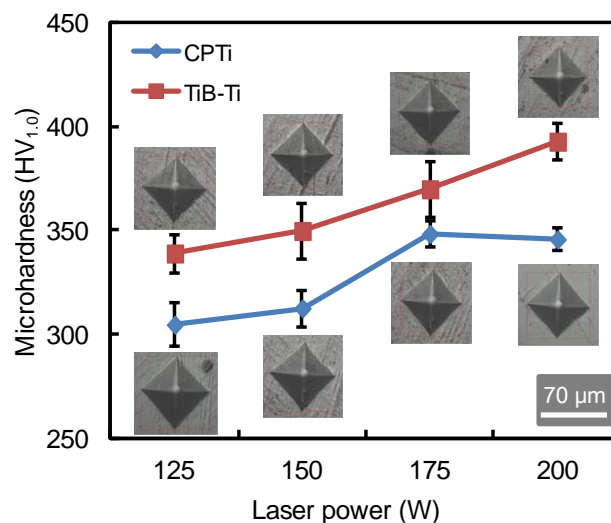


Figure 6.9 Effects of TiB reinforcement and laser power on microhardness of the fabricated parts.

possible reasons was that the formation of thermal cracks, resulting from very high energy input, limited the enhancement of microhardness [25]. For TiB-TMCs, an overall increment of the microhardness of the parts was obtained when the laser power increased from 125 W to 200 W. Besides higher densification degree, greater grain refinement, and larger residual stress, higher TiB generation degree (high degree of reaction between B and Ti) caused by high laser power levels could be another important reason for this tendency. The microhardness of TiB-TMCs was always larger than that of CP-Ti parts at the same laser power. The improvement of the microhardness could be attributed to the formation of the hard TiB reinforcement, the refinement of Ti grains induced by TiB reinforcement, and the present of the 3DQCN microstructure with crosslinking microstructural TiB aggregating at the Ti grain boundaries [3,12,55]. In addition, the TiB reinforcement hindered the propagation of dislocations and contributed to the dislocation strengthening, thus improving microhardness [56].

By optimizing laser power (200 W) and adding B particles (1.6 wt.%) to form TiB ceramic phase, the microhardness could achieve an improvement of 29.3%. Table 6.1 compares the microhardness of the LENS-fabricated CP-Ti parts and TiB-TMCs with those fabricated by other conventional methods (including casting, powder metallurgy (PM), and spark plasma sintering) and shows that the LENS-fabricated CP-Ti parts and TiB-TMCs exhibited higher microhardness. As a rapid-solidified and

Table 6.1 Wear performance of CP-Ti parts and TiB-TMCs

Material type	Processing method	Microhardness (HV)	Wear resistance ( $\times 10^{-3} \text{mm}^3/\text{N}\cdot\text{m}$ )	Data sources
Ti	Casting	200.3 $\pm$ 5.4	/	[57]
	PM	297	14.3	[58]
	LENS (200 W)	345.5 $\pm$ 5.4	6.1 $\pm$ 1.1	This paper
TiB-TMCs (8.5 vol.% TiB)	PM	/	13.8	[58]
	Spark plasma sintering	338.3	/	[59]
	LENS (200 W)	392.6 $\pm$ 8.9	2.4 $\pm$ 0.4	This paper

finely-controlled process, LENS enabled large degree of grain refinement, thus rendering enhanced microhardness.

### 6.3.3.2 Effects on wear resistance

Figure 6.10 shows the results of dry sliding wear tests. Experimental data clearly indicated that due to the present of TiB, TiB-TMCs exhibited shorter sliding track depths and had superior friction wear resistance in comparison to the CP-Ti parts. The present of the TiB reinforcement, the crosslinking microstructure (in Figure 6.5(b)), and the 3DQCN microstructure (in Figure 6.5(c)), favored the improvement of friction wear resistance. For both CP-Ti parts and TiB-TMCs, the sliding track depths and wear rates were found to be significantly decreased with the increase of laser power from 125 W to 200 W. The improved densification degree with fewer interior defects (in Figure 6.8), the high TiB generation degree (in Figure 6.8), the enhanced microhardness (in Figure 6.9), and the high residual thermal stress could be possible reasons of strengthened friction wear resistance induced by increased laser power. The wear rate of TiB-TMC processed at 200 W laser power decreased by an order of magnitude to  $2.4 \times 10^{-3} \text{ mm}^3/\text{Nm}$ , which was 87.3% less than that of the CP-Ti part processed at 125 W laser power. Table 6.1 shows the comparison of wear resistance of the parts fabricated by different methods. Results show that the LENS-fabricated CP-

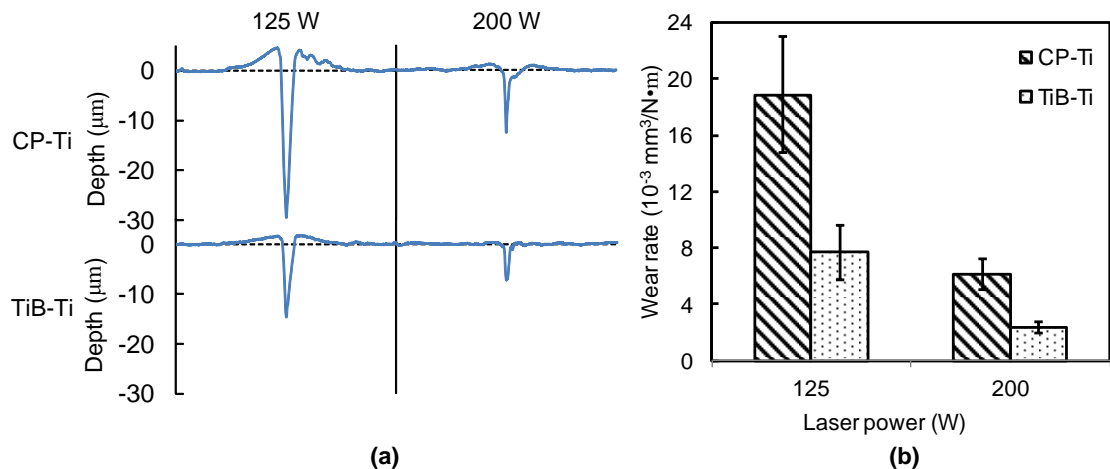


Figure 6.10 (a) Depths after dry sliding wear tests under different conditions; (b) Effects of TiB reinforcement and laser power on wear rate of the fabricated parts.

Ti parts and TiB-TMCs demonstrated superior wear resistance, as compared with PM-fabricated CP-Ti parts and TiB-TMCs. This was ascribed to the reduced grain size and refined TiB whiskers in LENS process [3, 12].

Figure 6.11 shows the worn surfaces, induced by dry sliding wear tests, of CP-Ti part and TiB-TMC fabricated by LENS at 200 W laser power. For CP-Ti part, the long and wide grooves indicated severe abrasion and plastic deformation during the dry sliding wear test. The surface morphology was formed with ductile flows as the counter-face ball ploughed across the surface and removed materials, as shown in Figure 6.11(b). Compared with CP-Ti part, the abrasive track of TiB-TMC was thinner with milder grooves. During dry sliding wear test, the TiB whiskers were worn against

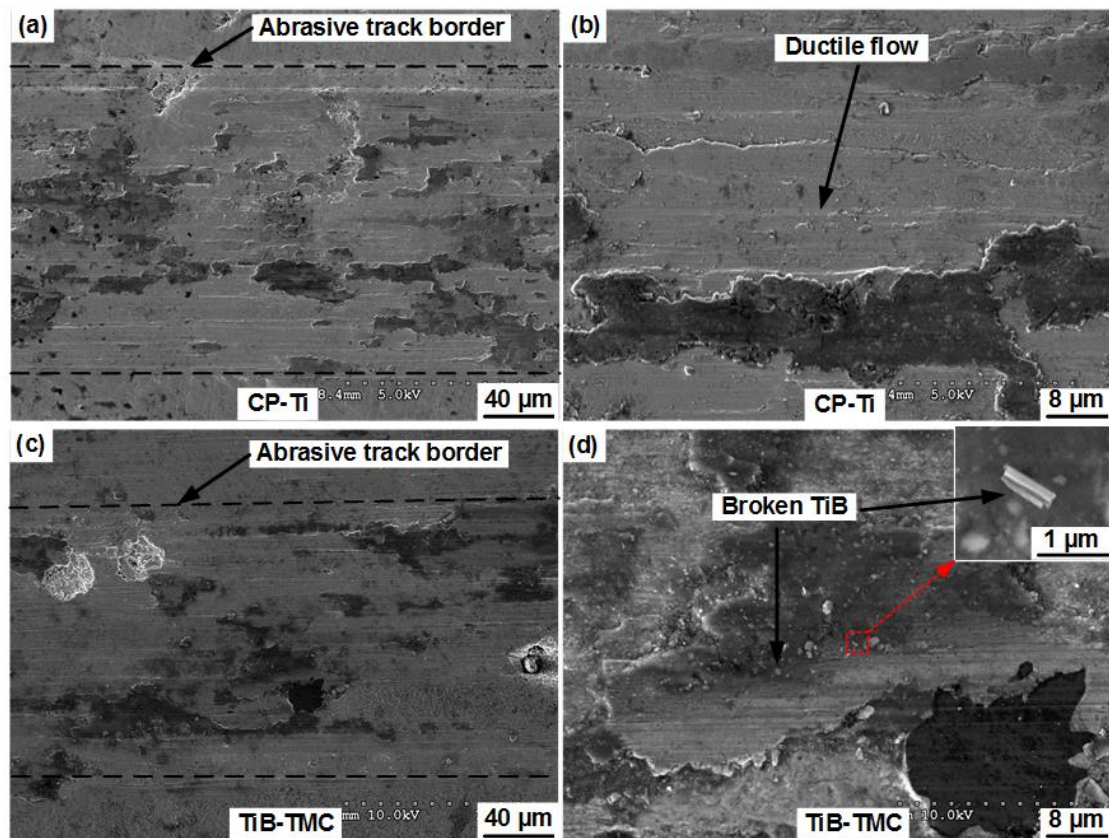


Figure 6.11 Worn surfaces of CP-Ti part at (a) lower magnification and (b) higher magnification as well as TiB-TMC at (c) lower magnification and (d) higher magnification.

the counter-face ball, thus improving wear resistance of the TiB-TMC. The broken TiB whiskers can be seen on the worn surface of TiB-TMC, as shown in Figure 6.11(d).

#### **6.4 Conclusions**

In this investigation, innovative 3DQCN microstructural TiB-TMCs with the crosslinking eutectic TiB nanofibers aggregating at the Ti grain boundaries were fabricated by in-situ LENS process. The effects of reinforcement and energy input on parts quality, microstructure characterizations, indentation wear resistance, and friction wear resistance were investigated. The main conclusions of this paper were drawn as follows:

(1) Top surfaces of LENS-fabricated TiB-TMC and CP-Ti part were compared, showing that “balling” phenomenon was obvious for the LENS-fabricated TiB-TMC due to the present of TiB reinforcement. At higher laser power level, the qualities of the bulk parts were remarkably improved, with fewer interior defects of lack of fusion and micro-pores. Distribution of TiB in Ti matrix was improved by ball milling treatment prior to LENS process.

(2) In LENS process, new phase of TiB was generated in form of both prismatic primary TiB and needle-like eutectic TiB as a result of the in-situ reaction between Ti and B. The novel flower-like microstructure, crosslinking microstructure, and 3DQCN microstructure were observed and their formation mechanisms were investigated. The 3DQCN microstructure was beneficial to mechanical properties due to its specific quasi-continuous network and three-dimensional characterizations.

(3) Effects of the TiB reinforcement and the innovative microstructures inside TiB-TMCs on indentation wear resistance (microhardness) and friction wear resistance were analyzed, showing that these two wear resistance properties were significantly improved due to the present of TiB reinforcement, as compared with CP-Ti parts. By increasing laser power, indentation wear resistance and friction wear resistance were also remarkably enhanced.

## References

- [1] Hu, Y. B., Wang, H., Ning, F. D., & Cong, W. L. (2016). Laser engineered net shaping of commercially pure titanium: Effects of fabricating variables. In ASME 2016 International Manufacturing Science and Engineering Conference.
- [2] Attar, H., Prashanth, K. G., Zhang, L. C., Calin, M., Okulov, I. V., Scudino, S., Yang, C., & Eckert, J. (2015). Effect of powder particle shape on the properties of in situ Ti-TiB composite materials produced by selective laser melting. *Journal of Materials Science & Technology*, 31(10), 1001-1005.
- [3] Attar, H., Bönisch, M., Calin, M., Zhang, L. C., Scudino, S., & Eckert, J. (2014). Selective laser melting of in situ titanium-titanium boride composites: processing, microstructure and mechanical properties. *Acta Materialia*, 76, 13-22.
- [4] Guo, C., Zhou, J. S., Chen, J. M., Zhao, J. R., Yu, Y. J., & Zhou, H. D. (2010). Improvement of the oxidation and wear resistance of pure Ti by laser cladding at elevated temperature. *Surface and Coatings Technology*, 205(7), 2142-2151.
- [5] Grögler, T., Zeiler, E., Franz, A., Plewa, O., Rosiwal, S. M., & Singer, R. F. (1999). Erosion resistance of CVD diamond-coated titanium alloy for aerospace applications. *Surface and Coatings Technology*, 112(1), 129-132.
- [6] Elias, C. N., Lima, J. H. C., Valiev, R., & Meyers, M. A. (2008). Biomedical applications of titanium and its alloys. *JOM*, 60(3), 46-49.
- [7] Suárez-Fernández, M. B., Soldado, A. B., Sanz-Medel, A., Vega, J. A., Novelli, A., & Fernández-Sánchez, M. T. (1999). Aluminum-induced degeneration of astrocytes occurs via apoptosis and results in neuronal death. *Brain Research*, 835(2), 125-136.
- [8] Gülsoy, H. Ö., Özbey, S., Pazarlioglu, S., Çiftci, M., & Akyurt, H. (2016). Sintering and mechanical properties of titanium composites reinforced nano sized Al<sub>2</sub>O<sub>3</sub> particles. *International Journal of Materials, Mechanics and Manufacturing*, 4(2), 111-114.
- [9] Das, M., Balla, V. K., Kumar, T. S., Bandyopadhyay, A., & Manna, I. (2016). Tribological, electrochemical and in vitro biocompatibility properties of SiC reinforced composite coatings. *Materials & Design*, 95, 510-517.
- [10] Balla, V. K., Bhat, A., Bose, S., & Bandyopadhyay, A. (2012). Laser processed TiN reinforced Ti6Al4V composite coatings. *Journal of the Mechanical Behavior of Biomedical Materials*, 6, 9-20.
- [11] Zhang, Y. Z., Wei, Z. M., Shi, L. K., & Xi, M. Z. (2008). Characterization of laser powder deposited Ti-TiC composites and functional gradient materials. *Journal of Materials Processing Technology*, 206(1), 438-444.
- [12] Hu, Y. B., Zhao, B., Ning, F. D., Wang, H., & Cong, W. L. (2017). In-situ ultrafine three-dimensional quasi-continuous network microstructural TiB reinforced titanium matrix composites fabrication using laser engineered net shaping. *Materials Letters*, 195, 116-119.
- [13] Miklaszewski, A., Jurczyk, M. U., & Jurczyk, M. (2011). Surface modification of pure titanium by TiB precipitation. *Solid State Phenomena*, 183, 131-136.

- [14] Gorsse, S., Le Petitcorps, Y., Matar, S., & Rebillat, F. (2003). Investigation of the Young's modulus of TiB needles in situ produced in titanium matrix composite. *Materials Science and Engineering: A*, 340(1), 80-87.
- [15] Lu, W. J., Zhang, D., Zhang, X. N., Wu, R. J., Sakata, T., & Mori, H. (2001). Microstructural characterization of TiB in in situ synthesized titanium matrix composites prepared by common casting technique. *Journal of Alloys and Compounds*, 327(1-2), 240-247.
- [16] Fan, Z. Y., Niu, H. J., Miodownik, A. P., Saito, T., & Cantor, B. (1996). Microstructure and mechanical properties of in situ Ti/TiB MMCs produced by a blended elemental powder metallurgy method. *Key Engineering Materials*, 127, 423-430.
- [17] Zhang, Y., Sun, J., & Vilar, R. (2011). Characterization of (TiB + TiC)/TC<sub>4</sub> in situ titanium matrix composites prepared by laser direct deposition. *Journal of Materials Processing Technology*, 211(4), 597-601.
- [18] Tamirisakandala, S., Miracle, D. B., Srinivasan, R., & Gunasekera, J. S. (2006). Titanium alloyed with boron. *Advanced Materials and Processes*, 164(12), 41-43.
- [19] Emamian, A., Corbin, S. F., & Khajepour, A. In-Situ formation of TiC using laser cladding. Eustathopoulos, N., Nicholas, M. G., & Drevet, B. (Eds.). (1999). *Wettability at high temperatures (Vol. 3)*. Elsevier.
- [20] Tjong, S. C., & Ma, Z. Y. (2000). Microstructural and mechanical characteristics of in situ metal matrix composites. *Materials Science and Engineering: R: Reports*, 29(3), 49-113.
- [21] Ma, J. W., Jia, Z. Y., Wang, F. J., Gao, Y. Y., & Liu, Z. (2016). A new cutting force modeling method in high-speed milling of curved surface with difficult-to-machine material. *The International Journal of Advanced Manufacturing Technology*, 84(9-12), 2195-2205.
- [22] Jia, Z. Y., Song, D. N., Ma, J. W., Hu, G. Q., & Su, W. W. (2017). A NURBS interpolator with constant speed at feedrate-sensitive regions under drive and contour-error constraints. *International Journal of Machine Tools and Manufacture*, 116, 1-17.
- [23] Song, B., Zhao, X., Li, S., Han, C. J., Wei, Q. S., Wen, S. F., Liu, J., & Shi, Y. S. (2015). Differences in microstructure and properties between selective laser melting and traditional manufacturing for fabrication of metal parts: A review. *Frontiers of Mechanical Engineering*, 10(2), 111-125.
- [24] Gao, Y. Y., Ma, J. W., Jia, Z. Y., Wang, F. J., Si, L. K., & Song, D. N. (2016). Tool path planning and machining deformation compensation in high-speed milling for difficult-to-machine material thin-walled parts with curved surface. *The International Journal of Advanced Manufacturing Technology*, 84(9-12), 1757-1767.
- [25] Gu, D. D., Meiners, W., Wissenbach, K., & Poprawe, R. (2012). Laser additive manufacturing of metallic components: materials, processes and mechanisms. *International Materials Reviews*, 57(3), 133-164.

- [26] Agarwala, M., Bourell, D., Beaman, J., Marcus, H., & Barlow, J. (1995). Direct selective laser sintering of metals. *Rapid Prototyping Journal*, 1(1), 26-36.
- [27] Candel, J. J., Amigó, V., Ramos, J. A., & Busquets, D. (2010). Sliding wear resistance of TiCp reinforced titanium composite coating produced by laser cladding. *Surface and Coatings Technology*, 204(20), 3161-3166.
- [28] Thijs, L., Verhaeghe, F., Craeghs, T., Van Humbeeck, J., & Kruth, J. P. (2010). A study of the microstructural evolution during selective laser melting of Ti-6Al-4V. *Acta Materialia*, 58(9), 3303-3312.
- [29] Kruth, J. P., Levy, G., Klocke, F., & Childs, T. H. C. (2007). Consolidation phenomena in laser and powder-bed based layered manufacturing. *CIRP Annals-Manufacturing Technology*, 56(2), 730-759.
- [30] Unocic, R. R. R. (2002). A fundamental investigation of process efficiencies in the laser engineered net shaping (LENS) solid freeform fabrication process. *Theses and Dissertations*, Paper 754.
- [31] Li, Y. Z., Hu, Y. B., Cong, W. L., Zhi, L., & Guo, Z. N. (2017). Additive manufacturing of alumina using laser engineered net shaping: Effects of deposition variables. *Ceramics International*, 43(10), 7768-7775.
- [32] Ning, F. D., Hu, Y. B., Liu, Z. C., Cong, W. L., Li, Y. Z., & Wang, X. L. (2017). Ultrasonic vibration-assisted laser engineered net shaping of Inconel 718 parts: a feasibility study. 45th SME North American Manufacturing Research Conference, June 4-8, 2017, Los Angeles, CA, USA.
- [33] Atwood, C. J., Smugeresky, J. E., & Gill, D. D. (2006). Laser engineered net shaping (LENS) for the repair and modification of NWC metal components. Sandia National Laboratories, No. SAND2006-6551.
- [34] Ning, F., & Cong, W. (2016). Microstructures and mechanical properties of Fe-Cr stainless steel parts fabricated by ultrasonic vibration-assisted laser engineered net shaping process. *Materials Letters*, 179, 61-64.
- [35] Liu, D., Lippold, J. C., Li, J., Rohklin, S. R., Vollbrecht, J., & Grylls, R. (2014). Laser engineered net shape (LENS) technology for the repair of Ni-base superalloy turbine components. *Metallurgical and Materials Transactions A*, 45(10), 4454-4469.
- [36] Hu, Y. B., & Li, J. Z. (2014). Ultra-short laser melting of copper nanoparticles: a molecular dynamics study. *International Journal of Energy for a Clean Environment*, 15(1), 1-25.
- [37] Das, M., Bhattacharya, K., Dittrick, S. A., Mandal, C., Balla, V. K., Kumar, T. S., Bandyopadhyay, A., & Manna, I. (2014). In situ synthesized TiB-TiN reinforced Ti6Al4V alloy composite coatings: microstructure, tribological and in-vitro biocompatibility. *Journal of the Mechanical Behavior of Biomedical Materials*, 29, 259-271.
- [38] Wu, Q. L., & Li, W. G. (2011). The microstructure and wear properties of laser-clad WC-Cr<sub>3</sub>C<sub>2</sub> cermet coating on steel substrate. *Materials Transactions*, 52(3), 560-563.
- [39] Garcia-Sanz, F. J., Mayor, M. B., Arias, J. L., Pou, J., Leon, B., & Perez-Amor, M. (1997). Hydroxyapatite coatings: A comparative study between plasma-

- spray and pulsed laser deposition techniques. *Journal of Materials Science: Materials in Medicine*, 8(12), 861-865.
- [40] Murray, J. L., Liao, P. K., & Spear, K. E. (1986). The B-Ti (Boron-Titanium) system. *Bulletin of Alloy Phase Diagrams*, 7(6), 550-555.
- [41] Wei, S., Zhang, Z. H., Wang, F. C., Shen, X. B., Cai, H. N., Lee, S. K., & Wang, L. (2013). Effect of Ti content and sintering temperature on the microstructures and mechanical properties of TiB reinforced titanium composites synthesized by SPS process. *Materials Science and Engineering: A*, 560, 249-255.
- [42] Nowell, M. M., & Wright, S. I. (2005). Orientation effects on indexing of electron backscatter diffraction patterns. *Ultramicroscopy*, 103(1), 41-58.
- [43] Na, S. H., Kim, S. H., Lee, Y. W., & Sohn, D. S. (2002). Effect of ball-mill treatment on power characteristics, compaction and sintering behaviors of ex-AUC and ex-ADU UO<sub>2</sub> powder. *Nuclear Engineering and Technology*, 34(1), 60-67.
- [44] Niu, H. J., & Chang, I. T. H. (1999). Selective laser sintering of gas and water atomized high speed steel powders. *Scripta Materialia*, 41(1), 25-30.
- [45] Aizenshtein, M., Froumin, N., & Frage, N. (2014). Experimental study and thermodynamic analysis of high temperature interactions between boron carbide and liquid metals. *Engineering*, 6(13), 849.
- [46] Shen, P., Fujii, H., & Nogi, K. (2006). Wettability of polycrystalline rutile TiO<sub>2</sub> by molten Al in different atmospheres. *Acta Materialia*, 54(6), 1559-1569.
- [47] Tamirisakandala, S., Bhat, R. B., Tiley, J. S., & Miracle, D. B. (2005). Grain refinement of cast titanium alloys via trace boron addition. *Scripta Materialia*, 53(12), 1421-1426.
- [48] Tang, J. X., Cheng, J. H., Zeng, Z. Q., & Miao, H. Z. (2000). Diffusion path and reaction mechanism between Ti and B<sub>4</sub>C. *Journal of Inorganic Materials-Beijing*, 15(5), 884-888.
- [49] Banerjee, R., Genc, A., Collins, P. C., & Fraser, H. L. (2004). Comparison of microstructural evolution in laser-deposited and arc-melted in-situ Ti-TiB composites. *Metallurgical and Materials Transactions A*, 35(7), 2143-2152.
- [50] Huang, L. J., Geng, L., & Peng, H. X. (2015). Microstructurally inhomogeneous composites: Is a homogeneous reinforcement distribution optimal?. *Progress in Materials Science*, 71, 93-168.
- [51] Huang, L. J., Geng, L., & Peng, H. X. (2010). In situ (TiBw+ TiCp)/Ti<sub>6</sub>Al<sub>4</sub>V composites with a network reinforcement distribution. *Materials Science and Engineering: A*, 527(24), 6723-6727.
- [52] Gu, D. D., Meng, G. B., Li, C., Meiners, W., & Poprawe, R. (2012). Selective laser melting of TiC/Ti bulk nanocomposites: Influence of nanoscale reinforcement. *Scripta Materialia*, 67(2), 185-188.
- [53] Mercelis, P., & Kruth, J. P. (2006). Residual stresses in selective laser sintering and selective laser melting. *Rapid Prototyping Journal*, 12(5), 254-265.

- [54] German, R. M. Powder Metallurgy Science, (Metal Powder Industries Federation, Princeton, NJ, 1994). and in Powder Metallurgy Processing, edited by H. Kuhn and A. Lawley (Academic Press, New York, 1978), 102.
- [55] Makuch, N., Kulka, M., Dziarski, P., & Przystacki, D. (2014). Laser surface alloying of commercially pure titanium with boron and carbon. *Optics and Lasers in Engineering*, 57, 64-81.
- [56] Humpherys, F. J. (1988). Mechanical and physical behavior of metallic and ceramic composites. Denmark: Riso Nat Lab.
- [57] Rocha, S. S. D., Adabo, G. L., Henriques, G. E. P., & Nóbilo, M. A. D. A. (2006). Vickers hardness of cast commercially pure titanium and Ti-6Al-4V alloy submitted to heat treatments. *Brazilian dental journal*, 17(2), 126-129.
- [58] Alman, D. E., & Hawk, J. A. (1999). The abrasive wear of sintered titanium matrix–ceramic particle reinforced composites. *Wear*, 225, 629-639.
- [59] Hiroshi, I. Z. U. I., Akinori, O. O. T. A., Matsuura, K., & Kamegawa, S. (2016). Tensile behavior of TiB-reinforced Ti matrix composites with different titanium powders. *Mechanical Engineering Journal*, 3(4), 15-00571.

## CHAPTER VII

### LENS OF TiB-TMCS – TiB GROWTH AND PART PERFORMANCE

Paper title:

Laser deposition – additive manufacturing of in-situ TiB reinforced titanium matrix composites: TiB growth and part performance

Published in:

The International Journal of Advanced Manufacturing Technology, 2017, Vol. 93, No. 9-12, pp. 3409-3418

Authors' names:

Yingbin Hu<sup>a</sup>, Fuda Ning<sup>a</sup>, Xinlin Wang<sup>a,b</sup>, Hui Wang<sup>a</sup>, Bo Zhao<sup>c</sup>, Weilong Cong<sup>a,\*</sup>, and Yuzhou Li<sup>a,d</sup>

Authors' affiliations:

<sup>a</sup>Department of Industrial, Manufacturing, & Systems Engineering, Texas Tech University, Lubbock, Texas, 79409, USA

<sup>b</sup>School of Mechanical Engineering, Dalian University of Technology, Dalian, Liaoning, 116024, China

<sup>c</sup>College of Arts & Sciences Microscopy, Texas Tech University, Lubbock, TX 79409, USA

<sup>d</sup>School of Electromechanical Engineering, Guangdong University of Technology, Guangzhou, Guangdong, 510006, China

\*Corresponding author:

Department of Industrial, Manufacturing, & Systems Engineering, Texas Tech University, Lubbock, TX 79409-3061, USA. Email address: weilong.cong@ttu.edu

## **Abstract**

Ceramic reinforced Ti matrix composites (TMCs) have been widely used under severe friction and heavy loading conditions due to their superior properties. Among different types of ceramic reinforcements, TiB is considered as one of the most suitable ceramic reinforcement materials for TMCs because of its high strength and stiffness, excellent interfacial bonding with Ti matrix, and low induced stress. As a laser additive manufacturing process, laser deposition-additive manufacturing (LD-AM) has been successfully utilized to fabricate Ti based materials. However, investigations on LD-AM of in-situ TiB reinforced TMCs are limited. This investigation, for the first time, reports the tomography analysis of TiB reinforcement within Ti matrix and the formation of novel flower-like microstructure. The influences of reaction energy on part performance have been explored. In addition, the effects of input fabrication variables (including laser power and Z-axis increment) on part performance (including density, microhardness, and compressive properties) have been investigated, providing guidance on selection of input fabrication variables for future research.

## **Keywords**

TiB growth; Titanium matrix composites; Laser deposition-additive manufacturing; Part performance; Fracture features.

## **7.1 Introduction**

Compared with titanium (Ti) and its alloys, ceramic reinforced Ti matrix composites (TMCs) exhibit higher indentation wear resistance and better load endurance properties, enabling their applications under severe friction and heavy loading conditions (e.g. tooth's root implants [1], actuator struts [2], etc.). The ceramic reinforcements mainly include TiB [3-7], TiC [8,9], TiN [10], SiC [2,11], WC [12], etc. Due to the unique benefits such as high strength and stiffness and excellent interfacial bonding, TiB is considered as one of the most suitable ceramic reinforcement materials for TMCs [3-5]. In addition, stress within TMCs can be weakened or even eliminated, owing to the comparable thermal expansion coefficients

between TiB and Ti [3,4].

Traditional manufacturing processes, such as casting [4,13] and powder metallurgy (PM) [6], have been applied for the fabrication of ceramic reinforced TMCs. Kim et al. successfully fabricated TiB/TiC reinforced TMCs using casting, and then conducted dry sliding tests on the TMCs [13]. Results showed that the wear performance of TMCs was higher than that of pure Ti. TiB reinforced TMCs were reported to be produced by PM with a 40% increase of stiffness, compared with that of pure Ti [6]. However, these traditional manufacturing processes showed shortcomings of long manufacture cycle time, high energy consumption, high reinforcement agglomeration, large grain structure, etc [7]. In response to these problems, it is crucial to investigate a high-efficiency, cost-effective, and finely controlled manufacturing technology. Laser additive manufacturing (LAM) technology is such a manufacturing technology that has been developed to produce metallic components. As reported, many works have been done on the LAM processed Ti based materials [5,8,14-16]. Compared with other LAM processes (such as selective laser sintering/melting), laser deposition-additive manufacturing (LD-AM) process exhibits more specific advantages, including capabilities of parts remanufacturing and functionally gradient materials fabrication, small heat affected zone, etc. [14,16-20]. In this investigation, the LD-AM process is carried out by a laser engineered net shaping (LENS) machine (450, Optomec Inc., Albuquerque, NM, USA).

The illustration of LD-AM process is shown in Figure 7.1. At the beginning, the laser beam is ejected from the laser source and melts the selected area of the substrate to form a molten pool. Then, the molten pool increases as continuously catching powders supplied by the powder feeder. When the laser beam leaves, the molten pool is solidified rapidly due to the rapid heat dissipation. Based on the three-dimensional (3D) file, the deposition head moves along the designed trajectory to create the first layer. Afterwards, the deposition head ascends one layer thickness to the new set position. Treated as the new “substrate”, the first layer is partially melted with the formation of the second layer. Finally, the bulk part will be built by repeating

these steps layer by layer.

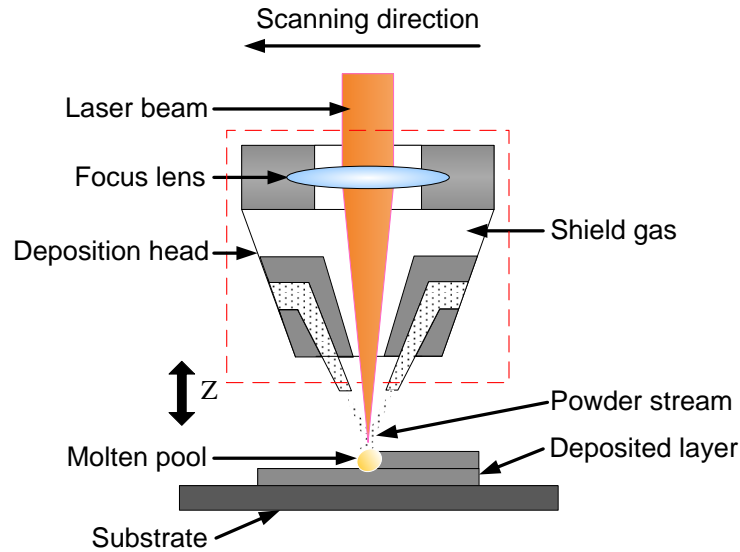


Figure 7.1 Illustration of LD-AM process.

Up till now, only limited investigations have been reported on LD-AM of in-situ TiB reinforced TMCs (TiB-TMCs). By LD-AM process, Banerjee et al. successfully fabricated TiB-TMCs with TiB reinforcement homogeneously dispersing within Ti matrix [21]. DuttaMajumdar et al. developed TiB-TMCs as cladding layers on the Ti6Al4V substrate by melting premixed Ti and boron (B) powder using LD-AM process [22]. Results showed that the microhardness of the cladding layers was much higher than that of the substrate.

This study, for the first time, reports the tomography analysis and spatial distribution of TiB reinforcement within Ti matrix as well as the formation of a flower-like microstructure. The relationship between reaction energy and part performance has been explored. In addition, the effects of laser power and Z-axis increment on density (the ratio between fabricated part density and fully dense part density), microhardness, and compressive properties of fabricated parts have been investigated. The obtained results will provide a guidance on the selection of input fabrication variables for future research.

## 7.2 Experiments and measurements procedures

### 7.2.1 Powder materials and powder treatment

The CP-Ti powder (Atlantic Equipment Engineers Inc., Upper Saddle River, NJ, USA) with an average particle size of 150  $\mu\text{m}$  and a purity of 99.7% was utilized. The average particle size of the B powder (Chemsavers, Inc., Bluefield, WV, USA) was 2  $\mu\text{m}$  and the purity was higher than 96%.

As reported, when the B content was 1.6 wt.%, eutectic solidification would occur with the generation of finer eutectic TiB reinforcement, leading to the enhancement of fracture toughness and bending strength of fabricated TMCs [6,23]. Therefore, the weight ratio of 98.4 : 1.6 between Ti and B powders was adopted. Prior to LENS process, Ti and B powders were mixed using a planetary ball milling machine (ND2L, Torrey Hills Technologies LLC., San Diego, CA, USA). The ball milling parameters were set as: milling time of four hours, ball-to-powder weight ratio of 5:1, and fixed rotation speed of 200 rpm.

Figures 7.2(a) and 7.2(b) show the morphologies of the as-received CP-Ti powder and as-received B powder, respectively. Compared with as-received CP-Ti powder, the CP-Ti powder after ball milling process was more spherical in shape and more uniform in size without significant size reduction, as shown in Figure 7.2(c). It was reported that the spherical powder shape and uniform powder distribution were beneficial to the part quality [24,25].

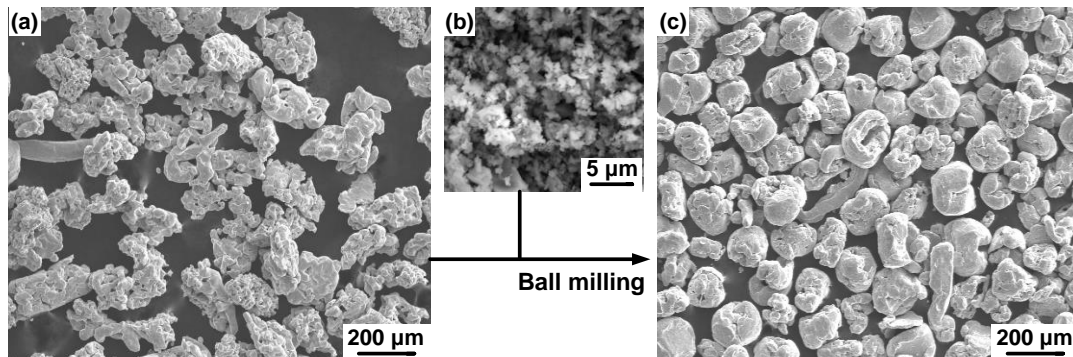


Figure 7.2 SEM morphologies of (a) the as-received CP-Ti powder, (b) the as-received B powder, and (c) the four-hour premixed CP-Ti and B powders.

### 7.2.2 Experimental conditions

Table 7.1 lists the input fabrication variables (including laser power and Z-axis increment) in an experiment matrix. Other input fabrication variables, such as deposition head scanning speed, hatch distance, powder feeding rate, number of layers, scanning orientation, oxygen level, etc., were optimized based on parametric selection results, as shown in Table 7.2. A zigzag scanning pattern with a 90° orientation changing for each layer was adopted. And it began with 45°.

Table 7.1 Input fabrication variables in an experiment matrix

No.	Laser power (W)	Z-axis increment (mm)
1	125	
2	150	
3	175	0.42
4*	200	
5		0.30
6	200	0.36
7*		0.42
8		0.48

\*Duplicate experiments will not be re-conducted.

Table 7.2 Fixed input fabrication variables

Input fabrication variables	Values or ranges
Deposition head scanning speed (mm/s)	11
Hatch distance (mm)	0.38
Powder feeding rate (g/s)	0.028
Number of layers	20
Scanning orientation (°)	45, 135, 225, and 315
Oxygen level (ppm)	<500

For each combination of input fabrication variables, replicated parts were fabricated. The dimensions of the parts were 8 mm × 8 mm × 20 layers. To conduct compressive tests, parts with dimensions of  $\Phi 6$  mm × 15 layers were also fabricated.

### 7.2.3 Measurement procedures

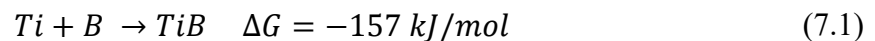
The densities of the fabricated parts were measured using the Archimedes method. The pores of the fabricated parts were observed using an optical microscope (OM) (Eclipse TS100, Graticules Ltd., Kent, England). The scanning electron microscope (SEM) (Crossbeam 540, Carl Zeiss AG, Oberkochen, Germany), equipped with energy-dispersive X-ray spectroscopy (EDXS) system and tomography system, was used to observe morphologies of the powders and to analyze the microstructural characterizations, phase composition, and tomography of the fabricated parts. The detectors of Crossbeam 540 were capable of detecting B. Prior to OM and SEM observations, the sectioned parts were ground and polished on a MetaServ 250 single grinder-polisher machine (49-10055, Buehler, Lake Bluff, IL, USA), and then etched using a Kroll's Reagent (HF: 3%; HNO<sub>3</sub>: 6%; water: balance) (Etchant Store, Suite N Glendora, CA, USA) for 15 seconds.

The microhardness was tested using a Vickers hardness tester (900-390, Phase II, Upper Saddle River, NJ, USA) under 9.8 N load and ten-second dwell time. Ten indents were taken at different locations of each fabricated parts where the distance between the adjacent locations was at least 0.5 mm. To obtain better results, both planar sides of each fabricated cylindrical part were ground and polished on the grinder-polisher machine. Then, compressive tests were performed by a tensile tester (AGS-50kNXD, Shimadzu, Kyoto, Kyoto Prefecture, Japan) at a constant cross-head speed of 0.005 mm/s. For each condition, the tests were repeated three times.

## 7.3 Experiment results and discussion

### 7.3.1 TiB growth

In LENS process, reaction between elemental Ti and B powders took place. It was reported that TiB would be mainly formed if B content in the reaction zone was less than 18 – 18.5 wt.% [26]. The reaction formula was [27]:



The negative sign of  $\Delta G$  (the Gibb free energy) indicated that the reaction was

exothermic reaction, thus releasing energy that could be utilized to facilitate melting process.

Figure 7.3 shows the phase composition analysis of a TiB-TMC sample, which was processed at the laser power of 200 W and Z-axis increment of 0.42 mm. To have a better understanding of the atomic ratio between Ti and B element and phase compositions, all the other non-relevant elements (e.g. O, C, K, etc.) generated during the manufacturing process were filtered. At spectrum 1, the atomic ratio between Ti and B was almost 1:1, which meant that the particle detected was TiB. At spectrum 2, there was no phase of B, indicating that the relatively darker areas were the Ti matrix.

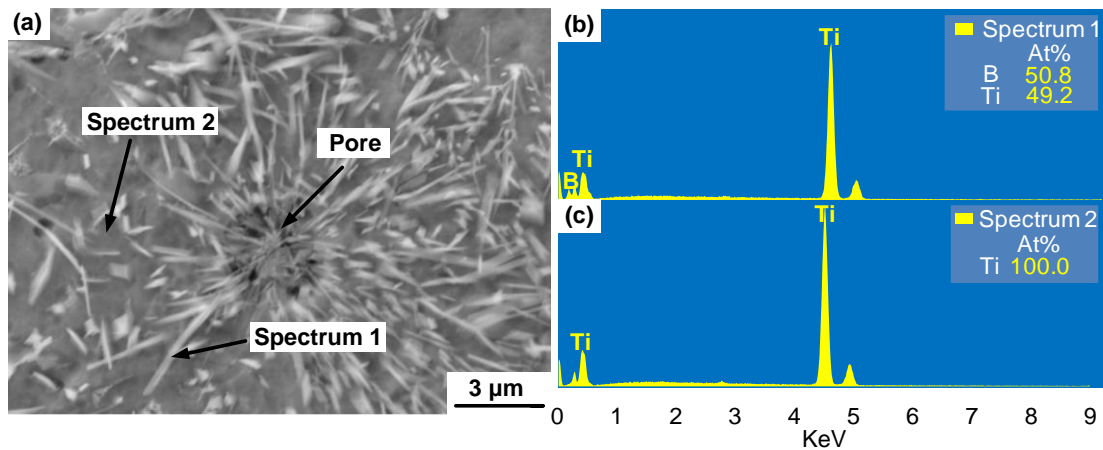


Figure 7.3 Phase composition analysis of a TiB-TMC sample: (a) SEM image; EDXS spectrums for compositions of (b) spectrum 1 and (c) spectrum 2.

A tomography image of the TiB-TMC sample is shown in Figure 7.4(a). The TiB particles emanated to the surrounding area from the center (pores) and were embedded into the Ti matrix, forming a flower-like microstructure. The schematic illustration of TiB growth mechanism is shown in Figure 7.4(b) and 7.4(c). It can be considered that B particles reacted with surrounding Ti particles, generating TiB particles and leaving pores behind. The newly formed TiB particles exhibited a long prismatic shape with a high aspect ratio. A tomography video, which shows spatial distribution of TiB reinforcement within Ti matrix, is provided by the author's publication [28].

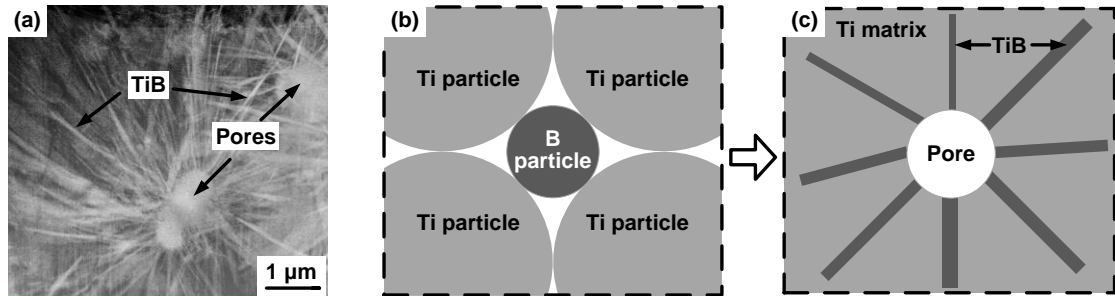


Figure 7.4 Formation mechanism of the flower-like microstructure: (a) Tomography image of TiB distribution among Ti matrix; Schematic illustration of TiB growth (b) before LD-AM process and (c) after LD-AM process.

Figure 7.5(a) shows the SEM image of the TiB reinforcement. The cross-sectional dimension of TiB reinforcement was less than 1 μm and the surface of the TiB reinforcement was flat. Figure 7.5(b) and 7.5(c) illustrate the basic building block – trigonal prism and crystal structure of TiB, respectively. As shown in Figure 7.5(b), the B atom located at the center of a trigonal prism building block with six Ti atoms at the vertexes. It was reported that TiB exhibited B27 structure [29], the trigonal prism building blocks stacked in columnar arrays sharing two of their rectangular faces with

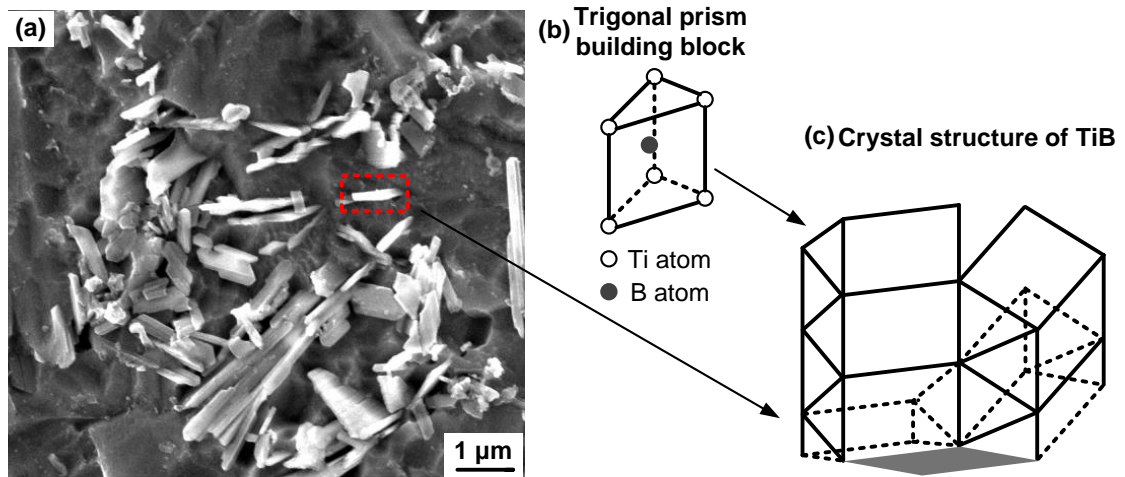


Figure 7.5 TiB growth: (a) SEM image of cross-sectional TiB reinforcement; Schematic illustration of (b) trigonal prism building block and (c) crystal structure of TiB.

neighboring prisms along the B27[010] direction [29,30], as shown in Figure 7.5(c). Therefore, based on the “Periodic Bond Chain” theory, TiB grains grew faster along [010] direction than along other directions, forming the long prismatic shape [30,31].

### 7.3.2 Part performance

#### 7.3.2.1 Effects of laser power on density

Figure 7.6 shows the effects of laser power on densities of both TiB-TMCs and CP-Ti parts. The average value from three measurements, under each combination of input fabrication variables, was used to represent the experimental results. The standard deviation of three measurements was used to represent both positive and negative values of error bars. For CP-Ti parts, an overall increase in density (up to 95.4%) was found when the laser power increased from 125 W to 200 W. Figure 7.7 shows the pores of parts processed at different levels of laser power. At 125 W, the part was only partially melted with a huge portion of pores. When laser power increased from 125 W to 150 W, the pores were reduced with an improved part quality. By further increasing laser power, the size of the pores became smaller due to the larger energy input, thus rendering a larger density. Besides CP-Ti parts, TiB-TMCs showed similar results. With the increase of laser power, the density of TiB-TMCs increased to 95.6%.

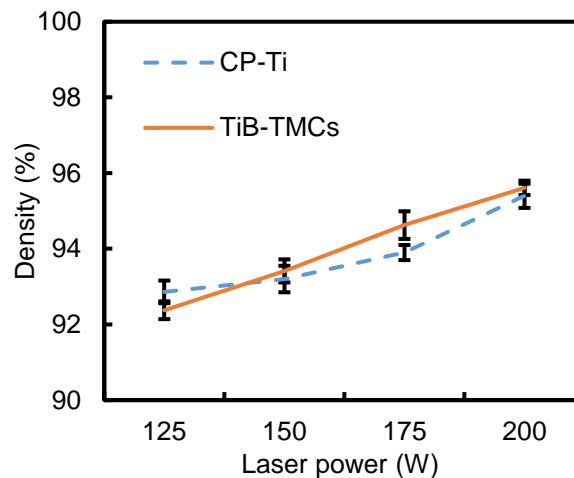


Figure 7.6 Effects of laser power on density.

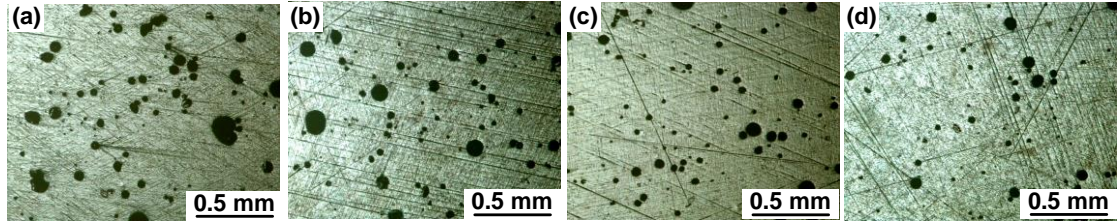


Figure 7.7 Optical Microscope (OM) imaging of cross sections of CP-Ti parts processed at (a) 125 W, (b) 150 W, (c) 175 W, and (d) 200 W laser power with the same magnification.

The relationship of densities between TiB-TMCs and CP-Ti parts was mainly affected by three factors: laser absorption, reaction induced pores, and reaction generated energy. At 125 W, the presence of B restricted laser absorption of TiB-TMCs [32], reducing the energy that could be utilized by TiB-TMCs. In addition, reaction-induced pores existed in TiB-TMCs. Therefore, the average density of TiB-TMCs was lower than that of CP-Ti parts processed at 125 W. By increasing laser power to 150 W and 175 W, the reaction between Ti and B was more sufficient and the B particles became fewer, as compared with those at 125 W, resulting in higher energy generated and fewer pores. Therefore, the densities of TiB-TMCs, processed at 150 W and 175 W, were higher than those of corresponding CP-Ti parts. At 200 W laser power, due to the combined action of the aforementioned three factors, the densities of TiB-TMCs were similar to those of CP-Ti parts.

### 7.3.2.2 Effects of Z-axis increment on density

Figure 7.8 shows the effects of Z-axis increment on the densities of both TiB-TMCs and CP-Ti parts. For CP-Ti parts, the density decreased when the Z-axis increment increased from 0.30 mm to 0.48 mm. At 0.30 mm, the densities of CP-Ti parts could be as high as 98.1%. Figure 7.9 shows the pores of CP-Ti parts processed at different Z-axis increment values. It can be concluded that smaller Z-axis increment led to fewer and smaller sizes of pores. This conclusion was also found in TiB-TMCs. At Z-axis increment of 0.30 mm, the density of TiB-TMCs was 97.5%.

Such phenomenon was mainly attributed to the fact that the Z-axis increment

may not be exactly the same with the layer thickness. If the Z-axis increment value was exactly the same with the layer thickness, as shown in Figure 7.10(a) (Case 1), the focal point would be on the top surface of each layer. If the Z-axis increment value was larger than layer thickness, as shown in Figure 7.10(b) (Case 2), the focal point would be above the top surface of each layer. The energy generated in Case 2 was less than that in Case 1, being insufficient to fully melt the powders. In this investigation, the layer thickness was 0.3 mm. Therefore, the parts processed at Z-axis increment of 0.36 mm, 0.42 mm, and 0.48 mm would be less dense as compared with those processed at Z-axis increment of 0.30 mm. The densities of TiB-TMCs were similar to those of CP-Ti parts processed at the same Z-axis increment.

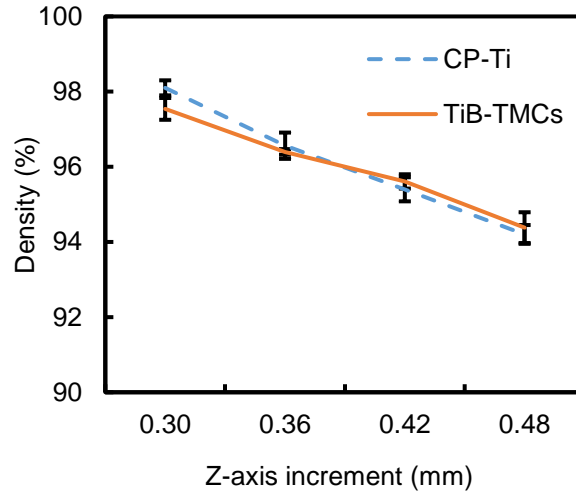


Figure 7.8 Effects of Z-axis increment on density.

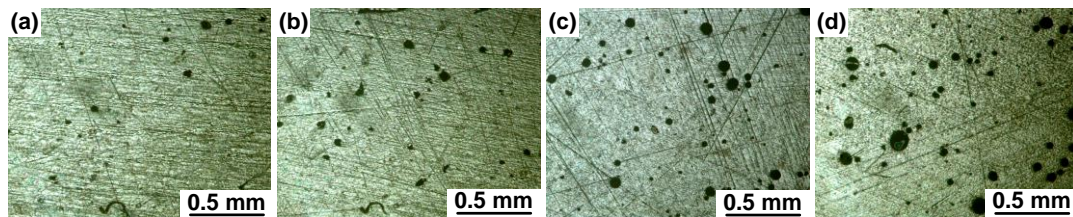


Figure 7.9 Optical Microscope (OM) imaging of cross sections of CP-Ti parts processed at (a) 0.30 mm, (b) 0.36 mm, (c) 0.42 mm, and (d) 0.48 mm Z-axis increment with the same magnification.

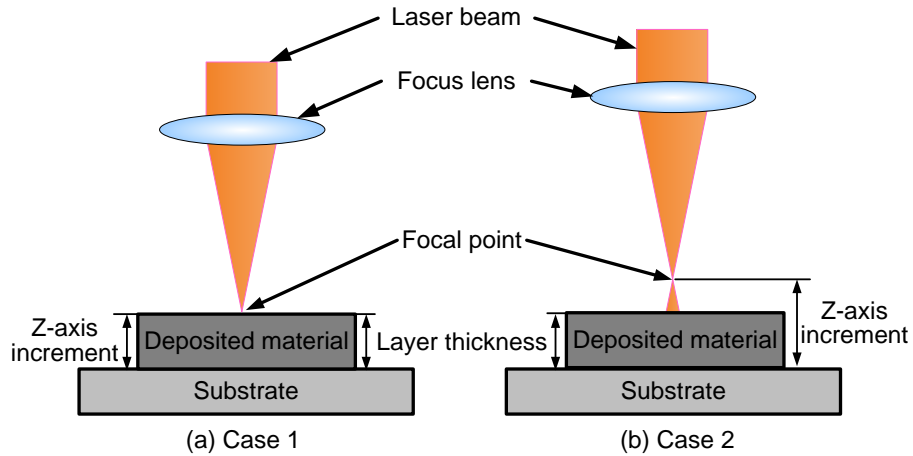


Figure 7.10 Illustration of relationship between Z-axis increment and layer thickness.

### 7.3.2.3 Effects of laser power on microhardness

The effects of laser power on microhardness of fabricated parts are shown in Figure 7.11. To obtain reliable results, the microhardness tests were conducted on the areas free from pores. The average value of ten measurements, under each combination of input fabrication variables, was used to represent the height of each bar in this histogram. The standard deviation of ten measurements was used to represent both positive and negative values of error bars.

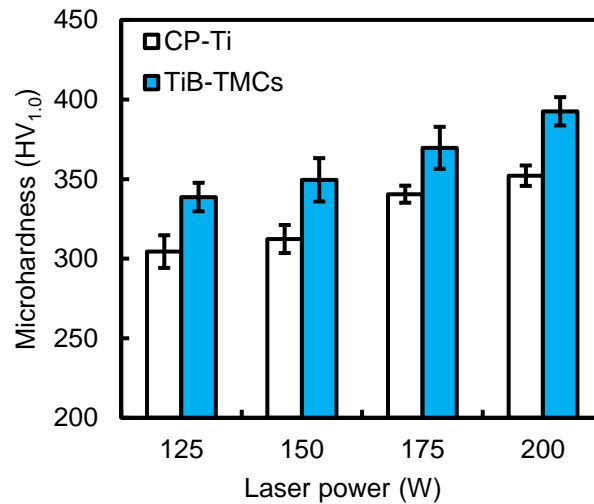


Figure 7.11 Effects of laser power on microhardness.

It can be seen from Figure 7.11 that for CP-Ti parts, the microhardness

increased with the laser power increasing from 125 W to 200 W. The major reasons were greater grain refinement and larger residual stress induced by higher laser power, which resulted in the increase of microhardness [14,33,34]. Similar to CP-Ti parts, the microhardness of TiB-TMCs increased with the laser power increasing from 125 W to 200 W.

It also can be seen that the microhardness of TiB-TMCs was significantly larger than that of CP-Ti parts processed at the same level of laser power. The enhancement of microhardness could be attributed to the presence of rigid TiB reinforcement and the Ti grain refinement induced by TiB generation [4,21,35,36].

#### 7.3.2.4 Effects of Z-axis increment on microhardness

Figure 7.12 shows the effects of Z-axis increment on microhardness. The microhardness slightly changed with the increase of Z-axis increment for both TiB-TMCs and CP-Ti parts. The reason could be explained as follows.

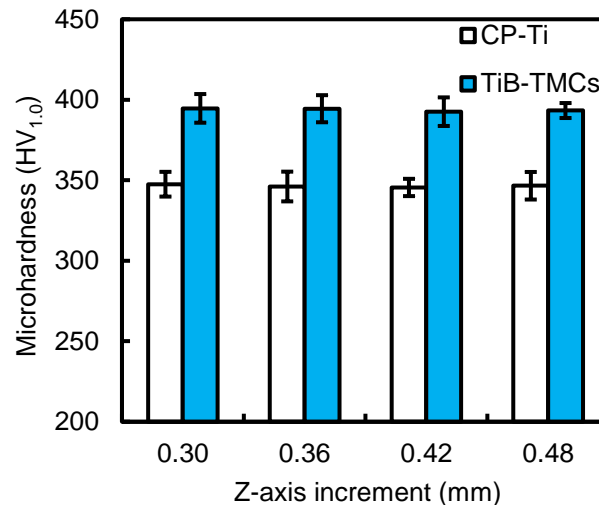


Figure 7.12 Effects of Z-axis increment on microhardness.

The major difference of the parts processed at different Z-axis increments was the density. As discussed in Section 7.3.2.2, the parts processed at larger Z-axis increment had more pores than those processed at smaller Z-axis increment. Since the microhardness tests were conducted on the areas free from pores, the microhardness

was slightly affected by the pores of the parts, thus being slightly affected by Z-axis increment. The TiB-TMCs exhibited higher microhardness than CP-Ti parts did, which indicated a positive influence of TiB reinforcement on microhardness.

### 7.3.2.5 Effects on compressive properties

Compressive tests were performed to investigate the effects of input fabrication variables and TiB reinforcement on compressive properties and fracture features of TiB-TMCs and CP-Ti parts. Figure 7.13 shows the compressive true stress-strain curves of TiB-TMCs and CP-Ti parts processed at 125 W and 200 W laser power. The Z-axis increment was fixed at 0.42 mm. In general, the true stress increased rapidly at the beginning, and then slowly increased until reaching the maximum ultimate compressive strength (UCS). Afterwards, the true stress dropped with the increase of true strain until fracture occurred.

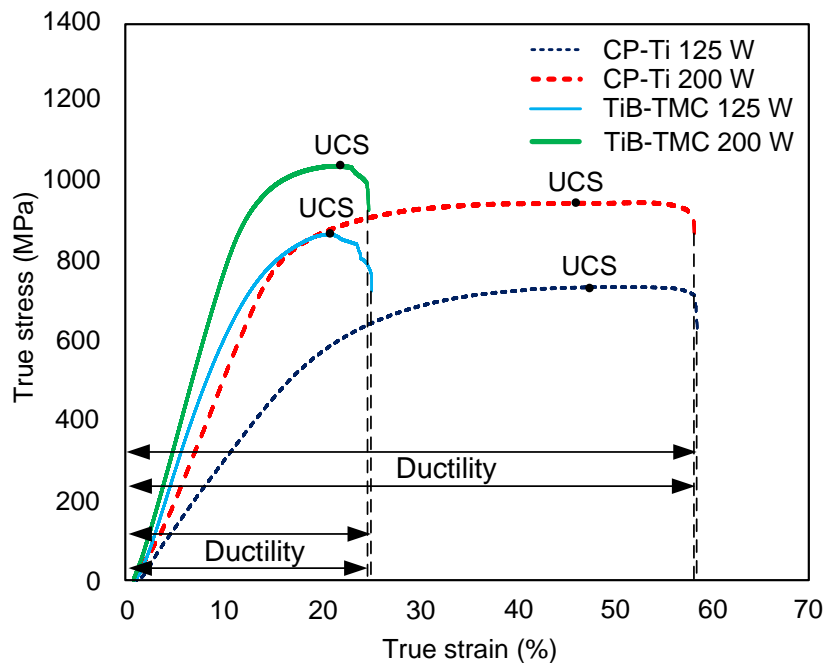


Figure 7.13 Compressive true stress-strain curves of TiB-TMCs and CP-Ti parts processed at different laser power.

It can be seen that CP-Ti parts processed at 200 W exhibited larger UCS than those processed at 125 W. This could be ascribed to the fact that higher laser power

led to higher density, greater grain refinement, and larger residual stress, resulting in the increase of UCS [33,34]. The ductility of the parts processed at 200 W was similar to those processed at 125 W. This was due to the following reasons: (1) The greater grain refinement and larger residual stress induced by the increased laser power would slightly affect the ductility of CP-Ti parts [37]; and (2) The ductility was not susceptible to the pores inside the fabricated parts, therefore, the ductility would not be significantly influenced by the density change caused by the laser power change [23]. Similarly, the TiB-TMCs processed at 200 W showed larger UCS but similar ductility, as compared with TiB-TMCs processed at 125 W.

The UCS of TiB-TMC was much larger than that of CP-Ti part processed under the same laser power. The improvement of UCS was mainly attributed to the presence of rigid TiB reinforcement. The ductility of TiB-TMC was smaller than that of CP-Ti part. The existence of brittle TiB reinforcement in TMC led to the decreased ductility of the composite material. The effects of Z-axis increment on compressive properties were negligible.

During compressive tests, both TiB-TMCs and CP-Ti parts were broken into two or more fragments, leaving different features on fracture surfaces, as shown in Figure 7.14. Both CP-Ti parts and TiB-TMCs were processed at 200 W laser power and 0.42 mm Z-axis increment. For CP-Ti parts, as shown in Figures 7.14(a) and 7.14(b), the ductile fracture features prevailed with smooth fracture facets. The flat fracture surface indicated a linear crack path through this surface during the splitting of the CP-Ti part. Therefore, it can be concluded that under this combination of input fabrication variables, the fabricated CP-Ti part exhibited ductile fracture features with high ductility (as shown in Figure 7.13). For TiB-TMCs, as shown in Figures 7.14(c) and 7.14(d), the brittle fracture features dominated with dimples and tearing-ridge lines. The relatively rough surface indicated a rugged nonlinear crack path through this surface during splitting of the TiB-TMCs. It was reported that during deformation, due to the high stress induced by reinforcement, the load would transfer from the matrix to the reinforcement. Then, the premature fracture began from these brittle TiB particles,

following by coalescence of micro-cracks, and ended in the failure of the part [23]. Since in-situ processed composites had strong interfacial bonding, the dislocations hardly occurred at the interfaces between reinforcement and matrix [38].

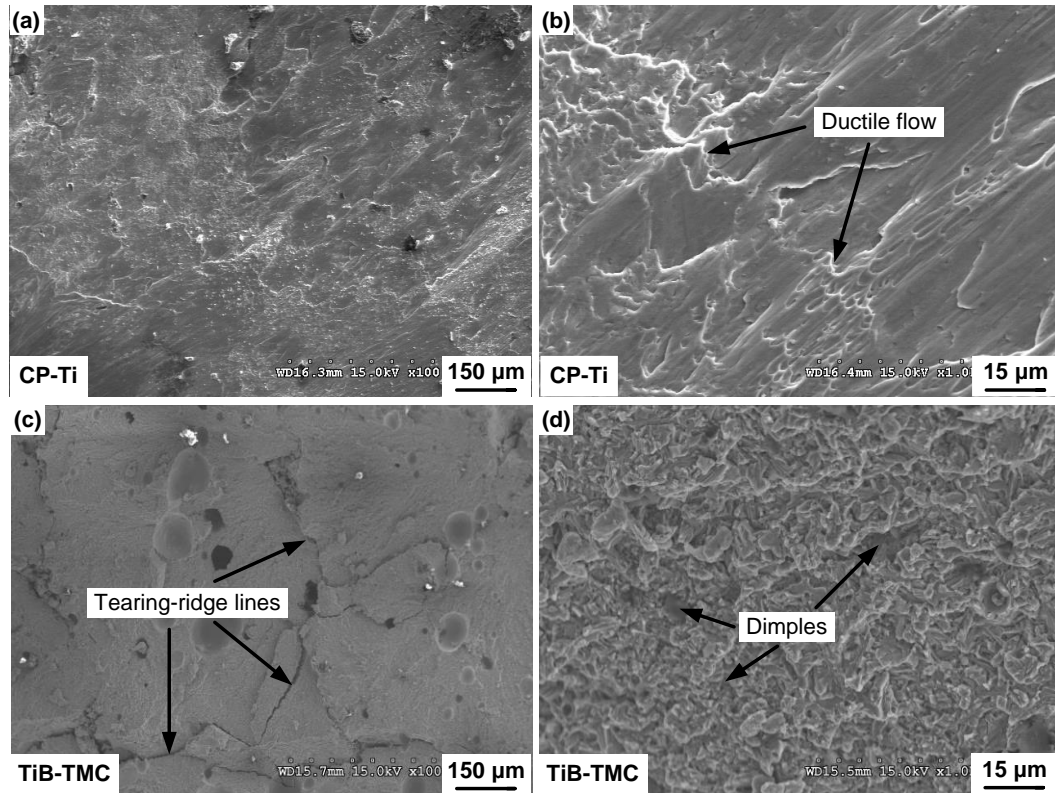


Figure 7.14 Fracture features: (a) CP-Ti part at lower magnification; (b) CP-Ti part at higher magnification; (c) TiB-TMC at lower magnification; and (d) TiB-TMC at higher magnification.

## 7.4 Conclusions

In this investigation, bulk TiB-TMCs and CP-Ti parts were fabricated by in-situ LD-AM process. Tomography analysis demonstrated the growth of TiB and its spatial distribution within Ti matrix. The effects of input fabrication variables (including laser power and Z-axis increment) on part performance (including density, microhardness, and compressive properties) were studied. Major conclusions of this investigation are drawn below:

(1) The exothermic reaction between Ti and B could assist LD-AM process in two aspects: Firstly, the TiB-TMCs were in-situ, instead of ex-situ, fabricated and the in-situ processed TiB-TMCs demonstrated strong interfacial bonding; Secondly, the energy released during the reaction was utilized to facilitate melting process.

(2) As a result of reaction, a flower-likier microstructure was formed with TiB reinforcement being embedded into the Ti matrix. The newly formed TiB particles exhibited a long prismatic shape with a high aspect ratio.

(3) The densities increased with the increase of laser power and the decrease of Z-axis increment. By increasing laser power and decreasing Z-axis increment, almost fully dense parts could be produced. The difference of densities between TiB-TMCs and CP-Ti parts was mainly attributed to the combined action of laser absorption, reaction induced pores, and reaction generated energy.

(4) For both TiB-TMCs and CP-Ti parts, the microhardness increased with the increase of laser power but slightly changed with the increase of Z-axis increment. Due to the exhibition of hard TiB reinforcement, the microhardness of TiB-TMCs was higher than that of CP-Ti parts.

(5) With the laser power increasing, the UCS increased but ductility slightly changed. Z-axis increment had negligible effects on compressive properties. The presence of the rigid TiB reinforcement led to the increase of UCS but decrease of ductility. SEM imaging analysis was conducted on the fracture surfaces of CP-Ti parts and TiB-TMCs. For CP-Ti parts, the ductile fracture features prevailed with smooth fracture facets. For TiB-TMCs, the brittle fracture features dominated with dimples and tearing ridge lines.

## References

- [1] Laoui, T., Santos, E., Osakada, K., Shiomi, M., Morita, M., Shaik, S. K., Tolochko, N. K., Abe, F., & Takahashi, M. (2006). Properties of titanium dental implant models made by laser processing. *Proceedings of the Institution of Mechanical Engineers, Part C: Journal of Mechanical Engineering Science*, 220(6), 857-863.
- [2] Spowart, J. E., & Clyne, T. W. (1999). The axial compressive failure of titanium reinforced with silicon carbide monofilaments. *Acta Materialia*, 47(2), 671-687.
- [3] Hu, Y. B., Zhao, B., Ning, F. D., Wang, H., & Cong, W. L. (2017). In-situ ultrafine three-dimensional quasi-continuous network microstructural TiB reinforced titanium matrix composites fabrication using laser engineered net shaping. *Materials Letters*, 195, 116-119.
- [4] Tamirisakandala, S., Miracle, D. B., Srinivasan, R., & Gunasekera, J. S., (2006). Titanium alloyed with boron. *Advanced Materials and Processes*, 164(12), 41-43.
- [5] Attar, H., Prashanth, K. G., Zhang, L. C., Calin, M., Okulov, I. V., Scudino, S., Yang, C., & Eckert, J. (2015). Effect of powder particle shape on the properties of in situ Ti-TiB composite materials produced by selective laser melting. *Journal of Materials Science & Technology*, 31(10), 1001-1005.
- [6] Gorse, S., Le Petitcorps, Y., Matar, S., & Rebillat, F. (2003). Investigation of the Young's modulus of TiB needles in situ produced in titanium matrix composite. *Materials Science and Engineering: A*, 340(1), 80-87.
- [7] Banerjee, R., Collins, P. C., Genc, A., & Fraser, H. L. (2003). Direct laser deposition of in situ Ti-6Al-4V-TiB composites. *Materials Science and Engineering: A*, 358(1), 343-349.
- [8] Liu, W., & DuPont, J. N. (2003). Fabrication of functionally graded TiC/Ti composites by laser engineered net shaping. *Scripta Materialia*, 48(9), 1337-1342.
- [9] Emamian, A., Corbin, S. F., & Khajepour, A. In-Situ formation of TiC using laser cladding. Eustathopoulos, N., Nicholas, M. G., & Drevet, B. (Eds.). (1999). *Wettability at high temperatures (Vol. 3)*. Elsevier.
- [10] Balla, V. K., Bhat, A., Bose, S., & Bandyopadhyay, A. (2012). Laser processed TiN reinforced Ti6Al4V composite coatings. *Journal of the Mechanical Behavior of Biomedical Materials*, 6, 9-20.
- [11] Poletti, C., Balog, M., Schubert, T., Liedtke, V., & Edtmaier, C. (2008). Production of titanium matrix composites reinforced with SiC particles. *Composites Science and Technology*, 68(9), 2171-2177.
- [12] Vreeling, J. A., Ocelik, V., & De Hosson, J. T. M. (2002). Ti6Al4V strengthened by laser melt injection of WCp particles. *Acta Materialia*, 50(19), 4913-4924.
- [13] Kim, I. Y., Choi, B. J., Kim, Y. J., & Lee, Y. Z. (2011). Friction and wear behavior of titanium matrix (TiB+TiC) composites. *Wear*, 271(9), 1962-1965.
- [14] Hu, Y. B., Wang, H., Ning, F. D., & Cong, W. L. (2016). Laser engineered net shaping of commercially pure titanium: Effects of fabricating variables. In

- ASME 2016 11th International Manufacturing Science and Engineering Conference, pp. V001T02A035-V001T02A035.
- [15] Balla, V. K., DeVasConCellos, P. D., Xue, W., Bose, S., & Bandyopadhyay, A. (2009). Fabrication of compositionally and structurally graded Ti-TiO<sub>2</sub> structures using laser engineered net shaping (LENS). *Acta Biomaterialia*, 5(5), 1831-1837.
  - [16] Wang, X. L., Deng, D. W., Qi, M., & Zhang, H. C. (2016). Influences of deposition strategies and oblique angle on properties of AISI316L stainless steel oblique thin-walled part by direct laser fabrication. *Optics & Laser Technology*, 80, 138-144.
  - [17] Ning, F. D., Cong, W. L., Hu, Y. B., & Wang, H. (2016). Additive manufacturing of carbon fiber-reinforced plastic composites using fused deposition modeling: Effects of process parameters on tensile properties. *Journal of Composite Materials*, 51(4), 451-462.
  - [18] Gu, D. D., Meiners, W., Wissenbach, K., & Poprawe, R. (2012). Laser additive manufacturing of metallic components: materials, processes and mechanisms. *International Materials Reviews*, 57(3), 133-164.
  - [19] Ning, F. D., & Cong, W. L. (2016). Microstructures and mechanical properties of Fe-Cr stainless steel parts fabricated by ultrasonic vibration-assisted laser engineered net shaping process. *Materials Letters*, 179, 61-64.
  - [20] Li, Y. Z., Hu, Y. B., Cong, W. L., Zhi, L., & Guo, Z. N. (2017). Additive manufacturing of alumina using laser engineered net shaping: Effects of deposition variables. *Ceramics International*, 43(10), 7768-7775.
  - [21] Banerjee, R., Collins, P. C., & Fraser, H. L. (2002). Laser deposition of in situ Ti-TiB composites. *Advanced Engineering Materials*, 4(11), 847-851.
  - [22] DuttaMajumdar, J., & Li, L. (2010). Development of titanium boride (TiB) dispersed titanium (Ti) matrix composite by direct laser cladding. *Materials Letters*, 64(9), 1010-1012.
  - [23] Attar, H., Bönisch, M., Calin, M., Zhang, L. C., Scudino, S., & Eckert, J. (2014). Selective laser melting of in situ titanium-titanium boride composites: processing, microstructure and mechanical properties. *Acta Materialia*, 76, 13-22.
  - [24] Niu, H. J., & Chang, I. T. H. (1999). Selective laser sintering of gas and water atomized high speed steel powders. *Scripta Materialia*, 41(1), 25-30.
  - [25] Ning, F. D., Hu, Y. B., Liu, Z. C., Cong, W. L., Li, Y. Z., & Wang, X. L. (2017). Ultrasonic vibration-assisted laser engineered net shaping of Inconel 718 parts: a feasibility study. 45th SME North American Manufacturing Research Conference, June 4-8, 2017, Los Angeles, CA, USA.
  - [26] Panda, K. B., & Chandran, K. R. (2003). Synthesis of ductile titanium-titanium boride (Ti-TiB) composites with a beta-titanium matrix: The nature of TiB formation and composite properties. *Metallurgical and Materials Transactions A*, 34(6), 1371-1385.
  - [27] Barin, I. (1997). *Thermochemical Data of Pure Substances*, Thermochemical Data of Pure Substances. Wiley-VCH.

- [28] Hu, Y. B., Ning, F. D., Wang, X. L., Wang, H., Cong, W. L., & Li, Y. Z. (2017). Laser deposition-additive manufacturing of in-situ TiB reinforced titanium matrix composites: TiB growth and part performance. *The International Journal of Advanced Manufacturing Technology*. Doi:10.1007/s00170-017-0769-0.
- [29] Decker, B. F., & Kasper, J. S. (1954). The crystal structure of TiB. *Acta Crystallographica*, 7(1), 77-80.
- [30] Lu, W. J., Xiao, L., Geng, K., Qin, J. N., & Zhang, D. (2008). Growth mechanism of in situ synthesized TiBw in titanium matrix composites prepared by common casting technique. *Materials Characterization*, 59(7), 912-919.
- [31] Chandrasekar, P., Balusamy, V., Chandran, K. R., & Kumar, H. (2007). Laser surface hardening of titanium-titanium boride (Ti-TiB) metal matrix composite. *Scripta Materialia*, 56(7), 641-644.
- [32] Safari, A. (2001). Processing of advanced electroceramic components by fused deposition technique. *Ferroelectrics*, 263(1), 45-54.
- [33] Tolochko, N. K., Khlopkov, Y. V., Mozzharov, S. E., Ignatiev, M. B., Laoui, T., & Titov, V. I. (2000). Absorptance of powder materials suitable for laser sintering. *Rapid Prototyping Journal*, 6(3), 155-161.
- [34] Song, B., Dong, S. J., Zhang, B. C., Liao, H. L., & Coddet, C. (2012). Effects of processing parameters on microstructure and mechanical property of selective laser melted Ti6Al4V. *Materials & Design*, 35, 120-125.
- [35] Lin, Y. H., Lei, Y. P., Fu, H., & Lin, J. (2015). Mechanical properties and toughening mechanism of TiB<sub>2</sub>/NiTi reinforced titanium matrix composite coating by laser cladding. *Materials & Design*, 80, 82-88.
- [36] Meng, Q. C., Feng, H. B., Chen, G. C., Yu, R. H., Jia, D. C., & Zhou, Y. (2009). Defects formation of the in situ reaction synthesized TiB whiskers. *Journal of Crystal Growth*, 311(6), 1612-1615.
- [37] Quan, Y. J., Chen, Z. H., Gong, X. S., & Yu, Z. H. (2008). Effects of heat input on microstructure and tensile properties of laser welded magnesium alloy AZ31. *Materials Characterization*, 59(10), 1491-1497.
- [38] Huang, L. J., Geng, L., & Peng, H. X. (2015). Microstructurally inhomogeneous composites: Is a homogeneous reinforcement distribution optimal?. *Progress in Materials Science*, 71, 93-168.

## CHAPTER VIII

### LENS OF TiB-TMCS – IN-SITU ULTRAFINE 3DQCN MICROSTRUCTURE

Paper title:

In-situ ultrafine three-dimensional quasi-continuous network microstructural TiB reinforced titanium matrix composites fabrication using laser engineered net shaping

Published in:

Materials Letters, Vol. 195, pp. 116-119

Authors' names:

Yingbin Hu<sup>a</sup>, Bo Zhao<sup>b</sup>, Fuda Ning<sup>a</sup>, Hui Wang<sup>a</sup>, and Weilong Cong<sup>a,\*</sup>

Authors' affiliations:

<sup>a</sup>Department of Industrial, Manufacturing, & Systems Engineering, Texas Tech University, Lubbock, Texas, 79409, USA

<sup>b</sup>College of Arts & Sciences Microscopy, Texas Tech University, Lubbock, TX 79409, USA

\*Corresponding author:

Department of Industrial, Manufacturing, & Systems Engineering, Texas Tech University, Lubbock, TX 79409-3061, USA. Email address: weilong.cong@ttu.edu

## **Abstract**

In this study, we created an innovative ultrafine three-dimensional quasi-continuous network (3DQCN) microstructure by in-situ laser engineered net shaping (LENS) of TiB reinforced titanium matrix composites (TiB-TMCs). As a rapid solidification process, the LENS process enabled high degree of Ti grain refinement. The in-situ processed eutectic TiB aggregated at these Ti grain boundaries, forming the ultrafine 3DQCN microstructure. The microstructural characterizations of the ultrafine 3DQCN microstructure were investigated. Effects of the TiB reinforcement and the ultrafine 3DQCN microstructure on the mechanical performance of the fabricated parts were studied. The results demonstrated that the TiB-TMCs with the ultrafine 3DQCN microstructure exhibited superior mechanical properties.

## **Keywords**

Titanium alloys; Metallic composites; Laser processing; Grain refinement; Grain boundaries

## **8.1 Introduction**

The low hardness and poor wear resistance of Ti and its alloys greatly restricted their wide applications under severe friction and wear conditions [1]. Fabrication of ceramic reinforced Ti matrix composites (TMCs) became a great solution to the problem above. Traditional ceramic reinforced TMCs manufacturing processes had high energy consumption and shape-restriction shortcomings [2-5]. In response to these problems, laser additive manufacturing technologies, mainly including selective laser melting (SLM) and laser engineered net shaping (LENS), were developed to produce ceramic reinforced TMCs [6-10]. Compared with SLM process, LENS process exhibited more advantages, such as capability of producing functionally graded materials, capability of surface modification, and small substrate deformation [8-10]. Therefore, LENS process was widely utilized to produce ceramic reinforced TMCs with superior mechanical properties over Ti.

Among different kinds of ceramic reinforcement materials (e.g. carbide [1,2], nitride [2,3], boride [2,4,6], etc.), TiB was considered as an ideal reinforcement that

showed more specific advantages: (1) Reinforcement was chemically compatible with matrix [2]; (2) The similar densities and thermal expansion coefficients between TiB and Ti could reduce or even eliminate residual stresses at reinforcement-matrix interfaces [5]; and (3) A relatively small amount of reinforcement could largely increase the composites' modulus and strength [5]. Despite the improvements exhibited by LENS processed TiB reinforced TMCs (TiB-TMCs), problems resulted from lowered fracture toughness and ductility still existed [2].

In this investigation, innovative ultrafine three-dimensional quasi-continuous network (3DQCN) microstructural TiB-TMCs were successfully fabricated for the first time by in-situ LENS process. It was reported that the generation of 3DQCN microstructure could improve fracture toughness [4]. The specific 3D microstructure enabled isotropic reinforcement in all directions and was beneficial to uniformly load transferring and distributing [2]. Thus, in this work, formation mechanism of the ultrafine 3DQCN will be investigated. In addition, effects of ultrafine 3DQCN and TiB reinforcement on the mechanical performance of the fabricated parts will be evaluated.

## **8.2 Experiments and measurements procedures**

The bulk parts were fabricated by an Optomec LENS system. Based on preliminary results, the powder feeding rate, deposition head scanning speed, layer thickness, and hatch distance were fixed at optimal values of 0.028 g/s, 11 mm/s, 0.42 mm, and 0.38 mm, respectively. Two levels of laser power (125 W and 200 W) were selected for comparisons. The parts with dimensions of 8 mm × 8 mm × 20 layers were for microhardness test and those with dimensions of  $\Phi$ 6 mm × 15 layers were for compressive test.

The CP-Ti powders with the average particle size of 150  $\mu$ m and B powders with the average particle size of 2  $\mu$ m were used. For TiB-TMCs fabrication, the weight ratio of 98.4 : 1.6 between Ti and B powders was adopted for the purpose of generating eutectic TiB whiskers, being beneficial to fracture toughness and bending

strength [5]. Prior to LENS process, the CP-Ti and B powders were mixed by planetary ball mill machine at rotation speed of 200 rpm, ball-to-powder weight ratio of 5:1, and milling time of four hours, in order to well distribute B powders into Ti powders without significant size reduction and Ti-B reaction.

Microstructure characterizations of the fabricated parts were observed using the scanning electron microscope (SEM), integrated with an electron backscatter diffraction (EBSD) detector. Before observation, the parts were etched with Kroll's Reagent (HF: 3%; HNO<sub>3</sub>: 6%; and water: balance) for ten seconds.

Microhardness tests were performed on a Vickers hardness tester with 9.8 N load and ten seconds dwelling time. Ten measurements were conducted on each part. For each kind of fabrication condition, compressive tests were conducted four times at a constant cross-head speed of 0.005 mm/s by using a tensile tester.

### **8.3 Experiment Result and Discussion**

#### **8.3.1 Formation mechanisms**

The 3DQCN microstructure was reported in fabrication by reactive hot pressing (RHP, sintering) [2,4,5] and casting [3]. In RHP process, as illustrated in Figure 8.1(a), Ti particles and relatively finer TiB<sub>2</sub> particles (for providing B element) were premixed to make the rigid TiB<sub>2</sub> particles embedded onto the outside surfaces of Ti particles [2]. With the sintering process of RHP, outer boundaries of Ti particles were melted, generating atomic bonding to join Ti particles together. In the meantime, the chemical reaction between Ti and TiB<sub>2</sub> ( $\text{Ti} + \text{TiB}_2 \rightarrow 2\text{TiB}$ ) took place at the boundaries of Ti particles and generated TiB [11]. The TiB whiskers formed, grew, and connected at most boundaries of Ti particles, forming 3DQCN microstructure. The unit size, which was around 50 – 200 μm, and the shape of the network microstructure were determined by the original Ti particles [4].

The formation mechanism of 3DQCN microstructure in casting process, as shown in Figure 8.1(b), was different from that in RHP (sintering) process. In casting process, the premixed Ti and B powders were fully melted and reacted for formation

of TiB [12]. During solidification,  $\beta$ Ti nuclei were firstly formed/separated from the liquid and then grown into crystal grains. On account of extremely low solid solubility of B in Ti matrix, the newly formed TiB was expelled from  $\beta$ Ti nuclei to the surrounding liquid, aggregating at the boundaries of Ti crystal grains [12]. Due to long-time crystallization, the slow casting solidification process resulted in relatively large 3DQCN unit sizes of around 100 – 200  $\mu\text{m}$  [3].

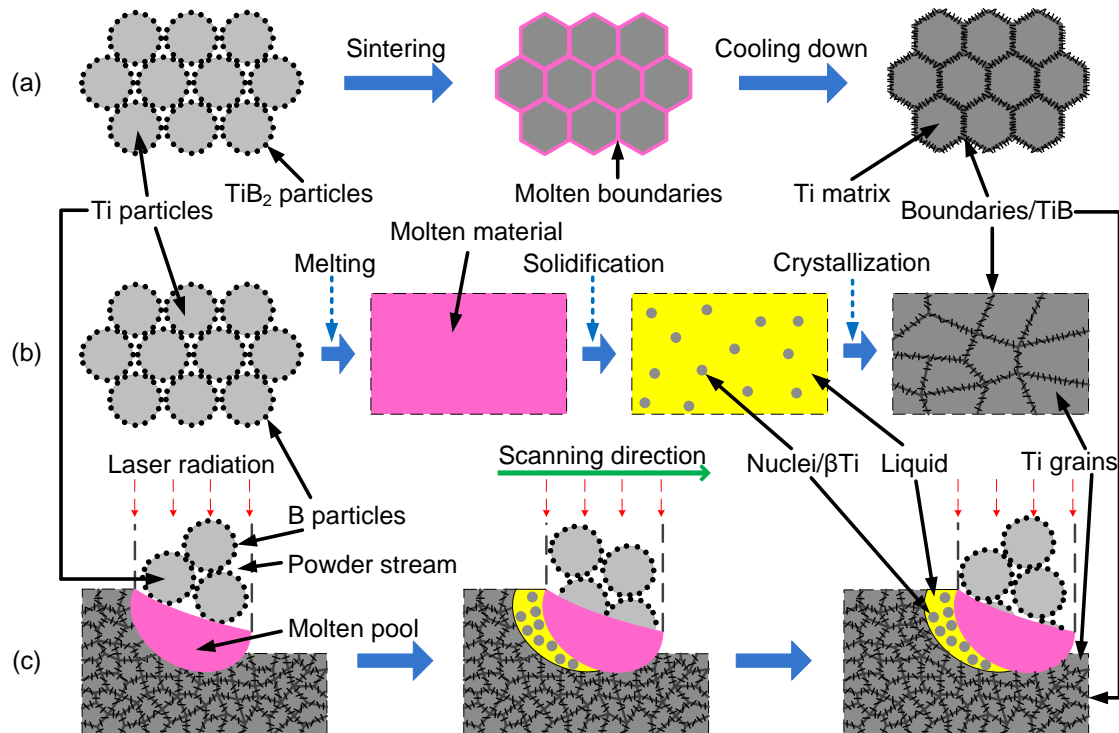


Figure 8.1 Formation mechanisms of 3DQCN microstructure in (a) RHP (sintering), (b) casting, and (c) LENS processes.

The aforementioned conventional processes (e.g. RHP and casting) fabricated parts exhibited worse reinforcement aggregation uniformity and coarser microstructure [5]. It was reported that grain refinement would significantly enhance strength and toughness [5]. In this investigation, a refined 3DQCN microstructure was successfully formed by in-situ LENS process. Figure 8.1(c) shows the formation mechanism of 3DQCN microstructure in LENS process. With the small-size laser spot, the molten pool formed could be finely controlled, resulting in uniform

distributions of energy input and B element. Similar to casting process, the premixed Ti and B powders were fully melted in the molten pool due to laser radiation in LENS process. McCartney et al. [13] reported that the rapid solidification processes would cause a significant reduction in grain size. As a rapid solidification process, the LENS process enabled high undercooling degree, leading to an increased nucleation rate and more nuclei [13]. Since each nucleus would grow into one grain, a great amount of Ti grains with ultrafine grain size could be expected.

### 8.3.2 Microstructural characterizations

Figure 8.2 shows a stereo corner image taken from a fabricated part and corresponding microstructures on each side of the corner. Similar network-microstructure morphologies can be observed for all three sides. The QCN microstructure, forming along the Ti grain boundaries, was spatially distributed as a 3DQCN microstructure. The bright boundaries were identified by EBSD as orthorhombic TiB with Pearson symbol  $oP8$ , spacegroup  $Pnma$ , No. 62. Compared with RHP and casting processes, the unit size of LENS processed 3DQCN microstructure was extremely smaller ( $50 - 200 \mu\text{m}$  v.s.  $3 - 5 \mu\text{m}$ ). Besides rapid

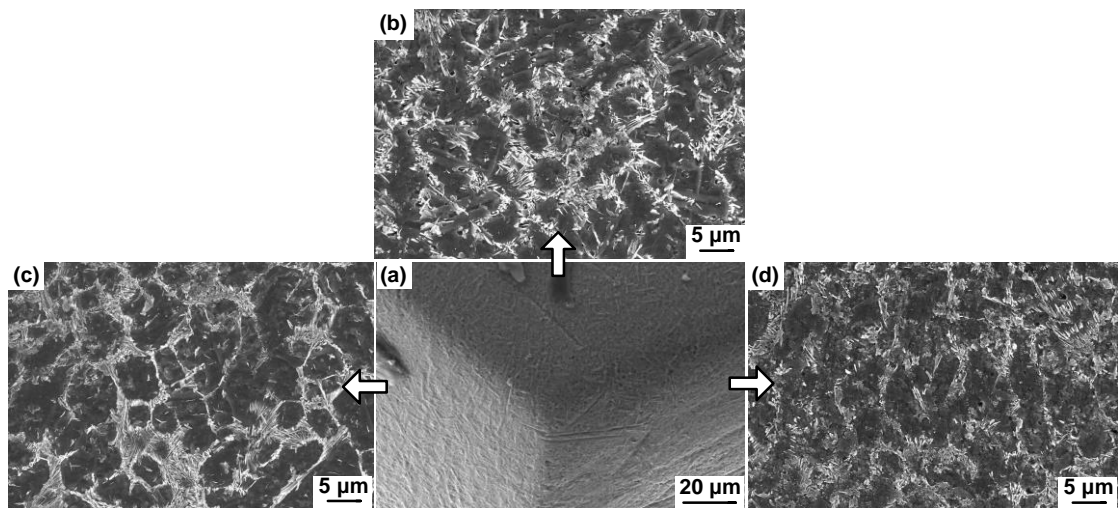


Figure 8.2 SEM observations of ultrafine 3DQCN microstructure: (a) The stereo corner taken from the fabricated parts; Detailed microstructure of (b) top side, (c) left side, and (d) right side.

solidification, the ultrafine unit sizes of the network microstructure could also be ascribed to the Ti grain refinement caused by TiB generation [5]. It can be considered that an ultrafine 3DQCN microstructure could be created by exploiting LENS process. The reduced unit size of 3DQCN microstructure would lead to the enhancement of strength and toughness [5].

Figure 8.3(a) and 8.3(b) show the microstructure characterizations of the parts processed at laser power of 125 W. The random and non-uniform distribution of TiB (TiB-deficient regions) in the Ti matrix, as illustrated in Figure 8.3(a) and 8.3(b), could be partially ascribed to the poor flowability, leaving no enough time for TiB to form the 3DQCN microstructure. The size of TiB ranged from nanometers to micrometers. As illustrated in Figure 8.3(b), both primary TiB and eutectic TiB were

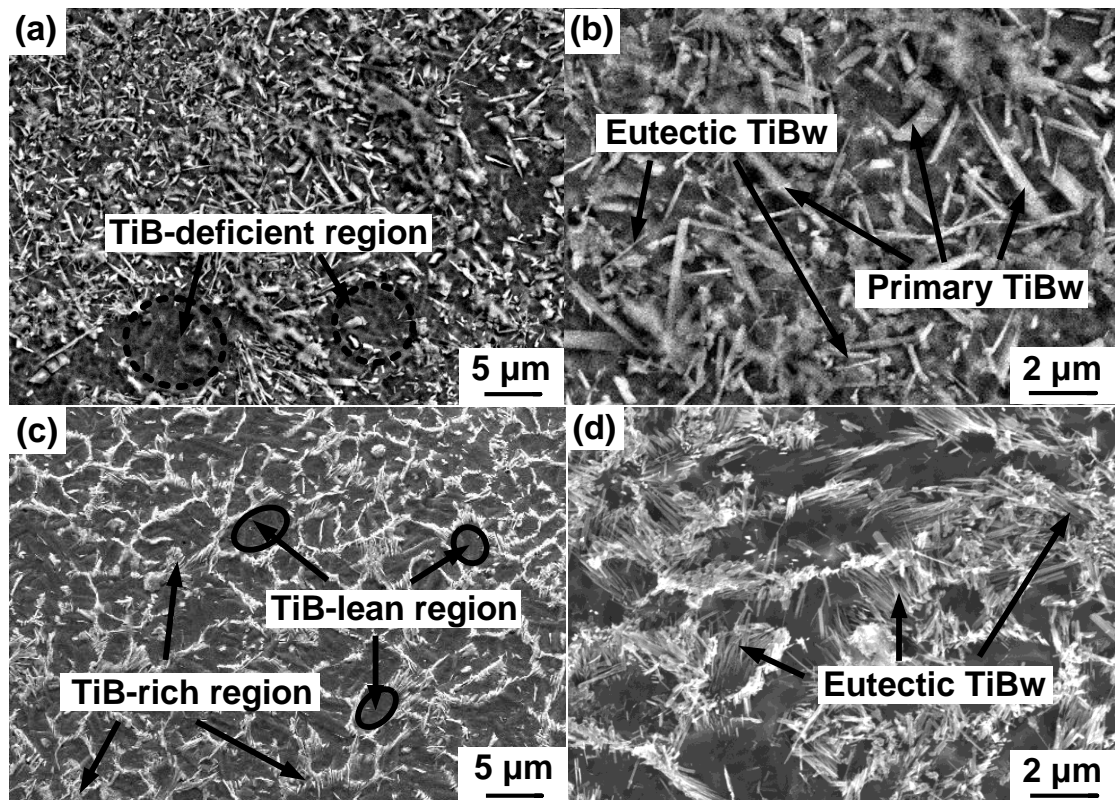


Figure 8.3 SEM observations of TiB-TMCs microstructure characterizations: Processed at 125 W laser power at (a) low and (b) high magnifications; Processed at 200 W laser power at (c) low and (d) high magnifications.

formed, and the primary TiB took up a great proportion. Figure 8.3(c) and 8.3(d) show the characterizations of ultrafine 3DQCN microstructure processed at 200 W laser power. The energy induced by 200 W laser power was high enough to form the ultrafine 3DQCN microstructure, with TiB rich in some regions but lean in the other regions. By successfully forming the TiB-lean regions for the TiB-TMCs, the fracture toughness and ductility of the fabricated parts could be improved [2]. In the meantime, the exhibition of strong TiB-rich regions would contribute to strengthening effect of the TiB-TMCs. Figure 8.3(d) shows the needle-like nano-sized eutectic TiB as a result of eutectic solidification. The fine eutectic TiB was superior to coarse primary TiB since the effects of eutectic TiB were not as adverse as the effects of primary TiB on the fracture-sensitive mechanical properties [14]. Traversing across grain boundaries, the TiB connected neighbouring Ti grains and reinforced Ti grain boundaries [2].

### 8.3.3 Mechanical properties

Table 8.1 shows the comparisons of the microhardness and compressive properties between TiB-TMCs and CP-Ti parts fabricated at different laser powers. At laser power of 125 W, 3DQCN microstructure was not formed in the fabricated TiB-TMCs. Compared with CP-Ti parts, TiB-TMCs led to higher microhardness and ultimate compressive strength (UCS) at the expense of ductility (maximum strain). The improvement of microhardness and UCS could be attributed to the newly generated TiB phase and the refinement of Ti grains induced by TiB phase. “Brittleness” effect caused by ceramic TiB phase was the main reason for the decrease of ductility [2]. By increasing laser power to 200 W, the TiB-TMCs with ultrafine 3DQCN microstructure exhibited larger microhardness, UCS, and ductility than that

Table 8.1 Comparisons of the microhardness and compressive properties

Materials	Laser power (W)	3DQCN microstructure	Microhardness (HV <sub>1.0</sub> )	UCS (MPa)	Max. strain (%)
CP-Ti	125	Without	304 ± 10	761 ± 96	64.9 ± 3.2
TiB-TMCs	125	Without	339 ± 9	884 ± 41	20.8 ± 2.1
TiB-TMCs	200	With	393 ± 9	1051 ± 28	26.2 ± 0.7

without 3DQCN fabricated at 125 W. The existence of the ductile TiB-lean phase in the ultrafine 3DQCN microstructure processed at 200 W contributed to the improvement of ductility.

#### **8.4 Conclusions**

This investigation provided an innovative way to form ultrafine 3DQCN microstructure by in-situ LENS of TiB-TMCs. Laser power had a great impact on the formation of the ultrafine 3DQCN microstructure, and not all laser powers would generate such microstructure. As a result of strengthening effect of adding ceramic TiB reinforcement, the values of microhardness and UCS of TiB-TMCs were much higher than those of CP-Ti parts processed at the same laser power. In TiB-TMCs fabrication, increased portion of needle-like nano-sized eutectic TiB as well as improved part quality led to microhardness and UCS enhancement with laser power increasing.

## References

- [1] Candel, J. J., Amigó, V., Ramos, J. A., & Busquets, D. (2010). Sliding wear resistance of TiCp reinforced titanium composite coating produced by laser cladding. *Surface and Coatings Technology*, 204(20), 3161-3166.
- [2] Huang, L. J., Geng, L., & Peng, H. X. (2015). Microstructurally inhomogeneous composites: is a homogeneous reinforcement distribution optimal?. *Progress in Materials Science*, 71, 93-168.
- [3] Morikawa, D., Ramkumar, J., Mabuchi, H., Tsuda, H., Matsui, T., & Morii, K. (2002). Microstructure and mechanical properties of Ti-BN cast alloys prepared by reactive arc-melting. *Materials Transactions*, 43(9), 2193-2196.
- [4] Huang, L. J., Wang, S., Dong, Y. S., Zhang, Y. Z., Pan, F., Geng, L., & Peng, H. X. (2012). Tailoring a novel network reinforcement architecture exploiting superior tensile properties of in situ TiBw/Ti composites. *Materials Science and Engineering: A*, 545, 187-193.
- [5] Tamirisakandala, S., Miracle, D. B., Srinivasan, R., & Gunasekera, J. S. (2006). Titanium alloyed with boron. *Advanced Materials and Processes*, 164(12), 41-43.
- [6] Attar, H., Bönisch, M., Calin, M., Zhang, L. C., Scudino, S., & Eckert, J. (2014). Selective laser melting of in situ titanium-titanium boride composites: processing, microstructure and mechanical properties. *Acta Materialia*, 76, 13-22.
- [7] Liu, W. P., & DuPont, J. N. (2003). Fabrication of functionally graded TiC/Ti composites by laser engineered net shaping. *Scripta Materialia*, 48(9), 1337-1342.
- [8] Balla, V. K., Bhat, A., Bose, S., & Bandyopadhyay, A. (2012). Laser processed TiN reinforced Ti6Al4V composite coatings. *Journal of the Mechanical Behavior of Biomedical Materials*, 6, 9-20.
- [9] Hu, Y. B., Wang, H., Ning, F. D., & Cong, W. L. (2016). Laser engineered net shaping of commercially pure titanium: effects of fabricating variables. In *ASME 2016 11th International Manufacturing Science and Engineering Conference* (pp. V001T02A035-V001T02A035). American Society of Mechanical Engineers.
- [10] Ning, F. D., & Cong, W. L. (2016). Microstructures and mechanical properties of Fe-Cr stainless steel parts fabricated by ultrasonic vibration-assisted laser engineered net shaping process. *Materials Letters*, 179, 61-64.
- [11] Feng, H. B., Meng, Q. C., Zhou, Y., & Jia, D. C. (2005). Spark plasma sintering of functionally graded material in the Ti-TiB<sub>2</sub>-B system. *Materials Science and Engineering: A*, 397(1), 92-97.
- [12] Banerjee, R. (2013). Titanium boride formation and its subsequent influence on morphology and crystallography of alpha precipitates in titanium alloys (Doctoral dissertation, University Of North Texas).
- [13] McCartney, D. G. (1989). Grain refining of aluminium and its alloys using inoculants. *International Materials Reviews*, 34(1), 247-260.

- [14] Tamirisakandala, S., Bhat, R. B., Miracle, D. B., Boddapati, S., Bordia, R., Vanover, R., & Vasudevan, V. K. (2005). Effect of boron on the beta transus of Ti-6Al-4V alloy. *Scripta Materialia*, 53(2), 217-222.

## CHAPTER IX

### LENS OF TiB-TMCS – EFFECTS OF 3DQCN ON STRENGTHENING AND TOUGHENING

Paper title:

Laser deposition-additive manufacturing of TiB-Ti composites with novel three-dimensional quasi-continuous network microstructure: effects on strengthening and toughening

Published in:

Composites Part B: Engineering, Vol. 133, pp. 91-100

Authors' names:

Yingbin Hu<sup>a</sup>, Weilong Cong<sup>a,\*</sup>, Xinlin Wang<sup>a,b</sup>, Yuanchen Li<sup>a,c</sup>, Fuda Ning<sup>a</sup>, and Hui Wang<sup>a</sup>

Authors' affiliations:

<sup>a</sup>Department of Industrial, Manufacturing, & Systems Engineering, Texas Tech University, Lubbock, Texas, 79409, USA

<sup>b</sup>School of Mechanical Engineering, Dalian University of Technology, Dalian, Liaoning, 116024, China

<sup>c</sup>Key Laboratory of Mechanism Theory and Equipment Design of Ministry of Education, Tianjin University, Tianjin, 300072, China

\*Corresponding author:

Department of Industrial, Manufacturing, & Systems Engineering, Texas Tech University, Lubbock, TX 79409-3061, USA. Email address: weilong.cong@ttu.edu

## **Abstract**

Although TiB reinforced titanium matrix composites (TiB-TMCs) exhibit superior wear resistance and strength, they still demonstrate severe problems resulted from lowered toughness and ductility, as compared with titanium and its alloys. To reduce these problems, this paper tailors a three-dimensional quasi-continuous network (3DQCN) microstructure within TiB-TMCs by in-situ laser deposition-additive manufacturing process. Results show that the laser power has great impacts on the formation of 3DQCN microstructure and the 3DQCN microstructure is beneficial to both strengthening and toughening effects on TiB-TMCs. To have a quantitative understanding of strengthening effects, this paper, for the first time, has modeled the yield strength of TiB-TMCs with 3DQCN microstructure.

## **Keywords**

TiB-TMCs; Mechanical properties; Analytical modeling; Powder processing; Laser engineered net shaping

## **9.1 Introduction**

Owing to their high wear resistance and high strength at elevated temperature, titanium matrix composites (TMCs) are widely applied under severe friction and heavy load-bearing conditions [1,2]. Ceramic materials (e.g. TiB [3,4], TiN [5], TiC [6], SiC [7], etc.) reinforced TMCs have attracted a great amount of attentions and been extensively investigated. Among different types of ceramic materials, in-situ reacted TiB is considered as one of the most suitable ceramic reinforcements for TMCs. Firstly, TiB is a stable phase since there is no intermediate phase between TiB and titanium (Ti). Secondly, the metallurgical bonding between TiB and Ti is enabled by in-situ process [5]. Thirdly, TiB and Ti have similar densities and thermal expansion coefficients, therefore, thermal stresses at their interfaces can be minimized [8,9]. Fourthly, the strength of TMCs can be effectively enhanced by adding a small amount of TiB [8]. To facilitate experiments, models have been developed to predict the yield strength of metal matrix composites (MMCs) [10-12]. With improved parameters associated with the dislocation strengthening effect, Ramakrishnan

developed a model to predict the yield strength of MMCs with micro-sized reinforcement [10]. Zhang et al. extended the application of the model to nano-sized reinforcement by considering strengthening effects of nanocomposites [11]. However, Sanaty-Zadeh pointed out that not enough strengthening effects (such as grain refinement strengthening effect) were considered in these models, which affected the precision of models [12]. In addition, the effects of reinforcement shape on strengthening were not included in these models. This investigation, for the first time, quantitatively analyzes and models the strengthening effects of TiB reinforced titanium matrix composites (TiB-TMCs). The model takes both the combined effects of grain refinement strengthening, TiB strengthening, and dislocation strengthening as well as the effects of reinforcement shape (whisker) into account.

Despite the strengthening effects, TiB-TMCs demonstrate severe problems resulted from lowered toughness and ductility, as compared with Ti and its alloys [13-15]. It was reported by Attar et al. that the ductility of TiB-TMCs was only one third of that of Ti parts [16]. To reduce or eliminate these problems, Huang et al. proposed and tailored a three-dimensional quasi-continuous network (3DQCN) microstructure in TiB-TMCs using reactive hot pressing (RHP) process [17]. Compared with TiB-TMCs without 3DQCN microstructure, the TiB-TMCs with 3DQCN microstructure exhibited higher ductility. In addition, the existence of the 3DQCN microstructure could effectively restrict the formation of coarse Ti grains, thus rendering better mechanical properties. Besides RHP, Morikawa et al. also reported the 3DQCN microstructure in TiB-TMCs fabricated by casing process [18]. These traditional manufacturing processes (including RHP and casting) show disadvantages of high energy consumption and high reinforcement agglomeration [19-21]. In addition, the parts fabricated by these processes are shape-restricted and coarse-grained [22-29]. Facing to these problems, it is crucial to investigate an energy-effective, finely-controlled, and near-net-shaping manufacturing process for TiB-Ti composites. Laser additive manufacturing (LAM) is such a technology that possesses these characteristics [30-32]. Among all LAM processes, laser deposition-additive

manufacturing (LD-AM) demonstrates benefits of small substrate deformation, changeable powder mixture ratio, and controllable cooling rate [3,24,33-35]. In recent years, work has been done on LD-AM of TiB-Ti composites. However, limited investigations have been reported on conditions under which TiB-TMCs with tailored microstructures can be fabricated. This investigation provides an innovative way of forming a novel ultrafine 3DQCN microstructure inside TiB-TMCs by in-situ LD-AM process. The effects of 3DQCN microstructure on toughening has been investigated.

## **9.2 Experiments and measurements procedures**

### **9.2.1 Powder materials and powder treatment**

The commercially pure Ti (CP-Ti) powder (Atlantic Equipment Engineers Inc., Upper Saddle River, NJ, USA) used in this investigation had an average particle size of 150  $\mu\text{m}$  and a purity of 99.7%. The boron (B) powder (Chemsavers, Inc., Bluefield, WV, USA) had an average particle size of 2  $\mu\text{m}$  and a purity of 96%. It was reported that the eutectic solidification would occur with the generation of fine-eutectic TiB reinforcement when the B content was 1.6 wt.% [3,16]. Compared with the coarse-primary TiB reinforcement, the fine-eutectic TiB reinforcement was more beneficial to the strengthening and toughening effects on TMCs [3,9]. Therefore, the weight ratio of 98.4 : 1.6 between Ti and B powders was adopted. To well mix CP-Ti and B powders, a planetary ball milling machine (ND2L, Torrey Hills Technologies LLC., San Diego, CA, USA) was utilized with the parameters of: ball-to-powder weight ratio of 5:1; fixed rotation speed of 200 rpm; and milling time of four hours. Figure 9.1 shows the planetary ball milling process. At the beginning, the as-received CP-Ti powder (Figure 9.1(a)) and B powder (Figure 9.1(b)) were placed into milling bowls (Figure 9.1(c)). To keep balance, four milling bowls were symmetrically distributed on the sun wheel. During ball milling process, the milling bowls and the sun wheel rotated in opposite directions. The milling balls and the powders would alternately roll on the milling bowls' inner walls and strike the opposite sides of the walls [36,37]. It can be seen from Figure 9.1(d) that after the ball milling process, the CP-Ti powder was more spherical in shape and more uniform in size, as compared with as-received CP-Ti

powder. In addition, the B powder was well embedded onto the surface of the CP-Ti powder, as shown in Figure 9.1(e).

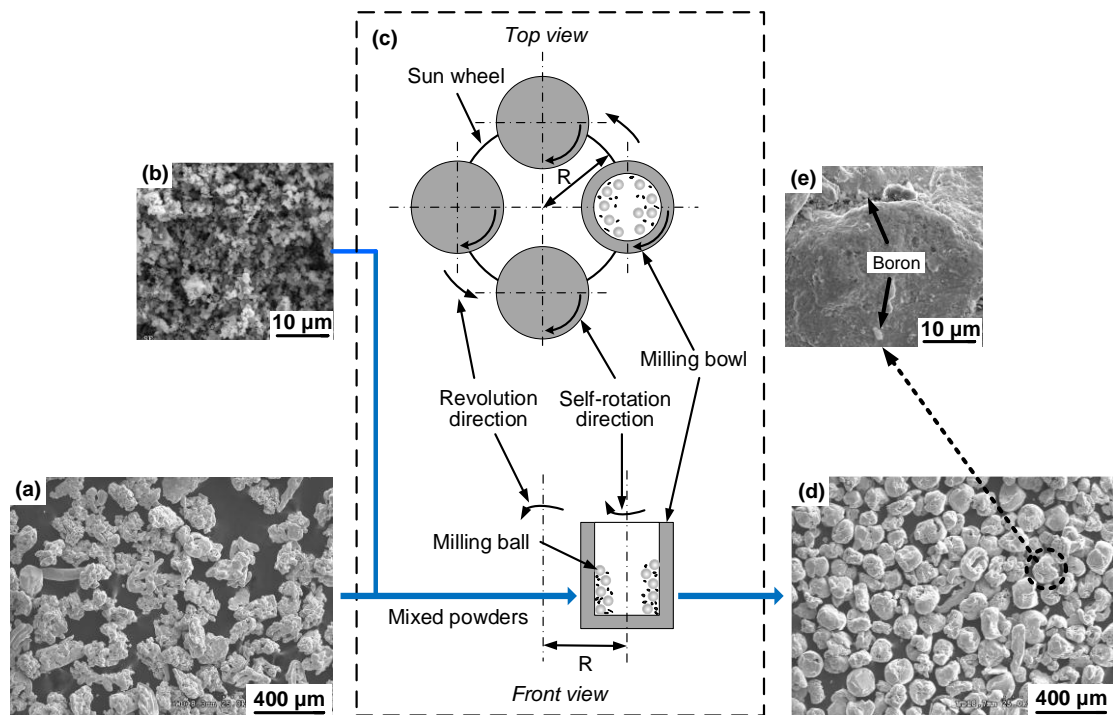


Figure 9.1 Planetary ball milling process. (a) As-received CP-Ti powder; (b) As-received B powder; (c) Schematic illustration of ball milling process; (d) Four-hour ball milling mixed CP-Ti and B powders; and (e) High-magnification of a single CP-Ti particle with B particles embedded on the surface.

### 9.2.2 Experimental set-up and experimental conditions

In this investigation, the LD-AM process was carried out by a laser engineered net shaping (LENS) machine (450, Optomec Inc., Albuquerque, NM, USA). As illustrated in Figure 9.2, the LENS machine comprised four major systems: laser system (with a standard IPG fiber laser), chamber system, powder and inert gas delivery system, and control system. To prevent Ti from being oxidized at high temperature, the sealed chamber was purged with the inert argon gas to an extremely low oxygen level ( $< 200$  ppm) before fabrication process. During fabrication, the laser beam (generated by the laser system) and the powder stream with the inert gas

(generated by the powder and inert gas delivery system) were simultaneously ejected to the substrate workpiece, forming a molten pool which could catch powders. Once the laser beam was moved, the molten pool would be solidified quickly. According to the design, the deposit head was moved along the trajectory to form the first layer. Afterwards, space for another layer deposition was made with the ascending of the deposit head to the new set position. These processes were repeated many times until building the designed 3D structure.

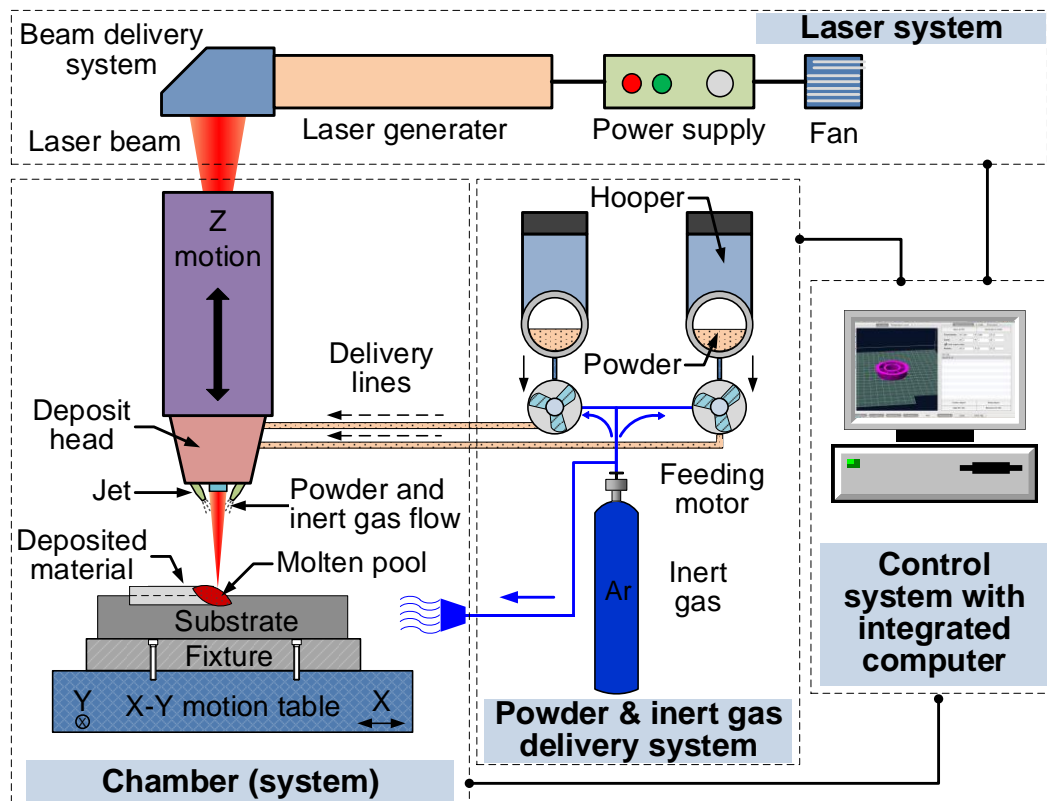


Figure 9.2 Schematic illustration of LENS experimental set-up.

Table 9.1 lists the values or ranges of input fabrication variables. In LD-AM process, laser power was an important factor that could directly determine the laser energy density ( $E$ ) and affect the qualities of fabricated parts and the formation of 3DQCN microstructure. The laser energy density was defined as the energy supplied by the laser beam to a volumetric unit of powder material [38].

$$E = \frac{P}{v \cdot h \cdot d} \quad (9.1)$$

where,  $P$  is the laser power;  $v$  is the deposit head scanning speed;  $h$  is the hatch distance (offset between two neighboring laser tracks); and  $d$  is the layer thickness. Four levels of laser power used in this investigation were 125 W, 150 W, 175 W, and 200 W. Based on Equation 9.1, corresponding laser energy densities were calculated as 71 J/mm<sup>3</sup>, 85 J/mm<sup>3</sup>, 99 J/mm<sup>3</sup>, and 113 J/mm<sup>3</sup>. Four replicated parts were fabricated under each level of laser power. The dimensions of the parts were 8 mm × 8 mm × 20 layers.

Table 9.1 Input fabrication variables

<b>Input fabrication variables</b>	<b>Values or ranges</b>
Laser power (W)	125, 150, 175, and 200
Laser mode	Continuous
Beam diameter of laser (mm)	0.40
Wavelength of laser (μm)	1.07
Deposit head scanning speed (mm/s)	11
Hatch distance (mm)	0.38
Laser thickness (mm)	0.42
Powder feeding rate (g/s)	0.028
Number of layers	20
Scanning orientation (°)	45, 135, 225, and 315
Oxygen level (ppm)	<200

### 9.2.3 Measurement procedures

The morphologies of the powders and microstructure characterizations of the fabricated parts were analyzed using a scanning electron microscope (SEM) (Crossbeam 540, Carl Zeiss AG, Oberkochen, Germany), which was equipped with an electron backscatter diffraction (EBSD) system. After SEM analysis, the working stage was tilted to the 70° orientation from horizontal to meet the requirement of EBSD pattern acquisition. With an integrated AZtec software (Oxford Instruments, Abingdon, UK), phase compositions of the fabricated parts were investigated by the EBSD system under 20 kV acceleration voltage. To index an EBSD pattern, the basic processes included detecting the diffraction bands, measuring the angles between the

bands, and matching these bands to the database for the given material [39]. Prior to SEM and EBSD analyses, the sectioned parts were ground and polished on a MetaServ 250 single grinder-polisher machine (49-10055, Buehler, Lake Bluff, IL, USA). To have better results on microstructure characterizations, the polished parts were etched using a Kroll's Reagent (HF: 3%; HNO<sub>3</sub>: 6%; water: balance) (Etchant Store, Suite N Glendora, CA, USA) for 15 seconds.

To conduct compressive tests, the fabricated parts were post-processed (including cutting, grinding, and polishing) to the cylindrical shape with the dimensions of  $\Phi 6 \text{ mm} \times 8.4 \text{ mm}$ . The compressive properties were tested using a tensile tester (AGS-50kNXD, Shimadzu, Kyoto, Kyoto Prefecture, Japan) at a constant cross-head speed of 0.005 mm/s. The tests were repeated three times under each condition.

The average grain size were measured according to the ASTM E112-13 linear intercept method [40]. The basic steps are summarized as:

Step 1: Draw several line segments on a given plane and measure the total length ( $L$ ) of all line segments;

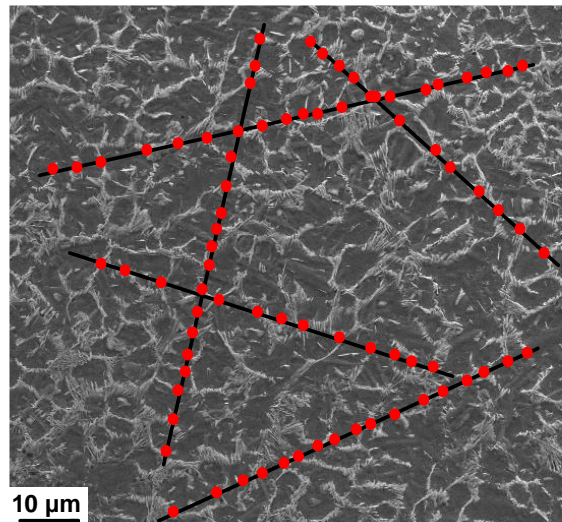


Figure 9.3. The cross-section of TiB-TMC with randomly distributed line segments.

Step 2: Count the total number ( $N$ ) of times of all line segments cutting across grain boundaries;

Step 3: Calculate the average grain size as:  $L/N$ .

Figure 9.3 shows the cross-section of TiB-Ti composite with randomly distributed line segments. The red dots were located at the positions where the line segments intersected grain boundaries. The average grain size was calculated as the total length of five segments over the total number of red dots. To avoid experimental error, the measurements were conducted on four cross-sections of TiB-Ti composites. This measurement method was also applied for CP-Ti parts.

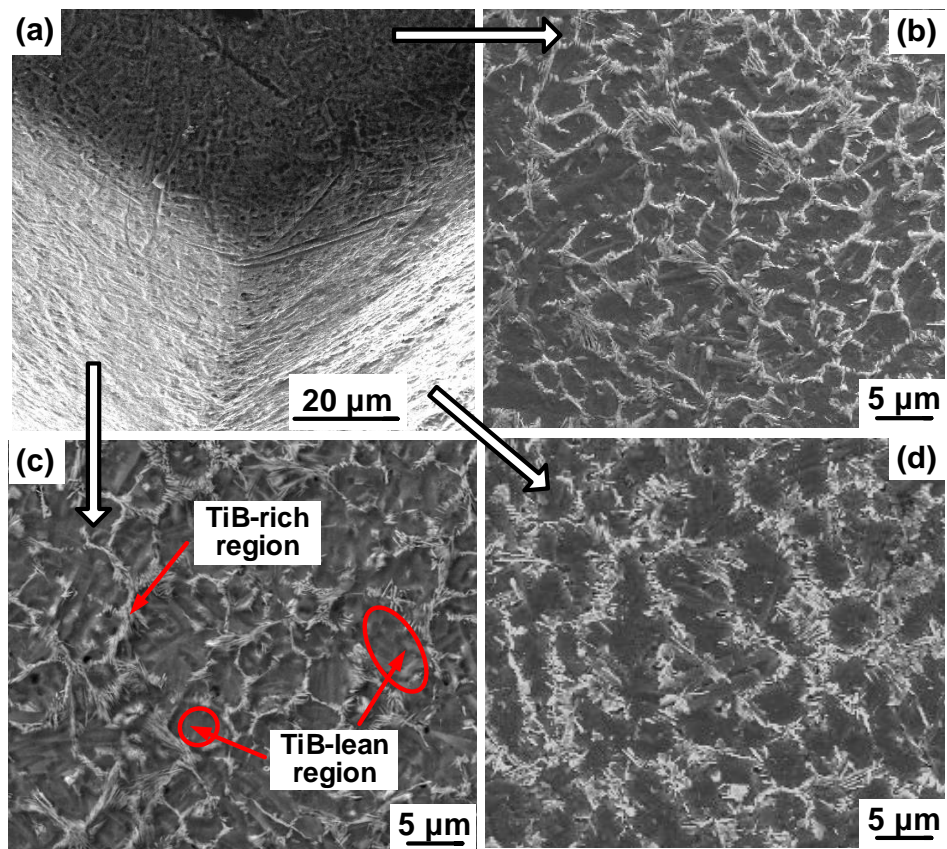


Figure 9.4. SEM analysis on (a) a stereo corner image taken from the fabricated part and detailed 3DQCN microstructures on the (b) top side, (c) left side, and (d) right side.

### 9.3 Results and discussion

#### 9.3.1 Microstructure characterizations

Figure 9.4 shows a stereo corner image taken from a fabricated part, processed at 200 W, and corresponding detailed microstructures on each side of the corner. Quasi-continuous network (QCN) microstructures with TiB rich in some regions but lean in the other regions were observed for all three sides. As reported, the Ti matrix could be strengthened due to the exhibition of TiB-rich regions [15]. The TiB-lean regions were able to improve the toughness and ductility of the fabricated parts. The QCN microstructures were spatially distributed as a 3DQCN microstructure. The 3D structure was beneficial to load transferring and distributing [3,41-43]. EBSD analysis was conducted on TiB-rich regions, showing that the crystal TiB exhibited orthorhombic structure with Pearson symbol  $oP8$ , spacegroup  $Pnma$ , No. 62. The initial and indexed Kikuchi patterns derived from TiB were shown in Figures 9.5(a) and 9.5(b), respectively.

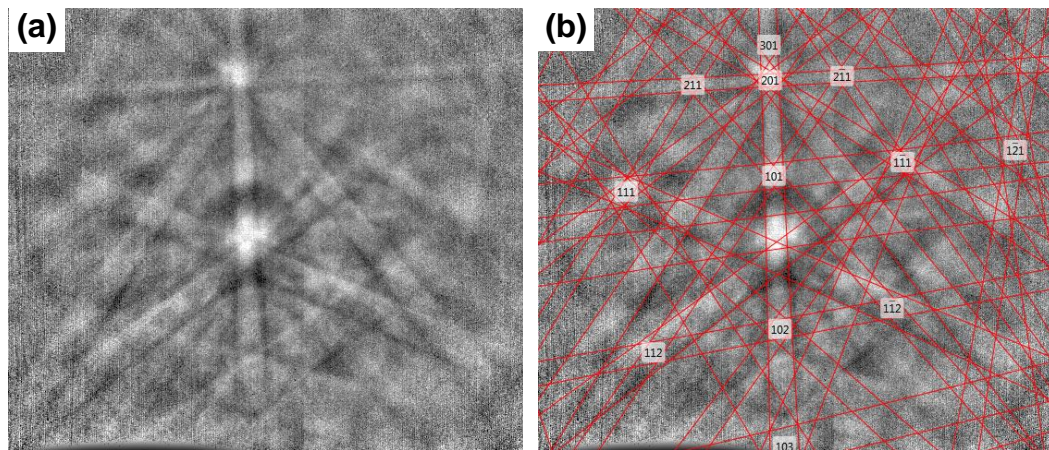


Figure 9.5 EBSD analysis on TiB-rich region showing the (a) initial and (b) indexed Kikuchi patterns.

The formation mechanism of the 3DQCN microstructure, as is shown in Figure 9.6, would follow these stages:

Stage 1: Laser radiated on the workpiece with the generation of a molten pool. The molten pool would catch powders supplied by the powder stream. Due to the high

input energy, Ti and B reacted and formed TiB. The newly formed TiB as well as the other supplied powders were then fully melted into molten material.

Stage 2: After the laser beam was moved to the next position, the material inside the molten pool started to be solidified. At the beginning, the TiB nucleated and then grew into long whiskers, providing heterogeneous nucleation sites for the liquid Ti. The liquid Ti was both heterogeneously nucleated at surfaces of TiB whiskers and homogeneously nucleated from the liquid, generating  $\beta$ Ti nuclei. Due to the growth of  $\beta$ Ti nuclei, TiB whiskers were pushed into the liquid ahead of the nuclei-liquid interface. The TiB whiskers would not be engulfed by  $\beta$ Ti nuclei owing to the low solubility of TiB in  $\beta$ Ti [44,45].

Stage 3: TiB whiskers aggregated at Ti grain boundaries, forming the 3DQCN microstructure in the previous molten pool area. In the meantime, the  $\beta$ Ti transformed into the  $\alpha$ Ti [46].

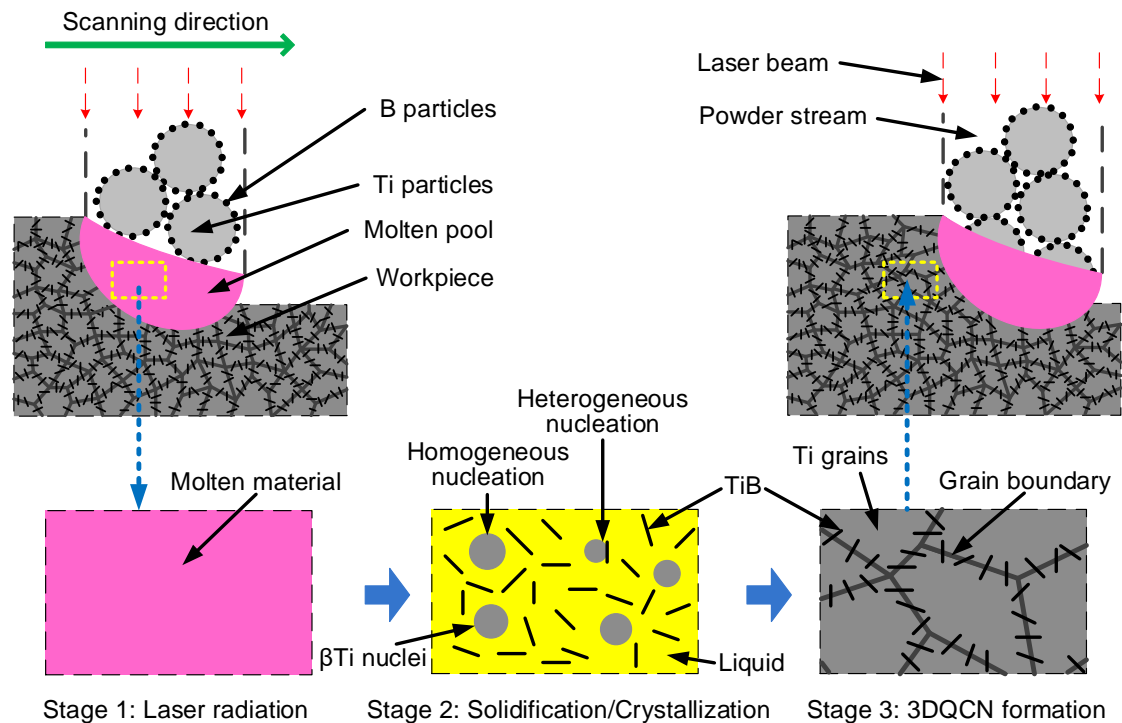


Figure 9.6 Schematic illustration of the formation mechanism of 3DQCN microstructure.

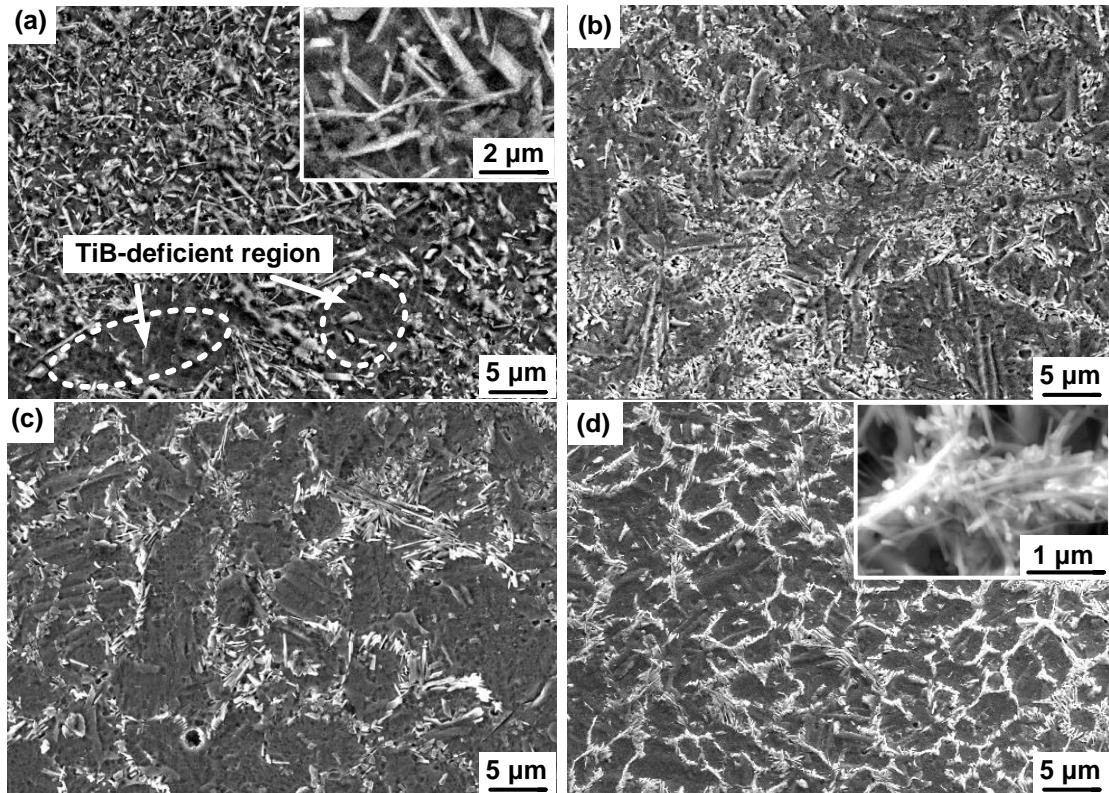


Figure 9.7 Effects of laser power on microstructures of the parts processed at (a) 125 W, (b) 150 W, (c) 175 W, and (d) 200 W, respectively.

Figure 9.7 shows the effects of laser power on microstructures of the parts processed at 125 W, 150 W, 175 W, and 200 W, respectively. At laser power of 125 W, the 3DQCN was not formed. At this level, the laser energy input was insufficient to trigger strong Marangoni convection, liquid capillary force, and flowability [3,6]. Therefore, the rearrangement of TiB reinforcement in the Ti matrix was restricted by the low level of laser power, which was unable to form the 3DQCN microstructure. The TiB reinforcement showed a disordered and non-uniform (TiB-deficient regions) distribution in the Ti matrix. A greater portion of micro-sized primary TiB coexisted with a smaller portion of nano-sized eutectic TiB. At laser power of 125 W, the weight ratio between Ti and B at different regions in the molten pool was not exactly 98.4 : 1.6. The liquid molten pool would solidify as follows: Liquid  $\rightarrow$  Liquid + Primary TiB  $\rightarrow$  Primary TiB + Eutectic TiB +  $\beta$ Ti  $\rightarrow$  Primary TiB + Eutectic TiB +  $\alpha$ Ti [4]. With

the laser power increasing from 125 W to 175 W, the TiB reinforcement tended to be aggregated orderly, forming a partial 3DQCN microstructure. In addition, the size of the TiB reinforcement became smaller. With a further increase of laser power to 200 W, the 3DQCN microstructure was completely formed. This could be ascribed to the fact that the higher laser power led to stronger Marangoni convection, larger liquid capillary force, and better flowability, thus improving the rearrangement of TiB reinforcement in Ti matrix and then forming the 3DQCN microstructure. In addition, the higher laser power led to a better material-contact in the molten pool and resulted in a greater degree of eutectic solidification as follows: Liquid  $\rightarrow$  Eutectic TiB +  $\beta$ Ti  $\rightarrow$  Eutectic TiB +  $\alpha$ Ti. As shown in Figure 9.7(d), the high-magnification SEM analysis along the grain boundary indicated that the eutectic TiB reinforcement was nano-sized, coherently crosslinked, and bonded with each other.

### 9.3.2 Compressive properties

As reported, compressive tests were not as susceptible as tensile tests to minor defects. The minor defects inside the solid parts could cause premature failure and then affect property analysis [16,47]. Therefore, in this investigation, compressive tests were performed and compressive properties were analyzed.

#### 9.3.2.1 Strengthening mechanism

The grain refinement induced by TiB reinforcement would generate a greater grain boundary area to impede dislocation motion, thus enhancing the strength of composites [48]. Based on the Hall-Petch relationship [49,50], the increase of yield strength caused by grain refinement could be expressed as:

$$\Delta\sigma_{HP} = k_{HP} \left( \frac{1}{\sqrt{d_2}} - \frac{1}{\sqrt{d_1}} \right) \quad (9.2)$$

where,  $k_{HP}$  is the Hall-Petch constant for Ti; and  $d_2$  and  $d_1$  are the average grain sizes of TiB-TMCs and CP-Ti parts, respectively.

The increment in yield strength contributed by the presence of TiB was expressed as [51,52]:

$$\Delta\sigma_{TiB} = \sigma_{y-Ti} \cdot V_{TiB} \cdot \frac{1}{2} \cdot l_{TiB}/d_{TiB} \cdot C_0 \quad (9.3)$$

where,  $\sigma_{y-Ti}$  is the yield strength of Ti matrix;  $V_{TiB}$  is the volume fraction of TiB;  $l_{TiB}/d_{TiB}$  is the aspect ratio of TiB (TiB whiskers were treated as cylinders with average length of  $l_{TiB}$  and average diameter of  $d_{TiB}$ ); and  $C_0$  is the orientation factor. From a macroscopic view, the TiB reinforcement was randomly distributed among the Ti matrix. Therefore, based on the 3D random array model [52],  $C_0 = 0.125$ .

The increment in yield strength induced by dislocation strengthening could be expressed as [53]:

$$\Delta\sigma_{dis} = \sqrt{(\Delta\sigma_{oro})^2 + (\Delta\sigma_{the})^2 + (\Delta\sigma_{geo})^2} \quad (9.4)$$

where,  $\Delta\sigma_{oro}$  is the Orowan stress which represents the stress needed for a dislocation to cross an array of TiB whiskers;  $\Delta\sigma_{the}$  is the stress increment caused by the thermal expansion mismatch between the TiB reinforcement and the Ti matrix; and  $\Delta\sigma_{geo}$  represents the stress increment due to strain gradient effects induced by geometrical distributions of dislocations.

The Orowan stress was described by the Orowan-Ashby equation [54]:

$$\Delta\sigma_{oro} = \frac{0.13G_{Ti}b_{Ti}}{\lambda} \ln \frac{D_{TiB}}{2b_{Ti}} \quad (9.5)$$

where,  $G_{Ti}$  is the shear modulus of the Ti matrix;  $b_{Ti}$  is the Burgers vector of the Ti matrix; and  $D_{TiB}$  is the equivalent diameter of TiB reinforcement and could be expressed as:

$$D_{TiB} = \sqrt[3]{1.5d_{TiB}^2 l_{TiB}} \quad (9.6)$$

$\lambda$  is the interparticle spacing, expressed as [11,55]:

$$\lambda \approx D_{TiB} \left[ (2V_{TiB})^{-\frac{1}{3}} - 1 \right] \quad (9.7)$$

The stress increment caused by the thermal expansion mismatch could be neglected since the thermal expansion coefficients between TiB and Ti were very

similar.

The stress increment due to strain gradient effects could be expressed as [56]:

$$\Delta\sigma_{geo} = 0.4G_{Ti}\sqrt{\epsilon_{T-Ti}b_{Ti}V_{TiB}/D_{TiB}} \quad (9.8)$$

where,  $\epsilon_{T-Ti}$  is the compressive true strain of Ti matrix.

To sum up, the increment in yield strength of TiB-TMCs were mainly attributed to grain refinement strengthening effect, TiB strengthening effect, and dislocation strengthening effect. Based on Ramakrishnan's approach [10], the yield strength of TiB-TMCs could be expressed as:

$$\sigma_{yc} = \sigma_{y-Ti} \left( 1 + \frac{\Delta\sigma_{HP}}{\sigma_{y-Ti}} \right) \left( 1 + \frac{\Delta\sigma_{TiB}}{\sigma_{y-Ti}} \right) \left( 1 + \frac{\Delta\sigma_{dis}}{\sigma_{y-Ti}} \right) \quad (9.9)$$

where,  $\sigma_{yc}$  is the yield strength of TiB-Ti composites.

Table 9.2 Properties and parameters

Properties and parameters	Values or ranges	Data sources
$k_{HP}$ (MPa· $\mu\text{m}^{1/2}$ )	328	[57]
$d_2$ ( $\mu\text{m}$ )	4.83	Measured
$d_1$ ( $\mu\text{m}$ )	18.67	Measured
$V_{TiB}$ (%)	8.68%	Calculated
$l_{TiB}/d_{TiB}$	8.35 (125 W), 9.27 (150 W), 10.89 (175 W), 13.32 (200 W)	Measured & Calculated
$C_0$	0.125	[52]
$D_{TiB}$ ( $\mu\text{m}$ )	1.09 (125 W), 0.88 (150 W), 0.76 (175 W), 0.65 (200 W)	Measured & Calculated
$G_{Ti}$ (GPa)	45	[48]
$b_{Ti}$ (nm)	0.295	[58]

Using Equations 9.2 to 9.9 and data from Tables 9.2 and 9.3, yield strength values of TiB-TMCs processed at different levels of laser power were predicted and presented in Figure 9.8. Besides, the tested yield strength values of TiB-TMCs and CP-Ti parts were also shown in Figure 9.8. The average value from three measurements, under each combination of input fabrication variables, was used to represent the experimental results. The standard deviation of three measurements was used to represent both positive and negative values of error bars.

Table 9.3 Compressive properties of CP-Ti parts and TiB-TMCs

	Laser power	3DQCN	$\sigma_y$ (Mpa)	$\sigma_u$ (Mpa)	$\epsilon_T$ (%)	$U_T$ (J/mm <sup>3</sup> )
CP-Ti parts	125	N/A	773±11	836±12	55.8±2.0	393±19
	150	N/A	787±15	851±14	56.5±1.7	408±15
	175	N/A	779±18	842±16	54.9±2.3	397±11
	200	N/A	779±12	843±13	55.7±0.9	399±13
TiB-TMCs	125	No	940±14	1016±15	26.5±0.8	201±13
	150	Partial	974±12	1053±11	28.9±0.5	235±9
	175	Partial	996±21	1077±18	31.9±1.1	267±7
	200	Yes	1010±11	1092±13	36.4±1.3	320±10

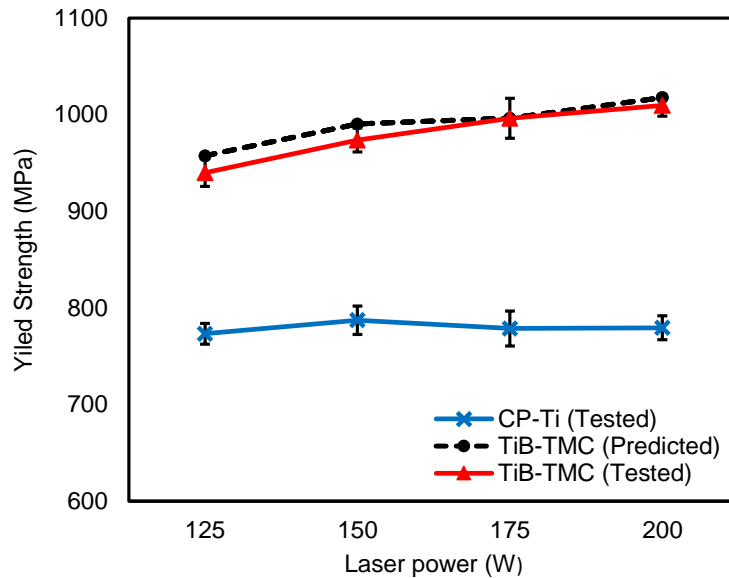


Figure 9.8 Effects of laser power on yield strengths of CP-Ti parts and TiB-TMCs.

With the laser power increasing from 125 W to 200 W, the yield strength values of CP-Ti parts was slightly changed, indicating that the laser power had little impact on the yield strength values of CP-Ti parts. It can be considered that the predicted yield strength values were in good consistent with tested yield strength values of TiB-Ti composites. With the increase of laser power, both the predicted and tested yield strength values of TiB-TMCs were increased. This could be ascribed to the fact that the aspect ratio ( $l_{TiB}/d_{TiB}$ ) of TiB increased and the equivalent diameter ( $D_{TiB}$ ) of TiB decreased with the laser power increasing, as shown in Table 9.2. Based on Equations 9.3 and 9.8, the increase of laser power led to the increases of  $\Delta\sigma_{TiB}$  and  $\Delta\sigma_{geo}$ , thus increasing the yield strength of TiB-Ti composites.

As shown in Table 9.3, the ultimate strength ( $\sigma_u$ ) had similar trends with those of yield strength. With the laser power increasing, the ultimate strength of CP-Ti parts was slightly changed, however, the ultimate strength of TiB-TMCs was increased.

### ***9.3.2.2 Toughening mechanism and fracture features***

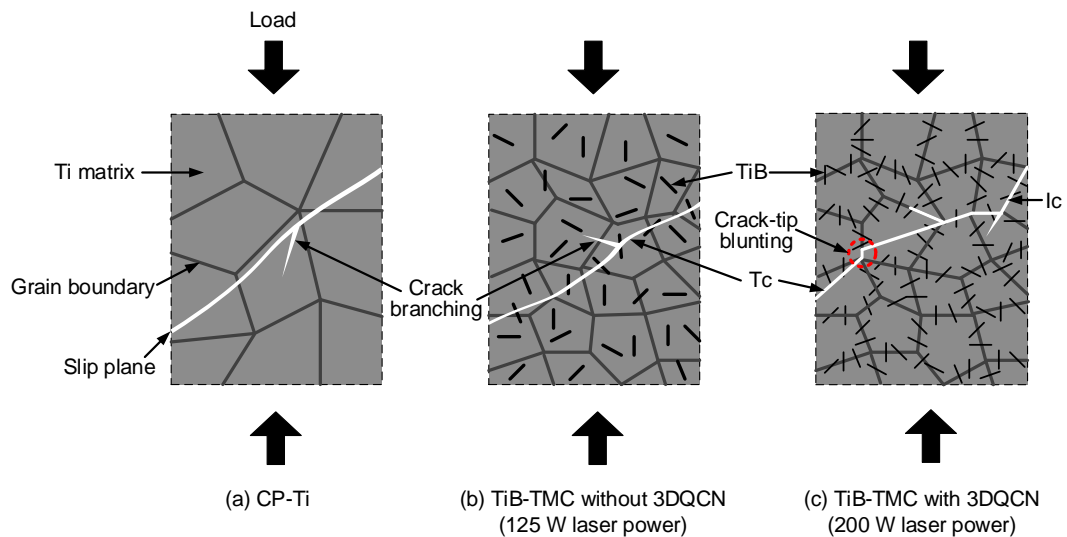
The laser power had small influence on the true strain ( $\epsilon_T$ , ductility) of CP-Ti parts. However, the true strain of TiB-TMCs increased with the increase of laser power. Toughness, the ability of a material to absorb energy up to fracture, was related to the true strain and could be expressed as [59]:

$$U_T = \int_0^{\epsilon_T} \sigma(\epsilon) d\epsilon \quad (9.10)$$

where,  $\epsilon_T$  is the true strain; and  $\sigma(\epsilon)$  is the stress function.

For CP-Ti parts, the toughness was slightly changed with the laser power increasing. In other words, under this combination of input fabrication variables, the effects of laser power on the toughness of CP-Ti parts were not significant. The toughness of TiB-TMCs was smaller than that of CP-Ti parts processed at the same level of laser power. At the laser power of 125 W, the average toughness of TiB-TMCs was 201 J/mm<sup>3</sup>, being only 51% of that of CP-Ti parts. The “brittleness” of TiB-TMCs was ascribed to the presence of ceramic TiB reinforcement [3]. With the

increase of laser power from 125 W to 200 W, the average toughness of TiB-TMCs was significantly increased from 201 J/mm<sup>3</sup> to 320 J/mm<sup>3</sup>. The toughening effects on TiB-TMCs could be attributed to the formation of 3DQCN microstructure and the refinement of TiB reinforcement at high level of laser power. Detailed toughening mechanisms at high level of laser power were summarized as: (1) For TiB-TMCs with 3DQCN microstructure, the cracks propagated not only along the rigid TiB-rich regions (Ti grain boundaries, intercrystalline) but also across the ductile TiB-lean regions (Ti grains, transcrystalline) [15], as illustrated in Figure 9.9(c); (2) When a propagating crack encountered the ductile TiB-lean region of the 3DQCN microstructure, the crack-tip would be blunted and deflected. The generation and growth of a new crack required additional fracture energy, thus increasing the toughness of composites. Such phenomenon was proved in Figure 9.10. Compared with the single-straight crack in the TiB-Ti composite without 3DQCN microstructure, multiple curved cracks were observed for the TiB-Ti composite with 3DQCN microstructure; and (3) The refinement of TiB reinforcement caused by laser power increasing also contributed to the toughening of TiB-TMCs [60].



(Tc represents transcrystalline cracks and Ic represents intercrystalline cracks)

Figure 9.9 Illustration of different failures modes in compressive tests.

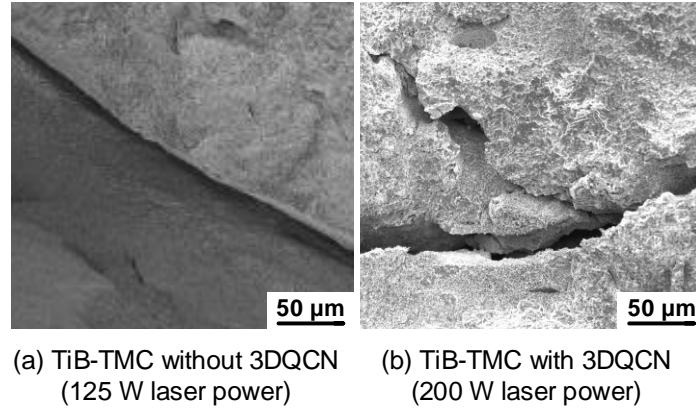
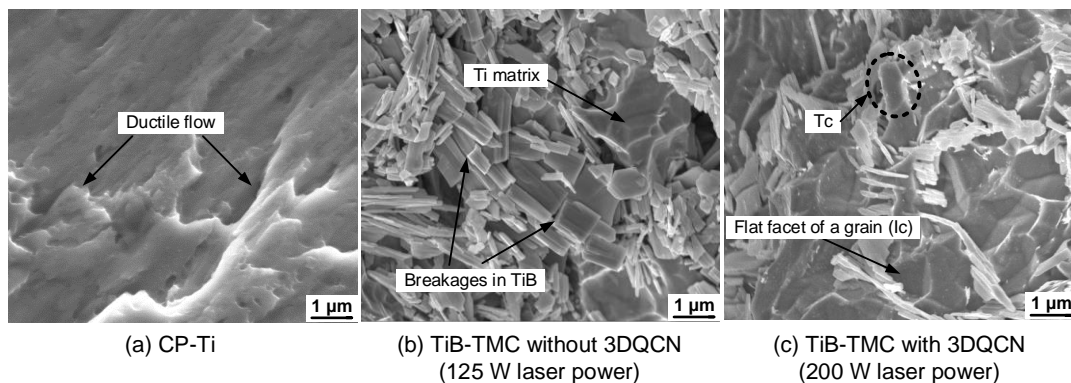


Figure 9.10 Crack profiles in compressive tests.

During compressive tests, the tested parts were broken into two or more fragments. Figure 9.11 shows the features on fracture interfaces of CP-Ti part, TiB-Ti composite without 3DQCN microstructure (125 W laser power), and TiB-Ti composite with 3DQCN microstructure (200 W laser power), respectively. For the CP-Ti part, as shown in Figure 9.11(a), the relatively smooth fracture facets indicated a linear crack passing through this interface, leaving ductile flows. The ductile fracture features enabled high toughness and ductility of the CP-Ti part, as proved in Table 9.3. On the fracture interface of the TiB-Ti composite without 3DQCN microstructure, the broken TiB whiskers were randomly distributed within the Ti matrix. Due to the high stress induced by the reinforcement, the load would transfer from the matrix to the



(Tc represents transcrystalline cracks and Ic represents intercrystalline cracks)

Figure 9.11 Fracture features in compressive tests.

reinforcement during the splitting of the tested part. As a result, multiple breakages along one TiB whisker occurred, as shown in Figure 9.11(b). The TiB-Ti composite with 3DQCN microstructure exhibited flat facets of grains on its fracture interface, as shown in Figure 9.11(c), indicating that the crack propagated mainly along the grain boundaries of Ti matrix (intercrystalline). The splitting of Ti grains resulted in indented edges (as circled in Figure 9.11(c)) on the fracture interface, thus confirming the transcrystalline propagation of the crack.

#### **9.4 Conclusions**

In this investigation, 3DQCN microstructural TiB-TMCs were fabricated by in-situ LD-AM process. For the first time, the effects of laser power on the formation of 3DQCN microstructure as well as mechanical properties (such as compressive yield strength and toughness) were analyzed. Major conclusions were drawn below:

(1) Laser power had a great impact on the rearrangement of TiB reinforcement in the Ti matrix and hugely influenced the formation of 3DQCN microstructure. Results showed that the 3DQCN microstructure was from non-existence to existence by increasing laser power from 125 W to 200 W.

(2) The yield strength of TiB-TMCs was modeled by taking grain refinement, TiB reinforcement, and dislocation strengthening effects into account. The predicted yield strength values were in good consistent with tested yield strength values of TiB-Ti composites. Due to the increased aspect ratio of TiB and decreased TiB-whisker size, the yield strength of TiB-TMCs increased with the laser power increasing.

(3) Owing to the presence of brittle TiB reinforcement, TiB-TMCs without 3DQCN microstructure (125 W laser power) exhibited smaller ductility and toughness, as compared with CP-Ti parts. By increasing laser power, the 3DQCN microstructure started to appear and contribute to toughening effects on TiB-Ti composites.

(4) The fracture interface of TiB-TMCs without 3DQCN microstructure (125 W laser power) was dominated with randomly distributed TiB whiskers and dimples.

Analyses on fracture interface of TiB-TMCs with 3DQCN microstructure (200 W laser power) indicated that the crack propagated both along the grain boundaries and across the grains of the Ti matrix.

## References

- [1] Laoui, T., Santos, E., Osakada, K., Shiomi, M., Morita, M., Shaik, S. K., Tolochko, N. K., Abe, F., & Takahashi, M. (2006). Properties of titanium dental implant models made by laser processing. *Proceedings of the Institution of Mechanical Engineers, Part C: Journal of Mechanical Engineering Science*, 220(6), 857-863.
- [2] Spowart, J. E., & Clyne, T. W. (1999). The axial compressive failure of titanium reinforced with silicon carbide monofilaments. *Acta Materialia*, 47(2), 671-687.
- [3] Hu, Y. B., Zhao, B., Ning, F. D., Wang, H., & Cong, W. L. (2017). In-situ ultrafine three-dimensional quasi-continuous network microstructural TiB reinforced titanium matrix composites fabrication using laser engineered net shaping. *Materials Letters*, 195, 116-119.
- [4] Banerjee, R., Genc, A., Collins, P. C., & Fraser, H. L. (2004). Comparison of microstructural evolution in laser-deposited and arc-melted in-situ Ti-TiB composites. *Metallurgical and Materials Transactions A*, 35(7), 2143-2152.
- [5] Balla, V. K., Bhat, A., Bose, S., & Bandyopadhyay, A. (2012). Laser processed TiN reinforced Ti6Al4V composite coatings. *Journal of the Mechanical Behavior of Biomedical Materials*, 6, 9-20.
- [6] Gu, D. D., Meng, G. B., Li, C., Meiners, W., & Poprawe, R. (2012). Selective laser melting of TiC/Ti bulk nanocomposites: Influence of nanoscale reinforcement. *Scripta Materialia*, 67(2), 185-188.
- [7] Das, M., Balla, V. K., Basu, D., Bose, S., & Bandyopadhyay, A. (2010). Laser processing of SiC-particle-reinforced coating on titanium. *Scripta Materialia*, 63(4), 438-441.
- [8] Tamirisakandala, S., Miracle, D. B., Srinivasan, R., & Gunasekera, J. S. (2006). Titanium alloyed with boron. *Advanced Materials and Processes*, 164(12), 41-43.
- [9] Gorsse, S., Le Petitcorps, Y., Matar, S., & Rebillat, F. (2003). Investigation of the Young's modulus of TiB needles in situ produced in titanium matrix composite. *Materials Science and Engineering: A*, 340(1), 80-87.
- [10] Ramakrishnan, N. (1996). An analytical study on strengthening of particulate reinforced metal matrix composites. *Acta Materialia*, 44(1), 69-77.
- [11] Zhang, Z., & Chen, D. L. (2006). Consideration of Orowan strengthening effect in particulate-reinforced metal matrix nanocomposites: a model for predicting their yield strength. *Scripta Materialia*, 54(7), 1321-1326.
- [12] Sanaty-Zadeh, A. (2012). Comparison between current models for the strength of particulate-reinforced metal matrix nanocomposites with emphasis on consideration of Hall-Petch effect. *Materials Science and Engineering: A*, 531, 112-118.
- [13] Sinclair, I., & Gregson, P. J. (1997). Structural performance of discontinuous metal matrix composites. *Materials Science and Technology*, 13(9), 709-726.
- [14] Hu, Y. B., Ning, F. D., Wang, X. L., Wang, H., Zhao, B., Cong, W. L., & Li, Y. Z. (2017). Laser deposition-additive manufacturing of in situ TiB reinforced

- titanium matrix composites: TiB growth and part performance. *The International Journal of Advanced Manufacturing Technology*, 93(9-12), 3409-3418.
- [15] Huang, L. J., Geng, L., & Peng, H. X. (2015). Microstructurally inhomogeneous composites: is a homogeneous reinforcement distribution optimal?. *Progress in Materials Science*, 71, 93-168.
- [16] Attar, H., Bönisch, M., Calin, M., Zhang, L. C., Scudino, S., & Eckert, J. (2014). Selective laser melting of in situ titanium-titanium boride composites: processing, microstructure and mechanical properties. *Acta Materialia*, 76, 13-22.
- [17] Huang, L. J., Geng, L., & Peng, H. X. (2011). In situ TiBw/Ti composites with a novel quasi-continuous network reinforcement architecture. 18<sup>th</sup> International Conference on Composite Materials.
- [18] Morikawa, D., Ramkumar, J., Mabuchi, H., Tsuda, H., Matsui, T., & Morii, K. (2002). Microstructure and mechanical properties of Ti-BN cast alloys prepared by reactive arc-melting. *Materials Transactions*, 43(9), 2193-2196.
- [19] Ning, F. D, Cong, W. L, Hu, Y. B, & Wang, H. (2017). Additive manufacturing of carbon fiber-reinforced plastic composites using fused deposition modeling: Effects of process parameters on tensile properties. *Journal of Composite Materials*, 51(4), 451-462.
- [20] Jin, X., Deng, Y. Q., Cai, W. R., Lau, W. M., Hui, D., Yan, H., Mei, J., & Liu, Y. (2016). Material design and process development of electrostatically patterning silver capsuled composite particle for preparing conductive tracks on flexible substrate. *Composites Part B: Engineering*, 105, 111-115.
- [21] Zhang, Y. Z., Sun, J. C., & Vilar, R. (2011). Characterization of (TiB + TiC)/TC4 in situ titanium matrix composites prepared by laser direct deposition. *Journal of Materials Processing Technology*, 211(4), 597-601.
- [22] Song, B., Zhao, X., Li, S., Han, C. J., Wei, Q. S., Wen, S. F., Liu, J., & Shi, Y. S. (2015). Differences in microstructure and properties between selective laser melting and traditional manufacturing for fabrication of metal parts: A review. *Frontiers of Mechanical Engineering*, 10(2), 111-125.
- [23] Darwish, A. M., Moore, S., Mohammad, A., Bastian, T., Dorlus, W., Sarkisov, S., Patel, D., Mele, P., Koplitz, B., & Hui, D. (2017). Polymer nano-composite films with inorganic upconversion phosphor and electro-optic additives made by concurrent triple-beam matrix assisted and direct pulsed laser deposition. *Composites Part B: Engineering*, 109, 82-90.
- [24] Li, Y. Z., Hu, Y. B., Cong, W. L., Zhi, L., & Guo, Z. N. (2017). Additive manufacturing of alumina using laser engineered net shaping: Effects of deposition variables. *Ceramics International*, 43(10), 7768-7775.
- [25] Wang, X., Jiang, M., Zhou, Z. W., Gou, J. H., & Hui, D. (2017). 3D printing of polymer matrix composites: A review and prospective. *Composites Part B: Engineering*, 110, 442-458.
- [26] Wu, X. (2006). Review of alloy and process development of TiAl alloys. *Intermetallics*, 14(10), 1114-1122.

- [27] Czél, G., Jalalvand, M., Wisnom, M. R., & Czigány, T. (2017). Design and characterisation of high performance, pseudo-ductile all-carbon/epoxy unidirectional hybrid composites. *Composites Part B: Engineering*, 111, 348-356.
- [28] Bhaumik, S. K. (2000). Synthesis and sintering of monolithic and composite ceramics under high pressures and high temperatures. *Metals Materials and Processes*, 12(2 & 3), 215-232.
- [29] Mileiko, S. T. (2017). Fracture-toughness/notch-sensitivity correlation for metal-and ceramic-based fibrous composites. *Composites Part B: Engineering*, 116, 1-6.
- [30] Kobryn, P. A., & Semiatin, S. L. (2001). The laser additive manufacture of Ti-6Al-4V. *JOM Journal of the Minerals, Metals and Materials Society*, 53(9), 40-42.
- [31] Darwish, A. M., Sagapolutele, M. T., Sarkisov, S., Patel, D., Hui, D., & Koplitz, B. (2013). Double beam pulsed laser deposition of composite films of poly (methyl methacrylate) and rare earth fluoride upconversion phosphors. *Composites Part B: Engineering*, 55, 139-146.
- [32] Hu, Y. B., & Li, J. Z. (2017). Selective laser alloying of elemental titanium and boron powder: Thermal models and experiment verification. *Journal of Materials Processing Technology*, 249, 426-432.
- [33] Mudge, R. P., & Wald, N. R. (2007). Laser engineered net shaping advances additive manufacturing and repair. *Welding Journal-New York*, 86(1), 44.
- [34] Ning, F. D., Hu, Y. B., Liu, Z. C., Cong, W. L., Li, Y. Z., & Wang, X. L. (2017). Ultrasonic vibration-assisted laser engineered net shaping of Inconel 718 parts: a feasibility study. *Procedia Manufacturing*, 10, 771-778.
- [35] Darwish, A. M., Burkett, A., Blackwell, A., Taylor, K., Sarkisov, S., Patel, D., Koplitz, B., & Hui, D. (2015). Polymer–inorganic nano-composite thin film upconversion light emitters prepared by double-beam matrix assisted pulsed laser evaporation (DB-MAPLE) method. *Composites Part B: Engineering*, 68, 355-364.
- [36] Hu, Y. B., Wang, H., Ning, F. D., & Cong, W. L. (2016). Laser engineered net shaping of commercially pure titanium: Effects of fabricating variables. In *ASME 2016 11th International Manufacturing Science and Engineering Conference* (pp. V001T02A035-V001T02A035). American Society of Mechanical Engineers.
- [37] Abdellahi, M., & Bahmanpour, M. (2014). A novel technology for minimizing the synthesis time of nanostructured powders in planetary mills. *Materials Research*, 17(3), 781-791.
- [38] Gu, D. D., Meiners, W., Wissenbach, K., & Poprawe, R. (2012). Laser additive manufacturing of metallic components: materials, processes and mechanisms. *International Materials Reviews*, 57(3), 133-164.
- [39] Nowell, M. M., & Wright, S. I. (2005). Orientation effects on indexing of electron backscatter diffraction patterns. *Ultramicroscopy*, 103(1), 41-58.

- [40] ASTM E112-13. (2013). Standard test methods for determining average grain size, ASTM international, West Conshohocken, PA.
- [41] Kaludjerović, B. V., Srećković, M., Jančićević, M., Kovačević, A., & Bojanić, S. (2017). Influence of Nd<sup>3+</sup>: YAG laser irradiation on the properties of composites with carbon fibers. *Composites Part B: Engineering*, 125, 165-174.
- [42] Castellani, C., Lindtner, R. A., Hausbrandt, P., Tschegg, E., Stanzl-Tschegg, S. E., Zanoni, G., Beck, S., & Weinberg, A. M. (2011). Bone-implant interface strength and osseointegration: Biodegradable magnesium alloy versus standard titanium control. *Acta Biomaterialia*, 7(1), 432-440.
- [43] Tran, P., Ngo, T. D., Ghazlan, A., & Hui, D. (2017). Bimaterial 3D printing and numerical analysis of bio-inspired composite structures under in-plane and transverse loadings. *Composites Part B: Engineering*, 108, 210-223.
- [44] Tamirisakandala, S., Bhat, R. B., Tiley, J. S., & Miracle, D. B. (2005). Grain refinement of cast titanium alloys via trace boron addition. *Scripta Materialia*, 53(12), 1421-1426.
- [45] Li, M., Huang, J., Zhu, Y. Y., Li, Z. G., & Wu, Y. X. (2016). Growth morphology and solidification behavior of in-situ synthesized TiN and TiB. *Materials Transactions*, 57(1), 15-19.
- [46] Elmer, J. W., Palmer, T. A., Babu, S. S., Zhang, W., & DebRoy, T. (2004). Phase transformation dynamics during welding of Ti-6Al-4V. *Journal of Applied Physics*, 95(12), 8327-8339.
- [47] Węclawski, B. T., Fan, M. Z., & Hui, D. (2014). Compressive behaviour of natural fibre composite. *Composites Part B: Engineering*, 67, 183-191.
- [48] Callister, W. D., & Rethwisch, D. G. (2007). *Materials science and engineering: an introduction* (Vol. 7, pp. 665-715). New York: Wiley.
- [49] Hall, E. O. (1951). The deformation and ageing of mild steel: III discussion of results. *Proceedings of the Physical Society. Section B*, 64(9), 747.
- [50] Petch, N. J. (1953). The cleavage strength of polycrystals. *Journal of Iron and Steel Research, International*, 174, 25-28.
- [51] Fukuda, H., & Chou, T. W. (1982). A probabilistic theory of the strength of short-fibre composites with variable fibre length and orientation. *Journal of Materials Science*, 17(4), 1003-1011.
- [52] Guo, X., Wang, L., Wang, M., Qin, J., Zhang, D., & Lu, W. (2012). Effects of degree of deformation on the microstructure, mechanical properties and texture of hybrid-reinforced titanium matrix composites. *Acta Materialia*, 60(6), 2656-2667.
- [53] Humpherys, F. J. (1988). *Mechanical and physical behavior of metallic and ceramic composites*. Denmark: Riso Nat Lab.
- [54] Dieter, G. E., & Bacon, D. J. (1986). *Mechanical metallurgy* (Vol. 3). New York: McGraw-Hill.
- [55] Meyers, M. A., & Chawla, K. K. (1999). *Mechanical behaviour of materials*. Saddle River, NJ: Prentice-Hall; 1999.
- [56] Brown, L. M. Stobbs. *WM* (1976). *Philosophical Magazine*, 34, 351.

- [57] Kohn, D. H., & Ducheyne, P. (1991). Tensile and fatigue strength of hydrogen-treated Ti-6Al-4V alloy. *Journal of Materials Science*, 26(2), 328-334.
- [58] Odegard, B. C., & Thompson, A. W. (1974). Low temperature creep of Ti-6Al-4V. *Metallurgical Transactions*, 5(5), 1207-1213.
- [59] Roylance, D. (2001). *Stress-strain curves*. Massachusetts Institute of Technology study, Cambridge.
- [60] Varol, T., & Canakci, A. (2013). Effect of particle size and ratio of B<sub>4</sub>C reinforcement on properties and morphology of nanocrystalline Al<sub>2</sub>O<sub>3</sub>-B<sub>4</sub>C composite powders. *Powder Technology*, 246, 462-472.

## CHAPTER X

### CONCLUSIONS & SCIENTIFIC CONTRIBUTIONS

#### 10.1 Conclusions

In this dissertation, a review on laser deposition-additive manufacturing (LD-AM) of ceramics and cerami reinforced composites was provided. Investigations on LD-AM of zirconia toughened alumina (ZTA) and TiB reinforced titanium matrix composites (TiB-TMCs) were conducted to reveal microstructures and improve mechanical properties. The major conclusions are drawn as follows:

(1) A novel ultrasonic vibration-assisted LD-AM process for fabrication of bulk ZTA parts was performed in this dissertation. The effects of ultrasonic vibration on crack suppression, microstructure, and mechanical properties of the fabricated parts were studied. Results showed that the initiation of cracks and the crack propagation in the deposition direction were suppressed in the parts fabricated by LD-AM process with ultrasonic vibration. Compared with the part fabricated without ultrasonic vibration, the part fabricated with ultrasonic vibration exhibited smaller grain size, better material dispersion, higher microhardness, higher wear resistance, and better compressive properties. In compressive tests, the fracture interface of parts fabricated without ultrasonic vibration mainly demonstrated intercrystalline cracking, however, both intercrystalline cracking and transcrystalline cracking occurred in the parts fabricated with ultrasonic vibration.

(2) At lower levels of  $ZrO_2$  content,  $ZrO_2$  particles tended to aggregate at grain boundaries of  $Al_2O_3$  matrix, forming a network microstructure. The network microstructure was quasi-continuous and spatially distributed as a 3DQCN microstructure, which benefited ZTA parts on enhancing their mechanical performance. At higher levels of  $ZrO_2$  content, eutectic microstructure dominated the whole part. The eutectic microstructure contained randomly oriented colonies with granular  $ZrO_2$  grains presenting at boundaries of these colonies. With the increase of  $ZrO_2$  content 0 wt.% to 41.5 wt.%, the microhardness was firstly increased then

decreased, whereas the fracture toughness increased. Phase transformation (*t*-ZrO<sub>2</sub> to *m*-ZrO<sub>2</sub>) toughening effects, crack bridging, crack branching, and crack deflecting were the reasons for toughening ZTA parts.

(3) In order to achieve better surface quality of LENS-fabricated ZTA parts, an efficient and effective rotary ultrasonic machining (RUM) process was utilized for surface grinding of ZTA parts. Experimental results showed that the surface quality of ZTA parts were significantly improved after RUM process. In addition, the introduction of ultrasonic vibration in RUM was beneficial for reducing cutting force.

(4) The effects of TiB reinforcement on part quality, microstructure characterization, microhardness, and wear resistance were analyzed. Due to the in-situ reaction between Ti and B, new phase of TiB was generated in form of both prismatic primary TiB and needle-like eutectic TiB. In addition, a flower-liker microstructure was formed with TiB reinforcement being embedded into the Ti matrix. The newly formed TiB particles exhibited a long prismatic shape with a high aspect ratio. The presence of TiB reinforcement led to the “balling” phenomenon at the surfaces of fabricated parts. Compared with CP-Ti parts, TiB-TMCs exhibited higher microhardness and higher wear resistance. Within the certain range (125 W – 200 W), high level of laser power was beneficial for improving part quality and enhancing microhardness and wear resistance.

(5) The effects of laser power and Z-axis increment on densities and compressive properties of both TiB-TMCs and CP-Ti parts were investigated. Results showed that the densities of parts increased with the increase of laser power and the decrease of Z-axis increment. The difference of densities between TiB-TMCs and CP-Ti parts was mainly attributed to the combined actions of laser absorption, reaction induced pores, and reaction generated energy. With the laser power increasing, the UCS increased but ductility slightly changed. Z-axis increment had negligible effects on compressive properties. The presence of the rigid TiB reinforcement led to the increase of UCS but decrease of ductility. SEM imaging analysis was conducted on the fracture surfaces of CP-Ti parts and TiB-TMCs. For CP-Ti parts, the ductile

fracture features prevailed with smooth fracture facets. For TiB-TMCs, the brittle fracture features dominated with dimples and tearing ridge lines.

(6) In this dissertation, innovative 3DQCN microstructural TiB-TMCs with the crosslinking eutectic TiB nanofibers aggregating at the Ti grain boundaries were fabricated by in-situ LENS process. The formation mechanism of the 3DQCN microstructure was investigated. It was found that the laser power had a great impact on the formation of 3DQCN microstructure. Results showed that the 3DQCN microstructure was from non-existence to existence by increasing laser power from 125 W to 200 W. Compared with TiB-TMCs without 3DQCN microstructure, TiB-TMCs with 3DQCN microstructure demonstrated higher ductility and higher toughness. SEM analyses showed that the fracture interface of TiB-TMCs without 3DQCN microstructure was dominated with randomly distributed TiB whiskers and dimples. Analyses on fracture interface of TiB-TMCs with 3DQCN microstructure indicated that the crack propagated both along the grain boundaries and across the grains of the Ti matrix.

## **10.2 Scientific contributions**

The major scientific contributions of this dissertation are:

(1) This dissertation proved the feasibility and strengthes of intergrating LD-AM with ultrasonic vibration and explored material melting and solidification mechanisms in ultrasonic vibration assied LD-AM process, in order to improve fabrication quality and enhance mechanical properties of fabricated ZTA parts.

(2) This dissertation discovered novel microstructures and generated knowledge on the relationship between novel microstructures and the mechanical performance of ZTA parts with different levels of ZrO<sub>2</sub> content, which would facilitate ceramic materials development and broaden the applications of LD-AM process in the major industries where ceramic materials are heavily used.

(3) This dissertation generated fundamental knowledge and provided engineering solutions to toughen TiB-TMCs through tailoring 3DQCN microstructure

and exploring the governing processing-microstructure-property relationships, in order to broaden the application fields of ceramic reinforced metal matrix composites.

(4) In this dissertation, the spatial distribution of TiB within titanium matrix and formation mechanisms of 3DQCN microstructure were explored. The yield strength of TiB-TMCs with 3DQCN microstructure was modeled by taking grain refinement, TiB reinforcement, and dislocation strengthening effects into account. In addition, the toughening mechanism due to the presence of 3DQCN microstructure was investigated.

## APPENDIX A

### PUBLICATIONS DURING PH.D. STUDY

#### Journal Articles

- [1] **Hu, Y. B.**, Cong W. L., Wang, X. L., Li, Y. C., Ning, F. D., & Wang, H. (2018). Laser deposition-additive manufacturing of TiB-Ti composites with novel three-dimensional quasi-continuous network microstructure: effects on strengthening and toughening. *Composites Part B: Engineering*, 133, 91-100.
- [2] **Hu, Y. B.**, Ning, F. D., Cong, W. L., Li, Y. C., Wang, X. L., & Wang, H. (2018). Ultrasonic vibration-assisted laser engineering net shaping of ZrO<sub>2</sub>-Al<sub>2</sub>O<sub>3</sub> bulk parts: effects on crack suppression, microstructure, and mechanical properties. *Ceramics International*, 44(3), 2752-2760.
- [3] **Hu, Y. B.**, Ning, F. D., Wang, H., Cong, W. L., & Zhao, B. (2018). Laser engineered net shaping of quasi-continuous network microstructural TiB reinforced titanium matrix bulk composites: microstructure and wear performance. *Optics & Laser Technology*, 99, 174-183.
- [4] **Hu, Y. B.**, & Cong, W. L. (2018). A review on laser deposition-additive manufacturing of ceramics and ceramic reinforced metal matrix composites. *Ceramics International*, 44(17), 20599-20612. ([Most download paper](#))
- [5] **Hu, Y. B.**, & Li, J. Z. (2017). Selective laser alloying of elemental titanium and boron powder: thermal models and experiment verification. *Journal of Materials Processing Technology*, 249, 426-432.
- [6] **Hu, Y. B.**, Zhao, B., Ning, F. D., Wang, H., & Cong, W. L. (2017). In-situ ultrafine three-dimensional quasi-continuous network microstructural TiB reinforced titanium matrix composites fabrication using laser engineered net shaping. *Materials Letters*, 195, 116-119.
- [7] **Hu, Y. B.**, Ning, F. D., Wang, X. L., Wang, H., Cong, W. L., & Li, Y. Z. (2017). Laser deposition-additive manufacturing of in situ TiB reinforced titanium matrix composites: TiB growth and part performance. *The International Journal of Advanced Manufacturing Technology*, 93(9-12), 3409-3418.
- [8] **Hu, Y. B.**, & Li, J. Z. (2016). Ultra-short laser melting of copper nanoparticles: a molecular dynamics study. *International Journal of Energy for a Clean Environment*, 17(1), 1-25.

#### Conference Proceedings

- [9] **Hu, Y. B.**, Wang, H., & Cong, W. L. (2019). Laser deposition-additive manufacturing of graphene oxide reinforced IN718 alloys: effects on surface quality, microstructure, and mechanical properties. Accepted at *Proceedings of the 2019 Manufacturing Science and Engineering Conference (MSEC2019-2985)*.

- [10] **Hu, Y. B.**, Wang, H., Li, Y. C., Ning, F. D., & Cong, W. L. (2018). Surface grinding of ZTA parts fabricated by laser engineered net shaping process: effects of ZrO<sub>2</sub> content and ultrasonic vibration. *Proceedings of the 2018 Manufacturing Science and Engineering Conference (MSEC2018-6663)*, June 18 – 22, 2018, College Station, TX, USA. DOI:10.1115/MSEC2018-6663
- [11] **Hu, Y. B.**, Maharubin, S., Cong, W. L. & Tan, Z. (2018). Laser engineered net shaping of titanium-silver alloy for orthopedic implant. *Proceedings of the 2018 Manufacturing Science and Engineering Conference (MSEC2018-6611)*, June 18 – 22, 2018, College Station, TX, USA. DOI:10.1115/MSEC2018-6611
- [12] **Hu, Y. B.**, Wang, H., Ning, F. D., Cong, W. L., & Li, Y. Z. (2017). Surface grinding of optical BK7/K9 glass using rotary ultrasonic machining: an experimental study. *Proceedings of the ASME 2017 International Manufacturing Science and Engineering Conference (MSEC2017-2780)*, June 04 – 08, 2017, Los Angeles, CA, USA. DOI:10.1115/MSEC2017-2780.
- [13] **Hu, Y. B.**, Wang, H., Ning, F. D., & Cong, W. L. (2016). Laser engineered net shaping of commercially pure titanium: effects of fabricating variables. *Proceedings of the ASME 2016 International Manufacturing Science and Engineering Conference (MSEC2016-8812)*, June 27 – July 01, 2016, Blacksburg, VA, USA. DOI:10.1115/MSEC2016-8812.
- [14] **Hu, Y. B.**, Wang, H., Ning, F. D., & Cong, W. L. (2016) Compressive property comparisons between laser engineered net shaping of in situ TiB-Ti composites and CP-Ti materials. *2016 Annual International Solid Freeform Fabrication Symposium*, August 08 – 10, Austin, 2016, TX, USA.